Aus der
Klinik für Neurologie
des Universitätsklinikums Bonn
Direktor: Univ.-Prof. Dr. med. Thomas Klockgether

Bildgebende Biomarker bei degenerativen Ataxieerkrankungen

Habilitationsschrift
zur Erlangung der venia legendi
der Hohen Medizinischen Fakultät
der Rheinischen Friedrich-Wilhelms-Universität Bonn
für das Lehrgebiet
„Neurologie“

Vorgelegt von
Dr. med. Jennifer Faber
aus Andernach
Wissenschaftliche Mitarbeiterin
an der Rheinischen Friedrich-Wilhelms-Universität Bonn
Bonn 2025

Meinem Mann Jonathan und meinen Töchtern Hannah und Ulrike

Die folgenden fünf Originalarbeiten liegen der kumulativen Habilitationsschrift zu Grunde, welche ihre wesentlichen Ergebnisse zusammenfasst und diskutiert.

1. **Faber J**, Giordano I, Jiang X, Kindler C, Spottke A, Acosta-Cabronero J, Nestor PJ, Machts J, Düzel E, Vielhaber S, Speck O, Dudesek A, Kamm C, Scheef L, Klockgether T. Prominent White Matter Involvement in Multiple System Atrophy of Cerebellar Type. *Mov Disord.* 2020; 35(5):816-824 (IF: 10,34); doi: 10.1002/mds.27987
2. Oender D*, **Faber J***, Wilke C, Schaprian T, Lakghomi A, Mengel D, Schöls L, Traschütz A, Fleszar Z, Dufke C, Vielhaber S, Machts J, Giordano I, Grobe-Einsler M, Klopstock T, Stendel C, Boesch S, Nachbauer W, Timmann-Braun D, Thieme AG, Kamm C, Dudesek A, Tallaksen C, Wedding I, Filla A, Schmid M, Synofzik M, Klockgether T. Evolution of Clinical Outcome Measures and Biomarkers in Sporadic Adult-Onset Degenerative Ataxia. *Mov Disord.* 2023; 38(4):654-664 (IF: 9,70); doi: 10.1002/mds.29324
3. **Faber J**, Schaprian T, Berkan K, Reetz K, França MC Jr, de Rezende TJR, Hong J, Liao W, van de Warrenburg B, van Gaalen J, Durr A, Mochel F, Giunti P, Garcia-Moreno H, Schoels L, Hengel H, Synofzik M, Bender B, Oz G, Joers J, de Vries JJ, Kang JS, Timmann-Braun D, Jacobi H, Infante J, Joules R, Romanzetti S, Diedrichsen J, Schmid M, Wolz R, Klockgether T. Regional Brain and Spinal Cord Volume Loss in Spinocerebellar Ataxia Type 3. *Mov Disord.* 2021; 36(10):2273-2281 (IF: 9,70); doi: 10.1002/mds.28610
4. **Faber J***, Kügler D*, Bahrami E*, Heinz LS, Timmann D, Ernst TM, Deike-Hofmann K, Klockgether T, van de Warrenburg B, van Gaalen J, Reetz K, Romanzetti S, Oz G, Joers JM, Diedrichsen J; ESMI MRI Study Group; Reuter M. CerebNet: A fast and reliable deep-learning pipeline for detailed cerebellum sub-segmentation. *Neuroimage*. 2022; 264:119703 (IF: 7,4); doi: 10.1016/ j.neuroimage.2022.119703
5. **Faber J**, Berger M, Carlo W, Hübener-Schmid J, Schaprian T, Santana MM, Grobe-Einsler M, Onder D, Koyak B, Giunti P, Garcia-Moreno H, Gonzalez-Robles C, Lima M, Raposo M, Vieira Melo AR, de Almeida LP, Silva P, Pinto MM, van de Warrenburg BP, van Gaalen J, Jeroen de Vries J, Oz G, Joers JM, Synofzik M, Schöls L, Riess O, Infante J, Manrique L, Timmann D, Thieme A, Jacobi H, Reetz K, Dogan I, Onyike C, Povazan M, Schmahmann J, Ratai EM, Schmid M, Klockgether T. Stage-dependent biomarker changes in spinocerebellar ataxia type. Ann Neurol. 2024 Feb;95(2):400-406. Epub 2023 Dec 5. PMID: 37962377.(IF: 11,20); doi: 10.1002/ana.26824.

Tag der Habilitationskolloquiums: 22.04.2024

1. Inhaltsverzeichnis

Abkürzungsverzeichnis

ASO	Antisense-Oligonukleotid
FRDA	Friedreich-Ataxie
FXTAS	Fragiles X-assoziiertes Tremor-Ataxie-Syndrom
INAS	Inventory of non-ataxia signs
MRT	Magnetresonanztomographie
MSA-C	Multisystematrophie vom zerebellären Typ
NfL	Neurofilament light
PolyQ-SCA	Polyglutamin-Spinozerebelläre Ataxie
RFC1	Replication factor C subunit 1
SARA	Scale for the assessment and rating of ataxia
SAOA	Sporadic adult-onset ataxia
SCA	Spinozerebelläre Ataxie
TBSS	Tract-based spatial statistics
VBM	Voxel-based morphometry

2. Einleitung

2.1. Ataxien

Ataxien sind eine heterogene Gruppe von Erkrankungen. Neben erworbenen Ursachen, wie zum Beispiel alkoholische Kleinhirndegeneration oder Ischämien des Kleinhirns, gibt es genetische und sporadisch-degenerative Formen. Allen Ataxieerkrankungen gemein ist eine Symptomatik aus Gang- und Gleichgewichts- sowie Koordinations- und Sprechstörungen. Ataxien kommen weltweit vor und zählen zu den seltenen Erkrankungen mit einer Prävalenz von 10 - 20 : 100.000 Einwohnern (Tsuji, Onodera et al. 2008, Durr 2010, Ruano, Melo et al. 2014). Einschränkend sollte allerdings erwähnt werden, dass epidemiologische Studien nur in begrenztem Umfang vorliegen und die Zahlen der hereditären Ataxien maßgeblich von der Verfügbarkeit genetischer Testungen abhängen. Die Prävalenz variiert je nach geografischer Lage und ethnischer Zugehörigkeit erheblich, hohe Prävalenzen für SCA2 finden sich etwa auf Kuba (Orozco Diaz, Nodarse Fleites et al. 1990), für SCA3 auf den Azoren (Bettencourt, Santos et al. 2008).

2.1.1. Spinozerbelläre Ataxien

Spinozerebelläre Ataxien (SCA) sind eine heterogene Gruppe autosomal-dominant vererbter Ataxien. Es sind über 40 verschiedene SCAs bisher identifiziert worden. Erst kürzlich wurde eine weiteren SCA identifiziert (Pellerin, Danzi et al. 2023). Der Terminus „spinozerebellär“ wurde ursprünglich gewählt, um die gleichzeitige Beteiligung des Rückenmarks und des Kleinhirns an diesen Erkrankungen zu beschreiben. Bei zahlreichen SCAs ist das Rückenmark jedoch nicht betroffen, gleichzeitig treten pathologische Veränderungen in weiteren Regionen des Nervensystems auf, einschließlich des peripheren Nervensystems. Dennoch wird der Begriff SCA im Allgemeinen zur Bezeichnung der autosomal-dominanten Ataxien verwendet, unabhängig von der Pathologie im Nervensystem.
Die nach aktuellem Kenntnisstand weltweit häufigste Form ist die SCA3. Gemeinsam mit SCA1, SCA2 und SCA6 macht sie über die Hälfte aller SCA-Familien weltweit aus (Paulson 2012, Klockgether, Mariotti et al. 2019). SCA1, 2, 3, 6 sowie 7 und 17 liegt –

wie bei der Huntington-Krankheit - eine Verlängerung einer CAG-Basentriplett-Wiederholung in den jeweiligen krankheitsspezifischen Genen zu Grunde. Die verlängerte CAG-Wiederholungssequenz führt zu einer verlängerten Sequenz von Glutamin in den je resultierenden Proteinen. Diese SCAs als sogenannte Polyglutamin-SCAs, PolyQ-SCAs, zusammengefasst und für einige sind Assays zur Bestimmung des krankheitsspezifischen Proteins, wie beispielsweise ATXN3 bei SCA3, verfügbar (Prudencio, Garcia-Moreno et al. 2020, Hubener-Schmid, Kuhlbrodt et al. 2021). Für weitere SCAs sind genetische Veränderungen, wie etwa Missense-Mutationen, Nonsense-Mutationen, Insertionen oder Deletionen, ursächlich. Darüber hinaus kommen auch andere genetische Veränderungen vor, beispielsweise intronische Mutationen mit verlängerten Wiederholungssequenzen bestimmter Basenfolgen (Paulson, Shakkottai et al. 2017, Ashizawa, Oz et al. 2018, Klockgether, Mariotti et al. 2019). Entsprechend dieser enormen genetischen Heterogenität, sind auch die neuropathologischen Befunde der einzelnen SCAs unterschiedlich. Gemeinsam ist allen SCAs – entsprechend dem Vererbungsmuster – ein durch die jeweilige Mutation bedingter toxischer oder negativer Mechanismus. Für die häufigsten SCAs liegen die meisten neuropathologische Studien vor. Teils, wie beispielsweise bei SCA1, hat auch die Wildtyp-Aktivität einen Einfluss auf den Krankheitsprozess. Ein gemeinsames pathologisches Merkmal aller PolyQ-SCA ist die Aggregation und Anhäufung des krankheitsspezifischen Proteins in intraneuronalen Ablagerungen, meist in den Kernen von Neuronen (Seidel, Siswanto et al. 2012). Weiterhin nicht abschließend geklärt ist, inwieweit die Aggregation der Proteine direkt toxisch wirkt oder eine Art Schutzmaßnahme der Zelle darstellt, um die abnormen Proteine abzutrennen. Einerseits weisen überlebende, nicht untergegangene Neuronen in menschlichen Gehirnen entsprechende Aggregate auf, andererseits behindern die Aggregate zelluläre Prozesse und Homöostase (Gunawardena, Her et al. 2003, Arrasate, Mitra et al. 2004, Seidel, den Dunnen et al. 2010, Duennwald 2011, Gruber, Hornburg et al. 2018). Zunehmend rücken auf zellulärer Ebene, insbesondere bei der SCA3, neben Neuronen auch immer mehr die Gliazellen in den Fokus der krankheitsspezifischen Pathologie (McLoughlin, Moore et al. 2018, Putka, Mato et al. 2023).

Der Erkrankungsbeginn für SCA1, 2 und 3 liegt im mittleren Erwachsenenalter, für SCA6 im höheren Erwachsenenalter. SCA6 zeigt eine reine Kleinhirnpathologie wohingegen, SCA1, 2 und 3 umfassende Neurodegeneration unter Einschluss von

Rückenmark, Basalganglien und des peripheren Nervensystems zeigen (Paulson, Shakkottai et al. 2017, Klockgether, Mariotti et al. 2019). Genetische Untersuchungen sind wichtiger Bestandteil der diagnostischen Abklärung von Ataxieerkrankungen. Im Rahmen der klinischen Diagnostik erfolgt bei bekannter Mutation in der Familie eine gezielte genetische Testung. Bei Hinweisen auf einen autosomal-dominanten Erbgang ohne spezifisch hinweisende klinische Merkmale im Phänotyp, erfolgt eine Paneldiagnostik der häufigsten SCAs. Aber auch bei informativer oder negativer Familienanamnese, letzteres insbesondere bei SCA6, stellen die SCAs bei entsprechendem Erkrankungsalter und nach Ausschluss erworbener Ursachen, mittels Bildgebung und Laborscreening, eine wichtige Differentialdiagnose dar.

Zum aktuellen Zeitpunkt gibt es keine kausale Therapieoption. Die Behandlung und klinische Versorgung von SCAs konzentrieren sich daher auf symptomatische Therapien. Die wesentlichen Bausteine sind regelmäßige Physiotherapie, Ergotherapie und Logopädie sowie die gezielte Behandlung einzelner, nicht-ataktischer Symptome wie etwa Spastik oder ein Restless-Legs-Syndrom. Die Heterogenität der SCAs erschwert letztlich die Entwicklung von Therapien, da spezifische therapeutische Ansätze erforderlich sind. Im Bereich der PolyQ-SCA sind die ersten Phase-I Studien mit dem gentherapeutischen Ansatz sogenannter Antisense-Oligonukleotide (ASO) gestartet (ClinicalTrials.gov Identifier: NCT05160558, NCT05822908). Antisense-Oligonukleotide binden auf Ebene der mRNA und verhindern oder reduzieren so die Synthese des krankheitsspezifischen Proteins. In tierexperimentelle Daten zeigten diese Ansätze vielversprechende Daten (McLoughlin, Moore et al. 2018, Klockgether, Ashizawa et al. 2022). Die erste ASO-Studie in SCA3 wurde allerdings aufgrund von nicht-klinischen Sicherheitsdaten vorzeitig beendet. Gentherapeutische Ansätze sind insofern von besonderem Interesse, da sie (i) direkt auf die Ursache der Erkrankung zielen und (ii) im Falle von Sicherheit und Wirksamkeit eine Behandlung bereits vor Symptombeginn ermöglichen. Damit verbunden ist die Hoffnung, möglicherweise den Symptombeginn zeitlich nach hinten zu verschieben oder gar zu verhindern. Um entsprechende klinische Prüfungen im präsymptomatischen Krankheitsstadium zu ermöglichen, kommt der Identifikation von Biomarkern, insbesondere für Progression und Stratifikation bzw. Prognose, eine besondere Bedeutung zu. Klinisch-neurologische Untersuchungen sind hier, der Abwesenheit von Symptomen geschuldet, nicht sensitiv.

2.1.2. Sporadisch-degenerative Ataxien

Die Diagnose einer sporadisch-degenerativen Ataxie des Erwachsenenalters kann gestellt werden, wenn kein Hinweis auf eine erworbene oder erbliche Ataxie besteht. Im Rahmen der genetischen Diagnostik sollten hier insbesondere die häufigsten spät beginnenden erblichen Ataxien ausgeschlossen wurden. Das hohe Alter bei Erstmanifestation führt häufig dazu, dass die Familienanamnese nicht informativ ist. Dazu zählen neben SCA6, unter anderem auch das Fragile X-assoziierte Tremor-Ataxie-Syndrom (FXTAS) und Friedreich-Ataxie (FRDA, sogenannte late-onset FRDA) sowie insbesondere auch die in den letzten Jahren neu identifizierten ursächliche genetischen Krankheiten replication factor C subunit 1 (RFC1)-Krankheit und SCA27B (Cortese, Simone et al. 2019, Cortese, Tozza et al. 2020, Pellerin, Danzi et al. 2023). Der klinische Phänotyp dieser genetischen Formen ist oftmals mit einer scheinbar sporadischen, spät beginnenden Ataxie vereinbar. Die neu identifizierten Genmutationen und auch umfangreiche Screening-Untersuchungen in Patientenkohorten mit spät beginnender Ataxie zeigen, dass sicherlich ein nicht unerheblicher Prozentsatz der als sporadisch-degenerativ klassifizierten Ataxien durch eine genetische Mutation bedingt sind (Cortese, Tozza et al. 2020, Oender, Faber et al. 2023, Wilke, Pellerin et al. 2023). Innerhalb der sporadischen Ataxien des höheren Erwachsenenalters ist die Multisystematrophie vom zerebellären Typ (MSA-C) als neuropathologisch definierte Entität, abzugrenzen.

2.1.2.1. Multisystematrophie vom zerebellären Typ

Die Multisystematrophie vom zerebellären Typ (MSA-C) ist eine neuropathologisch definierte Entität. Pathognomonisch sind alpha-Synuklein-Einschlüsse in Oligodendroglia.(Wenning, Stefanova et al. 2008). Klinisch ist die MSA durch autonome Störungen und einen rasch progredienten Verlauf gekennzeichnet. Eine definitive Diagnose von MSA erfordert den Nachweis von oligodendroglialen Einschlüssen ihrem Rahmen einer Autopsie (Tu, Galvin et al. 1998, Wakabayashi, Hayashi et al. 1998). Spezifische Diagnosekriterien erlauben die klinische Diagnose einer MSA zu Lebzeiten. Die 2008 etablierten klinischen Diagnosekriterien unterschieden zwischen „wahrscheinlichen“ oder „möglichen“ MSA (Gilman, Wenning

et al. 2008). Sie wurden kürzlich überarbeitet. Die 2022 veröffentlichten Kriterien der Movement Disorder Society unterscheiden zwischen klinisch nachgewiesener („clinically established“) und klinisch wahrscheinlicher („clinically probable“) MSA. Die neuen Diagnosekriterien umfassen nun ein neben klinischen Zeichen ein bildgebendes Kriterium für die Diagnosestellung einer „klinisch nachgewiesenen“ MSA (Wenning, Stankovic et al. 2022). Ziel war es, die diagnostische Genauigkeit zu verbessern, insbesondere in frühen Krankheitsstadien. Eine Validierung der Kriterien in prospektiven klinischen beziehungsweise klinisch-pathologischen Studien muss zwingend noch folgen. Die Diagnosekriterien decken wesentliche klinische Charakteristika ab. Ein Kernsymptom ist das schwere autonome Versagen, etwa orthostatische Dysregulation mit Blutdruckabfall nach Lagewechsel in die aufrechte Position, Dranginkontinenz oder erhöhtes Restharnvolumen. Weiterhin sind rascher Progress insbesondere von Dysarthrie und Dysphagie unterstützende klinische Kriterien in der Diagnosestellung. Als bildgebende Kriterien für die MSA-C werden unter anderem das „hot-cross-bun“-Zeichen sowie Atrophie von Pons und mittlerem Kleinhirnstiel geführt. Diese Abstufung zwischen klinisch nachgewiesener und wahrscheinlicher MSA zeigt bereits, dass insbesondere bei Erkrankungsbeginn die Diagnosestellung erschwert sein kann, solange der klinische Phänotyp nicht vollständig apparent ist. Gleichzeitig ist für die Beratung der Patient*innen aufgrund des zu erwartenden deutlich rascheren Progresses eine wegweisende Diagnosestellung wichtig. Therapeutisch stehen aktuell keine medikamentösen Therapieoptionen zur Verfügung. Eine Phase-II-Studie mit alpha-Synuklein-Antikörpern ist aktuell gestartet (ClinicalTrials.gov Identifier: NCT05526391).

2.1.2.2. Sporadische Ataxien des höheren Erwachsenenalters (SAOA)

Als sporadische Ataxien des Erwachsenenalters (sporadic adult onset ataxia, SAOA) werden Ataxien bezeichnet, die im Erwachsenenalter beginnen, einen progredienten Verlauf aufweisen, ohne Hinweis auf eine genetische oder symptomatische Ursache der Beschwerden sind, und die die Diagnosekriterien für eine MSA (Wenning, Stankovic et al. 2022) nicht erfüllen. Der Ausschluss der häufigsten genetischen Ursachen ist ebenfalls obligat. Üblicherweise ist der Krankheitsverlauf einer SAOA milder als der der MSA-C, es können jedoch auch hier milde autonome Störungen (v.a. der Miktion), sensorische Defizite oder Pyramidenbahnzeichen auftreten. MR-

tomographisch zeigt sich meist eine isolierte zerebelläre Atrophie. Wie bereits im Abschnitt 2.1.2.1 zur MSA-C betont, kann das für die MSA-C charakteristische autonome Versagen erst verzögert nach Beginn der ataktischen Symptome auftreten. Insbesondere in den ersten Jahren nach Auftreten der Ataxie muss mit einer klinischen „Konversion“ gerechnet werden (Oender, Faber et al. 2023). Regelmäßige Wiedervorstellung zur Verlaufsbeurteilung sind daher obligat. Aufgrund der zunehmenden Zahl an identifizierten Mutationen, die ursächlich für Ataxien insbesondere im höheren Erwachsenenalter sind, empfiehlt es sich außerdem, die genetische Diagnostik in regelmäßigen Abständen erneut zu evaluieren und ggf. zu erweitern.

2.1.2.3. Klinische Skalen & Definition Erkrankungsbeginn bei Ataxien

2.1.2.3.1. Scale for the Assessment and Rating of Ataxia, SARA

Die Schweregradbeurteilung einer Ataxie erfolgt mit der Scale for the assessent and rating of ataxia (SARA) (Schmitz-Hubsch, du Montcel et al. 2006). Acht verschiedene Kategorien werden gewichtet beurteilt: Gang (0-8), Stand (0-6), Rumpfstablität beim Sitzen (0-4), Sprechstörung (0-4), Hyper- oder Hypometrie bei Fingerfolgebewegungen (separate Bewertung der rechten und linken Seite mit Mittelwertbildung, 0-4), Beurteilung des Intentionstremors im Finger-Nase-Wechsel (separate Bewertung der rechten und linken Seite mit Mittelwertbildung, 0-4), Beurteilung der Diadochokinese in einer raschen Handbewegung mit Wechsel von Supination zu Pronation (separate Bewertung der rechten und linken Seite mit Mittelwertbildung, 0-4) und schließlich Abweichen im Knie-Hacke-Versuch (separate Bewertung der rechten und linken Seite mit Mittelwertbildung, 0-4). Die Bewertung der einzelnen Kategorien wird zu einem Summenwert addiert. Der resultierende Summenwert liegt zwischen 0, entsprechend keinerlei ataktischer Symptome, und einem Maximalwert von 40, entsprechend der größtmöglichen Ausprägung der Ataxie. Die Durchführung und Beurteilung sollte von entsprechend geschulten Personen erfolgen. Es steht ein Trainingstool mit der Möglichkeit einer Zertifizierung zur Verfügung (Grobe-Einsler, Amin et al. 2023). Die erfasste Symptomatik wird in der Gesamtheit beurteilt, es erfolgt keinerlei Unterscheidung, ob diese durch andere nicht-

ataktische Symptome neurologischer oder nicht-neurologischer Art bzw. Komorbiditäten bedingt ist. Beispielsweise kann eine Polyneuropathie die Gang- und Standfähigkeiten deutlich beeinträchtigen, oder auch eine kurz zurückliegende Hüft-Operation. Allerdings zeigen Untersuchungen einer verkürzten Variante des SARA eine hohe tagesformabhängige Fluktuation (Grobe-Einsler, Taheri Amin et al. 2021). Patient*innen führten im häuslichen Umfeld eine verkürzte Form des SARA zweimal täglich über 14 Tage durch und nahmen dies per Video auf. Die Aufnahmen (Ablauf, Abstände etc.) waren standardisiert. Die Videos wurden von geschulten Experten beurteilt. Einige Patient*innen zeigten eine hohe Fluktuation mit im Maximum Abweichungen zwischen Minimal- und Maximalwert von bis zu 5,5 Punkten. Dies reflektiert die häufig auch von Patienten angegeben Fluktuationen. Dies gilt es sicher zu beachten, im Hinblick auf die Beurteilung bei kleinen Fallzahlen, der Progression und auch im Hinblick auf die Planung klinischer Studien, wo SARA als sogenannter „Outcome“-Parameter den Zielpunkt einer klinischen Prüfung markiert. SARA als Instrument zur Erfassung von Ataxieschwere im Verlauf, das heißt als Progressionsmarker, ist etabliert. Für eine Vielzahl an vererbten als auch degenerativen Ataxien lagen in longitudinalen Beobachtungsstudien die jährlichen Progressionsraten meist zwischen einem und zwei Punkten Zunahme des SARA Summenwertes (Jacobi, du Montcel et al. 2015, Reetz, Dogan et al. 2021, Cunha, Petit et al. 2023, Oender, Faber et al. 2023, Traschutz, Adarmes-Gomez et al. 2023). Abschließend zu erwähnen ist, noch ein festgelegter Grenzwert. Im Rahmen der initialen Validierungskohorte an Gesunden wurde ein Schwellenwert von 3 Punkten festgelegt, entsprechend des Mittelwertes plus zwei Standardabweichungen. Bei einem SARA-Summenwert von 3 oder mehr Punkten werden die Untersuchten als "ataktisch" bewertet, bei SARA-Summenwert < 3 spricht man von "nicht-ataktisch". Bei Personen, die im Rahmen einer genetischen Untersuchung als Mutationsträger*innen beispielsweise einer SCA identifiziert wurden, wird zudem oftmals der Begriff "prä-ataktisch" verwendet. Aufgrund des autosomal-dominanten Erbgangs ist von der Entwicklung einer Ataxie im Verlauf auszugehen, sodass der Terminus "prä" hier gerechtfertigt ist. Im Gruppenvergleich zeigt bei sogenannten prä-ataktischen Mutationsträger*innen, oftmals ein leicht erhöhter Mittelwert des SARA, dessen Unterschied zu gesunden Kontrollen aber keine statistische Signifikanz erreicht (Jacobi, du Montcel et al. 2020, Faber, Schaprian et al. 2021).

2.1.2.3.2. Inventory of non-ataxia signs, INAS

Mit Ausnahme weniger Entitäten, wie beispielsweise die SCA6, zeigen zahlreiche degenerative Ataxieerkrankungen neben dem Kernsymptom der Ataxie weitere neurologische Symptome. Mit dem Inventory of non-ataxia signs (INAS) werden zahlreiche neurologische Symptome erfasst (Jacobi, Rakowicz et al. 2013). Die folgenden neurologischen Symptome werden erfasst: Hyperreflexie, Areflexie, Babinsi-Reflex, Spastik, Paresen, Muskelatrophie, Faszikulationen, Myoklonus, Rigidität, Chorea/Dyskinesie, Dystonie, Ruhetremor, sensorische Symptome in Form von Pallästhesie bimalleolär, Urinkontinenz, kognitive Dysfunktion und die Hirnstamm-assoziierten Okulomotirkstörungen verlangsamte Sakkaden sowie horizontale und vertikale Blickparese. Jedes der genannten Symptome wird bei Vorhandensein, unabhängig von der Ausprägung als „vorliegend“ gewertet. Daraus ergibt sich eine Anzahl von vorhandenen neurologischen Symptomen, die als INAS count bezeichnet wird. Der theoretische Maximalwert beträgt 16. Bis auf die Okulomotorikstörungen werden die übrigen Symptome zudem in Ihrem Schweregrade abgestuft erfasst. Neben den gelisteten Symptomen werden die folgenden weiteren Symptome erfasst, fließen aber nicht in den Summenwert ein: Downbeat-Nystagmus bei Fixation, horizontaler und vertikaler Blickrichtungsnystagmus, „square wave jerks“, hypo- und hypermetrische Sakkaden, sakkadierte Blickfolge, Sehschärfe, Diplopie sowie Dysphagie. Wenngleich zahlreiche degenerative Ataxien weitere neurologische Symptome aufweisen, so macht ein Vergleich der INAS-Werte zwischen Erkrankungen nur als ungefähre Abschätzung weiterer, nicht-ataktischer Symptome Sinn. Einschränkend soll darauf hingewiesen werden, dass ein INAS count von 4 in durchaus verschiedenen Konstellationen klinische sehr unterschiedlicher Phänotypen erreicht werden kann. Etwa beim gleichzeitigen Vorliegen von Areflexie, sensibler Störung der Pallästhesie, distal betonter Parese und Urininkontinenz als auch beim gleichzeitigen Vorliegen von Rigidität, positivem Babinski-Zeichen, Hyperreflexie und Spastik. Innerhalb einer Erkrankung hingegen kann der INAS und dessen Progression eine wesentliche Ergänzung darstellen. Eine Aufschlüsselung nach Symptomatik sollte je nach Fragestellung erfolgen.

2.1.2.3.3. Einteilung von Krankheitsstadien

Für Ataxien wurden verschiedene Stadieneinteilungen vorgeschlagen. Als Teil einer für die FRDA entwickelten klinischen Skala wurde eine funktionelle, auf dem Schweregrad der Gangstörung beruhende Einteilung entwickelt. Diese Einteilung sieht Abstufungen zwischen 0 (unbeeinträchtigt) bis 6 (rollstuhlgebunden oder bettlägerig) vor (Lynch, Farmer et al. 2006). Zwischenwerte in 0,5-Abständen sind möglich, sofern eine eindeutige Zuordnung zu den ganzzahligen Werten nicht möglich ist. Andere Stadieneinteilungen orientieren sich ebenfalls primär an der Gangstörung, erlauben aber eine Erhebung ohne klinische Untersuchung, beispielsweise durch Telefoninterviews. Hier erfolgt eine Abstufung in fünf Stadien zwischen „normal“, „Vorliegen einer Gangstörung/ataktisch“, „Notwendigkeit zur Nutzung einer Gehhilfe“, „Notwendigkeit zur Nutzung eines Rollstuhls“ sowie „Tod“ unterschieden (Klockgether, Ludtke et al. 1998). Die Einteilung in Krankheitsstadien eignet sich insbesondere dafür, Meilensteine der klinischen Verschlechterung zu erfassen.

2.1.2.3.4. Definition Symptombeginn & geschätzte Zeit bis Symptombeginn

Der Symptombeginn wird üblicherweise als vom Patienten selbst wahrgenommener Beginn einer Gangstörung definiert (Klockgether, Ludtke et al. 1998, Jacobi, du Montcel et al. 2020). Es gibt andere Ansätze, die das erste Symptom, das auftritt, wie beispielsweise Doppelbilder, als Symptombeginn werten. Basierend auf der Definition durch die beginnende Gangstörung wurden Schätzmodelle entwickelt, die bei den häufigsten SCAs eine Abschätzung der Zeit bis zum Symptombeginn erlauben. In die Berechnung fließt üblicherweise die Anzahl der CAG-Wiederholungen, also der genetischen Veränderungen ein, und gegebenenfalls noch das aktuelle Alter. Hierbei zeigten sich teilweise Abweichungen je nach Patientenkollektiv (Tezenas du Montcel, Durr et al. 2014, de Mattos, Leotti et al. 2019, Peng, Chen et al. 2021). Diese Schätzmodelle, mit der geschätzten Zeit bis zum Symptombeginn erlauben die Darstellung von Mutationsträgern vor und nach Symptombeginn auf einer

gemeinsamen Zeitachse. So ist es möglich, den Zeitverlauf verschiedener Parameter weitgehend kontinuierlich abzubilden. Einschränkend ist darauf hinzuweisen, dass es sich um Schätzungen handelt, die keinesfalls eine exakte Vorhersage für den Einzelfall erlauben und im Mittel eine tendenzielle Abweichung vom klinisch beobachteten Symptombeginn haben, der in der Regel vor dem errechneten lag (Jacobi, du Montcel et al. 2020). Allerdings ist auch die retrospektive Angabe unsicher: Angaben von Patienten und Angehörigen unterschieden sich im Mittel um ein Jahr (Globas, du Montcel et al. 2008).

2.2. Strukturelle MRT-Bildgebung bei Ataxien

Strukturelle Bildgebung mittels Magnetresonanztomographie (MRT) ist unerlässlicher Bestandteil im Rahmen der Diagnosestellung von Ataxieerkrankungen. Primäres Ziel ist es, erworbene Ursachen auszuschließen, sekundär können bildgebende Veränderungen wichtige Hinweise für die Diagnosestellung leisten. Strukturelle, durch MRT diagnostizierbare Veränderungen, die eine (erworbene) Ataxie zur Folge haben, sind beispielsweise Ischämien der hinteren Schädelgrube, aber auch entlang der zerebellären Projektionen, sowie entzündliche Veränderungen oder Raumforderungen (Marek, Paus et al. 2015, Stoodley, MacMore et al. 2016). Daneben kommt beispielsweise eine superfizielle Hämosiderose als Ursache von Ataxie in Betracht (Fearnley, Stevens et al. 1995, Weidauer, Neuhaus et al. 2023). Für die Diagnosestellung von degenerativen Ataxien sind das Ausmaß und die Verteilung von Atrophie des Kleinhirns, der Kleinhirnstiele, des Hirnstamms, des Rückenmarks und der Basalganglien von Bedeutung. Hinweise auf die zugrundeliegende Diagnose sind beispielsweise die isolierte, diffus verteilte Kleinhirnatrophie bei SCA6 oder die Atrophie des Kleinhirnwurms bei RFC1. Darüber hinaus gibt es für bestimmte Krankheiten charakteristische Signalveränderungen. Zu Letzteren zählt beispielsweise das sogenannte „hot-cross-bun“-Zeichen bei MSA-C. Bei der MSA-C wurde, wie in Abschnitt 2.1.2.1 bereits erläutert, das Vorhandensein von mindestens einem bildgebenden Merkmal als notwendige Voraussetzung in der Diagnosestellung einer klinisch nachgewiesenen MSA etabliert (Wenning, Stankovic et al. 2022).

Die strukturelle, diagnostische Bildgebung bei Ataxien sollte eine T1- und T2-gewichtete Bildgebung, umfassen, idealerweise ergänzt um DWI und Eisen-sensitive

Sequenzen. Verlaufsbildgebungen sind in der Regel nur bei sporadischen, bisher nicht als MSA-C klassifizierten Ataxien sowie bei klinisch unerwarteter Symptomatik und Befundwechsel indiziert. Für die Verlaufsbeurteilung nach Diagnosestellung hat MRT-Bildgebung im klinischen Kontext keine Relevanz. Verteilung und Muster der mittels MRT-Bildgebung nachweisbaren neurodegenerativen Veränderungen sind von wissenschaftlichem Interesse (Oz, Harding et al. 2020). Relevante Fragestellung ergeben im Bereich bildgebende Biomarker (i) zur Unterstützung der Diagnostik, wie beispielsweise bei MSA-C (Massey, Micallef et al. 2012, Carre, Dietemann et al. 2020, Faber, Giordano et al. 2020, Pellecchia, Stankovic et al. 2020), und (ii) als Progressionsmarker sowie als Parameter Stratifikation von Patient*innen, was insbesondere bei SCAs relevant ist. Letzteres umfasst insbesondere auch Veränderungen, die bereits vor dem klinischen Beginn der Ataxie auftreten. (Reetz, Costa et al. 2013, Adanyeguh, Henry et al. 2015, Reetz, Rodriguez-Labrada et al. 2018, Rezende, de Paiva et al. 2018). Neben den klassischen strukturellen MRT, T1/T2-Wichtung und diffusionsgewichtete MRT, sind, weitere strukturelle MRT-Aufnahmen zunehmend Gegenstand der Forschung. Hierzu zählen unter anderem Eisen-sensitive Sequenzen und die quantitativen Suszeptibilitätskartierung oder MR-Spektroskopie (Harding, Raniga et al. 2016) sowie Untersuchungen in Hochfeld-MRT (Stefanescu, Dohnalek et al. 2015, Joers, Deelchand et al. 2018). Insbesondere die Hochfeld-MRT mit dem starken exponentiellen Abfall des Magnetfeldes stellt eine Herausforderung dar, wenn infratentorielle Strukturen miterfasst werden sollen.

Im Folgenden werden die klassischen strukturellen MRT, T1/T2-Wichtung und diffusionsgewichtete MRT, näher dargestellt. Ziel ist die Identifikation von messbaren, bildgebenden Biomarkern, die entsprechend als diagnostische, Progressions- oder Stratifikations- bzw. prognostische Biomarker bezeichnet werden. In der Beurteilung von Veränderungen, beispielsweise zwischen verschiedenen Erkrankungen oder Patient*innen und Gesunden muss zwischen Verfahren unterschieden werden, die im Wesentlichen Gruppenunterschiede darstellen und solchen, die darüber hinaus auch die Möglichkeit bieten, über die Zeit den Verlauf von Degeneration intra-individuell abzubilden. Zu den Verfahren, die im wesentlichen Gruppenunterschiede darstellen gehören beispielsweise die Voxel-basierte Morphometrie (VBM) für die Beurteilung von Atrophien der grauen und weißen Substanz (Ashburner and Friston 2000, Ashburner 2007) mit Optionen für die Kleinhirn-optimierte VBM (Diedrichsen, Balsters et al. 2009, Diedrichsen and Zotow 2015) oder tract-based spatial statistics (TBSS) für

die Beurteilung von Veränderungen von Parametern, die aus diffusionsgewichteter Bildgebung abgeleitet werden. Übliche Parameter hier sind die fraktionale Anisotropie, ein Maß für die Gerichtetheit von Diffusion, sowie die mittlere Diffusivität, axiale und radiale Diffusion. Diese aus diffusionsgewichteter Bildgebung abgeleiteten Parameter eigenen sich im Besonderen um mikrostrukturelle Veränderungen in der weißen Substanz zu untersuchen und insbesondere die fraktionale Anisotropie wird oftmals als Marker für die Integrität der weißen Substanz verwendet. Beide Verfahren haben eine relativ hohe räumliche Auflösung und eigenen sich, um Verteilungsmuster von Veränderungen zu identifizieren (Hernandez-Castillo, King et al. 2018, Rezende, de Paiva et al. 2018, Piccinin, Rezende et al. 2020). Sie bieten einen ersten Anhaltspunkt, wo Veränderungen liegen. Auf entsprechenden Ergebnissen können andere Verfahren mit dem Vorteil der Darstellbarkeit intra-individueller Veränderungen aufbauen. Hierzu zählen etwa Volumetrie oder auch regional begrenzte Auslese bestimmter Parameter, entweder auf eine sogenannte „region of interest“ bezogen oder bestimmte anatomische Strukturen, etwa Fasertrakte. Exemplarisch wäre etwa das Vorgehen mittels VBM und TBSS Areale mit Veränderungen zwischen Patient*innen und Gesunden zu identifizieren und im Anschluss diese dann gezielt volumetrisch zu untersuchen oder aber dort „region of interest“ auszuwählen. Zeigen sich beispielsweise in der VBM Hinweise auf eine Atrophie der grauen Substanz des Kleinhirns und in der TBSS Veränderungen entlang des kortikospinalen Traktes, sind volumetrische Auswertungen des Kleinhirns und Auswertungen der Diffusionsparameter entlang des kortikospinalen Traktes sinnvolle weitergehende Analysen sein.

2.3. Zielsetzung

Die folgenden Kapitel stellen die Ergebnisse von insgesamt fünf klinischen Arbeiten zu bildgebenden Biomarkern bei degenerativen Ataxien dar. Ziel war es, bildgebende Veränderungen, die potentiell bildgebende Biomarkerkandidaten darstellen, zu identifizieren und Methoden zu deren Verbesserung zu etablieren. Der Fokus lag auf quantitativen Markern, schloss aber auch quantitative Marker mit ein. Bei den sporadischen Ataxien, SAOA und MSA-C, liegt der Schwerpunkt auf der Identifikation von diagnostischen Biomarker, die eine Unterscheidung zwischen MSA-C und SAOA erlauben, insbesondere in frühen Krankheitsstadien, in denen die Diskrimination noch nicht eindeutig anhand des klinischen Phänotyps erfolgen kann. Bei den SCAs lag der Schwerpunkt auf der Identifikation von bildgebenden Veränderungen im präataktischen Krankheitsstadium. In diesem Stadium kommt der Identifikation von Biomarkern eine besondere Bedeutung zu, da klinische Skalen in der Abwesenheit von Symptomen keine ausreichende Sensitivität besitzen.

3. Ergebnisteil

3.1. **Faber J**, Giordano I, Jiang X, Kindler C, Spottke A, Acosta-Cabronero J, Nestor PJ, Machts J, Düzel E, Vielhaber S, Speck O, Dudesek A, Kamm C, Scheef L, Klockgether T. Prominent White Matter Involvement in Multiple System Atrophy of Cerebellar Type. *Mov Disord*. 2020; 35(5):816-824.

Zielsetzung der Arbeit – Zielsetzung der Arbeit war es, strukturelle Unterschiede von SAOA und MSA-C zu untersuchen.

Methoden und Ergebnisse – Eingeschlossen wurden Teilnehmer einer Beobachtungsstudie mit standardisierter klinischer Untersuchung sowie standardisierter MRT-Bildgebung. Es wurden 12 MSA-C sowie 31 SAOA- und 55 gesunde Kontrollen untersucht. Die Diagnose MSA-C erfolgte anhand der klinischen Kriterien für eine wahrscheinliche MSA-C nach Gilman (Gilman, Wenning et al. 2008). Klinisch-neurologisch wurde zur Beurteilung des Schweregrades der Ataxie SARA (Schmitz-Hubsch, du Montcel et al. 2006) und zur Beurteilung der weiteren neurologischen Symptome INAS (Jacobi, Rakowicz et al. 2013) verwendet. Die demographischen und klinischen Charakteristika der Kohorte sind in Tabelle 1 (Faber et al., Mov Disord. 2020, p. 2) aufgeführt. Die MRT-Bildgebung umfasste T1-, sowie Diffusions-gewichtete Sequenzen (Details zum MRT Protokoll siehe Abschnitt „Imaging Acquisition and Preprocessing“, Faber et al., Mov Disord. 2020, p. 3). Die Auswertung erfolgte mittels Voxel-basierter Morphometrie (VBM) des Gesamthirns sowie spezifisch von Kleinhirn und Hirnstamm sowie „tract-based spatial statistics“, TBSS, und Traktographie. Die diffusionsgewichteten Aufnahmen wurden mittels üblichen Vorverarbeitungsverfahren der Tensorbildgebung ausgewertet und die daraus berechnete fraktionale Anisotropie als Marker für die strukturelle Integrität der weißen Substanz interpretiert.

Die VBM zeigte bei beiden Patientengruppen im Vergleich zu gesunden Kontrollen einen Volumenverlust der grauen und weißen Substanz im Bereich des Kleinhirns. Die Atrophie der grauen Substanz war prominent insbesondere in den Kleinhirnarealen, die mit motorischen Funktionen assoziiert sind. Darüber hinaus zeigte MSA-C eine Reduktion der weißen Substanz im Hirnstamm im Vergleich zu gesunden Kontrollen. Zwischen den beiden Patientengruppen fand sich kein statistisch signifikanter Unterschied im Volumen der grauen oder weißen Substanz. In der TBSS zeigte bei

MSA-C sowohl im Vergleich zu SAOA als auch zu den gesunden Kontrollen eine verringerte fraktionelle Anisotropie im Hirnstamm und im Kleinhirn. In der Traktographie fand sich eine reduzierte fraktionelle Anisotropie entlang des kortikospinalen Trakts ebenfalls nur bei MSA-C.

Schlussfolgerungen – Obwohl in der untersuchten Patientenkohorte Ausmaß und Verteilungsmuster der Atrophie der grauen und weißen Substanz zwischen MSA-C- und SAOA vergleichbar waren, zeigten die Ergebnisse der diffusionsgewichteten Sequenzen eine ausgeprägte mikrostrukturelle Beteiligung der weißen Substanz bei den MSA-C, die bei SAOA nicht vorhanden war. Die Ergebnisse unterstreichen, dass mikrostrukturelle Veränderungen der weißen Substanz zur Unterscheidung zwischen beiden Erkrankungen hilfreich sein können.

RESEARCH ARTICLE

Prominent White Matter Involvement in Multiple System Atrophy of Cerebellar Type

Jennifer Faber, MD,[1,2*] Ilaria Giordano, MD,[1,2] Xueyan Jiang, MS,[1] Christine Kindler, MD,[1,2] Annika Spottke, MD,[1,2] Julio Acosta-Cabronero, PhD,[3] Peter J. Nestor, MD, PhD,[4,5] Judith Machts, PhD,[6,7] Emrah Düzel, MD, PhD,[6,7] Stefan Vielhaber, MD,[6,7] Oliver Speck, PhD,[6,8,9] Ales Dudesek, MD,[10] Christoph Kamm, MD,[10] Lukas Scheef, MD, PhD,[1,11] and Thomas Klockgether, MD, PhD[1,2]

[1]*Clinical Research, German Center for Neurodegenerative Diseases, Bonn, Germany*
[2]*Department of Neurology, University Hospital Bonn, Germany*
[3]*Tenoke Ltd., Cambridge, United Kingdom*
[4]*Queensland Brain Institute, University of Queensland, Brisbane, Australia*
[5]*Neuroscience and Cognitive Health Program, Mater Hospital, South Brisbane, Australia*
[6]*German Center for Neurodegenerative Diseases, Magdeburg, Germany*
[7]*Department of Neurology, Otto-von-Guericke University, Magdeburg, Germany*
[8]*Department of Biomedical Magnetic Resonance, Faculty for Natural Sciences, Otto-von-Guericke University, Magdeburg, Germany*
[9]*Center for Behavioral Brain Sciences, Magdeburg, Germany*
[10]*Department of Neurology, University of Rostock, Rostock, Germany*
[11]*Department of Radiology, University of Bonn, Bonn, Germany*

ABSTRACT: Background: Sporadic degenerative ataxia patients fall into 2 major groups: multiple system atrophy with predominant cerebellar ataxia (MSA-C) and sporadic adult-onset ataxia (SAOA). Both groups have cerebellar volume loss, but little is known about the differential involvement of gray and white matter in MSA-C when compared with SAOA.
Objectives: The objective of this study was to identify structural differences of brain gray and white matter between both patient groups.
Methods: We used magnetic resonance imaging to acquire T1-weighted images and diffusion tensor images from 12 MSA-C patients, 31 SAOA patients, and 55 healthy controls. Magnetic resonance imaging data were analyzed with voxel-based-morphometry, tract-based spatial statistics, and tractography-based regional diffusion tensor images analysis.
Results: Whole-brain and cerebellar-focused voxel-based-morphometry analysis showed gray matter volume loss in both patient groups when compared with healthy controls, specifically in the cerebellar areas subserving sensorimotor functions. When compared with controls, the SAOA and MSA-C patients showed white matter loss in the cerebellum, whereas brainstem white matter was reduced only in the MSA-C patients. The tract-based spatial statistics revealed reduced fractional anisotropy within the pons and cerebellum in the MSA-C patients both in comparison with the SAOA patients and healthy controls. In addition, tractography-based regional analysis showed reduced fractional anisotropy along the corticospinal tracts in MSA-C, but not SAOA.
Conclusion: Although in our cohort extent and distribution of gray and white matter loss were similar between the MSA-C and SAOA patients, magnetic resonance imaging data showed prominent microstructural white matter involvement in the MSA-C patients that was not present in the SAOA patients. Our findings highlight the significance of microstructural white matter changes in the differentiation between both conditions. © 2020 The Authors. *Movement Disorders* published by Wiley Periodicals, Inc. on behalf of International Parkinson and Movement Disorder Society.

Key Words: diffusion tensor imaging; multiple system atrophy; sporadic ataxia; voxel based morphometry

*__Correspondence to:__ Dr. Jennifer Faber, Deutsches Zentrum für Neurodegenerative Erkrankungen, Klinische Forschung, Venusberg-Campus 1, 53127 Bonn; E-mail: jennifer.faber@dzne.de

Relevant conflicts of interests/financial disclosures: Nothing to report.

Published online 00 Month 2020 in Wiley Online Library (wileyonlinelibrary.com).

Received: 4 August 2019; **Revised:** 27 December 2019; **Accepted:** 30 December 2019

Published online 00 Month 2020 in Wiley Online Library (wileyonlinelibrary.com). DOI: 10.1002/mds.27987

Progressive ataxia frequently starts in adults without a familial background. These patients may suffer from an acquired ataxia, such as alcoholic cerebellar degeneration or paraneoplastic cerebellar degeneration. Others have a genetic cause despite negative family history.[1-3] In the majority of these patients, however, a genetic or acquired cause of ataxia cannot be identified suggesting a sporadic degenerative ataxia.

Sporadic degenerative ataxia patients fall into 2 major groups. In 1 group, the underlying brain disease is multiple system atrophy (MSA). MSA is characterized by widespread degeneration of the cerebellum, brainstem, basal ganglia, and spinal cord. Some of these patients have prominent degeneration of cerebellum and brainstem and typically present with sporadic ataxia (MSA with predominant cerebellar ataxia [MSA-C]), whereas those with prominent basal ganglia degeneration suffer from parkinsonism (MSA with predominant parkinsonism). The definitive diagnosis of MSA requires demonstration of oligodendroglial inclusions at autopsy,[4,5] but a probable diagnosis can be made with high predictive accuracy on clinical grounds alone. The essential diagnostic feature of MSA is severe autonomic failure defined by orthostatic blood pressure drop of at least 30 mmHg systolic after standing from a recumbent position or urinary incontinence.[6] The second group of sporadic ataxia is clinically distinguished from MSA-C by the lasting absence of severe autonomic failure. These patients have been designated as idiopathic late-onset cerebellar ataxia or sporadic adult onset ataxia (SAOA) of unknown etiology.[7,8] The few SAOA cases that have come to autopsy had degeneration restricted to the cerebellar cortex and inferior olives,[9,10] but it is not clear whether SAOA is a disease entity or rather a group of different conditions presenting with a uniform clinical syndrome of progressive cerebellar ataxia. Compared with MSA, SAOA takes a more benign course.[11,12] In the first years after ataxia onset, a distinction between MSA-C and SAOA is often not possible, as severe autonomic failure defining MSA-C may only manifest several years after ataxia onset.

Atrophy of the cerebellum and brainstem are common features of MSA-C and SAOA.[13-22] In addition, microstructural alterations of the white matter have been reported in previous studies in MSA-C patients.[21-24] We used multimodal imaging approach to assess structural alteration of the brain in a deeply phenotyped cohort of MSA-C and SAOA patients to identify magnetic resonance imaging (MRI) parameters that might help to differentiate both conditions.

Methods

Participants

All patients were participants of the SPORTAX study, a prospective natural history study that longitudinally assessed the disease course of sporadic ataxia in elderly patients (Sporadic Degenerative Ataxia With Adult Onset: Natural History Study (SPORTAX-NHS)).[11] The SPORTAX inclusion criteria are as follows: (1) progressive ataxia, (2) ataxia onset after the age of 40 years, (3) informative and negative family history (no similar disorders in first-degree and second-degree relatives; parents older than 50 years, or, if not alive, age at death of more than 50 years; no consanguinity of parents), and (4) no established acquired cause of ataxia (for details see Supporting Information Table 1). Participants were classified as MSA-C if they fulfilled the criteria for clinically probable MSA-C as defined in the second consensus statement by Gilman and colleagues.[6] In particular, all MSA-C patients presented with autonomic failure (Supporting Information Table 1 and Supporting Information Table 3). Participants not fulfilling the criteria for clinically probable MSA-C were classified as SAOA. The SPORTAX assessment protocol includes the Unified Multiple System Atrophy Rating Scale,[25] the Scale for the Assessment and Rating of Ataxia (SARA),[26] and the Inventory of Non-Ataxia Signs (INAS).[27] Detailed group characteristics are given in Table 1 and Supporting Information Table 3.

At 2 SPORTAX study sites (Bonn and Magdeburg), a MRI was acquired on all participants who gave consent and were able and willing to undergo MRI. To compare patient groups with healthy controls, we used MRI scans of healthy controls who participated in parallel studies using the identical MRI protocol. MRI scans of 12 MSA-C patients, 31 SAOA patients, and 55 healthy controls were included in the analysis (for details, see Supporting Information Table 2).

TABLE 1. Demographic characteristics of the study population

Group	Number (Site BN/Site MD)	Mean Age at Scan (Min–Max, SD)	Male (Percentage)	Mean Age of Onset (SD)	Mean Disease Duration in Years (SD)	Mean SARA Sum Score (SD)	Mean INAS Score (SD)	Mean UMSARS II Score (SD)
SAOA	31 (6/25)	64.2 (43–80, 10.6)	18 (58.1)	57.1 (10.6)	7.1 (5.5)[a]	13.2 (1.4)[a]	1.68 (1.3)[a]	13.2 (6.1)[a]
MSA-C	12 (9/3)	62.8 (46–74, 7.7)	7 (58.3)	58.5 (7.3)	4.0 (1.7)[a]	17.0 (3.7)[a]	4.33 (1.6)[a]	22.5 (8.2)[a]
HC	55 (18/37)	64.7 (46–78, 8.0)	21 (38.2)	NA	NA	NA	NA	NA

BN, Bonn; MD, Magdeburg; Min = minimum; Max = maximum; SD, standard deviation; SARA, Scale for the Assessment and Rating of Ataxia; INAS, Inventory of Non-Ataxia Signs; UMSARS, Unified Multiple System Atrophy Rating Scale; SAOA, sporadic adult-onset ataxia; MSA-C, multiple system atrophy with predominant cerebellar ataxia; HC, healthy control; NA, not available.
[a]Significant difference between SAOA and MSA-C patients, $P < 0.01$.

The study was approved by the local ethics committees. All participants provided written informed consent. This study is registered with ClinicalTrials.gov (NCT02701036).

Imaging Acquisition and Preprocessing

MRIs were acquired at both sites using a Siemens 3T scanner (Trio Tim in Bonn and Verio in Magdeburg, both Siemens Medical Systems, Erlangen, Germany). Both sites were equipped with the same gradient system and head coils (32 channel head coil) and used the same software release and MRI protocols.

Isotropic structural T1 images were acquired using a magnetization-prepared rapid gradient echo sequence with the following parameters: repetition time (TR) = 2500 ms, echo time (TE) = 4.37 ms, inversion time (TI) = 1100 ms, flip angle = 7°, receiver bandwith 140 Hz/Px, field of view = 256 mm × 256 mm × 192 mm with a voxel size of 1 mm isotropic, partial Fourier factor 7/8, and parallel imaging acceleration factor 2 (24 integrated reference lines) along the primary phase endcoding direction (anterior – posterior). Diffusion-weighted images were acquired using a twice-refocused single-shot echo planar imaging sequence with the following parameters: TR = 12100 ms, TE = 88 ms, field of view = 240 mm x 240 mm, 72 axial slices, with a voxel size of 2 mm isotropic, 1 scan without diffusion weighting (b0), and 30 diffusion-encoding directions with a b-value of 1000s/mm^2.

To reduce the sources of variance between scanners, several steps were taken before starting the study to harmonize the imaging methods across the participating sites. Both sites used SIEMENS scanners, and the imaging sequences were identical. The scans were acquired following the guidelines of the Imaging Network of the German Center for Neurodegeneration. For quality assurance and assessment, several steps were taken. The German Center for Neurodegeneration imaging network qualified each MRI site with a traveling head measurement prior to the start of the study and then provided every site with detailed standard operating procedures for the implementation of each protocol. All radiographers who operated MRIs in the study underwent centralized training to implement the standard operating procedures (ie, participants' positioning in the MRI scanner, sequence preparation steps, image angulation, participant instruction, and testing). A small MRI phantom built and designed by the American College of Radiology was used to monitor the performance of the MRI systems on a weekly basis. In addition, all scans had to pass a semiautomated check for conformity and scan quality during the data collection.

We included a bias field correction using the Advanced Normalization Tools software (http://stnava.github.io/ANTs). Spatially normalized T1 data were compared voxel-wise by using a conventional voxel-based morphometry (VBM) tool[28] for whole-brain analysis and the spatially unbiased infratentorial template (SUIT) with the corresponding toolbox for the cerebellar-focused analysis.[29] Both tools are included in the MATLAB-based statistical parametric mapping toolbox (MathWorks, Natick, Massachusetts, USA, https://www.fil.ion.ucl.ac.uk/spm/software/spm12). For SUIT-based analysis, all automatically generated cerebellar masks were visually inspected and, where necessary, manually corrected using FSLView as a part of the University of Oxford Centre for Functional MRI of the Brain, UK, (FMRIB) Software Library.[30] For spatial normalization in both pipelines, we used the Diffeomorphic Anatomical Registration using the exponentiated lie algebra algorithm with default settings including the multiplication by the determinate of the Jacobian matrix of deformation fields (modulation) to preserve local tissue volume during normalization.[29,31] For whole-brain VBM, gray and white matter probability segments were smoothed with a 8-mm Gaussian smoothing kernel (full-width at half-maximum (FWHM) = 8 mm), whereas for the SUIT pipeline cerebellar gray and white matter segments were smoothed using a 4-mm Gaussian kernel (FWHM = 4 mm).

Diffusion data were analyzed by using tract-based spatial statistics (TBSS)[32] for whole-brain analysis, as included in the FMRIB Software Library.[30] For tract-based regional analysis, we performed automated fiber-tract quantification (https://github.com/yeatmanlab/AFQ).[33] Diffusion data were preprocessed. First, all 30 within-subject diffusion-weighted images were aligned to the b0 scan. Affine transformations were calculated using the Advanced Normalization Tools software. Second, two preprocessing pipelines were used in this study: for the TBSS analysis, preprocessing included eddy current correction and tensor fitting as provided within the FMRIB's diffusion toolbox (https://fsl.fmrib.ox.ac.uk/fsl/fslwiki/FDT). For regional analysis, preprocessing also included eddy current correction and tensor-fitting steps, as included in the Vistasoft mrDiffusion software distribution (https://github.com/vistalab/vistasoft/, Stanford University, CA, USA). For TBSS analysis, we computed a study-wise space using the Advanced Normalization Tools software routines. Subsequently, all coregistered fractional anisotropy (FA) datasets were skeletonized. Skeletonized FA data were used for the statistical analysis. For FA analysis in specific fiber tracts, we used the fiber-tract quantification method (details about the tracking procedure for automated fiber-tract quantification are described in Yeatman and colleagues[33]). Their method can be briefly summarized as follows: first, the fanning out ends of tracts are cut; next, the medial, white matter associated part of each tract is subdivided into 100 equidistant nodes along the tract trajectory; and finally, for every node, a weighted mean FA value is calculated, resulting in a tract diffusion profile. The variation of FA along the tracts is the result of anatomical and geometric characteristics of each particular tract, for example, curvature, branching, or crossing fibers.[33] The tracking was performed in subject space.

Therefore, spatial normalization was not required. Measurements were carried out following the automated fiber-tract quantification toolbox[33] in the forceps major and minor of the corpus callosum, cingulum, uncinate and arcuate fasciculus, and inferior and superior longitudinal fasciculi as well as the inferior fronto-occipital fasciculus, the thalamic radiation, and the corticospinal tract. In addition to the FA, we delineated the values of radial diffusivity (RD) and axial diffusivity (AD) along the aforementioned fiber tracts.

Statistical Analysis

To examine the structural difference between groups, we set up a general linear model including scanner, age, and gender as well as total intracranial volume as nuisance covariates to account for their effects on brain structure. As the groups differed with respect to site at which the scan was performed, year of scan, and, for the diffusion tensor imaging (DTI) analysis, angulation of the scan, we also included these parameters as covariates of no interest. In addition, we performed analyses within the patient group including disease duration and SARA as additional covariates in the respective statistical models testing for group differences and performed analyses testing the correlation of disease duration and SARA with the gray and white matter alteration (VBM) and alterations in FA, RD, and AD (TBSS, tract-based regional analyses). INAS was not included because nonataxia signs characterized the MSA-C group leading to a (nonorthogonal) alignment of the parameters group (MSA-C vs. SAOA) and INAS. For the whole-brain and cerebellar voxel-wise analyses, we applied 2-sample *t* tests for each group comparison and gray and white matter segments were compared separately. We only included voxels in each analysis with tissue class probabilities greater than 20%. Statistical cut-offs included family-wise error correction (FWE) for multiple comparisons. We considered voxels with a P_{FWE} <0.01 as significant. Only clusters with an extend threshold of 10 were accepted. Effect sizes were calculated using Cohen's d. For the TBSS analysis, the threshold-free cluster enhancement method was applied with default settings. The statistical cut-off was set to P_{FWE} <0.01.

For tract-based regional FA, AD, and RD analysis, we carried out an analysis of covariance with the same covariates that were included in the whole-brain analysis models for each of the 100 nodes along each tract. Bonferroni correction was applied to correct for multiple comparisons. Group differences with a Bonferroni-corrected *P* value of $P < 0.001$ were considered significant.

For each analysis, we only accepted results that have been corrected for multiple comparisons at the most stringent significance level.

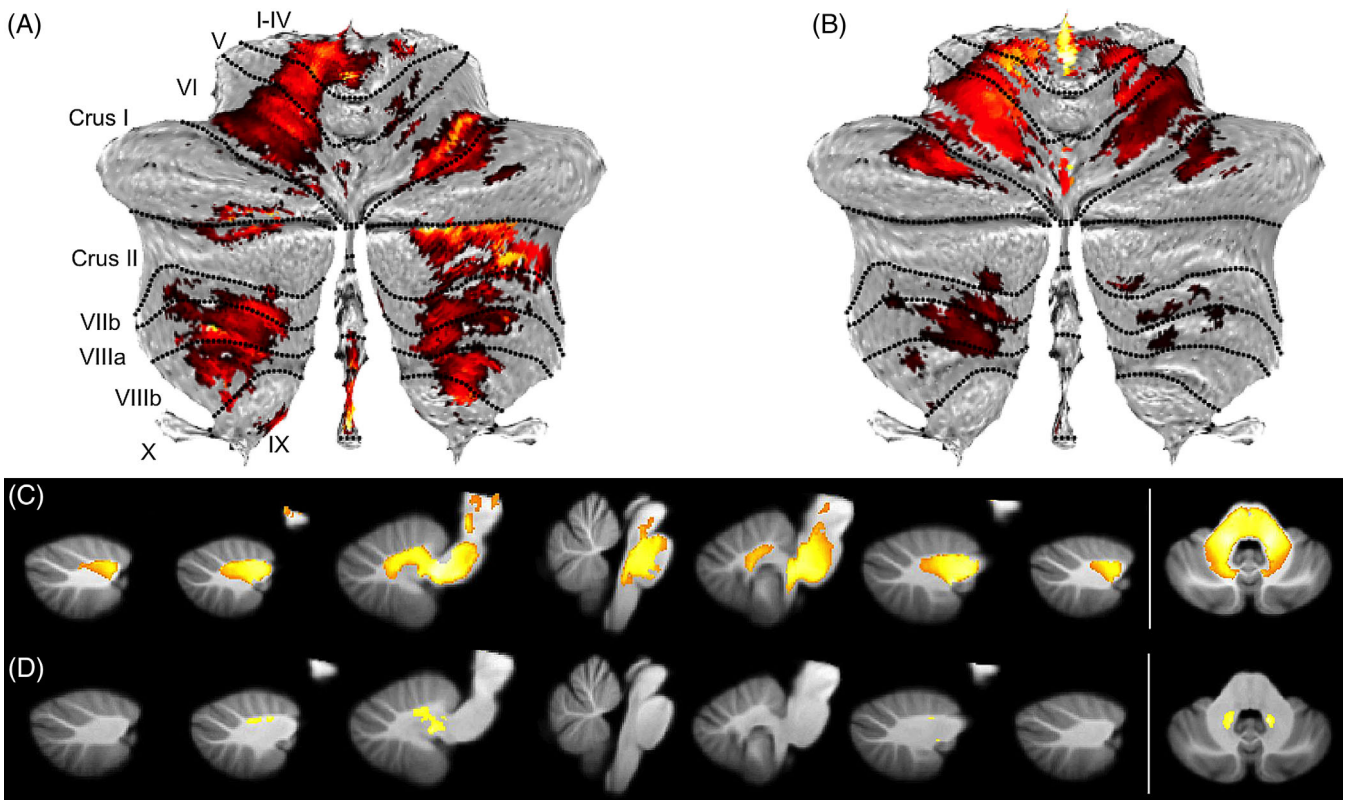

FIG. 1. Cerebellar focused voxel-based morphometry analysis in multiple system atrophy with predominant cerebellar ataxia and sporadic adult-onset ataxia compared with healthy controls ($P_{FWE} < 0.01$). (**A**) Gray matter atrophy projected onto a cerebellar flatmap in multiple system atrophy with predominant cerebellar ataxia. (**B**) Gray matter atrophy in sporadic adult-onset ataxia. (**C**) White matter atrophy projected on 7 sagittal and 1 axial slice in multiple system atrophy with predominant cerebellar ataxia. (**D**) White matter atrophy in sporadic adult-onset ataxia. [Color figure can be viewed at wileyonlinelibrary.com]

Results

Demographic and clinical data of the study population are given in Table 1 and Supporting Information Table 3. MSA-C patients, SAOA patients, and healthy controls did not differ with respect to age and sex distribution. When compared with the SAOA patients, disease duration in the MSA-C patients was shorter ($P < 0.01$), and the SARA and INAS count were higher ($P < 0.01$). Urinary dysfunction and orthostatic dysregulation ($P < 0.01$) as well as hyperreflexia ($P < 0.05$) and rigidity ($P < 0.01$) were significantly more frequent in the MSA-C patients when compared with the SAOA patients.

Whole-brain VBM did not reveal differences in gray or white matter volume between the MSA-C and SAOA patients, but the cerebellar gray and white matter of both patient groups were reduced when compared with healthy controls (Supporting Information Fig. 1). Furthermore, brainstem white matter in the MSA-C patients was reduced when compared with the healthy controls (Supporting Information Fig. 1).

The cerebellar VBM analysis using the SUIT toolbox returned gray matter volume reductions of both patient groups relative to healthy controls. Gray matter volume loss in patients was primarily found in the cerebellar areas subserving sensorimotor functions (Fig. 1).[34] The distribution of cerebellar gray matter volume loss was almost comparable in the SAOA and MSA-C patients, each in comparison with healthy controls. There was no significant difference between the SAOA and MSA-C patients. Cerebellar white matter was likewise reduced in both patient groups when compared with healthy controls. The MSA-C patients showed pronounced white matter loss in the cerebellum, the middle cerebellar peduncles, and the brainstem in comparison with healthy controls, whereas the SAOA patients in comparison with healthy controls only showed white matter loss in the cerebellar regions and middle cerebellar peduncles, but not the brainstem. The difference between the MSA-C and SAOA patients did not reach statistical significance.

When including disease duration and SARA as additional covariates in the statistical models, we did not find any significant difference between the MSA-C and SAOA patients, neither in the whole brain nor in the cerebellar VBM.

The effect sizes of the peak voxel in the whole-brain and cerebellar-focused gray and white matter VBM, for the comparison of MSA-C patients as well as for the comparison of SAOA patients with healthy controls were >1 (for details, see Supporting Information Table 5).

TBSS revealed reduced FA in the MSA-C patients both in comparison with the SAOA patients and healthy controls. Relative to healthy controls, the FA in the MSA-C patients was reduced in the pontine regions, the middle cerebellar peduncles, and the central portion of cerebellar white matter. Thus, major parts of the

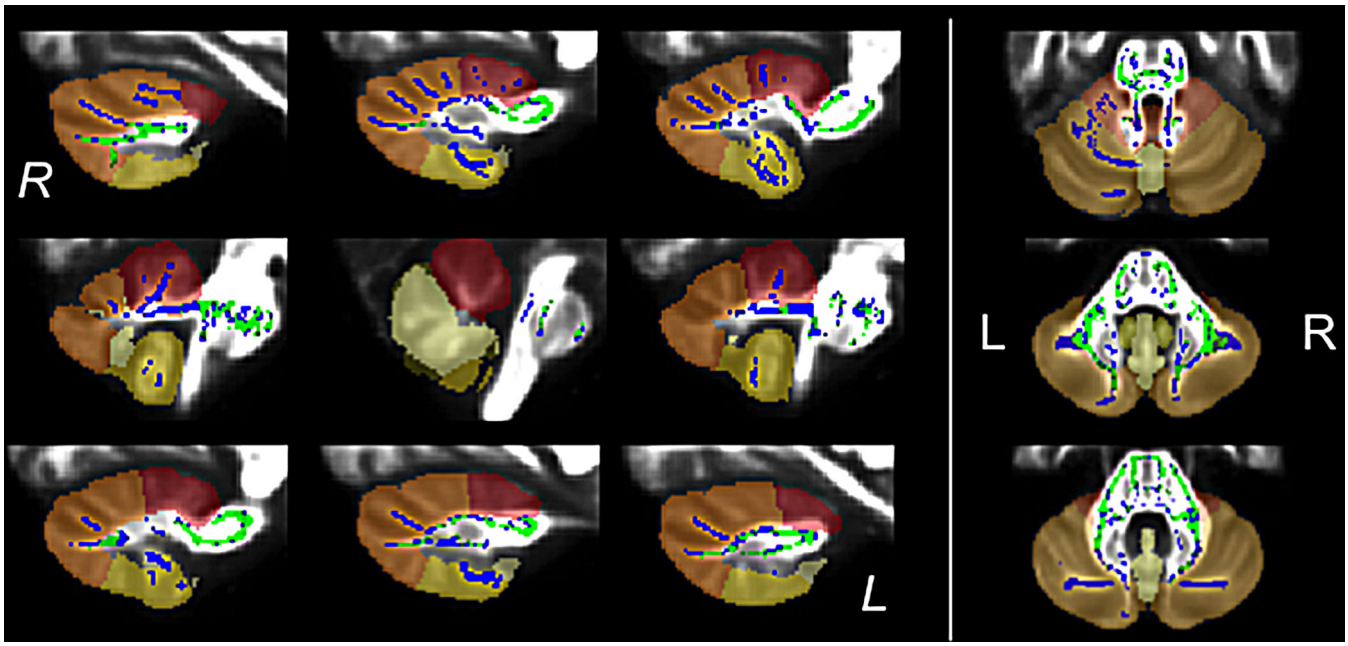

FIG. 2. Tract-based spatial statistics of fractional anisotropy in multiple system atrophy with predominant cerebellar ataxia compared with sporadic adult-onset ataxia and healthy controls. Reductions in multiple system atrophy with predominant cerebellar ataxia compared to sporadic adult-onset ataxia are shown in green, and reductions compared with healthy controls in blue ($P_{FWE} < 0.01$). Data are presented on 9 sagittal and 3 axial slices. The cerebellar subregions are colored for anatomical reference: anterior cerebellum in red, superior posterior cerebellum in orange, the inferior posterior cerebellum in yellow, and the vermis in bright yellow. [Color figure can be viewed at wileyonlinelibrary.com]

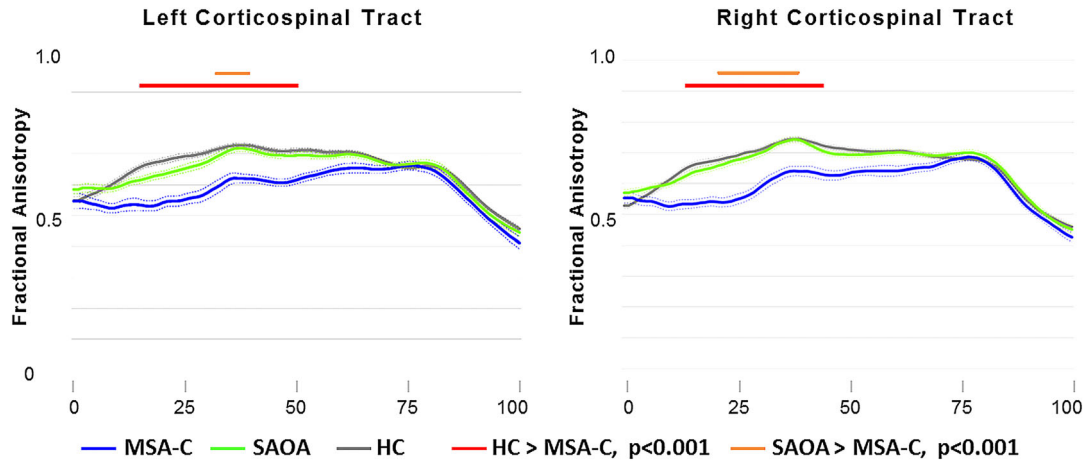

FIG. 3. Tractography-based regional analysis of fractional anisotropy along the corticospinal tract. Mean fractional anisotropy is given for multiple system atrophy with predominant cerebellar ataxia (MSA-C; blue), sporadic adult-onset ataxia (SAOA; green), and healthy controls (HC, gray). Sections of the corticospinal tract with significantly reduced fractional anisotropy in MSA-C compared with healthy controls are marked with a red line, and those with reduced fractional anisotropy compared with SAOA with an orange line ($P < 0.001$, Bonferroni). [Color figure can be viewed at wileyonlinelibrary.com]

anterior and posterior cerebellum (including white matter branching into the lobules I–IV bilaterally, V and VI right-sided, crus I, crus II, and lobule VIIb, VIIIb, and X bilaterally) were affected (Fig. 2). The comparison of MSA-C and SAOA patients revealed a similar, but less extended, pattern of FA reduction in the MSA-C patients (Fig. 2), involving the superior posterior part of the cerebellum including white matter branching into crus II bilaterally and lobule VIIb on the right side. The comparison of the SAOA patients with healthy controls did not reveal FA reduction in SAOA patients. However, there was a patchy pattern of increased FA in the SAOA patients around the left thalamus (Supporting Information Fig. 2). When adding disease duration or SARA sum score as an additional covariate in the statistical model, the distribution of decreased FA in the MSA-C patients in comparison with healthy controls was slightly less expanded, but the overall pattern remained unchanged (Supporting Information Fig. 2b and 2c).

We delineated the FA along the medial white matter–associated portion of the forceps major and minor of the corpus callosum and along the cingulum, uncinate, arcuate, inferior, and superior longitudinal and inferior fronto-occipital fasciculi, the thalamic radiation, and the corticospinal tracts across both hemispheres. Of note, the automated tracking method failed in only 29 times of 1764 total tracking attempts. The variation of the FA along the trajectories was consistent with previous reported tract characteristics for all tracts.[33] In the MSA-C group, the FA was reduced along the corticospinal tracts bilaterally both in comparison with healthy controls and SAOA patients (Fig. 3). However, the distribution of abnormalities was more widespread for the comparison with healthy controls than with the SAOA patients. In the right arcuate tract of the SAOA patients, the FA was reduced over a short distance representing less than 10% of the tract length (Supporting Information Fig. 3). No other significant group differences were detected.

In the delineation of AD and RD along the aforementioned white matter tracts, we did not find consistent patterns of alterations. There was a trend of increased RD in patients in comparison with healthy controls, but significant group differences were only observed in short distances representing less than 10% of the respective tracts. In detail, RD was increased in the MSA-C patients in both corticospinal tracts and the superior longitudinal fasciculus and the forceps minor of the corpus callosum in the SAOA patients, each in the comparison of the respective patient group with the group of healthy controls. AD was increased in both corticospinal tracts and the left inferior longitudinal fasciculus in the MSA-C patients and in the SAOA patients in the forceps minor of the corpus callosum and the left inferior fronto-occipital fasciculus. No significant differences between both patient groups were observed (Supporting Information Fig. 3).

There was no significant difference in the FA values along the corticospinal tract between MSA-C patients with or without pyramidal signs (for details, see Supporting Information Fig. 3d).

Discussion

This comparative MRI study provides a detailed analysis of brain volume changes and white matter microstructural alterations in MSA-C and SAOA. The gray matter volume loss detected by VBM had a similar

extent in both patient groups, which primarily involved the sensorimotor regions of the cerebellar cortex. In MSA-C, there was additional white matter volume loss in the cerebellum and brainstem. In SAOA, however, cerebellar white matter volume was only slightly reduced, and the brainstem was relatively preserved. DTI revealed widespread microstructural alterations of white matter in the MSA-C patients affecting the cerebellum, brainstem, and corticospinal tracts that were mostly absent in the SAOA patients.

A strength of our study is the multimodal approach that thoroughly assessed the structural integrity of brain gray and white matter tissue with different state-of-the-art MRI methods. This approach provides a more comprehensive view of brain morphology than that of previous studies focusing on either structural volume or DTI changes alone.[7,13,15,17,19,23,35-40]

Previous volumetric and VBM studies in MSA-C have consistently shown cerebellar and brainstem volume loss.[13,15,17,19,20,35-37,40] In SAOA, volume loss has been reported as being most prominent in the cerebellum, although some studies also detected involvement of the cerebellar peduncles and brainstem. A volumetric MRI study directly comparing MSA-C and SAOA found that the pattern of cerebellar atrophy was similar in both groups, but the brainstem volume was smaller in MSA-C than in SAOA.[15] The results of our study are consistent with these findings. In addition, they indicate that the loss of brainstem volume in MSA-C is mainly the result of the loss of white matter. We also found that in both patient groups, gray matter atrophy was most prominent in the sensorimotor regions of the cerebellum. Some of the previous volumetric and VBM studies reported gray matter loss in the basal ganglia and cortical regions in MSA-C patients.[13,19] We could not replicate those findings. This might be because of our small sample size and the very stringent significance level we applied to reduce the likelihood of false positive results.

Previous DTI studies in MSA-C reported abnormal diffusion parameters in the brainstem, most notably the pons, middle cerebellar peduncles, and cerebellar white matter.[22] In addition, supratentorial white matter, notably the corticospinal tract, internal capsule, corpus callosum, corona radiata, and cingulum were also affected.[16,17,21-23,41] In an early DTI study of 3 SAOA patients, an increase of the apparent diffusion coefficient, interpreted as a loss of white matter integrity, was found in the cerebellum and brainstem.[42] Another study directly comparing MSA-C and SAOA found markedly reduced FA values in afferent cerebellar tracts in MSA-C that allowed a fairly good discrimination from SAOA.[18] The results of our study confirm the presence of widespread white matter abnormalities in MSA-C, as indicated by reduced FA, affecting not only brainstem and cerebellar fiber tracts but also the corticospinal tracts. In contrast, there were only negligible FA abnormalities in SAOA. FA is a widely used diffusion parameter to describe microstructural alterations of white matter in the brain. The additional analysis of AD and RD did not show any consistent and extended alterations that one could consider as relevant, although RD showed a strong trend toward an increase in MSA-C patients (for details, see Supporting Information Fig. 3c).

The principal finding of this study is the prominent white matter involvement in MSA-C that distinguished MSA-C from SAOA. This corresponds well to the results of a postmortem study showing that cerebellar white matter degeneration in MSA was more pronounced than that of the cerebellar cortex.[43] Imaging and autopsy evidence of major white matter pathology in MSA is consistent with characterization of this disease as a primary oligodendrogliopathy.[44]

When compared with SAOA, MSA-C has a more severe phenotype and faster disease progression.[11] This is also reflected by the characteristics of the patient groups of this study. SARA and INAS scores of the MSA-C patients were higher than those of the SAOA patients, although the disease duration of the MSA patients was shorter. Including ataxia severity as a covariate in the analysis did not change the results in the group comparison, and we did not find any positive or negative correlation of SARA with gray or white matter volume or FA on the high significance level corrected for multiple comparisons. Because the observed group differences between MSA-C and SAOA were not influenced by ataxia severity, they rather reflect substantial differences in the brain pathology of MSA-C patients in comparison with SAOA patients.

The MSA-C patients showed a higher prevalence of clinical pyramidal tract signs than the SAOA patients. Correspondingly, an affection of the corticospinal tracts was observed in the MSA-C patients, but not in the SAOA patients.[11,16] A direct comparison of MSA-C patients with and without pyramidal tract signs did not reveal differences. Because of the very small subgroups, this analysis should be considered with caution. Nevertheless, these results underline the significance of disease-specific white matter alterations in MSA-C that are not present in SAOA.

As part of the prospective SPORTAX natural history study, all patients underwent an extensive clinical characterization including careful consideration of inclusion/exclusion criteria and diagnostic categories.[11] Nevertheless, this study, as all others in the field of sporadic degenerative ataxia, has to contend with the problem that some patients initially diagnosed as SAOA may develop severe autonomic failure at later time points requiring a change of the clinical diagnosis to MSA-C.[6,11] As the disease duration was considerably longer in the SAOA when compared with the MSA-C group, we are confident that the number of such future

"converters" in the SAOA group was low; however, within this ongoing prospective study the postmortem diagnostic confirmation was not available. Additional limitations of our study are the relatively small number of study subjects, lack of follow-up, and the uneven distribution of patients between the 2 study sites. To account for these limitations and reduce the likelihood of false positive results, we included additional covariates in the statistical analysis and reported only results with highly stringent statistical thresholds. By doing so, we may have underestimated effects and group differences.

In the multimodal imaging of our deeply phenotyped cohort, we did not find any differences in gray and white matter volumes between the MSA-C and SAOA patients, but a clear contrast of microstructural white matter alterations between the MSA-C and SAOA patients. The MSA-C patients showed alteration in the microstructure of the brainstem and cerebellar white matter as well as the corticospinal tract. Our results suggest that DTI abnormalities may aid the early diagnostic distinction between these 2 conditions, which remains a clinical challenge.[45] To this end, longitudinal studies of larger cohorts are required. In this respect, longitudinal DTI studies of SAOA patients that convert to MSA-C would be particularly informative. ■

Acknowledgment: We thank all patients and volunteers who participated in this study. We thank Frank Jessen, Department of Psychiatry, University of Cologne, for the contribution of control data from the DELCODE (German Center for Neurodegenerative Diseases (DZNE)–Longitudinal Cognitive Impairment and Dementia Study). We thank Heike Jacobi, Ina Vogt, and Marcus Grobe-Einsler for their assistance in the study execution.

References

1. Schols L, Szymanski S, Peters S, et al. Genetic background of apparently idiopathic sporadic cerebellar ataxia. Hum Genet 2000;107(2):132–137.
2. Moseley ML, Benzow KA, Schut LJ, et al. Incidence of dominant spinocerebellar and Friedreich triplet repeats among 361 ataxia families. Neurology 1998;51(6):1666–1671.
3. Abele M, Burk K, Schols L, et al. The aetiology of sporadic adult-onset ataxia. Brain 2002;125(5):961–968.
4. Wakabayashi K, Hayashi S, Kakita A, et al. Accumulation of alpha-synuclein/NACP is a cytopathological feature common to Lewy body disease and multiple system atrophy. Acta Neuropathol 1998;96(5):445–452.
5. Trojanowski JQ, Revesz T, Neuropathology Working Group on MSA. Proposed neuropathological criteria for the post mortem diagnosis of multiple system atrophy. Neuropathol Appl Neurobiol 2007;33(6):615–620.
6. Gilman S, Wenning GK, Low PA, et al. Second consensus statement on the diagnosis of multiple system atrophy. Neurology 2008;71(9):670–676.
7. Abele M, Minnerop M, Urbach H, Specht K, Klockgether T. Sporadic adult onset ataxia of unknown etiology: a clinical, electrophysiological and imaging study. J Neurol 2007;254(10):1384–1389.
8. Harding AE. "Idiopathic" late onset cerebellar ataxia. A clinical and genetic study of 36 cases. J Neurol Sci 1981;51(2):259–271.
9. Tsuchiya K, Ozawa E, Saito F, Irie H, Mizutani T. Neuropathology of late cortical cerebellar atrophy in Japan: distribution of cerebellar change on an autopsy case and review of Japanese cases. Eur Neurol 1994;34(5):253–262.
10. Ota S, Tsuchiya K, Anno M, Niizato K, Akiyama H. Distribution of cerebello-olivary degeneration in idiopathic late cortical cerebellar atrophy: clinicopathological study of four autopsy cases. Neuropathology 2008;28(1):43–50.
11. Giordano I, Harmuth F, Jacobi H, et al. Clinical and genetic characteristics of sporadic adult-onset degenerative ataxia. Neurology 2017;89(10):1043–1049.
12. Klockgether T. Sporadic adult-onset ataxia. Handb Clin Neurol 2018;155:217–225.
13. Brenneis C, Boesch SM, Egger KE, et al. Cortical atrophy in the cerebellar variant of multiple system atrophy: a voxel-based morphometry study. Mov Disord 2006;21(2):159–165.
14. Burk K, Buhring U, Schulz JB, Zuhlke C, Hellenbroich Y, Dichgans J. Clinical and magnetic resonance imaging characteristics of sporadic cerebellar ataxia. Arch Neurol 2005;62(6):981–985.
15. Burk K, Globas C, Wahl T, et al. MRI-based volumetric differentiation of sporadic cerebellar ataxia. Brain 2004;127(Pt 1):175–181.
16. da Rocha AJ, Maia AC Jr, da Silva CJ, et al. Pyramidal tract degeneration in multiple system atrophy: the relevance of magnetization transfer imaging. Mov Disord 2007;22(2):238–244.
17. Dash SK, Stezin A, Takalkar T, et al. Abnormalities of white and grey matter in early multiple system atrophy: comparison of parkinsonian and cerebellar variants. Eur Radiol 2019;29(2):716–724.
18. Fukui Y, Hishikawa N, Sato K, et al. Characteristic diffusion tensor tractography in multiple system atrophy with predominant cerebellar ataxia and cortical cerebellar atrophy. J Neurol 2016;263(1):61–67.
19. Minnerop M, Specht K, Ruhlmann J, et al. Voxel-based morphometry and voxel-based relaxometry in multiple system atrophy-a comparison between clinical subtypes and correlations with clinical parameters. Neuroimage 2007;36(4):1086–1095.
20. Yang H, Wang N, Luo X, et al. Cerebellar atrophy and its contribution to motor and cognitive performance in multiple system atrophy. Neuroimage Clin 2019;23:101891.
21. Zanigni S, Evangelisti S, Testa C, et al. White matter and cortical changes in atypical parkinsonisms: a multimodal quantitative MR study. Parkinsonism Relat Disord 2017;39:44–51.
22. Heim B, Krismer F, Seppi K. Structural imaging in atypical parkinsonism. Int Rev Neurobiol 2018;142:67–148.
23. Wang PS, Wu HM, Lin CP, Soong BW. Use of diffusion tensor imaging to identify similarities and differences between cerebellar and parkinsonism forms of multiple system atrophy. Neuroradiology 2011;53(7):471–481.
24. Wang PS, Yeh CL, Lu CF, Wu HM, Soong BW, Wu YT. The involvement of supratentorial white matter in multiple system atrophy: a diffusion tensor imaging tractography study. Acta Neurol Belg 2017;117(1):213–220.
25. Wenning GK, Tison F, Seppi K, et al. Development and validation of the Unified Multiple System Atrophy Rating Scale (UMSARS). Mov Disord 2004;19(12):1391–1402.
26. Schmitz-Hubsch T, du Montcel ST, Baliko L, et al. Scale for the assessment and rating of ataxia: development of a new clinical scale. Neurology 2006;66(11):1717–1720.
27. Jacobi H, Rakowicz M, Rola R, et al. Inventory of Non-Ataxia Signs (INAS): validation of a new clinical assessment instrument. Cerebellum 2013;12(3):418–428.
28. Ashburner J, Friston KJ. Voxel-based morphometry—the methods. Neuroimage 2000;11(6 Pt 1):805–821.
29. Diedrichsen J, Balsters JH, Flavell J, Cussans E, Ramnani N. A probabilistic MR atlas of the human cerebellum. Neuroimage 2009;46(1):39–46.
30. Smith SM, Jenkinson M, Woolrich MW, et al. Advances in functional and structural MR image analysis and implementation as FSL. Neuroimage 2004;23(suppl 1):S208–S219.

31. Ashburner J. A fast diffeomorphic image registration algorithm. Neuroimage 2007;38(1):95–113.

32. Smith SM, Jenkinson M, Johansen-Berg H, et al. Tract-based spatial statistics: voxelwise analysis of multi-subject diffusion data. Neuroimage 2006;31(4):1487–1505.

33. Yeatman JD, Dougherty RF, Myall NJ, Wandell BA, Feldman HM. Tract profiles of white matter properties: automating fiber-tract quantification. PLoS One 2012;7(11):e49790.

34. Diedrichsen J, Zotow E. Surface-based display of volume-averaged cerebellar imaging data. PLoS One 2015;10(7):e0133402.

35. Krismer F, Wenning GK. Multiple system atrophy: insights into a rare and debilitating movement disorder. Nat Rev Neurol 2017; 13(4):232–243.

36. Hauser TK, Luft A, Skalej M, et al. Visualization and quantification of disease progression in multiple system atrophy. Mov Disord 2006;21(10):1674–1681.

37. Specht K, Minnerop M, Muller-Hubenthal J, Klockgether T. Voxel-based analysis of multiple-system atrophy of cerebellar type: complementary results by combining voxel-based morphometry and voxel-based relaxometry. Neuroimage 2005;25(1):287–293.

38. Villanueva-Haba V, Garces-Sanchez M, Bataller L, Palau F, Vilchez J. Neuroimaging study with morphometric analysis of hereditary and idiopathic ataxia. Neurologia 2001;16(3):105–111.

39. Wullner U, Klockgether T, Petersen D, Naegele T, Dichgans J. Magnetic resonance imaging in hereditary and idiopathic ataxia. Neurology 1993;43(2):318–325.

40. Specht K, Minnerop M, Abele M, Reul J, Wullner U, Klockgether T. In vivo voxel-based morphometry in multiple system atrophy of the cerebellar type. Arch Neurol 2003;60(10):1431–1435.

41. Blain CR, Barker GJ, Jarosz JM, et al. Measuring brain stem and cerebellar damage in parkinsonian syndromes using diffusion tensor MRI. Neurology 2006;67(12):2199–2205.

42. Della Nave R, Foresti S, Tessa C, et al. ADC mapping of neurodegeneration in the brainstem and cerebellum of patients with progressive ataxias. Neuroimage 2004;22(2):698–705.

43. Matsusue E, Fujii S, Kanasaki Y, Kaminou T, Ohama E, Ogawa T. Cerebellar lesions in multiple system atrophy: postmortem MR imaging-pathologic correlations. Am J Neuroradiol 2009;30(9):1725–1730.

44. Wenning GK, Stefanova N, Jellinger KA, Poewe W, Schlossmacher MG. Multiple system atrophy: a primary oligodendrogliopathy. Ann Neurol 2008;64(3):239–246.

45. Kim HJ, Jeon B, Fung VSC. Role of magnetic resonance imaging in the diagnosis of multiple system atrophy. Mov Disord Clin Pract 2017;4(1):12–20.

Supporting Data

Additional Supporting Information may be found in the online version of this article at the publisher's web-site.

SGML and CITI Use Only
DO NOT PRINT

Author Roles

(1) Research project: A. Conception, B. Organization, C. Execution; (2) Statistical Analysis: A. Design, B. Execution, C. Review and Critique; (3) Manuscript: A. Writing of the first draft, B. Review and Critique.

J.F.: 1C, 2A, 2B, 3A
I.G.: 1B, 1C
X.J.: 2C
C. Kindler: 1C
A.S.: 1B
J.A.-C.: 2C
P.N.: 2C
J.M.: 1C
O.S.: 1C
E.D.: 1C
S.V.: 1C
A.D.: 1C
C. Kamm: 1C
L.S.: 2C
T.K.: 1A, 3B

Financial Disclosures of all authors (for the preceding 12 months)

J.A.-C. has equity and a full-time appointment at Tenoke Limited, which provides medical image processing services. C. Kamm received speaker honorarium from the German Society for muscle disease patients and Merz Pharma and consulting fees and speaker honorarium from Biogen GmbH. T.K. receives/has received research support from the Deutsche Forschungsgemeinschaft, the Bundesministerium für Bildung und Forschung, the Bundesministerium für Gesundheit, the Robert Bosch Foundation, the European Union, and the National Institutes of Health. He has received consulting fees from Biohaven and UBC. He has received a speaker honorarium from Novartis. J.F., I.G., X.J., C. Kindler, A.S., P.N., J.M., O.S., E.D., S.V., A.D., and L.S. have nothing to report.

3.2. Oender D*, **Faber J***, Wilke C, Schaprian T, Lakghomi A, Mengel D, Schöls L, Traschütz A, Fleszar Z, Dufke C, Vielhaber S, Machts J, Giordano I, Grobe-Einsler M, Klopstock T, Stendel C, Boesch S, Nachbauer W, Timmann-Braun D, Thieme AG, Kamm C, Dudesek A, Tallaksen C, Wedding I, Filla A, Schmid M, Synofzik M, Klockgether T. Evolution of Clinical Outcome Measures and Biomarkers in Sporadic Adult-Onset Degenerative Ataxia. Mov Disord. 2023; 38(4):654-664

Zielsetzung der Arbeit – Zielsetzung der Arbeit war es, die klinische Progression sowie den zeitlichen Verlauf von biochemischen und bildgebenden Biomarkern bei Patient*innen mit SAOA und MSA-C zur untersuchen.

Methoden und Ergebnisse – Eingeschlossen wurden Patient*innen mit einer zerebellärer Ataxie mit einem Erkrankungsbeginn nach dem 40. Lebensjahr nach Ausschluss der häufigsten erworbenen sowie genetischen Ursachen. Ein standardisiertes klinisches Assessment mit dem Einsatz verschiedener Skalen erfolgte bei jeder Visite. Die Ataxieschwere wurde mittels SARA erfasst (Schmitz-Hubsch, du Montcel et al. 2006). In Subgruppen erfolgte im Rahmen der klinischen Visiten zudem die Entnahme von Blutproben sowie Durchführung struktureller MRT nach standardisiertem Protokoll. Neurofilament light (NfL) als unspezifischer Marker für Neuronenverlust wurden aus EDTA-Plasma unter Verwendung einer Simoa-Plattform bestimmt. Volumina der Basalganglien, des Hirnstamms und Kleinhirns wurden automatisiert bestimmt und in Relation zum Ganzhirnvolumen gesetzt. Die Auswertung erfolgte basierend auf den relativen Volumina. Zur qualitativen Beurteilung von Signalveränderungen definierten wir den „pons and middle cerebellar peduncle abnormality score“ (PMAS). Die qualitative Beurteilung umfasste eine gewichtete Bewertung des „hot-cross-bun“-Zeichens, von Hyperintensitäten im mittleren Kleinhirnstiel sowie den Durchmesser des mittleren Kleinhirnstiels. „Mixed-effects models“ wurden verwendet um Veränderungen auf einer Zeitskala, die mit dem Auftreten der Ataxie begann, zu untersuchen. Insgesamt 436 Patient*innen mit sporadischer Ataxie erfüllten die Einschlusskriterien und wurden in die Studie aufgenommen. Im Rahmen der Studie erfolgte eine erweiterte genetische Testung. Bei 32 Patient*innen konnte hierdurch eindeutige oder wahrscheinliche genetische Diagnose gestellt werden. 130 Patient*innen erfüllten bereits bei Studieneinschluss die klinischen Kriterien einer wahrscheinlich MSA nach Gilman. 26 Patient*innen erfüllten

erst bei Verlaufsuntersuchungen die klinischen Kriterien einer wahrscheinlichen MSA nach Gilman. Für diese Patient*innen wurde der Terminus „klinische Konverter“ eingeführt. Die Progression der klinischen Parameter unterschied sich nicht zwischen den MSA-C, die die MSA-Kriterien bei Einschluss und denen, die sie erst im Verlauf erfüllten. Im Gegensatz dazu zeigten SAOA eine wesentlich langsamere klinische Progression. Im Hinblick auf die biochemischen und bildgebenden Biomarker zeigten sich ebenfalls Unterschiede zwischen MSA-C und SAOA: Bei Studieneinschluss lagen die NfL-Werte bei MSA-C deutlich über denen bei SAOA. Im Verlauf kam es bei SAOA zu einer kontinuierlich leichten Zunahme über die Zeit. In der MSA-C Gruppe hingegen sanken die NfL-Werte mit längerer Krankheitsdauer. Volumen von Pons und weißer Substanz des Kleinhirns, und der qualitative Beurteilungs-Score zeigten durchgehend niedrigere bzw. höhere Werte und einen rascheren Progress bei MSA-C. Mittels univariabler Cox-Regression wurden vier Parameter mit prognostischem Wert für die klinische Konversion zur MSA identifiziert. Dies waren die Erfüllung der Kriterien für eine mögliche MSA nach Gilmann, sowie NfL und der qualitative Bewertungs-Score als Risikofaktoren sowie das Volumen von Pons und weißer Substanz des Kleinhirns als protektive Faktoren. Der qualitative Berwertungs-Score war zudem ein Prädiktor für eine schnellere Progression in MSA-C.

Schlussfolgerungen – Die Studie liefert detaillierte Informationen über die unterschiedliche Entwicklung und prognostische Bedeutung von biochemischen und bildgebenden Biomarkern bei MSA-C und SAOA. Insbesondere wurde die Relevanz von bildgebenden Biomarkern neben NfL als prognostischen Markern für die MSA-C aufgezeigt.

RESEARCH ARTICLE

Evolution of Clinical Outcome Measures and Biomarkers in Sporadic Adult-Onset Degenerative Ataxia

Demet Oender, MD,[1,2] Jennifer Faber, MD,[1,2] Carlo Wilke, MD,[3] Tamara Schaprian, PhD,[1] Asadeh Lakghomi, MD,[4] David Mengel, PhD,[3] Ludger Schöls, MD,[3,5] Andreas Traschütz, MD, PhD,[3,5] Zofia Fleszar, MD,[3,5] Claudia Dufke, PhD,[6] Stefan Vielhaber, MD,[7,8] Judith Machts, PhD,[7,8] Ilaria Giordano, MD,[1,9] Marcus Grobe-Einsler, MD,[1,2] Thomas Klopstock, MD,[10,11,12] Claudia Stendel, MD,[10,11] Sylvia Boesch, MD,[13] Wolfgang Nachbauer, MD, PhD,[13] Dagmar Timmann-Braun, MD,[14] Andreas Gustafsson Thieme, MD,[14] Christoph Kamm, MD,[15,16] Ales Dudesek, MD,[15,16] Chantal Tallaksen, MD,[17] Iselin Wedding, MD,[17] Alessandro Filla, MD,[18] Matthias Schmid, PhD,[1,19] Matthis Synofzik, MD,[3,5] and Thomas Klockgether, MD[1,2*]

[1]*German Center for Neurodegenerative Diseases (DZNE), Bonn, Germany*
[2]*Department of Neurology, University Hospital Bonn, Bonn, Germany*
[3]*Department of Neurodegenerative Diseases and Hertie-Institute for Clinical Brain Research, University of Tübingen, Tübingen, Germany*
[4]*Department of Neuroradiology, University Hospital Bonn, Bonn, Germany*
[5]*German Centre for Neurodegenerative Diseases (DZNE), Tübingen, Germany*
[6]*Institute of Medical Genetics and Applied Genomics, University of Tübingen, Tübingen, Germany*
[7]*German Center for Neurodegenerative Diseases (DZNE), Magdeburg, Germany*
[8]*Department of Neurology, Otto-von-Guericke University, Magdeburg, Germany*
[9]*Department of Neurodegeneration and Geriatric Psychiatry, University Hospital Bonn, Bonn, Germany*
[10]*German Center for Neurodegenerative Diseases (DZNE), Munich, Germany*
[11]*Department of Neurology, Friedrich-Baur-Institute, Ludwig-Maximilians-University, Munich, Germany*
[12]*Munich Cluster for Systems Neurology (SyNergy), Munich, Germany*
[13]*Department of Neurology and Center for Rare Movement Disorders, Medical University Innsbruck, Austria*
[14]*Department of Neurology and Center for Translational Neuro- and Behavioral Sciences (C-TNBS), Essen University Hospital, Essen, Germany*
[15]*German Center for Neurodegenerative Diseases (DZNE), Rostock, Germany*
[16]*Department of Neurology, University of Rostock, Germany*
[17]*Institute of Clinical Medicine, University of Oslo, Oslo, Norway*
[18]*Department of Neurosciences Reproductive and Odontostomatological Sciences, Federico II University, Naples, Italy*
[19]*Department of Medical Biometry, Informatics and Epidemiology, University Hospital Bonn, Bonn, Germany*

ABSTRACT: Background: Sporadic adult-onset ataxias without known genetic or acquired cause are subdivided into multiple system atrophy of cerebellar type (MSA-C) and sporadic adult-onset ataxia of unknown etiology (SAOA).

Objectives: To study the differential evolution of both conditions including plasma neurofilament light chain (NfL) levels and magnetic resonance imaging (MRI) markers.

Methods: SPORTAX is a prospective registry of sporadic ataxia patients with an onset >40 years. Scale for the Assessment and Rating of Ataxia was the primary outcome measure. In subgroups, blood samples were taken and MRIs performed. Plasma NfL was measured via a single molecule assay. Regional brain volumes were automatically measured. To assess signal changes, we defined the pons and middle cerebellar peduncle abnormality score (PMAS). Using mixed-effects models, we analyzed changes on a time scale starting with ataxia onset.

Results: Of 404 patients without genetic diagnosis, 130 met criteria of probable MSA-C at baseline and 26 during follow-up suggesting clinical conversion to MSA-C. The remaining 248 were classified as SAOA. At

*__Correspondence to:__ Dr. Thomas Klockgether, Department of Neurology, University Hospital Bonn, Venusberg-Campus 1, 53127, Bonn, Germany; E-mail: klockgether@uni-bonn.de

Relevant conflicts of interest/financial disclosures: Authors declare no conflicts of interest related to this work.

Demet Önder and Jennifer Faber equally contributed to the work

Received: 12 September 2022; **Revised:** 11 November 2022; **Accepted:** 22 December 2022

Published online in Wiley Online Library (wileyonlinelibrary.com). DOI: 10.1002/mds.29324

baseline, NfL, cerebellar white matter (CWM) and pons volume, and PMAS separated MSA-C from SAOA. NfL decreased in MSA-C and did not change in SAOA. CWM and pons volume decreased faster, whereas PMAS increased faster in MSA-C. In MSA-C, pons volume had highest sensitivity to change, and PMAS was a predictor of faster progression. Fulfillment of possible MSA criteria, NfL and PMAS were risk factors, CWM and pons volume protective factors for conversion to MSA-C.

Conclusions: This study provides detailed information on differential evolution and prognostic relevance of biomarkers in MSA-C and SAOA.

Key Words: sporadic ataxia; multiple system atrophy; natural history; neurofilament light chain; volumetric MRI

Introduction

Sporadic adult-onset ataxias without known genetic or acquired cause are progressive diseases with an ataxia onset after 40 years.[1,2] Population-based studies reported prevalence rates of sporadic degenerative ataxias ranging from 2.2 to 12.4:100 000.[3-6]

In a subgroup of patients, multiple system atrophy (MSA) is the underlying disease. According to the second consensus statement on the diagnosis of MSA, a clinically probable diagnosis MSA with predominant cerebellar ataxia (MSA-C) is made in patients with progressive ataxia accompanied by severe autonomic failure. In contrast, the criteria for clinically possible MSA include only one feature suggestive of autonomic dysfunction.[7] The diagnostic criteria for probable MSA have high specificity, whereas those for possible MSA are more sensitive, but lack specificity.[8,9] Recently, revised criteria have been proposed.[10]

Sporadic ataxias distinct from MSA have been designated as sporadic adult-onset ataxia of unknown etiology (SAOA).[11] Other than MSA, SAOA is not a defined disease entity, although published autopsy cases showed a fairly uniform pattern of cortical cerebellar degeneration, often combined with secondary degeneration of the inferior olive.[12,13] Clinical diagnosis requires a careful exclusion of possible acquired or genetic causes.[14] Some patients initially diagnosed as SAOA develop severe autonomic failure years after ataxia onset suggesting clinical conversion to MSA.[15,16] Longitudinal clinical studies of SAOA are almost completely lacking, but the available data suggest that disease progression is considerably slower in SAOA than in MSA.[15,17]

There is an urgent need for biomarkers that are useful to differentiate MSA-C from SAOA, to monitor disease progression, to predict prognosis, and facilitate early detection of MSA-C. We previously found higher levels of serum neurofilament light chain (NfL) in MSA-C than in SAOA.[18] Longitudinal studies in MSA yielded conflicting results. One study reported a modest increase of NfL within 1 year,[19] whereas another found an initial increase followed by deceleration.[20] Further, NfL levels in cerebrospinal fluid predicted the conversion of pure autonomic failure to MSA.[21]

A volumetric magnetic resonance imaging (MRI) study comparing MSA-C and SAOA found cerebellar atrophy in both groups, whereas brainstem atrophy was more pronounced in MSA-C.[22] In a voxel-based morphometry (VBM) study, there were no gray matter differences between MSA-C and SAOA, but white matter tissue loss of the brainstem was present only in MSA-C.[23] In longitudinal MRI studies of MSA patients, cerebellum and pons showed the highest annual volume loss.[24,25] Many MSA patients have signal abnormalities in the pons, the "hot cross bun" sign, and the middle cerebellar peduncles (MCPs),[26-29] which have high specificity and positive predictive value for the diagnosis of MSA-C.[30,31]

To fill knowledge gaps about clinical evolution and biomarker characteristics of sporadic adult-onset ataxias without known genetic or acquired cause, we established the SPORTAX registry. In 2017, we reported the clinical baseline characteristics of 249 SPORTAX participants.[15] With the present analysis that is based on 436 SPORTAX participants, we wished to establish the natural history of sporadic degenerative ataxia and analyze long-term disease progression. In addition, we wanted to study the evolution of plasma NfL and quantitative MRI markers and to explore the potential of these biomarkers to differentiate between MSA-C and SAOA and to predict disease progression. We were further interested in determining the rate and predictors of clinical conversion to MSA-C.

Methods

Study Design and Patients

Inclusion of study participants into the prospective SPORTAX registry started on April 1, 2010. We recruited participants from ataxia clinics at 14 European centers. Inclusion criteria were as follows: (1) progressive ataxia; (2) ataxia onset after age 40 years; (3) informative and negative family history; (4) negative molecular genetic tests for Friedreich's ataxia (FRDA),

spinocerebellar ataxia type 1 (SCA1), SCA2, SCA3, SCA6, and fragile X mental retardation 1 (FMR1) premutation; and (5) no established acquired cause of ataxia. Details of criteria and workup are given in Supplementary Data **S1**. Whenever a patient revisited the study center follow-up assessments were done, if possible, on an annual basis.[15]

Patients were classified as MSA-C, if they fulfilled the diagnostic criteria for probable MSA at least at the last visit.[7] MSA-C patients were subdivided into those who met criteria already at baseline (MSA-C BL) and those who met criteria at one of the later visits suggesting clinical conversion to MSA-C (MSA-C CO). The remaining patients were labeled as SAOA.

Data export was performed on June 30, 2020. The study was approved by the local ethics committees. All participants provided written informed consent. This study is registered with ClinicalTrials.gov (NCT02701036).

Clinical Outcome Assessments

The primary measure of disease severity was the Scale for the Assessment and Rating of Ataxia (SARA).[32] As additional clinical scales, we used the Unified MSA Rating Scale part II (UMSARS-II)[33] and the Inventory of Non-Ataxia Signs (INAS), which is a clinical measure of non-ataxia involvement.[34] Patient-reported outcome measures included UMSARS-I, an activities of daily living (ADL) scale,[33] the Patient's Health Questionnaire (PHQ-9) for assessment of depression,[35] and the EQ-5D as a measure of health-related quality of life. EQ-5D includes a visual analog scale (EQ-5D VAS) that yields a number out of 0-100 between the anchors "worst imaginable health state" (0) and "best imaginable health state" (100).[36] All investigators were experienced in the use of the applied scales and questionnaires.

Exclusion of Genetic Causes

Genetic screening for replication factor C subunit 1 (*RFC1*) repeat expansions was performed, as previously described.[37-39] Details are given in Supplementary Data **S1**. In addition, 201 genes known to be associated with ataxia (gene set 1, Supplementary Data **S1**) were screened with next-generation sequencing (NGS), either with a high-coverage large-scale NGS panel (HaloPlex gene panel; Agilent, Santa Clara, CA) or by whole exome sequencing (WES) (Illumina NovaSeq 6000 platform, Agilent SureSelectXT library preparation kit) with the latter including 182 ataxia-overlap disease genes (gene set 2, Supplementary Data **S1**). Variants of 985 genes associated with neurodegenerative diseases (gene set 3, Supplementary Data **S1**) were also considered. For details on coverage and filter methods, see Supplementary Data **S1**. Pathogenicity of the resulting variants was determined according to American College with Human Genetics (ACMG) criteria.[40,41] Subjects were classified as having a genetic diagnosis based on the pathogenicity likelihood of the respective variants and the phenotypic match. That is, subjects were classified as: (1) definitive genetic diagnosis, if having a pathogenic or likely pathogenic variant and a phenotype typical of the genetic variant; (2) probable genetic diagnosis, if having a pathogenic or likely pathogenic variant and a phenotype broadly compatible with the genetic variant; and (3) no genetic diagnosis (all other subjects).

Plasma NfL Measurements

Plasma NfL was determined, as previously described for serum NfL.[42] At the study sites, EDTA plasma samples were frozen at −80°C within 1 hour after collection, stored in the local biobank and analyzed without any previous thaw–freeze cycle. Plasma levels of NfL were quantified using the Simoa NF-light Advantage kit (Lot 502183) on an Quanterix HD1 analyzer (Quanterix, Billerica, MA). All assays were performed by the same operator blinded to sample identity. EDTA plasma was centrifuged at 14,000 × g for 4 minutes, and the upper 90% transferred to the assay plate. Samples (dilution factor 1 in 4 in sample buffer) and calibrators were analyzed in duplicates. Two internal control samples were assessed both at the start and end of an assay plate. The repeatability was 3.7% (sample 1) and 5.7% (sample 2). The inter-assay variance between the runs across 5 days was 3.1% (sample 1) and 4.8% (sample 2).

MRI

MRIs were acquired at the study sites Magdeburg, Bonn, and Rostock using Siemens 3 T scanners (Siemens Medical Systems, Erlangen, Germany). All sites were equipped with the same gradient system and head coils (32 channel head coil), and used the same software release and MRI protocols. T1- and T2-weighted (T1w, T2w) images were acquired (Supplementary Data **S1**).

Volumes of the basal ganglia, namely caudate, putamen and pallidum, thalamus and brainstem volumes midbrain, pons and medulla oblongata as well as the estimated total intracranial volume (eTIV) were assessed in the N4biasfield (ants, version 2.1)[43] corrected T1w MRI using FreeSurfer (version 6.0).[44,45] Cerebellar subsegmentation was performed using CerebNet resulting in 25 cerebellar cortical and two hemispheric cerebellar white matter labels, which were combined to the total cerebellar gray matter and the total cerebellar white matter (CWM).[46] All volumes were divided by eTIV, and subsequent statistical analyses were based on these relative values.

Signal and structural abnormalities of the pons and MCP that could not be detected by volumetry and presence of putaminal atrophy were assessed by a trained neuroradiologist (A.L.) blinded to clinical information. For rating of pons and MCP we used the pons and MCP abnormality score (PMAS) ranging from 0 (normal) to 6 (most severely affected) (Supplementary Data **S1**).

Statistical Analysis

Statistical analyses were performed using R Software for Statistical Computing version 4.2.0 (www.r-project.org). *P* values <0.05 were considered significant.

To test whether biomarkers separated MSA-C from SAOA, a receiver operating characteristic (ROC) curve analysis with 10 000 bootstrap samples and the Delong approach to compare the area under the curves (AUCs) between nested logistic regression models was applied. Results are reported as AUC with 95% bootstrap confidence intervals (CI) and *P*-values (R packages pROC and caret).

For analysis of the temporal evolution of clinical outcomes and biomarkers, we applied linear mixed models. To account for dependencies between measurements from the same patient, patient-specific random intercepts and slopes were included. The time variable was the time from ataxia onset measured in years. Ataxia onset was defined by the onset of gait difficulties, as reported by the patient.[47] Linearity of the progression rate was tested with Rainbow test (R package lmtest) and graphical inspection of data. As the linear model best fitted the data for all metrics, we report linear models. We eliminated values of four patients with MSA-C and six with SAOA with extreme outliers of the SARA score at one visit. These outliers were identified by visual inspection of the residual graphs and verified by examining the raw data.

Sensitivity to change was assessed by calculating sensitivity to change ratio (SCS) using the mean slope of progression divided by the standard deviation of the slope with 95% CI. CI was determined by model-based (semi-) parametric bootstrap for mixed models with 10 000 runs (R package lme4).

To identify factors that affected the SARA progression rate, we added interaction effects of the tested factors with time to the linear mixed model. The tested factors were sex, age at ataxia onset, baseline clinical findings (SARA, INAS, pyramidal features, and extrapyramidal features), NfL, CWM and pons volume, and PMAS. Independent factors that were significant in the univariable analysis were included in a multivariable model only for SAOA because of an insufficient number of observations in MSA-C. Estimates derived from the model are given as means with 95% CI, standard error (SE), *P* value, and marginal and conditional R^2.

To study factors at baseline associated with the conversion to MSA-C, we used univariable Cox proportional hazard models of those subjects who did not fulfill probable MSA-C criteria at baseline. The tested factors were sex, age at ataxia onset, possible MSA criteria, NfL, CWM and pons volume, and PMAS. The time scale was time from onset. The proportional hazards assumption was checked by a graphical analysis of Schoenfeld residuals and a formal score test (R package survival).

Results

Study Population and Genetic Analysis

A total of 436 (246 male, 190 female) sporadic ataxia patients met the inclusion criteria and were enrolled. Median age at inclusion was 63 years (interquartile range [IQR], 57-71), age at ataxia onset 57 years (IQR, 51-63), and time from onset 5 years (IQR, 3-8).

RFC1 polymerase chain reaction (PCR) was performed in 360 study participants. NGS was done in 331 participants, in 184 using an ataxia-specific gene panel and in 147 by WES. In 32 participants (median age, 53 years, IQR, 47-61), a definite or probable genetic diagnosis was established. In 24 of them, we found variants in recessive genes (17x *RFC1*, 3x *SPG7*, *COQ8A*, *ATM*, *POLG*, and *SNX14*) in eight in dominant genes (3x *CACNA1A*, *CACNA1G*, *GFAP*, *OPA1*, *TMEM240*, and *TRPC3*).

Clinical Features of Patients without Genetic Diagnosis at Baseline

Of the 404 patients who had no definite or probable genetic diagnosis, 156 were classified as probable MSA-C and 248 as SAOA. A total of 130 of the MSA-C patients met diagnostic criteria at baseline (MSA-C BL), and 26 patients during follow-up suggesting clinical conversion to MSA-C (MSA-C CO).

Patient characteristics at baseline are given in Table 1. Although the time from ataxia onset was shorter in MSA-C than in SAOA, SARA, UMSARS-I, UMSARS-II, INAS, and PHQ-9 scores were higher, whereas median EQ-5D VAS was lower in MSA-C. SARA, UMSARS-I, and UMSARS-II were higher in MSA-C BL than in MSA-C CO. Although the time from ataxia onset was shorter in MSA-C than in SAOA, UMSARS-I was higher.

Biomarker Findings at Baseline

NfL data were available from 33 MSA-C and 65 SAOA patients (Supplementary Data **S1**). Baseline data are summarized in Table 2. NfL levels were higher both, in MSA-C and MSA-C CO, than in SAOA, but did not differ between MSA-C BL and MSA-C CO.

TABLE 1 *Characteristics of patients without genetic diagnosis at baseline*

	MSA-C	SAOA	*P* value MSA-C vs. SAOA	MSA-C BL	MSA-C CO	*P* value MSA-C BL vs. MSA-C CO	*P* value SAOA vs. MSA-C CO
N	156	248		130	26		
Males/females	87/69	145/103		74/56	13/13	0.655	0.533
Age (y)	62 (56–66)	65 (58–72)	0.002	62 (57–77)	61 (56–66)	0.695	0.061
Age at ataxia onset (y)	57 (52–63)	57 (51–65)	0.385	57 (52–63)	57 (53–63)	0.888	0.699
Time from ataxia onset (y)	4 (3–6)	5.5 (3–10)	<0.001	5 (3–6)	3 (2.0–4.75)	0.085	0.012
SARA	14.5 (12–20)	11.5 (8.5–14.25)	<0.001	15 (12.5–22)	12.25 (10–14)	<0.001	0.369
UMSARS-I	18 (12–25)	10 (6.75–14)	<0.001	20 (14–27)	12 (10–14)	<0.001	0.023
UMSARS-II	21 (15.5–26.5)	14 (10–19)	<0.001	21 (16–28)	17 (12.25–21)	0.005	0.067
INAS count	4 (3–5)	3 (1–4)	<0.001	4 (3–5)	3 (2–4.75)	0.233	0.080
PHQ-9	7 (5–12)	6 (3–10)	0.039	7 (5–12)	7 (5–9)	0.545	0.623
EQ-5D VAS	50 (30–60)	60 (47.5–75)	<0.001	50 (30–60)	50 (31.25–68)	0.473	0.052

Note: Data are given as median (IQR). Statistical comparisons between groups were made with Mann–Whitney *U*-test for quantitative and χ^2-test for qualitative variables.
Abbreviations: MSA-C, MSA with predominant cerebellar ataxia; MSA-C BL, patients with MSA-C at baseline; MSA-C CO, patients with clinical conversion to MSA- C during follow-up; SAOA, sporadic adult-onset ataxia of unknown etiology; SARA, Scale for the Assessment and Rating of Ataxia; UMSARS, Unified MSA Rating Scale; INAS, Inventory of Non-Ataxia Signs; PHQ-9, Patient's Health Questionnaire; EQ-5D VAS, EQ-5D visual analog scale; IQR, interquartile range.

TABLE 2 *Biomarker data at baseline*

	MSA-C	SAOA	*P* value MSA-C vs. SAOA	MSA-C BL	MSA-C CO	*P* value MSA-C BL vs. MSA-C CO	*P* value SAOA vs. MSA-C CO
N (NfL)	33	65		26	7		
Plasma NfL concentration	28.87 (19.49–36.81)	16.47 (12.44–22.79)	<0.001	30.29 (18.67–39.19)	24.41 (21.49–31.24)	0.560	0.024
N (MRI)	20	49		13	7		
CGM volume	0.058 (0.053–0.060)	0.061 (0.050–0.064)	0.243	0.059 (0.053–0.061)	0.056 (0.054–0.059)	0.878	0.511
CWM volume	0.008 (0.007–0.009)	0.011 (0.009–0.013)	<0.001	0.007 (0.006–0.009)	0.009 (0.008–0.010)	0.211	0.011
Medulla oblongata volume	0.003 (0.003–0.004)	0.003 (0.003–0-003)	0.069	0.003 (0.002–0.003)	0.003 (0.002–0.003)	0.817	0.353
Pons volume	0.006 (0.005–0.007)	0.008 (0.007–0.009)	<0.001	0.005 (0.004–0.006)	0.006 (0.006–0.007)	0.067	0.021
Midbrain volume	0.003 (0.003–0.004)	0.004 (0.003–0.004)	0.057	0.003 (0.003–0.004)	0.004 (0.004–0.004)	0.067	0.990
Thalamus volume	0.008 (0.008–0.009)	0.008 (0.008–0.009)	0.819	0.008 (0.008–0.008)	0.009 (0.008–0.010)	0.183	0.185
Caudate volume	0.004 (0.004–0.005)	0.004 (0.004–0.005)	0.859	0.004 (0.004–0.005)	0.004 (0.004–0.004)	0.938	0.951
Putamen volume	0.005 (0.005–0.006)	0.005 (0.005–0.006)	0.361	0.005 (0.004–0.006)	0.005 (0.005–0.005)	0.642	0.647
Pallidum volume	0.002 (0.002–0.002)	0.002 (0.002–0.002)	0.942	0.002 (0.002–0.002)	0.002 (0.002–0.003)	0.393	0.407
PMAS	4.0 (1.0–5.0)	0.00 (0.00–0.00)	<0.001	4.0 (4.0–6.0)	1.0 (1.0–3.0)	0.030	0.003
Putaminal atrophy (yes/no)	3/16	15/33	0.237	0/13	3/3	0.021	0.388

Note: Data are given as median (IQR). Volumes are expressed as fractions of the estimated total intracranial volume. Statistical comparisons between groups were made with Mann–Whitney *U*-test for quantitative and Fisher's exact test for qualitative variables.

Abbreviations: MSA-C, MSA with predominant cerebellar ataxia; MSA-C BL, patients with MSA-C at baseline; MSA-C CO, patients with conversion to MSA-C during follow-up; SAOA, sporadic adult-onset ataxia of unknown etiology; NfL, neurofilament light chain; CGM, cerebellar grey matter; CWM, cerebellar white matter; PMAS, pons and middle cerebellar peduncle abnormality score; IQR, interquartile range.

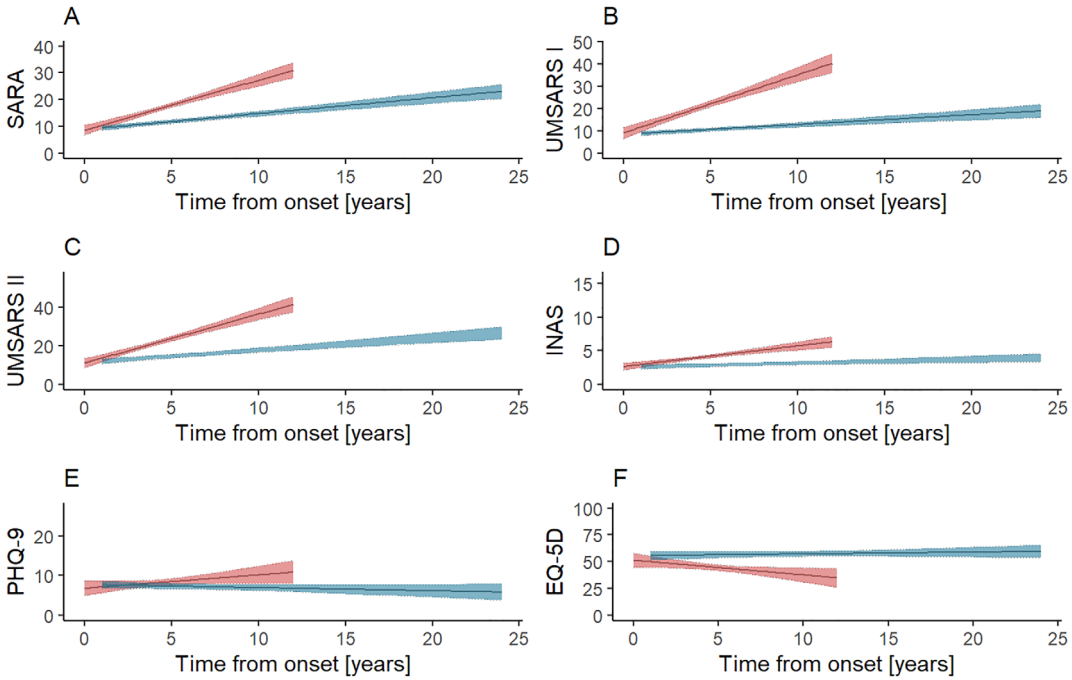

FIG. 1. Evolution of clinical outcome measures in MSA-C and SAOA. Estimated trajectories with 95% CIs of (A) SARA, (B) UMSARS-I, (C) UMSARS-II, (D) INAS, (E) PHQ-9, and (F) EQ-5D on a time scale starting with ataxia onset, with curves drawn using mixed-effects modeling. Trajectories with 95% CIs of MSA-C are given in red, trajectories of SAOA in blue. MSA-C, multiple system atrophy of cerebellar type; SAOA, sporadic adult-onset ataxia of unknown etiology; CI, confidence interval; SARA, Scale for the Assessment and Rating of Ataxia; UMSARS, Unified MSA Rating Scale; INAS, Inventory of Non-Ataxia Signs; PHQ-9, Patient's Health Questionnaire; EQ-5D VAS, EQ-5D visual analog scale

MRI data were available of 20 MSA-C and 49 SAOA patients (Supplementary Data **S1**). Baseline data are summarized in Table 2. Among the various MRI metrics, CWM volume, pons volume, and PMAS were significantly different between both, MSA-C and MSA-C CO, and SAOA indicating more severe tissue damage in MSA-C than in SAOA. MRI volumes did not differ between MSA-C BL and MSA-C CO. However, PMAS was higher in MSA-C BL than in MSA-C CO.

NfL separated MSA-C from SAOA with an AUC of 0.76 (95% CI 0.65-0.86), CWM volume with 0.84 (95% CI, 0.74-0.92), pons volume with 0.84 (95% CI, 0.74-0.92), and PMAS with 0.83 (95% CI, 0.72-0.93). There was no significant increase of AUC for nested models.

Evolution of Clinical Outcome Measures

Data from 837 visits were analyzed (Supplementary Table **S1**). Participants had a median number of 2 visits (IQR, 1-3). Mixed-effects modeling of the evolution of SARA, UMSARS-I, UMSARS-II, and INAS revealed a faster progression in MSA-C than in SAOA, whereas the slopes of PHQ-9 and EQ-5D VAS did not differ (Fig. 1, Supplementary Fig. **S1** and Supplementary Table S2). The evolution of single SARA items is graphically displayed in Supplementary Fig. S2. In MSA-C, scores of the gait item, stance item, and sitting item, in SAOA, score of the gait item contributed most to SARA progression. Comparison of the progression rates of clinical outcome measures between MSA-C BL and MSA-C CO did not reveal differences (Supplementary Fig. S3 and Supplementary Table S3).

Evolution of Biomarkers

Mixed-effects modeling revealed a mild decrease of NfL levels in MSA-C, whereas it did not change in SAOA (Fig. 2, Supplementary Fig. S4 and Supplementary Table S4). The decrease of NfL levels in MSA-C BL and MSA-C CO did not differ (Supplementary Fig. S5 and Supplementary Table S5).

CWM and pons volume decreased faster in MSA-C than in SAOA, whereas PMAS increased faster in MSA-C than in SAOA (Fig. 2, Supplementary Fig. S4 and Supplementary Table S4). The slopes of the changes of CWM volume, pons volume, and PMAS in MSA-C BL and MSA-C CO did not differ (Supplementary Fig. S5 and Supplementary Table S5).

Sensitivity to Change

In MSA-C, SCSs of SARA, UMSARS-I, and UMSARS-II were 0.619, 0.610, and 0.620, respectively. Those of the other clinical outcome measures had smaller absolute values ranging between −0.146 (EQ-5D) and 0.356 (INAS). In SAOA, the SCSs of the clinical outcome measures ranged between −0.064 (PHQ-9) and 0.386 (INAS) (Supplementary Table S2).

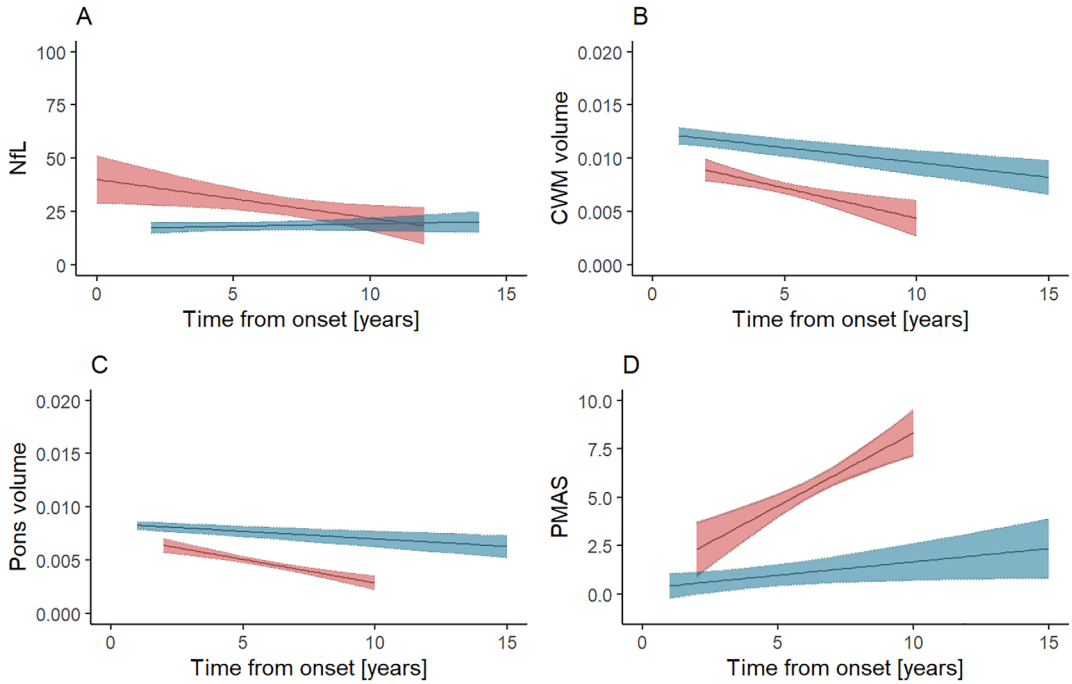

FIG. 2. Evolution of biomarkers in MSA-C and SAOA. Estimated trajectories with 95% CIs (A) NfL, (B) CWM volume, (C) pons volume, and (D) PMAS on a time scale starting with ataxia onset, with curves drawn using mixed-effects modeling. Trajectories with 95% CIs of MSA-C are given in red, trajectories of SAOA in blue. MSA-C, multiple system atrophy of cerebellar type; SAOA, sporadic adult-onset ataxia of unknown etiology; CI, confidence interval; NfL, neurofilament light chain; CWM, cerebellar white matter; PMAS, pons and middle cerebellar peduncle abnormality score

TABLE 3 *Predictors of conversion to MSA-C*

Risk factor	HR	95% CI	*P* value	N	N events	*P* (zhp)
Female sex	1.631	(0.730, 3.647)	0.233	266	24	0.14
Age at onset	1.011	(0.967, 1.057)	0.626	266	24	0.65
Possible MSA criteria	3.854	(1.635, 9.082)	0.002	263	24	0.59
NfL	1.138	(1.034, 1.254)	0.009	72	7	0.69
CWM volume	<0.0001	(0, Inf)	0.014	55	6	0.67
Pons volume	<0.0001	(0, Inf)	0.019	55	6	0.66
PMAS	2.557	(1.512, 4.315)	<0.001	56	6	0.29

Note: Analysis was performed using univariable Cox proportional hazard models.
Abbreviations: HR, hazard ratio; MSA-C, multiple system atrophy with prominent cerebellar ataxia; NfL, neurofilament light chain; CWM, cerebellar white matter; PMAS, pons and middle cerebellar peduncle abnormality score; *P* (zhp), *P* value of formal score test.

In MSA-C, SCS of pons volume had the highest absolute value (−1.137) followed by PMAS (−0.901) and CWM volume (−0.689), whereas the absolute value of the SCS of NfL was lower (−0.279). In SAOA, the SCS of CWM volume (−0.479) had the highest absolute value of all biomarkers studied (Supplementary Table S4).

Predictors of Disease Progression

In MSA-C, univariable modeling identified SARA as a predictor for slower (−0.08; 95% CI, −0.013 to −0.04; $P < 0.001$) and PMAS as a predictor for faster SARA progression (0.44; 95% CI, 0.01-0.90; $P = 0.046$). The significant factors for SAOA were female sex (0.33; 95% CI, 0.04-0.62; $P = 0.022$) and age at ataxia onset (0.02; 95% CI, 0.00-0.03; $P = 0.031$) (Supplementary Table S6). Multivariable modeling did not identify significant predictors.

Risk Factors for Clinical Conversion to MSA-C

Univariable Cox regression identified possible MSA criteria, NfL, and PMAS as risk factors, and CWM and pons volume as protective factors for clinical

conversion to MSA-C (Table 3). The small number of events did not allow a multivariable analysis.

Discussion

This registry study provides genetic, clinical, and biomarker data of a large cohort of patients with sporadic adult-onset degenerative ataxia. Analysis of clinical outcome measures supported previous observations of faster disease progression in MSA-C than in SAOA. A key finding is the characterization of plasma NfL and three quantitative MRI measures as markers that differentiate between MSA-C and SAOA and show different evolution in both conditions. In MSA-C, MRI signal abnormalities were predictors of faster disease progression. In addition, MRI measures and NfL together with clinical features were risk and protective factors, respectively, for clinical conversion to MSA-C.

An inherent weakness of many clinical studies in MSA-C and related conditions is the uncertainty about the definite diagnosis. There was no autopsy confirmation; therefore, we relied on the clinical diagnosis of MSA-C according to consensus criteria published in 2008.[7] Unfortunately, we were not able to reclassify study participants according to the updated diagnostic criteria,[10] because not all the required information was available. As additional genetic screening was not done in all participants, some participants may have had an identifiable genetic cause. Likewise, we cannot fully rule out that some suffered from an unrecognized immune-mediated ataxia. Because this was a registry study, in which study visits were combined with clinical routine visits, follow-up visits were done at different intervals, and there was substantial drop-out. We compensated for this by statistically modeling the data on a common time scale starting with ataxia onset. Only some of the centers sampled blood and acquired MRIs. Therefore, compared to the clinical measures, the amount of data on NfL and quantitative MRI measures was smaller, which limited the possibilities for analysis.

In a previous study of sporadic ataxia patients we found repeat mutations causing ataxia (FRDA, SCA1, SCA2, SCA3, and SCA6) in 13% of the participants.[48] We, therefore, defined negative tests for these mutations as an inclusion criterion for the SPORTAX registry. The present genetic studies revealed that 5% of the tested study participants had an *RFC1* mutation and another 5% variable autosomal recessive or dominant causative mutations identified by NGS. These rates are in line with previous findings in cohorts of sporadic degenerative ataxia, although comparison is difficult because of different inclusion criteria and test strategies.[49-52] The present findings together with those of our previous study allow the conclusion that a stepwise genetic screening including tests for repeat mutations and NGS yields a positive genetic diagnosis in 22% of patients with sporadic ataxia and an age of onset >40 years.

All clinical scales and UMSARS-I, that assesses ADL, showed faster progression of MSA-C than SAOA.[15,17] Notably, in MSA-C, UMSARS-I, had a sensitivity to change in the same range as the clinical scales, SARA and UMSARS-II. In the longitudinal European Friedreich's Ataxia Consortium for Translational Studies (EFACTS) study, an ADL scale was even slightly more sensitive than SARA.[53] Because of their high sensitivity, their obvious patient relevance and easy applicability, ADL scales may be useful outcome measures in interventional trials in ataxia. In SAOA, SARA had the highest sensitivity underlining the general usefulness of SARA for studying ataxia progression.

Approximately 10% of the patients who did not fulfill criteria for probable MSA at baseline converted to the clinical phenotype of probable MSA. SAOA patients had longer disease duration at inclusion, but follow-up was incomplete, it cannot be excluded that the SAOA group still included some MSA-C patients. Comparison of clinical progression and biomarker evolution of those with MSA-C at baseline and converters did not reveal differences showing that converters share the unfavorable course of MSA-C, even before formal diagnostic criteria are fulfilled. We identified possible MSA criteria as a risk factor for conversion. Further potential risk respectively protective factors were NfL and MRI markers (pons and CWM volume, PMAS), but these findings have to be interpreted with caution because of the small number of conversions and need to be verified in larger studies. Prediction may be further improved by considering DaTScan results.[17]

Compared to known values of healthy individuals,[42] plasma NfL levels were elevated both in MSA-C and SAOA, but were significantly higher in MSA-C. In MSA-C, NfL slightly decreased in the disease course, but remained at a high level. In addition, NfL was a risk factor for conversion to MSA-C. These findings are compatible with those of a recent study that reported an association of NfL levels with clinical progression, survival, and degree of brain atrophy in MSA. This study also found decreasing NfL levels in advanced stages.[20] This finding supports our earlier notion that NfL in neurodegenerative diseases is not marker of disease severity, but rather reflects the rate of ongoing neuronal decay.[42] This rate is even expected to decrease, once residual mass of pertinent brain regions is reduced in advanced stages. An alternative explanation would be that patients with longer disease duration and lower NfL levels represent those with a less aggressive course.

We identified three MRI markers—CWM and pons volume and PMAS—that differentiated between MSA-C and SAOA at baseline, progressed faster in MSA-C, and were risk factors for conversion to

MSA-C. Among all clinical measures and biomarkers, pons volume had the highest sensitivity to change. PMAS was also a predictor of disease progression in MSA-C. However, PMAS requires further validation studies.

The results of our study may aid clinicians in the diagnostic work-up and counseling of sporadic ataxia patients. They also have important implications for future research. In view of an increasing number of future trials of disease modifying interventions in MSA, MRI markers, in particular pontine volume, should be further validated as progression markers. NfL and MRI markers including PMAS may be also used to identify MSA-C patients for inclusion into clinical trials at an early disease stage. ●

Acknowledgment: We thank all individuals for participation in the study. T. Klockgether, L.S., T. Klopstock, S.B., W.N., and M. Synofzik are members of the European Reference Network for Rare Neurological Diseases (ERN-RD; project no. 739510). C.W., D.M., Z.F., and A. T. were supported via a Clinician Scientist Program grant by the University of Tübingen. We are thankful to Alejandra Leyva-Gutiérrez for technical execution of the NfL assay. Open Access funding enabled and organized by Projekt DEAL.

Funding Information

Parts of the analyses of this project were supported by the Deutsche Forschungsgemeinschaft (441409627) as part of the PROSPAX consortium under the frame of the European Joint Programme on Rare Diseases (EJP RD COFUND-EJP no. 825575 to M. Synofzik and as an associated partner D.T.).

Data Availability Statement

The data that support the findings of this study are available on request from the corresponding author. The data are not publicly available due to privacy or ethical restrictions.

References

1. Harding AE. "Idiopathic" late onset cerebellar ataxia. A clinical and genetic study of 36 cases. J Neurol Sci 1981;51:259–271.
2. Klockgether T. Sporadic ataxia with adult onset: classification and diagnostic criteria. Lancet Neurol 2010;9:94–104.
3. Tsuji S, Onodera O, Goto J, Nishizawa M. Sporadic ataxias in Japan--a population-based epidemiological study. Cerebellum 2008; 7:189–197.
4. Muzaimi MB, Thomas J, Palmer-Smith S, et al. Population based study of late onset cerebellar ataxia in south East Wales. J Neurol Neurosurg Psychiatry 2004;75:1129–1134.
5. Leone M, Bottacchi E, D'Alessandro G, Kustermann S. Hereditary ataxias and paraplegias in Valle d'Aosta, Italy: a study of prevalence and disability. Acta Neurol Scand 1995;91:183–187.
6. Polo JM, Calleja J, Combarros O, Berciano J. Hereditary ataxias and paraplegias in Cantabria, Spain. An epidemiological and clinical study. Brain 1991;114(Pt 2):855–866.
7. Gilman S, Wenning GK, Low PA, et al. Second consensus statement on the diagnosis of multiple system atrophy. Neurology 2008;71: 670–676.
8. Osaki Y, Ben-Shlomo Y, Lees AJ, Wenning GK, Quinn NP. A validation exercise on the new consensus criteria for multiple system atrophy. Mov Disord 2009;24:2272–2276.
9. Miki Y, Foti SC, Asi YT, et al. Improving diagnostic accuracy of multiple system atrophy: a clinicopathological study. Brain 2019; 142:2813–2827. https://doi.org/10.1093/brain/awz189
10. Wenning GK, Stankovic I, Vignatelli L, et al. The Movement Disorder Society criteria for the diagnosis of multiple system atrophy. Mov Disord 2022;37:1131–1148. https://doi.org/10.1002/mds.29005
11. Abele M, Minnerop M, Urbach H, Specht K, Klockgether T. Sporadic adult onset ataxia of unknown etiology: a clinical, electrophysiological and imaging study. J Neurol 2007;254:1384–1389.
12. Tsuchiya K, Ozawa E, Saito F, Irie H, Mizutani T. Neuropathology of late cortical cerebellar atrophy in Japan: distribution of cerebellar change on an autopsy case and review of Japanese cases. Eur Neurol 1994;34:253–262.
13. Ota S, Tsuchiya K, Anno M, Niizato K, Akiyama H. Distribution of cerebello-olivary degeneration in idiopathic late cortical cerebellar atrophy: clinicopathological study of four autopsy cases. Neuropathology 2008;28:43–50.
14. Kim M, Kim AR, Kim JS, et al. Clarification of undiagnosed ataxia using whole-exome sequencing with clinical implications. Parkinsonism Relat Disord 2020;80:58–64. https://doi.org/10.1016/j.parkreldis.2020.08.040
15. Giordano I, Harmuth F, Jacobi H, et al. Clinical and genetic characteristics of sporadic adult-onset degenerative ataxia. Neurology 2017;89(10):1043–1049.
16. Gilman S, Little R, Johanns J, et al. Evolution of sporadic olivopontocerebellar atrophy into multiple system atrophy. Neurology 2000;55:527–532.
17. Wirth T, Namer IJ, Monga B, et al. Progression of nigrostriatal denervation in cerebellar multiple system atrophy: a prospective study. Neurology 2022;98:232–236. https://doi.org/10.1212/WNL.0000000000013172
18. Wilke C, Bender F, Hayer SN, et al. Serum neurofilament light is increased in multiple system atrophy of cerebellar type and in repeat-expansion spinocerebellar ataxias: a pilot study. J Neurol 2018;265:1618–1624.
19. Zhang L, Cao B, Hou Y, et al. Neurofilament light chain predicts disease severity and progression in multiple system atrophy. Mov Disord 2022;37:421–426. https://doi.org/10.1002/mds.28847
20. Chelban V, Nikram E, Perez-Soriano A, et al. Neurofilament light levels predict clinical progression and death in multiple system atrophy. Brain 2022;145:4398–4408. https://doi.org/10.1093/brain/awac253
21. Singer W, Schmeichel AM, Shahnawaz M, et al. Alpha-synuclein oligomers and neurofilament light chain predict Phenoconversion of pure autonomic failure. Ann Neurol 2021;89:1212–1220. https://doi.org/10.1002/ana.26089
22. Burk K, Globas C, Wahl T, et al. MRI-based volumetric differentiation of sporadic cerebellar ataxia. Brain 2004;127:175–181.
23. Faber J, Giordano I, Jiang X, et al. Prominent white matter involvement in multiple system atrophy of cerebellar type. Mov Disord 2020;35:816–824. https://doi.org/10.1002/mds.27987
24. Paviour DC, Price SL, Jahanshahi M, Lees AJ, Fox NC. Longitudinal MRI in progressive supranuclear palsy and multiple system atrophy: rates and regions of atrophy. Brain 2006;129:1040–1049. https://doi.org/10.1093/brain/awl021
25. Reginold W, Lang AE, Marras C, Heyn C, Alharbi M, Mikulis DJ. Longitudinal quantitative MRI in multiple system atrophy and progressive supranuclear palsy. Parkinsonism Relat Disord 2014;20: 222–225. https://doi.org/10.1016/j.parkreldis.2013.10.002
26. Savoiardo M, Strada L, Girotti F, et al. Olivopontocerebellar atrophy: MR diagnosis and relationship to multisystem atrophy. Radiology 1990;174:693–696.
27. Schulz JB, Klockgether T, Petersen D, et al. Multiple system atrophy: natural history, MRI morphology, and dopamine receptor imaging

with 123IBZM-SPECT. J Neurol Neurosurg Psychiatry 1994;57:1047–1056.

28. Schrag A, Kingsley D, Phatouros C, et al. Clinical usefulness of magnetic resonance imaging in multiple system atrophy. J Neurol Neurosurg Psychiatry 1998;65:65–71.
29. Abe K, Hikita T, Yokoe M, Mihara M, Sakoda S. The "cross" signs in patients with multiple system atrophy: a quantitative study. J Neuroimaging 2006;16:73–77. https://doi.org/10.1177/1051228405279988
30. Burk K, Buhring U, Schulz JB, Zuhlke C, Hellenbroich Y, Dichgans J. Clinical and magnetic resonance imaging characteristics of sporadic cerebellar ataxia. Arch Neurol 2005;62:981–985.
31. Carré G, Dietemann JL, Gebus O, et al. Brain MRI of multiple system atrophy of cerebellar type: a prospective study with implications for diagnosis criteria. J Neurol 2020;267:1269–1277. https://doi.org/10.1007/s00415-020-09702-w
32. Schmitz-Hubsch T, Du Montcel ST, Baliko L, et al. Scale for the assessment and rating of ataxia: development of a new clinical scale. Neurology 2006;66:1717–1720.
33. Wenning GK, Tison F, Seppi K, et al. Development and validation of the unified multiple system atrophy rating scale (UMSARS). Mov Disord 2004;19:1391–1402.
34. Jacobi H, Rakowicz M, Rola R, et al. Inventory of non-ataxia signs (INAS): validation of a new clinical assessment instrument. Cerebellum 2013;12:418–428.
35. Spitzer RL, Kroenke K, Williams JB. Validation and utility of a self-report version of PRIME-MD: the PHQ primary care study. Primary care evaluation of mental disorders. Patient health questionnaire. JAMA 1999;282:1737–1744.
36. The EuroQol Group. EuroQol--a new facility for the measurement of health-related quality of life. Health Policy 1990;16:199–208.
37. Cortese A, Simone R, Sullivan R, et al. Biallelic expansion of an intronic repeat in RFC_1 is a common cause of late-onset ataxia. Nat Genet 2019;51:649–658. https://doi.org/10.1038/s41588-019-0372-4
38. Traschütz A, Cortese A, Reich S, et al. Natural history, phenotypic Spectrum, and discriminative features of multisystemic RFC1 disease. Neurology 2021;96:e1369–e1382. https://doi.org/10.1212/WNL.0000000000011528
39. Herrmann L, Gelderblom M, Bester M, et al. Multisystemic neurodegeneration caused by biallelic pentanucleotide expansions in RFC1. Parkinsonism Relat Disord 2022;95:54–56. https://doi.org/10.1016/j.parkreldis.2022.01.001
40. Richards S, Aziz N, Bale S, et al. Standards and guidelines for the interpretation of sequence variants: a joint consensus recommendation of the American College of Medical Genetics and Genomics and the Association for Molecular Pathology. Genet Med 2015;17:405–424.
41. Harrison SM, Biesecker LG, Rehm HL. Overview of specifications to the ACMG/AMP variant interpretation guidelines. Curr Protoc Hum Genet 2019;103:e93. https://doi.org/10.1002/cphg.93
42. Wilke C, Haas E, Reetz K, et al. Neurofilaments in spinocerebellar ataxia type 3: blood biomarkers at the preataxic and ataxic stage in humans and mice. EMBO Mol Med 2020;12:e11803. https://doi.org/10.15252/emmm.201911803
43. Tustison NJ, Avants BB, Cook PA, et al. N4ITK: improved N3 bias correction. IEEE Trans Med Imaging 2010;29:1310–1320. https://doi.org/10.1109/TMI.2010.2046908
44. Buckner RL, Head D, Parker J, et al. A unified approach for morphometric and functional data analysis in young, old, and demented adults using automated atlas-based head size normalization: reliability and validation against manual measurement of total intracranial volume. Neuroimage 2004;23:724–738. https://doi.org/10.1016/j.neuroimage.2004.06.018
45. Iglesias JE, van Leemput K, Bhatt P, et al. Bayesian segmentation of brainstem structures in MRI. Neuroimage 2015;113:184–195. https://doi.org/10.1016/j.neuroimage.2015.02.065
46. Faber J, Kügler D, Bahrami E, et al. CerebNet: a fast and reliable deep-learning pipeline for detailed cerebellum sub-segmentation. Neuroimage 2022;264:119703.
47. Klockgether T, Lüdtke R, Kramer B, et al. The natural history of degenerative ataxia: a retrospective study in 466 patients. Brain 1998;121:589–600.
48. Abele M, Burk K, Schols L, et al. The aetiology of sporadic adult-onset ataxia. Brain 2002;125:961–968.
49. Montaut S, Diedhiou N, Fahrer P, et al. Biallelic RFC1-expansion in a French multicentric sporadic ataxia cohort. J Neurol 2021;268:3337–3343. https://doi.org/10.1007/s00415-021-10499-5
50. Aboud Syriani D, Wong D, Andani S, et al. Prevalence of RFC1-mediated spinocerebellar ataxia in a north American ataxia cohort. Neurol Genet 2020;6:e440. https://doi.org/10.1212/NXG.0000000000000440
51. Wan L, Chen Z, Wan N, et al. Biallelic intronic AAGGG expansion of RFC1 is related to multiple system atrophy. Ann Neurol 2020;88:1132–1143. https://doi.org/10.1002/ana.25902
52. Bogdan T, Wirth T, Iosif A, et al. Unravelling the etiology of sporadic late-onset cerebellar ataxia in a cohort of 205 patients: a prospective study. J Neurol 2022;269:6354–6365. https://doi.org/10.1007/s00415-022-11253-1
53. Reetz K, Dogan I, Hilgers RD, et al. Progression characteristics of the European Friedreich's ataxia consortium for translational studies (EFACTS): a 2 year cohort study. Lancet Neurol 2016;15:1346–1354.

Supporting Data

Additional Supporting Information may be found in the online version of this article at the publisher's web-site.

SGML and CITI Use Only
DO NOT PRINT

Author Roles

(1) Research project: A. Conception, B. Organization, C. Execution; (2) Statistical Analysis: A. Design, B. Execution, C. Review and Critique; (3) Manuscript: A. Writing of the First Draft, B. Review and Critique.

D.Ö.: 1A, 1B, 1C, 3B
J.F.: 1A, 1B, 1C, 3B
I.G.: 1A, 1B, 1C, 3B
M.G.E.: 1A, 1B, 1C, 3B
M.Synofzik: 1A, 1B, 1C, 2B
C.W.: 1C, 3B
A.L.: 1C, 3B
D.M.: 1C, 3B
L.S.: 1C, 3B
A.T.: 1C, 3B
Z.F.: 1C, 3B
C.D.: 1C, 3B
S.V.: 1C, 3B
J.M.: 1C, 3B
T.Klopstock: 1C, 3B
C.S.: 1C, 3B
S.B.: 1C, 3B
W.N.: 1C, 3B
D.T.: 1C, 3B
A.G.T.: 1C, 3B
C.K.: 1C, 3B
A.D.: 1C, 3B
C.T.: 1C, 3B
I.W.:1C, 3B
A.F.: 1C, 3B
T.S.: 2B
M.Schmid: 2B
T.Klockgether: 1A, 1B, 2A

Financial Disclosures of all Authors (for the preceding 12 months)

J.F. is a funded as a fellow of the Hertie Network of Excellence in Clinical Neuroscience. T. Klopstock has received research support from the Bundesministerium für Bildung und Forschung (BMBF) and the European Commission (EC). He has received consultancy honoraria from Chiesi GmbH, OMEICOS Therapeutics, Pretzel Therapeutics, and the Dierks+Company Consulting GmbH. S.B. has received grants from the Fonds zur Förderung der wissenschaftlichen Forschung (FWF). She has received consultancy honoraria from REATA Pharmaceuticals and Merz Pharma. Dagmar Timmann has received grants from the German Research Foundation, the EU and the Bernd Fink Foundation. A. Thieme received grants from the German Research Foundation and German Heredataxia Society (DHAG). C.K. has received consultancy honoraria from Roche and Biogen, and speaker honoraria from Ipsen. M. Synofzik has received consultancy honoraria from Janssen, Ionis, Orphazyme, Servier, and AviadoBio. T. Klockgether has received research support from the Bundesministerium für Bildung und Forschung (BMBF) and the National Institutes of Health (NIH). He has received consultancy honoraria from Biogen, UCB, and Vico Therapeutics.

Supplementary material

Supplement to: Önder D et al. Clinical phenotype and biomarkers in sporadic degenerative ataxia: longitudinal data from the SPORTAX registry

Table of contents

Supplementary methods

Inclusion criteria

1. Progressive ataxia

2. Ataxia after onset after the age of 40 years

3. Informative and negative family history (no similar disorders in first- and second-degree relatives; parents older than 50 years, or, if not alive, age at death of more than 50 years, no consanguinity of parents)

4. No established acquired cause of ataxia:

a. Clinical: no onset of ataxia in association with stroke, encephalitis, sepsis, hyperthermia or heat stroke, chronic diarrhea, unexplained visual loss, alcohol abuse, chronic intake of anticonvulsant drugs, other toxic causes, malignancies; rapid progression defined as development of severe ataxia in less than 12 weeks; no insulin-dependent diabetes

b. Imaging: no evidence of multiple sclerosis, ischemia, hemorrhage or tumor of the posterior fossa; absence of signal abnormalities on T2/FLAIR-images except abnormalities compatible with MSA-C

c. Laboratory: negative molecular genetic test for FRDA (only required if there was no cerebellar atrophy on MRI), SCA1, SCA2, SCA3, SCA6, FMR1 premutation (only required if prominent tremor, cognitive impairment and signal abnormality on T2/FLAIR images in the middle cerebellar peduncle); antineuronal antibodies negative (only required, if time from onset less than 3 years; core set included anti-Hu, anti-Yo, anti-Ri, and anti-GAD antibodies; selection of additional antibodies left to the discretion of each center); normal levels of vitamin B12; VDRL negative; normal thyroid function).

RFC1 screening

The intronic genomic region of the RFC1 expansion was amplified from genomic DNA using a fluorescence-labelled PCR. The number of 5bp repeat motifs were calculated from the length of the alleles as determined by capillary electrophoresis (ABI3730, Applied Biosystems) allowing for an exact determination of repeat numbers up to 115 repeats. In addition, a “triple primer” approach was performed including a repeat-primed (rp)-PCR to target the frequent pathogenic motive (AAGGG),[1] and the non-pathogenic motive

(AAAAG).[2] The presence of an AAGGG RFC1 expansion was confirmed, if flanking PCR did not show an amplifiable fragment, and the rp-PCR for AAAAG did not show a peak, while the rp-PCR for the AAGGG showed the typical sawtooth peak.

High-coverage NGS panel

The core set of n=201 ataxia genes (gene set #1, see below) was sequenced in 184 subjects by a high-coverage custom HaloPlex gene panel (Agilent, Santa Clara, CA) using an NextSeq500 sequencer (Illu- mina, San Diego, CA) and paired-end 2x150 bp sequencing (671-kb target size). The mean vertical coverage was 413 reads, and a minimal coverage of 20 reads was achieved for 98.8% of the target region. Bioinformatic analysis of the variants were described previously (PMID: 28794257).

Whole Exome Sequencing

The core set of n=201 ataxia genes (gene set #1, see below) was sequenced in 147 other subjects, as part of a whole exome sequencing (WES), run on the Illumina NovaSeq 6000 platform using the Agilent SureSelectXT library preparation kit and the SureSelect Human All Exon V7 enrichment kit (Q30-value: 92.34%). Reads were aligned with BWA. Variants were called with Picard and FREEBAYES and annotated with ANNOVAR as part of the GENESIS platform (PMID 26173844). Loss-of-function and missense variants in ataxia genes were filtered for: sufficient quality (depth >10, GQ >20, QUAL >35), convolutional neural network criteria (CNN score >99.95% for SNVs and >99.4% for indels), rare minor alle frequency (MAF) (heterozygous variants in autosomal-dominant genes: MAF <0.0001 in gnomAD and <0.001 in-house; homozygous and compound-heterozygous variants in both recessive and dominant ataxia genes: MAF <0.01 both in gnomAD and in-house), and - for missense variants- high predicted functional impact (CADD score >20). In addition to the gene set #1, also variants in additional 182 ataxia-overlap disease genes were considered (gene set #2, see below) using the same filter criteria. Variants in other genes associated with neurodegenerative diseases (n = 985, gene set #3) were also considered, irrespective of their allele frequency and predicted functional impact, if these were reported as pathogenic or likely pathogenic in ClinVar.

Pathogenicity of the resulting variants was determined according to ACMG.[3,4]. Subjects were classified as having a genetic diagnosis based on the pathogenicity likelihood of the respective

variants and the phenotypic match. That is, subjects were classified as: (1) definitive genetic diagnosis, if having a pathogenic or likely pathogenic variant and a phenotype typical of the genetic variant; (i2) probable genetic diagnosis, if having a pathogenic or likely pathogenic variant and a phenotype broadly compatible with the genetic variant; (3) no genetic diagnosis (all other subjects).

Gene set #1 (n = 201) (core gene set)

ABCB7, ABCD1, ABHD12, ACO2, ADCK3, AFG3L2, AHI1, ALAS2, ALG6, AMACR, AMT, ANO10, APTX, ARL13B, ARSA, ARX, ATCAY, ATM, ATP2B2, ATP2B3, ATP7B, B4GALNT1, BTD, C10ORF2, CA8, CACNA1A, CACNA1G, CACNB4, CAMTA1, CC2D2A, CEP290, CLN5, CLN6, CLN8, COQ2, COQ6, COQY, CP, CSTB, CYP27A1, CYP7B1, DARS, DARS2, DDB2, DLAT, DNAJC19, DNAJC3, DNAJC5, EEF2, EIF2B1, EIF2B2, EIF2B3, EIF2B4, EIF2B5, ELOVL4, ELOVL5, EPM2A, ERCC2, ERCC3, ERCC4, ERCC5, ETFA, ETFB, ETFDH, FGF14, FLVCR1, FOLR1, FXN, GALC, GBA, GBA2, GBE1, GCDH, GCLC, GCSH, GFAP, GLB1, GLDC, GM2A, GPR56, GRID2, GRM1, HERC1, HEXA, HEXB, HPRT1, HSD17B4, HTRA1, IGDCC3, INPP5E, ITM2B, ITPR1, KCNA1, KCNA2, KCNC1, KCNC3, KCND3, KCNJ10, KIAA0226, KIF1A, KIF1C, KIF5C, L2HGDH, MARS2, MFSD8, MLC1, MRE11A, MTPAP, MTRR, MTTP, NEU1, NHLRC1, NKX2-1, NOL3, NPC1, NPC2, NPHP1, OPA1, OPA3, PAX6, PDHX, PDSS1, PDSS2, PDYN, PEX10, PEX2, PEX7, PHYH, PIK3R5, PLA2G6, PLEKHG4, PMM2, PMPCA, PNKP, PNPLA6, POLG, POLH, POLR3A, POLR3B, PPT1, PRICKLE1, PRKCG, PRPS1, PRRT2, RAB3A, RARS2, RELN, RNF170, RNF216, RPGRIP1L, RRM2B, SACS, SCYL1, SEC16A, SETX, SIL1, SKOR1, SLC17A5, SLC19A3, SLC1A3, SLC25A15, SLC25A46, SLC2A1, SLC39A8, SLC52A2, SLC9A1, SNX14, SPG7, SPR, SPTBN2, STUB1, SUN1, SUN2, SYNE1, SYT14, TBCC, TDP1, TGM6, TMEM216, TMEM240, TMEM67, TPP1, TRPC3, TSEN2, TSEN34, TSEN54, TSFM, TTBK2, TTC19, TTPA, VAMP1, VLDLR, VPS13A, VRK1, VWASB, WDR73, WFS1, WWOX, XPA, XPC, ZNF592

Gene set # 2 (n = 383) (ataxia plus ataxia-overlap diseases, including all genes from gene set #1)

ACO2, ADCK3, ALAS2, AMT, ARX, ATP2B2, C10ORF2, CACNA1A, CSTB, DARS, EPM2A, ETFA, ETFB, ETFDH, GBE1, GCLC, GCSH, GLDC, GM2A, HERC1, HTRA1,

ITM2B, KIF5C, MRE11A, MTRR, NHLRC1, NOL3, PAX6, POLH, RELN, RRM2B, SLC39A8, SUN1, SUN2, TSFM, WFS1, ABCB7, ABCD1, ABHD12, AFG3L2, AHI1, AIMP1, ALDH18A1, ALDH3A2, ALG6, ALS2, AMACR, AMPD2, ANG, ANO10, AP4B1, AP4E1, AP4M1, AP4S1, AP5Z1, APTX, ARG1, ARL13B, ARL3, ARL6IP1, ARMC9, ARSA, ARSI, ATCAY, ATL1, ATM, ATP13A2, ATP1A3, ATP2B3, ATP2B4, ATP7B, ATP8A2, ATXN8OS, AUH, B4GALNT1, B9D1, BEAN1, BICD2, BSCL2, BTD, C12orf65, C19orf12, C5orf42, CA8, CACNA1G, CACNB4, CAMTA1, CAPN1, CC2D2A, CCDC88C, CCT5, CEP104, CEP120, CEP290, CEP41, CLCN2, CLN5, CLN6, CLN8, COQ2, COQ6, COQ8A, CP, CPT1C, CSF1R, CSPP1, CTDP1, CWF19L1, CYP27A1, CYP2U1, CYP7B1, DAB1, DARS2, DDB2, DDHD1, DDHD2, DLAT, DNAJC19, DNAJC3, DNAJC5, DNM2, DNMT1, DSTYK, EEF2, EIF2B1, EIF2B2, EIF2B3, EIF2B4, EIF2B5, ELOVL4, ELOVL5, ENTPD1, EPT1, ERCC2, ERCC3, ERCC4, ERCC5, ERLIN1, ERLIN2, EXOSC3, FA2H, FAM126A, FAM134B, FARS2, FBXO7, FGF14, FIG4, FLRT1, FLVCR1, FOLR1, FUS, FXN, GAD1, GALC, GAN, GARS1, GBA, GBA2, GCDH, GCH1, GFAP, GJB1, GJC2, GLB1, GLRX5, GLTP, GNB1, GOSR2, GPR56, GPT2, GRID2, GRM1, HACE1, HEPACAM, HEXA, HEXB, HPRT1, HSD17B4, HSPD1, HYLS1, IBA57, IFIH1, IFRD1, INPP5E, INPP5K, IRF2BPL, ITPR1, KCNA1, KCNA2, KCNC1, KCNC3, KCND3, KCNJ10, KIAA0226, KIAA0556, KIAA0586, KIAA0753, KIDINS220, KIF1A, KIF1C, KIF5A, KIF7, KLC2, KLC4, KY, L1CAM, L2HGDH, LYST, MAG, MAN2B1, MARS1, MARS2, MFN2, MFSD8, MKS1, MLC1, MME, MRE11, MSTO1, MT-ATP6, MTPAP, MTTP, NARS2, NDUFS7, NEU1, NIPA1, NKX2-1, NKX6-2, NPC1, NPC2, NPHP1, NT5C2, NUBPL, OFD1, OPA1, OPA3, OPTN, PANK2, PCNA, PCYT2, PDE6D, PDHX, PDSS1, PDSS2, PDYN, PEX1, PEX10, PEX11B, PEX12, PEX13, PEX14, PEX16, PEX19, PEX2, PEX26, PEX3, PEX5, PEX6, PEX7, PGAP1, PHYH, PIBF1, PIK3R5, PLA2G6, PLEKHG4, PLP1, PMM2, PMPCA, PNKP, PNPLA6, POLG, POLR3A, POLR3B, PPT1, PRDX3, PRICKLE1, PRKCG, PRPS1, PRRT2, PTRH2, RAB3A, RAB3GAP2, RARS2, REEP1, REEP2, RNASEH2B, RNASET2, RNF168, RNF170, RNF216, RNU12, RPGRIP1L, RTN2, SACS, SCYL1, SERAC1, SETX, SIL1, SLC16A2, SLC17A5, SLC19A3, SLC1A3, SLC25A15, SLC25A46, SLC2A1, SLC33A1, SLC52A2, SLC9A1, SLC9A6, SMPD1, SNAP25, SNX14, SOD1, SOX10, SPAST, SPG11, SPG20, SPG21, SPG7, SPR, SPTAN1, SPTBN2, SQSTM1, STUB1, SYNE1, SYT14, TARDBP, TBCE, TCTN1, TCTN2, TCTN3, TDP1, TDP2, TECPR2, TFG, TGM6, TH, TMEM138, TMEM216, TMEM231, TMEM237, TMEM240, TMEM67, TPP1, TRAPPC11, TRPC3, TRPV4, TSEN2, TSEN34, TSEN54, TTBK2, TTC19, TTPA, TUBB2B, TUBB4A, TWNK, UBAP1, UBQLN2, UBTF, USP8, VAMP1, VAPB, VARS2, VCP, VLDLR, VPS13A,

VPS13D, VPS37A, VPS53, VRK1, WASHC5, WDR45, WDR48, WDR73, WDR81, WWOX, XPA, XPC, ZFR, ZFYVE26, ZFYVE27, ZNF423, ZNF592.

Gene set #3 (n = 985) (genes associated with neurodegenerative disease)

ACP33, ACTA1, ACTC1, ACTN2, ADSSL1, AGRN, AKAP9, ALPK3, ALSIN, ANK2, ANKRD1, ANXA11, AP4B, APAM1, APOA1BP, APP, ARHGEF10, ARL3, ASCC1, ATAD1, ATG5, ATP2B4, ATP9A, ATXN8, B4GALNT, B4GAT1, BAG3, BVES, C11orf73, CACNB2, CALM1, CALM2, CALR3, CAPN3, CASQ1, CASQ2, CAV3, CEP120, CFL2, CHAT, CHRNA1, CHRNB1, CHRND, CHRNE, CIZ1, CNTN1, COL12A1, COL13A1, COL6A2, COLQ, CPT1C, CRYAB, CSNK1D, CSRP3, CTNNA3, DCAF8, DES, DGAT2, DNAJB2, DNAJB6, DNAJC13, DOK7, DSC2, DSG2, DSP, DTNA, DUX4, DYSF, EIF2AK2, EMD, EPT1, ERBB3, ERBB4, EXOSC8, EYA4, FAM134B, FBXO38, FLNC, FLRT1, GAK, GATAD1, GJA5, GLRB, GLTP, GNB4, GOLGA2, GPD1L, GPR56, HARS, HCN4, HNRNPA2B1, HNRNPDL, HPRT, HSPB1, HSPB3, HSPB8, IKBKAP, ILK, ITM2B, JPH2, JPH3, JUP, KCNA5, KCNE2, KCNE3, KCNH2, KCNMA1, KCTD17, KIAA0415, KIAA0556, KIAA0753, KIAA1840, KIF1B, KLC2, KLHL41, KLHL9, LAMA4, LAMA5, LAMB2, LIMS2, LMOD3, LRSAM1, MAP3K20, MORC2, MSTN, MURC, MUSK, MYBPC3, MYH2, MYH7, MYL2, MYL3, MYL4, MYLK2, MYMK, MYO18B, MYO9A, MYOT, MYOZ2, MYPN, NEFH, NEXN, NPPA, NUP155, OBFC1, ORAI1, PABPN1, PARK2, PCCA/PCCB, PCNA, PDE8B, PHOX2A, PIBF1, PIP5K1C, PKP2, PLEKHG4, PLEKHG5, PLN, PMP2, PNPLA2, PNPLA6/NT, POMK, PRDM16, PRDX3, PRPH, PTPLA, PTRF, PYROXD1, RAB12, RAB3A, RBM20, RBM7, RNU12, RPH3A, RYR2, SACSIN, SAMD9L, SBF1, SCN2B, SCN3B, SCN4B, SCN5A, SELENON, SGCB, SGCD, SGCG, SLC18A3, SLC9A1, SMN1, SNTA1, SPARTIN, SPTBN4, STAC3, STIM1, SYNE2, SYT2, TBK1, TCAP, TECRL, TIA1, TMEM138, TMEM43, TMPO, TNNC1, TNNI2, TNNI3, TNNT1, TNNT2, TNNT3, TNPO3, TOR1AIP1, TPM1, TPM2, TPM3, TRDN, TRIM2, TRIM54, TRIM63, TRIP4, UBA1, UNC13B, VCL, VMA21, VWA3B, WARS, YARS, ZFHX2, ZFR, ZFYV327, ZNF423, SEPT9, AAAS, AARS, AARS2, ABCB7, ABCC9, ABCD1, ABHD12, ABHD5, ACAD9, ACADVL, ACAT1, ACBD5, ACOX1, ACTB, ACVR1, ADAR, ADCK3, ADCY5, ADGRG1, AFG3L2, AGL, AHI1, AIFM1, AIMP1, AKR1C2, ALAS2, ALDH18A1, ALDH3A2, ALG13, ALG14, ALG2, ALG6, ALS2, AMACR, AMPD2, ANG, ANO10, ANO3, ANO5, AP1S2, AP4B1, AP4E1, AP4M1, AP4S1, AP5Z1, APOE, APOPT1, APTX, AR, ARG1, ARL13B, ARL6IP1, ARMC9, ARSA, ARSI,

ARX, ASAH1, ASPA, ATCAY, ATL1, ATL3, ATM, ATN1, ATP13A2, ATP1A1, ATP1A2, ATP1A3, ATP2A1, ATP2B3, ATP7A, ATP7B, ATP8A2, ATPAF2, ATXN1, ATXN10, ATXN2, ATXN3, ATXN7, ATXN8OS, AUH, B3GALNT2, B4GALNT1, B9D1, BCAP31, BCS1L, BEAN1, BICD2, BIN1, BOLA3, BSCL2, BTD, C10orf2, C12orf65, C19orf12, C5orf42, C9orf72, CA2, CA8, CACNA1A, CACNA1B, CACNA1C, CACNA1G, CACNA1S, CACNA2D2, CACNB4, CAMTA1, CAPN1, CASK, CC2D2A, CCDC78, CCDC88C, CCT5, CDK16, CDKL5, CEP104, CEP290, CEP41, CHCHD10, CHCHD2, CHKB, CHMP1A, CHMP2B, CHRNG, CIC, CLCN1, CLCN2, CLN3, CLN5, CLN6, CLN8, CLP1, CLTCL1, CNBP, CNTNAP1, COA7, COASY, COG5, COL25A1, COL4A1, COL4A2, COL6A1, COL6A3, COQ2, COQ6, COQ8A, COQ9, COX10, COX15, COX20, COX6A1, CP, CPT2, CSF1R, CSPP1, CSTB, CTC1, CTDP1, CTSA, CTSD, CTSF, CWF19L1, CYP27A1, CYP2U1, CYP7B1, D2HGDH, DAB1, DAG1, DARS, DARS2, DCAF17, DCTN1, DCX, DDB2, DDC, DDHD1, DDHD2, DGUOK, DHTKD1, DLAT, DMD, DMPK, DMXL2, DNAJC12, DNAJC19, DNAJC3, DNAJC5, DNAJC6, DNM2, DNMT1, DOLK, DPAGT1, DPM1, DPM2, DPM3, DPYD, DST, DSTYK, DYNC1H1, EARS2, EEF2, EGR2, EIF2B1, EIF2B2, EIF2B3, EIF2B4, EIF2B5, ELOVL4, ELOVL5, ENO3, ENTPD1, EPM2A, ERCC2, ERCC3, ERCC4, ERCC5, ERCC6, ERCC8, ERLIN1, ERLIN2, ETFA, ETFB, ETFDH, EXOSC3, EXT1, FA2H, FAM111B, FAM126A, FARS2, FASTKD2, FBLN5, FBXO7, FGD4, FGF14, FHL1, FIG4, FKRP, FKTN, FLAD1, FLNA, FLVCR1, FLVCR2, FMR1, FOLR1, FOXC1, FOXG1, FRRS1L, FTL, FUCA1, FUS, FXN, GAA, GAD1, GALC, GAN, GARS, GBA, GBA2, GBE1, GCDH, GCH1, GDAP1, GFAP, GFM1, GFPT1, GJA1, GJB1, GJB3, GJC2, GLA, GLB1, GLDC, GLE1, GLRA1, GLRX5, GMPPB, GNAL, GNAO1, GNB1, GNE, GOSR2, GPAA1, GPT2, GRID2, GRM1, GRN, GYG1, GYS1, HACE1, HEPACAM, HEXA, HEXB, HINT1, HK1, HMBS, HNRNPA1, HOXD10, HPCA, HPRT1, HRAS, HSD17B4, HSPD1, HSPG2, HTRA1, HTT, HYLS1, IBA57, IDS, IFIH1, IFRD1, IGHMBP2, INF2, INPP5E, INPP5K, IRF2BPL, ISCA2, ISCU, ISPD, ITGA7, ITPR1, JAM3, KARS, KBTBD13, KCNA1, KCNA2, KCNC1, KCNC3, KCND3, KCNE1, KCNJ10, KCNJ18, KCNJ2, KCNJ5, KCNMA1, KCNQ1, KCNQ2, KCNQ3, KCNT1, KCTD7, KDM5C, KIAA0196, KIAA0226, KIAA0586, KIDINS220, KIF1A, KIF1C, KIF21A, KIF5A, KIF7, KLC4, KLHL40, KMT2B, KY, L1CAM, L2HGDH, LAMA2, LAMB1, LAMP2, LARGE, LDB3, LDHA, LITAF, LMNA, LMNB1, LPIN1, LRP4, LRRK2, LYRM7, LYST, MAG, MAN2B1, MAPT, MARS, MARS2, MATR3, MCOLN1, MECP2, MECR, MED25, MEF2C, MEGF10, MFF, MFN2, MFSD8, MIB1, MKS1, MLC1, MMACHC, MME, MPLKIP, MPV17, MPZ, MRE11, MRE11A, MRPL3, MRPL44, MRPS16, MSTO1, MT-ATP6, MT-ATP8, mt-ND6, MTFMT,

MTM1, MTMR2, MTO1, MTPAP, MTTP, MUT, MVK, MYBPC1, MYH3, MYH6, MYH8, NAGLU, NARS2, NAXE, NDE1, NDRG1, NDUFA2, NDUFAF1, NDUFAF3, NDUFS1, NDUFS2, NDUFS4, NDUFS7, NDUFS8, NDUFV1, NEB, NEFL, NEK1, NEU1, NFU1, NGF, NHLRC1, NIPA1, NKX2-1, NKX6-2, NOP56, NOTCH3, NPC1, NPC2, NPHP1, NT5C2, NTRK1, NTRK2, NUBPL, NUP62, OCLN, OCRL, OFD1, OPA1, OPA3, OPHN1, OPTN, PAFAH1B1, PANK2, PARK7, PAX2, PAX6, PC, PCDH12, PCLO, PCYT2, PDE10A, PDE6D, PDGFB, PDGFRB, PDHA1, PDHX, PDK3, PDSS1, PDSS2, PDYN, PEX1, PEX10, PEX11B, PEX12, PEX13, PEX14, PEX16, PEX19, PEX2, PEX26, PEX3, PEX5, PEX6, PEX7, PFKM, PFN1, PGAM2, PGAP1, PGK1, PGM1, PHGDH, PHKA1, PHYH, PIEZO2, PIK3R5, PINK1, PLA2G6, PLAA, PLEC, PLEKHG2, PLP1, PMM2, PMP22, PMPCA, PNKD, PNKP, PNPLA6, PNPLA8, POGLUT1, POLG, POLG2, POLR1A, POLR1C, POLR3A, POLR3B, POMGNT1, POMGNT2, POMT1, POMT2, PPP2R2B, PPT1, PRDM12, PREPL, PRF1, PRICKLE1, PRKAG2, PRKCG, PRKN, PRKRA, PRNP, PRPS1, PRRT2, PRUNE1, PRX, PSAP, PSAT1, PSEN1, PSEN2, PTRH2, PTS, PUS1, PYCR2, PYGM, QDPR, RAB11B, RAB39B, RAB3GAP2, RAB7A, RAF1, RAPSN, RARS, RARS2, RBCK1, REEP1, REEP2, RELN, RETREG1, RNASEH1, RNASEH2A, RNASEH2B, RNASEH2C, RNASET2, RNF168, RNF170, RNF216, RPGRIP1L, RRM2B, RTN2, RUBCN, RYR1, RYR3, SACS, SAMHD1, SAR1B, SBF2, SCN11A, SCN1A, SCN1B, SCN4A, SCN8A, SCN9A, SCO1, SCO2, SCP2, SCYL1, SDHA, SDHAF1, SDHB, SDHD, SEPSECS, SERAC1, SETX, SGCA, SGCE, SGPL1, SH3TC2, SIGMAR1, SIL1, SLC12A6, SLC13A5, SLC16A1, SLC16A2, SLC17A5, SLC19A3, SLC1A3, SLC1A4, SLC20A2, SLC22A5, SLC25A1, SLC25A12, SLC25A15, SLC25A20, SLC25A4, SLC25A42, SLC25A46, SLC2A1, SLC30A10, SLC33A1, SLC39A14, SLC52A2, SLC52A3, SLC5A7, SLC6A3, SLC6A4, SLC6A5, SLC9A6, SMCHD1, SMPD1, SNAP25, SNCA, SNORD118, SNX14, SOD1, SON, SOX10, SPART, SPAST, SPEG, SPG11, SPG20, SPG21, SPG7, SPR, SPTAN1, SPTBN2, SPTLC1, SPTLC2, SQSTM1, SRD5A3, STUB1, SUCLA2, SUMF1, SURF1, SYNE1, SYNJ1, SYT14, TACO1, TAF1, TARDBP, TAZ, TBC1D24, TBCE, TBP, TCTN1, TCTN2, TCTN3, TDP1, TDP2, TECPR2, TFG, TGFB3, TGM6, TH, THAP1, TIMM8A, TK2, TMEM106B, TMEM216, TMEM231, TMEM237, TMEM240, TMEM5, TMEM65, TMEM67, TOR1A, TPP1, TRAPPC11, TREM2, TREX1, TRIM32, TRPC3, TRPV4, TSEN2, TSEN34, TSEN54, TSFM, TTBK2, TTC19, TTN, TTPA, TTR, TUBA1A, TUBA4A, TUBA8, TUBB2B, TUBB3, TUBB4A, TUFM, TWNK, TYMP, TYROBP, UBAP1, UBQLN2, UBR4, UBTF, UCHL1, UNC13D, USP8, VAC14, VAMP1, VAMP2, VAPB, VARS2, VCP, VLDLR, VPS11, VPS13A, VPS13C, VPS13D, VPS35, VPS37A, VPS53, VRK1, WASHC5, WDR45,

WDR45B, WDR48, WDR73, WDR81, WFS1, WNK1, WWOX, XK, XPA, XPC, XPR1, XRCC1, YARS2, ZEB2, ZFYVE26, ZFYVE27, ZNF592

Availability of NfL and MRI data

NfL data were available from 147 patients. Baseline NfL data were available from 97 patients, in 41 of them with follow up. In 50 patients, first NfL measurement was done at a later visit than baseline, in 27 of them with follow up.

MRI scans were available from 79 patients. MRI was done at baseline in 69 patients, in 43 of them with follow-up. In 10 patients, first MRI was done at a later visit than baseline, in 5 of them with follow-up.

Fourty-three patients had both NfL and MRI (10 MSA-C, 33 SAOA).

MRI parameters

T1 weighted were acquired using a magnetization-prepared rapid gradient echo sequence (MPRAGE). TR = 2500 ms, TE = 4.37 ms, TI = 1100 ms, flip angle = 7 deg, FOV 256 mm x 256 mm, 192 slices with a voxel size of 1 mm isotropic.

T2 weigthed images were acquired (a) with TR = 6500 ms, TE = 80 ms, flip angle 180 deg, FOV 240 mm x 320 mm, 72 slices with a voxel size of 0.8 x 0.8 x 2 mm, and (b) using fluid attenuated inversion recovery with TR = 50000 ms, TE = 397 ms, TI 1800 ms, flip angle = 120 deg, FOV 256 mm x 256 mm, 192 slices with a voxel size of 1 mm isotropic.

Rating of signal and structural abnormalities of the pons and middle cerebellar peduncle (MCP)

Signal and structural abnormalities of the pons and MCP that could not be detected by volumetry were assessed by a trained neuroradiologist (AL) blinded to clinical information on T1w and T2w images.[5-8]

Hyperintensities of the pons known as hot cross bun sign were rated, as follows: 0 = absence of T2 hyperintensities; 1 = flat linear T2 hyperintensities in one plan (either transverse pontocerebellar pathways or formatio reticularis); 2 = flat T2 hyperintensities in two planes (anterior-posterio or left-right); 3 = marked and emphasized T2 hyperintensities in two planes.

Hyperintensities of the MCP were rated , as follows: 0 = absence of MCP hyperintensities; 1 = visually flat, suggestive T2 hyperintensities in typical localization detected on both sides, regardless of slight differences between right and left side; 2 = strong, extensive bilateral T2 hyperintensities, regardless of slight differences between right and left side.

The diameter of the MCP was measured in a parasagittal plane on both sides in a 3D T1 sequence. Mean values of both sides were calculated. Mean values above or equal to a cut-off of 8mm were counted as 0, values below 8 mm as 1.

All three assessments were added together yielding the Pons and MCP Abnormality Score (PMAS) ranging from 0 (normal) to 6 (most severely affected).

Figure 1

Evolution of clinical outcome measures in MSA-C and SAOA.

Spaghetti plots showing individual trajectories of (A) SARA, (B) UMSARS-I, (C) UMSARS-II, (D) INAS, (E) PHQ-9, and (F) EQ-5D on a time scale starting with ataxia onset.

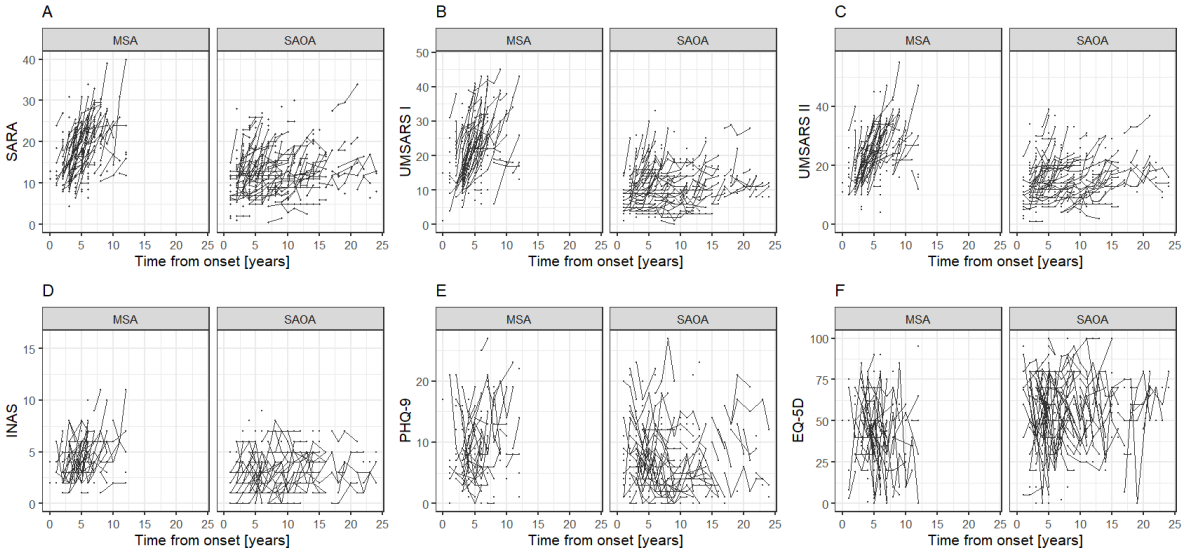

Figure 2

Temporal evolution of single SARA items in MSA-C and SAOA.

Regression lines with 95% CIs of the scores of each SARA item on a time scale starting with ataxia onset.

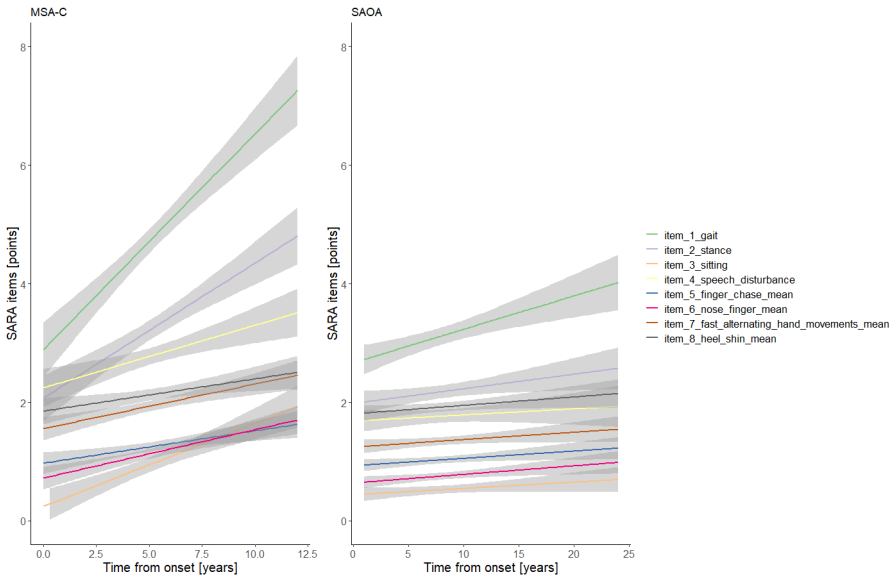

Figure 3

Evolution of clinical outcome measures in MSA-C BL and MSA-C CO.

Estimated trajectories with 95% CIs of (A) SARA, (B) UMSARS-I, (C) UMSARS-II, (D) INAS, (E) PHQ-9, and (F) EQ-5D on a time scale starting with ataxia onset, with curves drawn using mixed-effects modelling. Trajectories with 95% CIs of MSA-C BL are given in dark red, trajectories of MSA-C CO in light red.

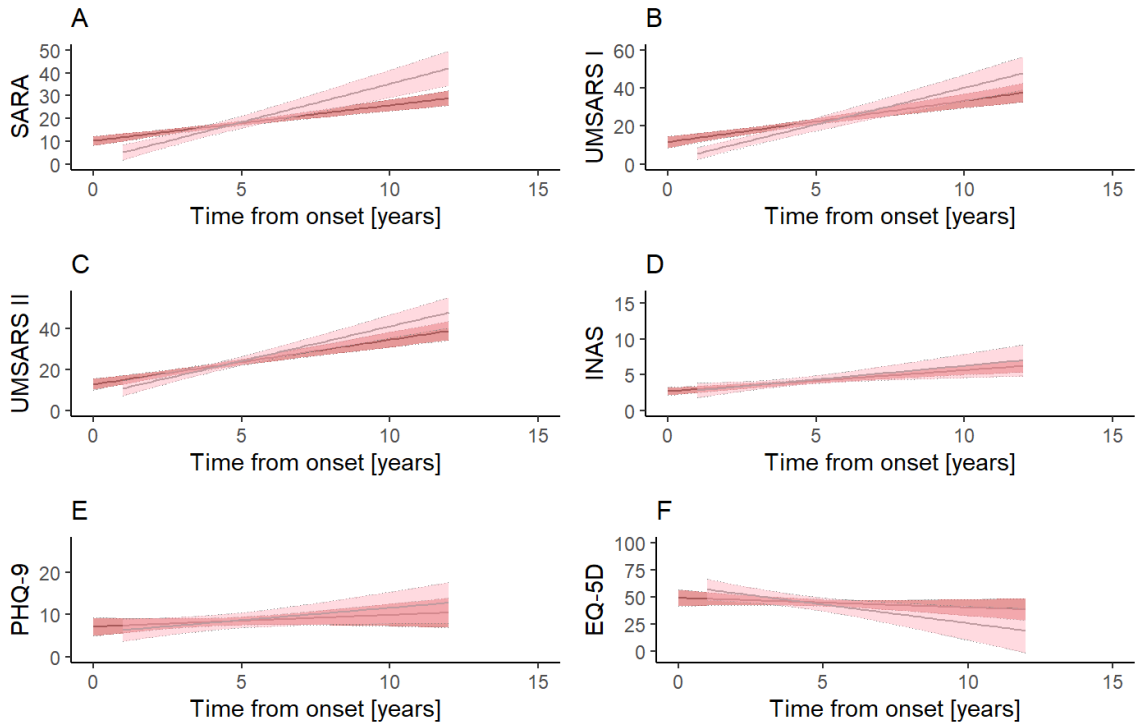

Figure 4

Evolution of biomarkers in MSA-C and SAOA.

Spaghetti plots showing individual trajectories of (A) NfL, (B) CWM volume, (C) pons volume, and (D) PM AS on a time scale starting with ataxia onset.

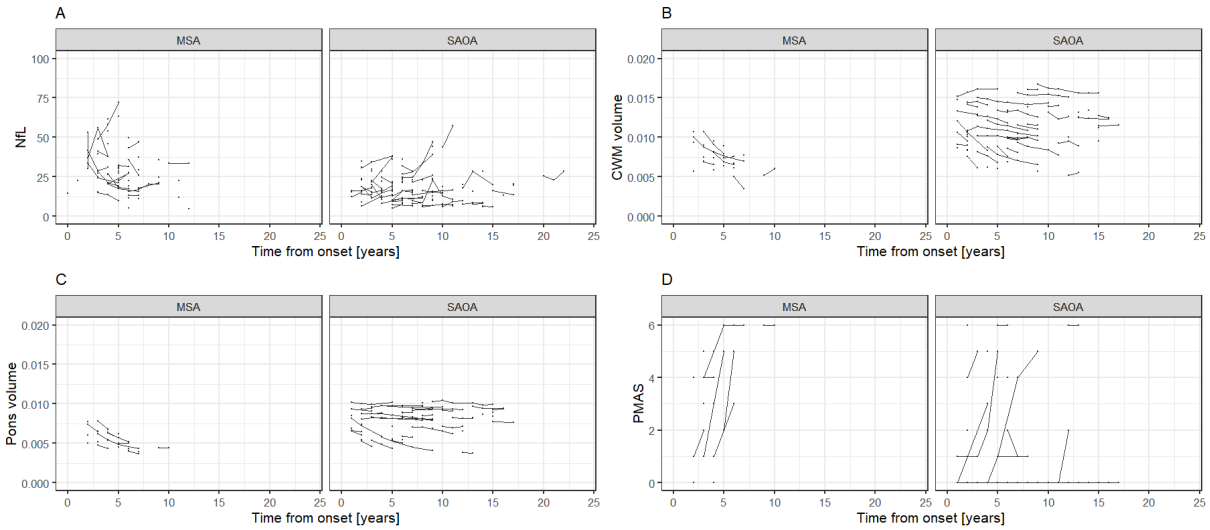

Figure 5

Evolution of biomarkers in MSA-C BL and MSA-C CO.

Estimated trajectories with 95% CIs of (A) NfL, (B) CWM volume, (C) pons volume, and (D) PMAS on a time scale starting with ataxia onset, with curves drawn using mixed-effects modelling. Trajectories with 95% CIs of MSA-C BL are given in dark red, trajectories of MSA-C CO in light red.

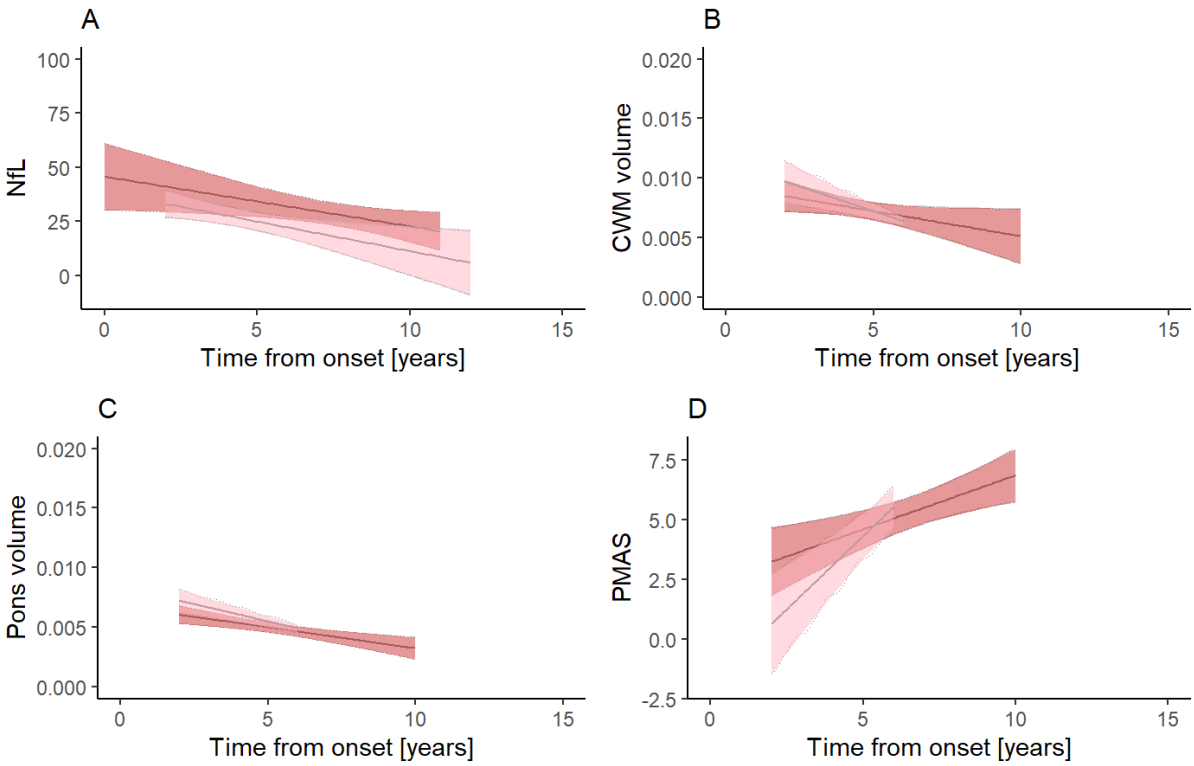

Table 1 Number of visits

Visit	Total	MSA-C	SAOA	MSA-C BL	MSA-C CO
Baseline	404	156	248	130	26
1st follow-up	198	73	125	47	26
2nd follow-up	105	37	68	19	18
3rd follow-up	62	18	44	9	9
4th follow-up	35	9	26	4	5
5th follow-up	17	2	15	1	1
6th follow-up	9	1	8	0	1
7th follow-up	4	1	3	0	1
8th follow-up	3	1	2	0	1
Total	837	298	539	210	88

Table 2 Parameters of mixed-effects modelling of the evolution of clinical outcome measures in MSA-C and SAOA

Predictors	Coefficient estimates	95% CIs	SE	P value	Marginal R^2	Conditional R^2	SCS	95% CIs
SARA								
MSA-C					0.35	0.86		
Intercept	8.67	[6.60,10.71]	0.91	<.001				
Time from onset [years]	1.87	[1.45,2.28]	0.18	<.001			0.619	[0.618,0.621]
SAOA					0.19	0.93		
Intercept	8.83	[7.78,9.93]	0.50	<.001				
Time from onset [years]	0.60	[0.44,0.76]	0.07	<.001			0.386	[0.385,0.387]
INAS								
MSA-C					0.15	0.56		
Intercept	2.65	[2.13,3.16]	0.25	<.001				
Time from onset [years]	0.31	[0.20,0.41]	0.05	<.001			0.356	[0.354,0.357]
SAOA					0.03	0.74		
Intercept	2.57	[2.22,2.94]	0.18	<.001				
Time from onset [years]	0.06	[0.02,0.10]	0.02	0.003			0.138	[0.137,0.139]
UMSARS-I								
MSA-C					0.33	0.90		
Intercept	9.18	[6.38,12.02]	1.29	<.001				
Time from onset [years]	2.60	[2.02,3.17]	0.26	<.001			0.610	[0.608,0.611]
SAOA					0.10	0.90		
Intercept	8.46	[7.21,9.78]	0.59	<.001				
Time from onset [years]	0.44	[0.25,0.63]	0.08	<.001			0.257	[0.256,0.258]
UMSARS-II								
MSA-C					0.35	0.89		
Intercept	11.13	[8.52,13.75]	1.19	<.001				
Time from onset [years]	2.56	[2.00,3.10]	0.25	<.001			0.620	[0.618,0.621]
SAOA					0.14	0.95		
Intercept	11.47	[10.02,12.97]	0.70	<.001				
Time from onset [years]	0.64	[0.44,0.84]	0.09	<.001			0.322	[0.321,0.323]
EQ-5D VAS								
MSA-C					0.03	0.22		
Intercept	51.32	[44.79,57.99]	3.31	<.001				
Time from onset [years]	-1.37	[-2.60,-0.17]	0.61	0.028			-0.146	[-0.148,-0.145]
SAOA					0.01	NA		
Intercept	55.59	[51.21,59.93]	0.22	<.001				
Time from onset [years]	0.17	[-0.22,0.55]	0.19	0.392			0.039	[0.038,0.040]
PHQ-9								
MSA-C					0.02	0.71		
Intercept	6.79	[4.97,8.58]	0.92	<.001				
Time from onset [years]	0.34	[-0.03,0.71]	0.19	0.077			0.119	[0.118,0.121]
SAOA					0.01	0.77		
Intercept	7.73	[6.66,8.79]	0.54	<.001				

Time from onset [years]	-0.08	[-0.19,0.04]	0.05	0.187			-0.064	[-0.064,-0.063]

Linear mixed models were applied with random effects on the linear time term and the intercept term for MSA-C and SAOA.

SCS = sensitivity to change ratio; MSA-C = MSA with predominant cerebellar ataxia; MSA-C BL = patients with MSA-C at baseline; MSA-C CO = patients with conversion to MSA- C during follow-up; SAOA = sporadic adult-onset ataxia of unknown aetiology; UMSARS = Unified MSA Rating Scale; INAS = Inventory of Non-Ataxia Signs; PHQ-9 = Patient's Health Questionnaire; EQ-5D VAS = EQ-5D visual analog scale

Table 3 Parameters of mixed-effects modelling of the evolution of clinical outcome measures in MSA-C BL and MSA-C CO

Predictors	Coefficient estimates	95% CIs	SE	P value	Marginal R^2	Conditional R^2	N
SARA							
MSA-C BL					0.28	0.81	207
Intercept	10.24	[8.03,12.38]	1.01	<.001			
Time from onset [years]	1.56	[1.53,2.49]	0.20	<.001			
MSA-C CO					0.51	0.97	73
Intercept	1.79	[-2.42,6.18]	1.95	0.37			
Time from onset [years]	3.34	[2.39,4.28]	0.43	<.001			
INAS							
MSA-C BL					0.15	0.51	208
Intercept	2.68	[2.10,3.25]	0.28	<.001			
Time from onset [years]	0.30	[0.19,0.41]	0.05	<.001			
MSA-C CO					0.19	0.73	74
Intercept	2.42	[1.10,3.70]	0.63	0.002			
Time from onset [years]	0.38	[0.12,0.67]	0.14	0.012			
UMSARS-I							
MSA-C BL					0.25	0.88	203
Intercept	11.64	[8.49,14.79]	1.50	<.001			
Time from onset [years]	2.17	[1.52,2.80]	0.31	<.001			
MSA-C CO					0.51	0.95	71
Intercept	1.74	[-2.41,6.29]	1.82	0.355			
Time from onset [years]	3.84	[2.82,4.82]	0.44	<.001			
UMSARS II							
MSA-C BL					0.27	0.88	205
Intercept	12.87	[9.96,15.75]	1.35	<.001			
Time from onset [years]	2.19	[1.57,2.79]	0.29	<.001			
MSA-C CO					0.32	0.77	74
Intercept	7.50	[2.04,13.56]	2.26	<.001			
Time from onset [years]	3.38	[2.09,4.51]	0.47	<.001			
VAS EQ-5D							
MSA-C BL					0.01	NA	182
Intercept	49.18	[41.73,56,73]	3.79	<.001			
Time from onset [years]	-0.88	[-2.28,0.48]	0.69	0.210			
MSA-C CO					0.24	NA	63
Intercept	60.41	NA	5.92	<.001			
Time from onset [years]	-3.45	NA	1.24	0.008			
PHQ-9							
MSA-C BL					0.01	0.74	171
Intercept	7.13	[4.99,9.25]	1.08	<.001			
Time from onset [years]	0.28	[-0.16,0.72]	0.22	0.220			
MSA-C CO					0.07	0.63	60
Intercept	5.72	[2.36,8.76]	1.54	<.001			

Time from onset [years]	0.59	[-0.04,1.18]	0.29	0.053			

Linear mixed models were applied with random effects on the linear time term and the intercept term for MSA-C BL and MSA-C CO.

MSA-C BL = patients with MSA-C at baseline; MSA-C CO = patients with conversion to MSA- C during follow-up; UMSARS = Unified MSA Rating Scale; INAS = Inventory of Non-Ataxia Signs; PHQ-9 = Patient's Health Questionnaire; EQ-5D VAS = EQ-5D visual analog scale

Table 4 Parameters of mixed-effects modelling of the evolution of biomarkers in MSA-C and SAOA

Predictors	Coefficient estimates	95% CIs	SE	P value	Marginal R^2	Conditional R^2	SCS	95% CIs
NfL								
MSA					0.05	0.86		
Intercept	40.15	[28.98,51.04]	5.57	<.001				
Time from onset [years]	-1.82	[-3.30,-0.35]	0.74	0.022			-0.279	[-0.281,-0.276]
SAOA		[-3.30,-0,35]			0.01	0.90		
Intercept	16.86	[13.28,20.41]	1.73	<.001				
Time from onset [years]	0.23	[-0.34,0.80]	0.27	0.398			0.070	[0.068,0.072]
CWM volume								
MSA					0.36	0.96		
Intercept	0.01	[0.008,0.012]	0.0008	<.001				
Time from onset [years]	-0.0006	[-0.0009,-0.0003]	0.0002	0.003			-0.689	[-0.694,-0.683]
SAOA					0.91	0.99		
Intercept	1.240e-02	[0.011,0.013]	3.990e-04	<.001				
Time from onset [years]	-2.788e-04	[-0.0004,-0.0002]	5.253e-05	<.001			-0.479	[-0.481,-0.476]
Pons volume								
MSA					0.47	0.98		
Intercept	0.007	[0.006,0.008]	0.0005	<.001				
Time from onset [years]	-0.0004	[-0.0006,-0.0003]	0.00007	<.001			-1.137	[-1.144,-1.130]
SAOA					0.06	0.99		
Intercept	0.008	[0.008,0.009]	0.0002	<.001				
Time from onset [years]	-0.00001	[-0.0002,-0.00008]	0.00003	<.001			-0.390	[-0.393,-0.389]
PMAS								
MSA					0.88	NA		
Intercept	0.82	[-1.07,2.70]	0.96	0.407				
Time from onset [years]	0.75	[0.46,1.04]	0.15	<.001			0.901	[0.896,0.907]
SAOA					0.04	0.99		
Intercept	0.29	[-0.44,1.07]	0.37	0.436				
Time from onset [years]	0.14	[0.002,0.271]	0.07	0.040			0.190	[0.188,0.192]

Linear mixed models were applied with random effects on the linear time term and the intercept term for MSA-C and SAOA.

SCS = sensitivity to change ratio; MSA-C = MSA with predominant cerebellar ataxia; SAOA = sporadic adult-onset ataxia of unknown aetiology; NfL = neurofilament light chain; PMAS = Pons and Middle cerebellar peduncle Abnormality Score

Table 5 Parameters of mixed-effects modelling of the evolution of biomarkers in MSA-C BL and MSA-C CO

Predictors	Coefficient estimates	95% CIs	SE	P value	Marginal R^2	Conditional R^2	N
NfL							
MSA-C BL					0.30	NA	49
Intercept	45.74	[30.56,60.83]	7.67	<.001			
Time from onset [years]	-2.30	[-4.25,-0,36]	0.98	0.026			
MSA-C CO					0.31	0.76	34
Intercept	38.65	[27.54,48.45]	4.66	<.001			
Time from onset [years]	-2.73	[-4.88,-0,78]	0.93	0.015			
CWM volume							
MSA-C BL					0.24	0.95	23
Intercept	0.009	NA	0.001	<.001			
Time from onset [years]	-0.0004	NA	0.0002	0.072			
MSA-C CO							12
Intercept	0.01	[0.009,0.014]	0.001	<.001	0.96	NA	
Time from onset [years]	-0.0008	[-0.001,-0.0005]	0.0002	0.007			
Pons volume							
MSA-C BL					0.43	0.97	23
Intercept	0.007	[0.006,0.008]	0.0005	<.001			
Time from onset [years]	-0.0004	[-0.0006,-0.0002]	0.00009	0.007			
MSA-C CO					0.51	0.98	12
Intercept	0.008	[0.007,0.01]	0.0006	<.001			
Time from onset [years]	-0.0006	[-0.0008,-0.0004]	0.00009	<.001			
PMAS							
MSA-C BL					0.25	0.96	23
Intercept	2.34	[0.177,4.374]	0.92	0.045			
Time from onset [years]	0.45	[0.182,0.819]	0.13	0.024			
MSA-C CO					0.90	NA	12
Intercept	-1.80	[-4.46,0.98]	1.35	0.240			
Time from onset [years]	1.23	[0.77,1.70]	0.23	0.001			

Linear mixed models were applied with random effects on the linear time term and the intercept term for MSA-C BL and MSA-C CO.

MSA-C BL = patients with MSA-C at baseline; MSA-C CO = patients with conversion to MSA- C during follow-up; NfL = neurofilament light chain; PMAS = Pons and Middle cerebellar peduncle Abnormality Score

Table 6 Predictors of SARA progression

Factors	Coefficient estimates	95% CI	SE	P value	Marginal R^2	Conditional R^2	N
MSA-C univariable							
Intercept	7.98	[5.47,10.49]	1.19	<.001	0.35	0.86	280
Time from onset	2.01	[1.55,2.63]	0.26	<.001			
Female sex	1.32	[-2.40,5.04]	1.90	0.490			
Female sex*Time from onset	-0.02	[-0.57,1.62]	0.18	0.258			
Intercept	8.79	[-3.64,21.34]	6.38	0.173	0.35	0.86	280
Time from onset	0.61	[-1.85,3.14]	1.27	0.631			
Age at onset	-0.01	[-0.23,0.21]	0.11	0.954			
Age at onset*Time from onset	0.02	[-0.02,0.07]	0.02	0.307			
Intercept	12.72	[7.86,17.74]	2.57	<.001	0.25	0.63	83
Time from onset	0.43	[-0.62,1.49]	0.57	0.447			
Intercept	-4.31	[-7.79,-0.78]	1.72	0.013	0.75	NA	280
Time from onset	2.26	[1.43,3.07]	0.41	<.001			
SARA	1.16	[0.93,1.38]	0.11	<.001			
SARA*Time from onset	-0.08	[-0.13,-0.04]	0.02	**<.001**			
Intercept	8.10	[4.87,11.37]	1.62	<.001	0.37	0.75	280
Time from onset	1.07	[0.46,1.68]	0.30	<.001			
INAS	0.74	[0.003,1.49]	0.38	0.051			
INAS*Time from onset	0.05	[-0.06,0.17]	0.06	0.372			
Intercept	0.97	[6.18,11.81]	1.34	<.001	0.35	0.86	280
Time from onset	1.75	[1.16,2.32]	0.28	<.001			
Pyramidal	-0.55	[-4.23,3.09]	1.85	0.766			
Pyramidal*Time from onset	0.21	[-0.52,0.95]	0.37	0.575			
Intercept	8.95	[6.60,11.33]	1.09	<.001	0.35	0.86	280
Time from onset	1.76	[1.28,2.22]	0.22	<.001			
Extrapyramidal	-1.03	[-4.93,2.88]	1.99	0.607			
Extrapyramidal*Time from onset	0.38	[-0.41,1.16]	0.40	0.348			
NfL	-0.05	[-0.20,0.11]	0.08	0.536			
NfL*Time from onset	0.03	[-0.01,0.07]	0.02	0.132			
Intercept	12.39	[-5.53,33.11]	9.22	0.190	0.63	NA	35
Time from onset	2.90	[-1.25,7.14]	2.11	0.183			
CWM-	-287.28	[-2542.23,1902.57]	1119.37	0.799			
CWM*Time from onset	-174.91	[-744.81,389.14]	287.42	0.548			
Intercept	16.26	[-4.93,37.41]	10.56	0.135	0.61	NA	35
Time from onset	2.59	[-2.19,7.55]	2.49	0.306			
Pons	-851.32	[-4532.94,2861.80]	1826.10	0.645			
Pons*Time from onset	-250.50	[-1230.08,714.62]	495.87	0.617			
Intercept	12.94	[4.47,21.24]	4.10	0.005	0.79	NA	35
Time from onset	-0.94	[-3.32,1.47]	1.25	0.461			
PMAS	0.03	[-1.85,1.86]	0.92	0.977			
PMAS*Time from onset	0.44	[-0.01,0.90]]	0.24	**0.046**			

SAOA univariable							
Intercept	9.10	[7.87,10.35]	0.62	<.001	0.20	0.93	513
Time from onset	0.47	[0.29,0.65]	0.09	<.001			
Female sex	-0.95	[-3.00,1.19]	1.02	0.356			
Female sex*Time from onset	0.33	[0.04,0.62]	0.14	**0.022**			
Intercept	8.36	[2.07,14.57]	3.17	<.001	0.18	0.93	513
Time from onset	-0.32	[-1.19,0.11]	0.43	0.461			
Age at onset	0.01	[-0.10,0.11]	0.05	0.931			
Age at onset*Time from onset	0.02	[0.00,0.03]	0.01	**0.031**			
Intercept	8.29	[4.78,11.92]	1.79	<.001	0.19	0.91	152
Time from onset	0.49	[0.05,0.94]	0.21	0.024			
Intercept	0.13	[-1.00,1.32]	0.57	0.813	0.84	NA	513
Time from onset	0.20	[0.04,0.36]	0.08	0.011			
SARA	0.99	[0.89,1.08]	0.05	<.001			
SARA*Time from onset	-0.01	[-0.02,0.01]	0.01	0.396			
Intercept	7.14	[5.76,8.56]	0.71	<.001	0.19	0.92	513
Time from onset	0.58	[0.40,0.77]	0.09	<.001			
INAS	0.76	[0.37,1.15]	0.19	<.001			
INAS*Time from onset	-0.03	[-0.07,0.01]	0.02	0.180			
Intercept	8.66	[7.44,9.93]	0.60	<.001	0.19	0.93	513
Time from onset	0.60	[0.41,0.78]	0.08	<.001			
Pyramidal	0.56	[-1.58,2.71]	1.09	0.607			
Pyramidal*Time from onset	-0.01	[-0.30,0.29]	0.15	0.968			
Intercept	8.55	[7.46,9.70]	0.54	<.001	0.19	0.93	513
Time from onset	0.56	[0.41,0.72]	0.07	<.001			
Extrapyramidal	1.14	[-1.57,3.93]	1.39	0.411			
Extrapyramidal*Time from onset	0.30	[-0.13,0.73]	0.22	0.165			
NfL	0.03	[-0.15,0.20]	0.09	0.752			
NfL*Time from onset	0.005	[-0.02,0.03]	0.01	0.638			
Intercept	15.81	[9.76,21.76]	3.06	<.001	0.21	0.87	129
Time from onset	0.35	[-0.52,1.20]	0.44	0.436			
CWM	-597.78	[-1112.85,-68.83]	263.28	0.028			
CWM*Time from onset	2.75	[-69.71,77.88]	37.52	0.941			
Intercept	15.52	[8.00,22.97]	3.85	<.001	0.18	0.88	129
Time from onset	0.39	[-0.67,1.47]	0.55	0.478			
Pons	-832.95	[-1760.19,116.16]	479.61	0.038			
Pons*Time from onset	2.09	[-127.13,132.35]	66.85	0.975			
Intercept	8.75	[7.08,10.51]	0.84	<.001	0.14	0.87	131
Time from onset	0.40	[0.18,0.63]	0.11	<.001			
PMAS	0.37	[-0.54,1.28]	0.47	0.429			
PMAS*Time from onset	0.00	[-0.14,0.14]	0.07	0.986			

P values of significant interactions between a factor and time from onset are marked in bold.

MSA-C = MSA with predominant cerebellar ataxia; SAOA = sporadic adult-onset ataxia of unknown aetiology; NfL = neurofilament light chain; PMAS = Pons and Middle cerebellar peduncle Abnormality Score

Supplementary references

1. Cortese A, Simone R, Sullivan R, et al. Biallelic expansion of an intronic repeat in RFC1 is a common cause of late-onset ataxia. Nature Genet. 2019; 51: 649–58. https://doi.org/10.1038/s41588-019-0372-4.
2. Rafehi H, Szmulewicz DJ, Bennett MF, et al. Bioinformatics-Based Identification of Expanded Repeats: A Non-reference Intronic Pentamer Expansion in RFC1 Causes CANVAS. Am. J. Hum. Genet. 2019; 105: 151–65. https://doi.org/10.1016/j.ajhg.2019.05.016.
3. Richards S, Aziz N, Bale S, et al. Standards and guidelines for the interpretation of sequence variants: a joint consensus recommendation of the American College of Medical Genetics and Genomics and the Association for Molecular Pathology. Genet. Med. 2015; 17: 405–24.
4. Harrison SM, Biesecker LG, Rehm HL. Overview of Specifications to the ACMG/AMP Variant Interpretation Guidelines. Curr Protoc Hum Genet 2019; 103: e93. https://doi.org/10.1002/cphg.93.
5. Abe K, Hikita T, Yokoe M, Mihara M, Sakoda S. The "cross" signs in patients with multiple system atrophy: a quantitative study. J Neuroimaging 2006; 16: 73–77. https://doi.org/10.1177/1051228405279988.
6. Burk K, Buhring U, Schulz JB, Zuhlke C, Hellenbroich Y, Dichgans J. Clinical and magnetic resonance imaging characteristics of sporadic cerebellar ataxia. Arch. Neurol. 2005; 62: 981–85.
7. Nair SR, Tan LK, Mohd Ramli N, Lim SY, Rahmat K, Mohd Nor H. A decision tree for differentiating multiple system atrophy from Parkinson's disease using 3-T MR imaging. Eur Radiol 2013; 23: 1459–66. https://doi.org/10.1007/s00330-012-2759-9.
8. Nicoletti G, Fera F, Condino F, et al. MR imaging of middle cerebellar peduncle width: differentiation of multiple system atrophy from Parkinson disease. Radiology 2006; 239: 825–30. https://doi.org/10.1148/radiol.2393050459

3.3. **Faber J**, Schaprian T, Berkan K, Reetz K, França MC Jr, de Rezende TJR, Hong J, Liao W, van de Warrenburg B, van Gaalen J, Durr A, Mochel F, Giunti P, Garcia-Moreno H, Schoels L, Hengel H, Synofzik M, Bender B, Oz G, Joers J, de Vries JJ, Kang JS, Timmann-Braun D, Jacobi H, Infante J, Joules R, Romanzetti S, Diedrichsen J, Schmid M, Wolz R, Klockgether T. Regional Brain and Spinal Cord Volume Loss in Spinocerebellar Ataxia Type 3. *Mov Disord.* 2021; 36(10):2273-2281

Zielsetzung der Arbeit – Zielsetzung der Arbeit war es, in einer großen retrospektiven Sammlung von T1-gewichteten Magnetresonanztomographischen Aufnahmen die Volumina von Großhirn, Hirnstamm und Kleinhirn sowie die Querschnittsfläche des oberen Zervikalmarks bei SCA3-Mutationsträgern, insbesondere unter Einschluss des prä-ataktischen Krankheitsstadiums, zu quantifizieren.

Methoden und Ergebnisse – Es lagen mehr als 300 T1-gewichtete MRT-Aufnahmen vor. Nach Ausschluss nicht geeigneter MRT mit beispielsweise Bewegungsartefakten oder zu geringer Auflösung, wurden 210 MRTs von ataktischen und 48 MRTs von prä-ataktischen SCA3-Mutationsträgern sowie 63 MRTs vongesunden Kontrollen in die Auswertung eingeschlossen. Mittels eines Multi-Atlas Ansatzes erfolgte die Segmentierung von Strukturen des Großhirns, Kleinhirns und Hirnstamms; mittels spincal-cord-toolbox erfolgte die Bestimmung der Querschnittsflächen des oberen Zervikalmarks in zwei Höhen.

Die Metriken der zervikalen Rückenmarkssegmente C3 und C2, der Medulla oblongata, der Pons und des Pallidum sowie des vorderen Kleinhirnlappens waren bereits bei prä-ataktischen Mutationsträger*innen im Vergleich zu gesunden Kontrollen reduziert. Die Werte der zervikalen Rückenmarkssegmente C2 und C3, der Medulla oblongata, des Pons, des Mittelhirns, der Kleinhirnlappen Crus II und X, der weißen Substanz des Kleinhirns und des Pallidums waren bei ataktischen im Vergleich zu nicht-ataktischen SCA3 Mutationsträger*innen reduziert. Von allen untersuchten Parametern nahm das Ponsvolumen im Krankheitsverlauf am stärksten ab. Exemplarisch berechneten wir basierend auf der Annahme eines linearen Zeitverlauf zudem Effektstärken. Letztlich zeigte sich hier eine geringe Überlegenheit des Pons-Volumens gegenüber SARA. Aufgrund des querschnittlichen Studiendesigns haben die Effektstärken nur eine eingeschränkte Aussagekraft und sollten mit Vorsicht interpretiert werden. Ein multivariates Modell mit Alter, Geschlecht, Ataxieschwere

sowie CAG-Wiederholungssequenz des verlängerten Allels erklärte 46,33 % der Varianz des Ponsvolumens.

Schlussfolgerungen – Die Neurodegeneration ist messbar durch Volumenverlust und beginnt bei SCA3 vor dem Auftreten der Symptome. Das Volumen der Pons zeigt eine kontinuierliche Abnahme im Krankheitsverlauf vor- und nach Symptombeginn und ist damit ein Kandidat für die Verwendung als bildgebender Progressionsmarker bei SCA3.

RESEARCH ARTICLE

Regional Brain and Spinal Cord Volume Loss in Spinocerebellar Ataxia Type 3

Jennifer Faber, MD,[1,2*] Tamara Schaprian, PhD,[1] Koyak Berkan, MD,[1] Kathrin Reetz, MD,[3,4] Marcondes Cavalcante França, Jr, MD, PhD,[5,6] Thiago Junqueira Ribeiro de Rezende, Msc,[5,6] Jiang Hong, MD,[7] Weihua Liao, MD,[8] Bart van de Warrenburg, MD, PhD,[9] Judith van Gaalen, MD,[9] Alexandra Durr, MD, PhD,[10] Fanny Mochel, MD,[10] Paola Giunti, MD,[11,12] Hector Garcia-Moreno, MD,[11,12] Ludger Schoels, MD,[13,14] Holger Hengel, MD,[13,14] Matthis Synofzik, MD,[13,14] Benjamin Bender, MD,[15] Gulin Oz, PhD,[16] James Joers, PhD,[16] Jereon J. de Vries, MD,[17] Jun-Suk Kang, MD,[18] Dagmar Timmann-Braun, MD,[19] Heike Jacobi, MD,[20] Jon Infante, MD, PhD,[21] Richard Joules, PhD,[22] Sandro Romanzetti, PhD,[4] Jorn Diedrichsen, PhD,[23] Matthias Schmid, PhD,[1,24] Robin Wolz, PhD,[22] and Thomas Klockgether, MD[1,2]

[1]*DZNE, German Center for Neurodegenerative Diseases, Bonn, Germany*
[2]*Department of Neurology, University Hospital Bonn, Bonn, Germany*
[3]*Department of Neurology, RWTH Aachen University, Bonn, Germany*
[4]*JARA-Brain Institute Molecular Neuroscience and Neuroimaging, Forschungszentrum Jülich, Jülich, Germany*
[5]*Brazilian Institute of Neuroscience and Neurotechnology (BRAINN), Campinas, Brazil*
[6]*Department of Neurology, University of Campinas, Campinas, Brazil*
[7]*Department of Neurology, Xiangya Hospital, Central South University, Changsha, China*
[8]*Department of Radiology, Xiangya Hospital, Central South University, Changsha, People's Republic of China*
[9]*Department of Neurology, Radboud University Medical Centre, Donders Institute for Brain, Cognition and Behaviour, Nijmegen, The Netherlands*
[10]*Sorbonne Université, Paris Brain Institute, AP-HP, INSERM, CNRS, Pitié-Salpêtrière University Hospital, Paris, France*
[11]*Ataxia Centre, Department of Clinical and Movement Neurosciences, UCL Queen Square Institute of Neurology, London, United Kingdom*
[12]*National Hospital for Neurology and Neurosurgery, University College London Hospitals NHS Foundation Trust, London, United Kingdom*
[13]*Department of Neurodegenerative Diseases and Hertie-Institute for Clinical Brain Research, University of Tübingen, Tübingen, Germany*
[14]*German Centre for Neurodegenerative Diseases (DZNE), Tübingen, Germany*
[15]*Department of Diagnostic and Interventional Neuroradiology, University Hospital Tübingen, Tübingen, Germany*
[16]*Center for Magnetic Resonance Research, Department of Radiology, University of Minnesota, Minneapolis, Minnesota, USA*
[17]*Department of Neurology, University of Groningen, University Medical Center Groningen, Groningen, The Netherlands*

*__Correspondence to:__ Dr. Jennifer Faber, Klinik und Poliklinik für Neurologie, Universitätsklinikum Bonn, Venusberg-Campus 1, 53127 Bonn, Germany; E-mail: jennifer.faber@dzne.de

Relevant conflicts of interest/financial disclosures: M.C.F. was supported by grants from Brazilian governmental agencies (CNPq and FAPESP). B.v.W. received funding from ZonMW, EU Joint Programme — Neurodegenerative Disease Research (JPND) project, was supported under the aegis of JPND through funding from the Netherlands Organisation for Health Research and Development. A.D. received BIOSCA NCT01470729 sponsorship from Assistance Publique — Hôpitaux de Paris. P.G. received support from the EU Joint Programme — Neurodegenerative Disease Research (JPND) project and was supported under the aegis of JPND through funding from the Medical Research Council. H.G.-M. received a JPND grant rom the Medical Research Council and support from CureSCA3 and Fathers Foundation. L.S. received support from the EU Joint Programme - Neurodegenerative Disease Research (JPND) project and support under the aegis of JPND through the Federal Ministry of Education and Research (BMBF; funding codes 01ED1602A/B). G.O. — the study was in part funded by the National Ataxia Foundation. The Center for Magnetic Resonance Research is supported by the National Institute of Biomedical Imaging and Bioengineering (NIBIB) grant P41 EB027061 and the Institutional Center Cores for Advanced Neuroimaging award P30 NS076408. R.J. is a paid employee of IXICO Plc, contracted to undertake this work. The involvement of R.W. was funded by IXICO. T.K. received support from the EU Joint Programme — Neurodegenerative Disease Research (JPND) project and under the aegis of JPND through the Federal Ministry of Education and Research (BMBF; funding codes 01ED1602A/B).

Funding agencies: This publication is an outcome of ESMI, an EU Joint Programme - Neurodegenerative Disease Research (JPND) project (see www.jpnd.eu). The project is supported under the aegis of JPND through the following funding organizations: Germany, Federal Ministry of Education and Research (BMBF; funding codes 01ED1602A/B); Netherlands, The Netherlands Organisation for Health Research and Development; Portugal, Foundation for Science and Technology and Regional Fund for Science and Technology of the Azores; United Kingdom, Medical Research Council. This project has received funding from the European Union's Horizon 2020 research and innovation program under grant agreement 643417. At the US sites this work was in part supported by the National Ataxia Foundation and the National Institute of Neurological Disorders and Stroke (NINDS) grant R01 NS080816. The Center for Magnetic Resonance Research is supported by the National Institute of Biomedical Imaging and Bioengineering (NIBIB) grant P41 EB027061, and the Institutional Center Cores for Advanced Neuroimaging award P30 NS076408 and S10 OD017974 grant.

Received: 3 November 2020; **Revised:** 17 March 2021; **Accepted:** 18 March 2021

Published online in Wiley Online Library (wileyonlinelibrary.com). DOI: 10.1002/mds.28610

[18]Department of Neurology, Goethe University, Frankfurt am Main, Germany
[19]Department of Neurology, Essen University Hospital, Essen, Germany
[20]Department of Neurology, University Hospital of Heidelberg, Heidelberg, Germany
[21]Neurology Service, University Hospital Marques de Valdecilla-IDIVAL, University of Cantabria, Centro de Investigacion Biomedica en Red de Enfermedades Neurodegenerativas (CIBERNED), Santander, Spain
[22]IXICO Plc, London, United Kingdom
[23]Brain Mind Institute, Departmentof Computer Science, Department of Statistics, University of Western Ontario, London, Canada
[24]Institute of Medical Biometry, Informatics and Epidemiology, University Hospital Bonn, Bonn, Germany

ABSTRACT: Background: Given that new therapeutic options for spinocerebellar ataxias are on the horizon, there is a need for markers that reflect disease-related alterations, in particular, in the preataxic stage, in which clinical scales are lacking sensitivity.
Objective: The objective of this study was to quantify regional brain volumes and upper cervical spinal cord areas in spinocerebellar ataxia type 3 in vivo across the entire time course of the disease.
Methods: We applied a brain segmentation approach that included a lobular subsegmentation of the cerebellum to magnetic resonance images of 210 ataxic and 48 preataxic spinocerebellar ataxia type 3 mutation carriers and 63 healthy controls. In addition, cervical cord cross-sectional areas were determined at 2 levels.
Results: The metrics of cervical spinal cord segments C3 and C2, medulla oblongata, pons, and pallidum, and the cerebellar anterior lobe were reduced in preataxic mutation carriers compared with controls. Those of cervical spinal cord segments C2 and C3, medulla oblongata, pons, midbrain, cerebellar lobules crus II and X, cerebellar white matter, and pallidum were reduced in ataxic compared with nonataxic carriers. Of all metrics studied, pontine volume showed the steepest decline across the disease course. It covaried with ataxia severity, CAG repeat length, and age. The multivariate model derived from this analysis explained 46.33% of the variance of pontine volume.
Conclusion: Regional brain and spinal cord tissue loss in spinocerebellar ataxia type 3 starts before ataxia onset. Pontine volume appears to be the most promising imaging biomarker candidate for interventional trials that aim at slowing the progression of spinocerebellar ataxia type 3.

Key Words: spinocerebellar ataxia; MRI; volumetry; biomarker

Spinocerebellar ataxia type 3/Machado–Joseph disease (SCA3) is worldwide the most common autosomal dominantly inherited ataxia disorder.[1] It is caused by unstable expansions of polyglutamine encoding CAG repeats in the *ATXN3* gene, resulting in the formation of abnormally elongated disease proteins. Although partial loss of the physiological role of ataxin-3 contributes to the development of SCA3, its pathogenesis is mainly because of newly acquired deleterious actions of elongated ataxin-3.

SCA3 is a multisystem disorder characterized by degeneration of spinocerebellar tracts, dentate nucleus, cerebellar cortex, brain stem nuclei, and basal ganglia.[2] The clinical syndrome is characterized by prominent cerebellar ataxia in combination with supranuclear gaze palsy and peripheral neuropathy.[3,4] SCA3 takes a progressive course and leads to severe disability and premature death, with a median survival after ataxia onset of 25 years.[5-7]

Currently, there is no causal treatment for SCA3. However, as the understanding of the molecular mechanisms is rapidly advancing, there are several new treatment approaches. Among the most promising ones are approaches for downregulating or silencing the *ATXN3* gene.[8] Like in other neurodegenerative diseases, in particular those with a clinically presymptomatic phase, there is a need for markers with known evolution throughout the time course of the disease that have the potential to map disease activity.

Magnetic resonance imaging (MRI) allows the study of structural abnormalities of the brain and spinal cord in vivo. Previous studies in patients with SCA3 showed a pattern of regional brain tissue loss that faithfully reflected the distribution of neurodegenerative changes described in autopsy studies[9-13] and revealed that regional volume loss already starts in the preataxia stage.[9] Three longitudinal volumetric studies in small numbers of patients with SCA3 suggested that MRI volume is more sensitive to change than clinical scales, which makes MRI volumes promising candidates for biomarkers in clinical trials.[14-16] This applies in particular to preventive trials in preataxic mutation carriers, as clinical measures lack sensitivity before ataxia onset. However, further steps toward the validation of MRI regional volumes as biomarkers for SCA3 are hampered by the small numbers of studied MRIs and the

time-consuming procedures for segmentation and volumetry.

In this study, we applied an automated method for MRI volumetry, which includes subsegmentation of the cerebellum into its lobules to a large number of existing T1-weighted MRIs of preataxic and ataxic *SCA3* mutation carriers that were acquired at 14 centers worldwide. The advantage of the applied method is that it provides individual single-point values that can be used in future longitudinal studies to map individual trajectories.

Materials and Methods

MRI Scans

We collected T1-weighted (T1W) MRIs of 295 *SCA3* mutation carriers and 72 healthy controls from 14 sites in 8 countries. There were no restrictions regarding manufacturer, software version, or field strength. Scans with a resolution of greater than 2 mm on at least 1 axis, based on the limited ability to accurately measure small regional brain volumes in scans with large voxel sizes, and scans that were acquired after application of contrast agents were excluded (for details, see Table S2 and Fig. S1). Age, sex, and total Scale for Assessment and Rating of Ataxia (SARA)[17] score of all SCA3 participants and healthy controls were available. Information about CAG repeat length was available for *SCA3* mutation carriers. Using a SARA cutoff value of 3, *SCA3* mutation carriers were divided into preataxic (SARA < 3) and ataxic (SARA ≥ 3) individuals.[17,18] This SARA threshold for ataxia was defined as the mean SARA +2 SDs of the healthy control group in the original SARA validation study.[17] For complementary analyses, which can be found in the Supplementary data, groups were defined on the basis of subject report, whether and since when gait disturbances were present, here using the terms *presymptomatic* and *symptomatic*. Scans with incomplete clinical information were excluded (for details, see Fig. S1). All participants gave their written informed consent.

Image Analysis

The T1W images of each subject were processed with a fully automated image-processing pipeline to obtain volumes of 122 distinct anatomical regions covering the entire brain and 7 compartments containing cerebrospinal fluid. For the cerebellar subsegmentation, a reference database was developed to provide a parcellation scheme including fine-granularity cerebellar subsegmentations on the level of cerebellar lobules into 30 disjoint volumes. These reference data set segmentations were generated from a gold standard segmentation set of 17 T1W images with manual segmentations of the cerebellar lobules provided by J. Diedrichsen (http://www.diedrichsenlab.org). The image-processing and segmentation methods are described in detail in the supplementary data. To enable comparison of subject volume, data adjustment to account for head size was undertaken, using a normalization factor that was estimated from a template registration approach based on Buckner et al.[19] In brief, the affine (9-parameter) transformation was computed for the subject T1W to the MNI152 linear T1 template. The magnitude of the scaling factors of the estimated affine matrix was then applied as a normalization factor to estimated volumes. For the final analysis, each 2 hemispheric volumes of hemispheric bilateral volumes were combined, and for the cerebellum the 8 subdivisions of the vermis were combined. In addition, the following compound volumes were analyzed: anterior lobe (cerebellar lobules I–V), superior posterior lobe (cerebellar lobules VI, VIIA [crus I, crus II], and VIIB), inferior posterior lobe (cerebellar lobules VIIIA, VIIIB, and IX), cerebellar gray matter (lobules I–X and vermis) and basal ganglia (pallidum, caudate, putamen). A full list of all volumes is given in Table S1, and an example segmentation is shown in Figure S2.

The upper portion of the cervical spinal cord was depicted on all available MRIs. Analysis of the C3 level was applicable in 256 cases and analysis of the C2 level in 297 of 321 cases. In a semiautomated approach, we used the Spinal Cord Toolbox[20] in combination with manual corrections of the automated delineation to compute the cross-sectional area under consideration of an angle correction along the center line. We calculated the mean of the angle-corrected cross-sectional areas for all slices of cervical spinal cord segments C2 and C3 separately. The image processing and segmentation methods are described in detail in the supplementary data. To improve readability, we do not state the term "mean cross-sectional area" each time, but instead we will subsume the values of the mean cross-sectional areas of C2 and C3 and brain regional volumes under the term "metric."

Statistical Analysis

All analyses were performed using R Software for Statistical Computing, version 3.5.1. R Foundation for Statistical Computing, Vienna.

To investigate group differences between ataxic *SCA3* mutation carriers, preataxic mutation carriers, and healthy controls, we used separate linear mixed-effects models (R package lme4) to analyze the relationship of each metric — each brain volume and the mean cross-sectional area of spinal cord levels C2 and C3 — with the covariables age, sex, and group (preataxic, ataxic, healthy control). The latter variables were represented by fixed effects, whereas scanner type was represented by a random effect. Group differences were

evaluated using the R package multcomp (function glht). In all metrics that showed a significant group effect, a post hoc multiple comparison via Benjamini–Hochberg correction was applied afterward.[21] Given the heterogeneous sample, we chose a strict significance level to reduce the probability of false-positive effects. $P < 0.001$ after post-hoc Benjamini–Hochberg correction[21] was considered significant. In a second analysis, analysis groups were defined by self-report as presymptomatic or symptomatic *SCA3* mutation carriers (Supplementary Data).

Only those metrics that showed a significant difference between preataxic *SCA3* mutation carriers, either compared with healthy controls or ataxic *SCA3* mutation carriers, were considered for the further analyses to meaningfully cover the entire time course of the disease (regional volume loss in relation to disease duration, influencing factors, sample sizes).

To describe the regional changes in relation to disease duration, we *z*-transformed each metric in relation to healthy controls of the same age and plotted *z* values against the time scale of estimated disease duration, as described in detail in the supplementary data. We used a uniform time scale for all *SCA3* mutation carriers, defined by the predicted time of ataxia onset calculated on the basis of CAG repeat length.[22] On this scale, negative values for disease duration indicate the predicted time to ataxia onset and positive values the time from the predicted onset. In a second analysis (Supplementary Data), we used a compound time scale. For presymptomatic carriers, we calculated the time to ataxia onset based on CAG repeat length and present age,[22] and in symptomatic carriers, we used the reported time from ataxia onset. The *x* axis was restricted to (−20 years; 20 years). We applied locally weighted scatterplot smoothing for interpolation to avoid any preassumptions about the curve course, for example, assuming a linear or parabolic curve course.

To identify factors that covary with regional volume loss, we applied linear regression analysis with SARA score, CAG repeat of the longer allele, age, and sex as independent variables. We calculated R^2, which indicates the overall proportion of the variance of each metric that is explained by the independent variables and the *P* value for each independent variable. Here, the *P* value indicates whether the respective variable contributes to the model in a statistically significant way.

As a measure of effect size, we calculated Cohen's d values for a presumed 50% reduction of the decrease of SARA and each MRI metric. Calculations were based on the estimated metric slopes of linear models with calculated disease duration as covariate. To allow comparison of the effect sizes of the MRI metrics, we calculated relative values by dividing Cohen's *d* of each MRI metric by Cohen's *d* of SARA.

Results

Demographic and Clinical Data

Of the 367 collected data sets, 46 had to be excluded (Fig. S1). We analyzed the remaining 321 data sets that comprised data from 210 ataxic *SCA3* mutation carriers, 48 preataxic *SCA3* mutation carriers, and 63 healthy controls. Demographic data are given in Table 1. Age differed among the 3 subgroups. Ataxic mutation carriers had the highest age (mean ± SD, 46.84 ± 11.24 years) and preataxic mutation carrier the lowest age (mean ± SD, 37.75 ± 9.47 years). Age of the control group was between the 2 groups of mutation carriers (mean ± SD, 42.81 ± 13.65 years). SARA score of the ataxic mutation carriers was on average ± SD, 12.41 ± 5.50). The mean SARA scores of preataxic mutation carriers (mean ± SD, 1.31 ± 0.94) and healthy controls (mean ± SD, 0.22 ± 0.46) was below the cutoff of 3. The number of CAG repeats of the longer allele was higher in ataxic (mean ± SD, 71.10 ± 4.23) than in the preataxic (mean ± SD, 68.29 ± 3.55) mutation carriers.

Group Comparisons

To identify regions subject to volume loss before ataxia onset in SCA3, we compared *SCA3* preataxic mutation carriers with healthy controls. Volumes of the following brain regions and mean cross-sectional areas of the spinal cord levels were reduced in preataxic mutation carriers compared with healthy controls: cervical spinal cord segments C2 and C3 ($P < 0.0001$), medulla oblongata

TABLE 1 *Demographic and characterizing cohort data*

	n	Age	Male/female	Age of onset[a]	Disease duration in years[a]	CAG repeats, longer allele	SARA sum score
Healthy controls	63	42.81 (13.65)	35/28	na	na	na	0.22 (0.46)
Preataxic	48	37.75 (9.47)	18/30	39.73 (7.87)	−1.98 (9.83)	68.29 (3.55)	1.31 (0.94)
Ataxic	210	46.84 (11.24)	118/92	34.12 (9.45)	12.67 (9.45)	71.10 (4.23)	12.41 (5.50)

Data are expressed as mean and standard deviation for age, age at onset, disease duration, CAG repeat length of the longer allele, and SARA sum score and as number for the group size and the male/female distribution.

[a]Estimated age at onset on the basis of CAG repeat length following the model provided by Tezenas et al (Tezenas du Montcel et al, 2014) and disease duration in years, defined as the actual age minus the estimated age at onset, resulting in negative values for the expected time to onset in preataxic *SCA3* mutation carriers and positive values for ataxic *SCA3* mutation carriers.

TABLE 2 *Group differences between preataxic and ataxic* SCA3 *mutations carriers and healthy controls (HC)*

Metric	Preataxic SCA3 < HC	Ataxic SCA3 < preataxic *SCA3*	Ataxic SCA3 < HC
Cervical spinal cord			
Cervical spinal cord, level C3, CSA[a]	**	**	**
Cervical spinal cord, level C2, CSA[a]	**	**	**
Brain stem			
Medulla oblongata	**	**	**
Pons	**	**	**
Midbrain		*	*
Cerebellum			
Cerebellum white matter		*	*
Cerebellum I–IV			*
Cerebellum V			*
Cerebellum VI			*
Cerebellum crus I			*
Cerebellum crusII		*	**
Cerebellum VIIb			*
Cerebellum IX			*
Cerebellum X		*	*
Cerebellum vermis[b]			*
Cerebrum			
Caudate			**
Pallidum	*	*	*
Thalamus			*
Compound volumes			
Cerebellum, anterior lobe[c]	*		*
Cerebellum, superior posterior lobe[d]			*
Cerebellum, inferior posterior lobe[e]			*
Cerebellum gray matter[f]			*
Basal ganglia[g]			*
Ventricles	Preataxic SCA3 > HC	Ataxic SCA3 > preataxic SCA3	**Ataxic SCA3 > HC**
Third ventricle		*	
Fourth ventricle			*

(Continues)

TABLE 2 *Continued*

Significance levels are given after post hoc Benjamini-Hochberg correction for multiple comparisons.
*$P < 0.0001$.
**$P < 0.000$.
[a]CSA, mean cross-sectional area.
[b]Entire vermis corresponding to the hemispheric lobules VI–X.
[c]Cerebellar lobules I–V.
[d]Cerebellar lobules VI, crus I, crus II, and VIIB.
[e]Cerebellar lobules VIIIA, VIIIB, and IX.
[f]Cerebellar lobules I–X and vermis.
[g]Palldium, caudate, and putamen.

($P < 0.0001$), pons ($P < 0.0001$), and pallidum ($P < 0.001$); see Table 2. None of the cerebellar lobules showed any significant volume loss in preataxic mutation carriers. However, when considering compound volumes, the anterior lobe of preataxic mutation carriers had reduced volume compared with healthy controls ($P < 0.001$; Table 2).

To define the atrophy pattern of manifest SCA3, we compared ataxic *SCA3* mutation carriers and healthy controls. Volumes of the following brain regions and mean cross-sectional areas of the spinal cord levels were smaller in ataxic mutation carriers compared with healthy controls: cervical spinal cord segments C2 and C3 ($P < 0.0001$), medulla oblongata ($P < 0.0001$), pons ($P < 0.0001$), midbrain ($P < 0.001$), cerebellar white matter ($P < 0.001$), cerebellar lobules I–IV ($P < 0.001$), V ($P < 0.001$), VI ($P < 0.001$), crus I ($P < 0.001$), crus II ($P < 0.0001$), VIIB ($P < 0.001$), IX ($P < 0.001$), and X ($P < 0.001$), cerebellar vermis ($P < 0.001$), thalamus ($P < 0.001$), caudate ($P < 0.0001$), and pallidum ($P < 0.001$); see Table 2. In addition, the volume of the fourth ventricle was larger than in controls ($P < 0.001$). Comparison of the compound volumes showed reductions of the anterior, superior-posterior, and inferior-posterior lobes ($P < 0.001$) and cerebellar gray matter ($P < 0.001$), as well as the basal ganglia ($P < 0.001$); see Table 2.

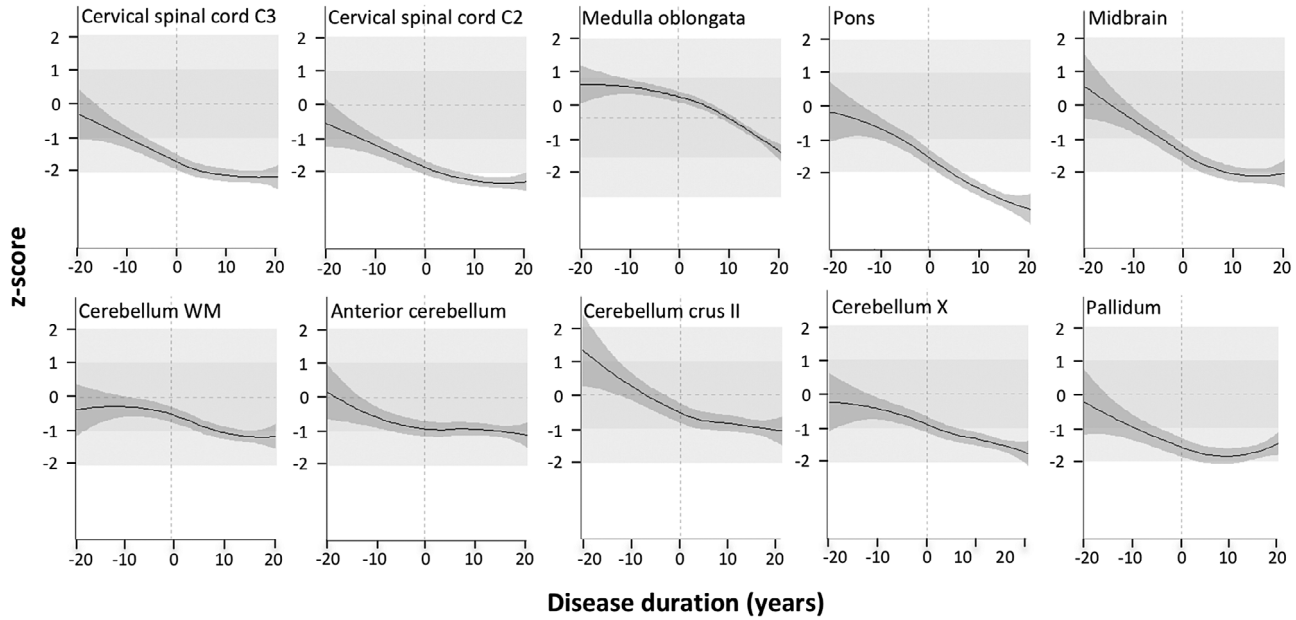

FIG. 1. Regional volume loss along the time course of the disease. Each metric, being mean cross-sectional area of cervical spinal cord levels C2 and C3 and volumes of medulla oblongata, pons, midbrain, cerebellar white matter, anterior lobe of the cerebellum, cerebellar lobules crus II and X. and pallidum of *SCA3* mutation carriers, was *z*-transformed in relation to healthy controls of the same age. The *x* axis represents the estimated disease duration in years. The estimated 95% confidence interval is given in dark gray. For a better orientation, the following reference lines and ranges are given: the vertical dashed line marks the estimated clinical onset; the horizontal dashed line marks the average of the healthy control group, represented by a *z* score of 0; the medium- and light-gray areas represent the range ± 1 and respective ±2 standard deviations of the healthy control group distribution.

Among the regions that showed smaller metrics in ataxic *SCA3* mutation carriers compared with healthy controls, a number of regions also showed reduced metrics compared with preataxic mutations carriers, indicating that these regions undergo progressive volume loss in the SCA3 disease course. These regions included cervical spinal cord segments C2 and C3 ($P < 0.0001$), medulla oblongata ($P < 0.0001$), pons ($P < 0.0001$), midbrain ($P < 0.001$), cerebellar lobules crus II and X ($P < 0.001$), cerebellar white matter ($P < 0.001$), and pallidum ($P < 0.001$); see Table 2. In addition, the volume of the third ventricle was larger than in controls ($P < 0.001$). Estimates, standard errors, and 95% confidence intervals (CIs) for each group comparison as well as the ANOVA statistics are given in Tables S3 and S4.

When we performed the same analysis in groups defined by self-report as presymptomatic or symptomatic *SCA3* mutation carriers, results were generally similar. However, the pallidum and anterior lobe of the cerebellum were not smaller in presymptomatic mutation carriers compared with healthy controls, whereas the superior posterior lobe and total cerebellar gray matter was smaller in presymptomatic compared with symptomatic *SCA3* mutation carriers (Table S5).

Regional Volume Loss in Relation to Disease Duration

To study regional volume loss in SCA3 in relation to disease duration, we applied local regression on a time scale defined by the predicted time of ataxia onset, calculated on the basis of CAG repeat length. On this scale, negative values indicate the predicted time to ataxia onset and positive values the time from the predicted onset. For this analysis, we selected those metrics that showed significant alterations in any comparison of preataxic mutation carriers, with either healthy controls or ataxic mutation carriers. Already around 10 to 15 years before ataxia onset, the metrics of cervical spinal cord segments C2 and C3 and the pallidum were reduced by about 1 standard deviation (SD) compared with healthy controls of the same age. Metrics of all regions steadily decreased until a period of 5 to 15 years after ataxia onset. Thereafter, volume loss decelerated, and metrics remained stable or even increased relative to controls, except for the pons and cerebellar lobule X. In the time interval lasting from 5 years before until 5 years after ataxia onset, the metrics of all regions decreased almost linearly. The decline was steepest in the pons and midbrain. At the time of ataxia onset, the metrics of cervical spinal cord segments C2 and C3, the pons, midbrain, and pallidum ranged between about 1 and 2 SD below the control group, whereas the other volumes, in particular the cerebellar volumes, were reduced by less than 1 SD (Fig. 1).

When we performed the same analysis on a compound time scale that used the calculated time to expected ataxia onset in presymptomatic mutation carriers and the reported time since ataxia onset in symptomatic mutation carriers, the results were generally similar (Fig. S4).

TABLE 3 *Linear regression analysis of potential factors determining regional volume loss in SCA3 including SARA sum score, CAG repeat length of the longer allele, age, and sex as independent variables and the respective metric as dependent variable*

Metric	Cervical spinal cord level C3	Cervical spinal cord level C2	Medulla oblongata	Pons	Midbrain	Cerebellum white matter	Cerebellum, anterior lobe	Cerebellum crus II	Cerebellum X	Pallidum
Adjusted R^2 x 100[a]	23.35	22.15	17.83	46.33	33.49	5.82	11.13	16.60	6.44	22.58
P[b]										
SARA	c	c	c	c	c					
CAG repeat of longer allele				c	c					c
Age				c	c		c	c		
Sex			c		c					

[a]Explained portion of the metrics variance, given by the adjusted R^2 multiplied with 100.
[b]P value for each independent variable SARA sum score, CAG repeat length of the longer allele, age, and sex, indicating whether the respective variable statistically significantly contributes to the model.
[c]$P < 0.001$.

TABLE 4 *Calculation of effect sizes relative to the effect size of SARA*

Metric	Slope	Standard error of slope	Relative Cohen's d[a]
Cervical spinal cord, level C3	−0.53	0.08	0.81
Cervical spinal cord, level C2	−0.43	0.08	0.68
Medulla oblongata	−24.50	4.55	0.61
Pons	−210.01	23.11	1.03
Midbrain	−72.76	8.46	0.97
Cerebellum white matter	−226.05	68.67	0.35
Cerebellum, anterior lobe	−39.51	16.78	0.26
Cerebellum crus II	−104.17	33.15	0.35
Cerebellum X	−5.93	1.50	0.45
Pallidum	−35.86	4.17	0.97

Linear models with the estimated disease duration were the basis for the estimated slope of all respective metrics as well as for the SARA sum score. As a measure of effect size, we calculated Cohen's d values for a presumed 50% reduction of the decrease of SARA and each MRI metric.
[a]Cohen's d is given in relation to SARA: relative Cohen's d = Cohen's d of the metric/Cohen's d of SARA.

Factors Determining Regional Volume Loss

To identify factors that covary with regional tissue loss in SCA3, we performed a linear regression analysis with SARA sum score, CAG repeat length of the longer allele, age, and sex as potential determining factors. Again, we selected those metrics for analyses that showed significant alterations in any comparison of preataxic mutation carriers, either with healthy controls or with ataxic mutation carriers. SARA sum score contributed highly significantly to the models of cervical spinal cord segments C2 and C3, the medulla oblongata, pons, and midbrain. Furthermore, CAG repeat length influenced pons, midbrain, and pallidum, age on pons, midbrain anterior cerebellum, and cerebellar crus II, and sex on medulla oblongata and midbrain (each $P < 0.001$). The multivariate models derived from this analysis explained between 5.82% and 46.33% of the variance of the respective metrics. The proportion of the explained variance was highest for the pons (46.33%) and midbrain (33.49%) and lowest for the cerebellar regions (5.82%–16.60%); see Table 3. Estimates, standardized beta, standard error, and 95% confidence intervals are given in Table S6.

Calculation of Effect Sizes

Based on the estimated slopes of linear models of regional volume changes in relation to disease duration, we calculated Cohen's d values as a measure of effect size for each metric, We report the effects sizes of each metric relative to the effect size of SARA to allow a

comparison. Cohen's *d* of pontine volume was larger than that of SARA (1.03 times the Cohen's *d* of SARA). Cohen's *d* values of cervical spinal cord segment C3 (0.81 times the Cohen's *d* of SARA) and C2 (0.68 times the Cohen's *d* of SARA), medulla oblongata (0.61 times the Cohen's *d* of SARA), midbrain (0.97 times the Cohen's *d* of SARA), and pallidum (0.97 times the Cohen's *d* of SARA) were in the same magnitude, but smaller than that of SARA (Table 4). For all cerebellar regions, Cohen's *d* values were less than 0.5 times the Cohen's *d* of SARA (Table 4).

Discussion

In this cross-sectional MRI study, we assessed regional tissue loss in a large cohort of preataxic and ataxic *SCA3* mutation carriers. We applied a refined and optimized brain segmentation approach that allowed reliable subsegmentation of the cerebellum into the cerebellar lobules. For the spinal cord, we relied on the assessment of the mean cross-sectional area of the upper cervical levels. The advantage of the applied methodology is that the availability of individual single-point metrics allows consideration of brain regional volumes as outcome measures in future interventional trials. To study the change of metrics in relation to disease duration, we used a uniform time scale defined by the predicted age of ataxia onset for all mutation carriers according to a previously published model.[18,22] To check whether this methodological approach treating all mutation carriers consistently distorts the disease course, we repeated the analysis using a compound time scale in which ataxia onset was calculated only in presymptomatic individuals, whereas in symptomatic individuals we used the reported age at onset. Both approaches led to similar results.

Our results in *SCA3* mutation carriers reflect the neurodegeneration pattern observed in autopsy studies very well[23-25] and confirm previous MRI studies in smaller numbers of patients.[9,14,16,26,27] We will discuss several aspects of this in more detail in the following section. Even though our data do not allow defining a clear temporal order of involvement of affected regions across the entire disease range, the inclusion of *SCA3* mutation carriers from the earliest preataxia to late symptomatic disease stages allowed us to detect regional volume changes occurring before the onset of ataxia. In the preataxic stage, volume loss of cerebellar regions was less pronounced than that of the affected extracerebellar regions including the spinal cord, brain stem, and pallidum, suggesting prominent involvement of extracerebellar regions at the onset of neurodegeneration. This observation is in line with the known pattern of SCA3 — in contrast to many other SCAs, in which the cerebellar cortex is severely affected, cerebellar involvement in SCA3 is mild and variable, and the Purkinje cell layer of the cerebellar cortex has even been reported to be completely spared in some autopsy studies.[23-25] The rather mild cerebellar volume loss and given that age was the only factor that covaried with cerebellar volume suggest that cerebellar degeneration in SCA3 may represent a secondary, age-related phenomenon. This is corroborated by evidence of an age-dependent decline of cerebellar volume in healthy individuals,[28,29] whereas parts of the brain stem such as the pons appear to be less affected by age-related volume loss.[30,31] Based on evidence from neuropathological studies and the results of previous voxel-based morphometric as well as diffusion MRI studies showing prominent white matter loss in patients with SCA3,[9,14,24,27,32] it is likely that the anatomical substrate of the volume changes of cervical spinal cord segments C2 and C3 and the medulla oblongata reflects pathology of afferent spinal pathways, in particular the spinocerebellar tracts. In addition, considering the neuropathological evidence of substantial neuronal loss in the dentate nucleus,[24] degeneration of the dentato-rubro-thalamo-cortical tract would also affect the thalamic and midbrain volumes.

Anatomically the pons is connected with the cerebellum via the middle cerebellar peduncles. As in other polyglutamine diseases, the expanded disease protein accumulates in neuronal nuclei forming ubiquitin-positive neuronal intranuclear inclusions (NIIs).[33,34] The distribution of NIIs does not fully match that of the neurodegeneration, but in SCA3, NIIs are abundant in pontine nuclei,[35] and atrophy of the pons is a common feature in the autopsy cases.[24] The pons volume showed the most continuous decline and steepest decrease around ataxia onset of all further studied metrics in our study. Furthermore, a model with ataxia severity, CAG repeat length, age, and sex could only explain a small proportion of the variance in cerebellar volume, whereas the pontine volume showed the highest proportion, with almost 50% of its variance explained by a model including these factors. This is remarkable, in particular, given the very heterogeneous sample of MRIs included in this study.

Calculation of effect size has 2 major limitations. First, our calculations were based on cross-sectional data, which do not allow an accurate estimation of between-subject variability in the longitudinal rate of change. However, as we calculated effect size for all metrics and SARA in the same way, we believe that the data are useful for comparison between metrics. Consequently, we provided effect sizes of the MRI metrics in relation to the effect size of SARA. Second, we assumed a linear progression throughout the whole time course of the disease, although the evolution of almost all metrics was nonlinear. The effect size of pontine volume marginally exceeded that of SARA. The effect size of all other metrics was smaller than that of SARA, although those of cervical spinal cord segment C2 and C3, pons, midbrain, and pallidum were of the same magnitude as that of SARA. The current values are not comparable to effect sizes calculated on the basis of longitudinal data.[14,16,36]

We suggest that extracerebellar regions represent the core sites of the disease process in SCA3. This suggestion

is based on the observed time course of volume changes and the close relation of the metrics of extracerebellar regions with clinical disease severity and CAG repeat length. Our observation that the effect size of the pontine volume was marginally higher than that of SARA and that a relevant proportion of pontine volume variance was explained with a model including ataxia severity, CAG repeat length, and age suggests that pontine volume is a promising biomarker candidate for interventional studies that aim to slow the progression of SCA3. However, longitudinal studies including of preataxic *SCA3* mutation carriers are inevitable to adequately test the validity of such imaging biomarker candidates.

References

1. Ruano L, Melo C, Silva MC, Coutinho P. The global epidemiology of hereditary ataxia and spastic paraplegia: a systematic review of prevalence studies. Neuroepidemiology 2014;42(3):174–183.
2. Rub U, Schols L, Paulson H, et al. Clinical features, neurogenetics and neuropathology of the polyglutamine spinocerebellar ataxias type 1, 2, 3, 6 and 7. Prog Neurobiol 2013;104:38–66.
3. Maciel P, Gaspar C, DeStefano AL, et al. Correlation between CAG repeat length and clinical features in Machado-Joseph disease. Am J Hum Genet 1995;57(1):54–61.
4. Schmitz-Hubsch T, Coudert M, Bauer P, et al. Spinocerebellar ataxia types 1, 2, 3, and 6: disease severity and nonataxia symptoms. Neurology 2008;71(13):982–989.
5. Jacobi H, du Montcel ST, Bauer P, et al. Long-term disease progression in spinocerebellar ataxia types 1, 2, 3, and 6: a longitudinal cohort study. Lancet Neurol 2015;14(11):1101–1108.
6. Diallo A, Jacobi H, Cook A, et al. Prediction of survival with long-term disease progression in Most common spinocerebellar ataxia. Mov Disord 2019;34(8):1220–1227.
7. Jardim LB, Hauser L, Kieling C, et al. Progression rate of neurological deficits in a 10-year cohort of SCA3 patients. Cerebellum 2010;9(3):419–428.
8. McLoughlin HS, Moore LR, Chopra R, et al. Oligonucleotide therapy mitigates disease in spinocerebellar ataxia type 3 mice. Ann Neurol 2018;84(1):64–77.
9. Rezende TJR, de Paiva JLR, Martinez ARM, et al. Structural signature of SCA3: from presymptomatic to late disease stages. Ann Neurol 2018;84(3):401–408.
10. Fahl CN, Branco LM, Bergo FP, D'Abreu A, Lopes-Cendes I, Franca MC Jr. Spinal cord damage in Machado-Joseph disease. Cerebellum 2015;14(2):128–132.
11. Guimaraes RP, D'Abreu A, Yasuda CL, et al. A multimodal evaluation of microstructural white matter damage in spinocerebellar ataxia type 3. Mov Disord 2013;28(8):1125–1132.
12. Hernandez-Castillo CR, King M, Diedrichsen J, Fernandez-Ruiz J. Unique degeneration signatures in the cerebellar cortex for spinocerebellar ataxias 2, 3, and 7. Neuroimage 2018;20:931–938.
13. Klaes A, Reckziegel E, Franca MC Jr, et al. MR imaging in spinocerebellar ataxias: a systematic review. Am J Neuroradiol 2016;37(8):1405–1412.
14. Adanyeguh IM, Perlbarg V, Henry PG, et al. Autosomal dominant cerebellar ataxias: imaging biomarkers with high effect sizes. Neuroimage 2018;19:858–867.
15. Reetz K, Rodriguez-Labrada R, Dogan I, et al. Brain atrophy measures in preclinical and manifest spinocerebellar ataxia type 2. Ann Clin Transl Neurol 2018;5(2):128–137.
16. Piccinin CC, Rezende TJR, de Paiva JLR, et al. A 5-year longitudinal clinical and magnetic resonance imaging study in spinocerebellar ataxia type 3. Mov Disord 2020;35(9):1679–1684.
17. Schmitz-Hubsch T, du Montcel ST, Baliko L, et al. Scale for the assessment and rating of ataxia: development of a new clinical scale. Neurology 2006;66(11):1717–1720.
18. Jacobi H, du Montcel ST, Romanzetti S, et al. Conversion of individuals at risk for spinocerebellar ataxia types 1, 2, 3, and 6 to manifest ataxia (RISCA): a longitudinal cohort study. Lancet Neurol 2020;19(9):738–747.
19. Buckner RL, Head D, Parker J, et al. A unified approach for morphometric and functional data analysis in young, old, and demented adults using automated atlas-based head size normalization: reliability and validation against manual measurement of total intracranial volume. Neuroimage 2004;23(2):724–738.
20. De Leener B, Levy S, Dupont SM, et al. SCT: spinal cord toolbox, an open-source software for processing spinal cord MRI data. Neuroimage 2017;145((Pt A)):24–43.
21. Benjamini YHY. Controlling the false discovery rate: a practical and powerful approach to multiple testing. J R Stat Soc, Series B 1995;57:289–300.
22. Tezenas du Montcel S, Durr A, Rakowicz M, et al. Prediction of the age at onset in spinocerebellar ataxia type 1, 2, 3 and 6. J Med Genet 2014;51(7):479–486.
23. Seidel K, Siswanto S, Brunt ER, den Dunnen W, Korf HW, Rub U. Brain pathology of spinocerebellar ataxias. Acta Neuropathol 2012;124(1):1–21.
24. Koeppen AH. The neuropathology of spinocerebellar ataxia type 3/Machado-Joseph disease. Adv Exp Med Biol 2018;1049:233–241.
25. Durr A, Stevanin G, Cancel G, et al. Spinocerebellar ataxia 3 and Machado-Joseph disease: clinical, molecular, and neuropathological features. Ann Neurol 1996;39(4):490–499.
26. Klockgether T, Skalej M, Wedekind D, et al. Autosomal dominant cerebellar ataxia type I. MRI-based volumetry of posterior fossa structures and basal ganglia in spinocerebellar ataxia types 1, 2 and 3. Brain 1998;121(Pt 9):1687–1693.
27. Schulz JB, Borkert J, Wolf S, et al. Visualization, quantification and correlation of brain atrophy with clinical symptoms in spinocerebellar ataxia types 1, 3 and 6. Neuroimage 2010;49(1):158–168.
28. Bernard JA, Leopold DR, Calhoun VD, Mittal VA. Regional cerebellar volume and cognitive function from adolescence to late middle age. Hum Brain Mapp 2015;36(3):1102–1120.
29. Han S, An Y, Carass A, Prince JL, Resnick SM. Longitudinal analysis of regional cerebellum volumes during normal aging. Neuroimage 2020;220:117062.
30. Lambert C, Chowdhury R, Fitzgerald TH, et al. Characterizing aging in the human brainstem using quantitative multimodal MRI analysis. Front Hum Neurosci 2013;7:462.
31. Luft AR, Skalej M, Schulz JB, et al. Patterns of age-related shrinkage in cerebellum and brainstem observed in vivo using three-dimensional MRI volumetry. Cereb Cortex 1999;9(7):712–721.
32. Lukas C, Schols L, Bellenberg B, et al. Dissociation of grey and white matter reduction in spinocerebellar ataxia type 3 and 6: a voxel-based morphometry study. Neurosci Lett 2006;408(3):230–235.
33. Paulson HL, Perez MK, Trottier Y, et al. Intranuclear inclusions of expanded polyglutamine protein in spinocerebellar ataxia type 3. Neuron 1997;19(2):333–344.
34. Schmidt T, Landwehrmeyer GB, Schmitt I, et al. An isoform of ataxin-3 accumulates in the nucleus of neuronal cells in affected brain regions of SCA3 patients. Brain Pathol 1998;8(4):669–679.
35. Seidel K, Siswanto S, Fredrich M, et al. On the distribution of intranuclear and cytoplasmic aggregates in the brainstem of patients with spinocerebellar ataxia type 2 and 3. Brain Pathol 2017;27(3):345–355.
36. Reetz K, Costa AS, Mirzazade S, et al. Genotype-specific patterns of atrophy progression are more sensitive than clinical decline in SCA1, SCA3 and SCA6. Brain 2013;136(Pt 3):905–917.

Supporting Data

Additional Supporting Information may be found in the online version of this article at the publisher's web-site.

SGML and CITI Use Only
DO NOT PRINT

Authors' Roles

1) Research project: 1A. Conception, 1B. Organization, 1C. Execution; 1D. Patient recruitment.
2) Statistical Analysis: 2A. Design, 2B. Execution, 2C. Review and Critique;
3) Manuscript: 3A. Writing of the first draft, 3B. Review and Critique.
J.F.: 1A, 1B, 1C, 1D, 2A, 2B, 2C, 3A.
T.S.: 2A, 2B.
K.B.: 1C.
K.R.: 1D, 2C, 3B.
M.C.F. Jr: 1D, 2C, 3B.
T.JR.R.: 1D, 2C, 3B.
J.H.: 1D, 2C, 3B.
W.L.: 1D, 2C, 3B.
B.v.W.: 1D, 2C, 3B.
J.v.G. 1D, 2C, 3B.
A.D.: 1D, 2C, 3B.
F.M.: 1D, 2C, 3B.
P.G.: 1D, 2C, 3B.
H.G.-M.: 1D, 2C, 3B.
L.S.: EU: 1D, 2C, 3B.
H.H.: 1D, 2C, 3B.
M.S.: 1D, 2C, 3B.
B.B.: 1D, 2C, 3B.
G.O.: 1D, 2C, 3B.
J.J.: 1D, 2C, 3B.
J.J.d.V.: 1D, 2C, 3B.
J.-S.K.: 1D,
D.T.-B.: 1D, 2C, 3B.
H.J.: 1D, 2C, 3B.
J.I.: 1D, 2C, 3B.
R.J.: 1C, 2C, 3B.
S.R.: 1D, 2C, 3B.
J.D.: 1D, 2C, 3B.
M.S.: 2A 2C, 3B.
R.W.: 1C 2C, 3B.
T.K.: 1A, 1D, 2A, 2C, 3B.

Financial Disclosures of All Authors (for Preceding 12 Months)

J.F.: received funding from the National Ataxia Foundation and as a fellow of the Hertie Academy for Clinical Neuroscience.
T.S.: none.
K.B.: none.
K.R.: received grants from the German Federal Ministry of Education and Research (BMBF 01GQ1402, 01DN18022), the German Research Foundation (IRTG 2150), and Alzheimer Forschung Initiative e.V. (NL-18002CB) and honoraria for presentations or advisory boards from Biogen and Roche.
M.C.F. Jr: received research grants from PTC and Pfizer; took part in advisory boards for Biogen, Avexis and PTC.
T.JR.R.: none.

J.H.: none.

W.L.: none.

B.v.W.: Gossweiler Foundation, uniQure, ZonMW, Hersenstichting, Radboud University Medical Centre grants, Uniqure (consultancy).

J.v.G.: supported by an Edmond J. Safra movement disorders fellowship (Michael J. Fox Foundation).

A.D.: receiving grants from the National Institut of Health (RO1), French National Hospital Clinical Research Program (PHRC), Agence National de Recherche (ANR), Triplet Therapeutics, Biogen, Minoryx Therapeutics, Roche, and Verum; serves on the advisory boards of Triplet Therapeutics and Minoryx Therapeutics.

F.M.: none.

P.G.: none.

H.G.-M.: Medical Research Council (JPND grant), CureSCA3, and Fathers Foundation.

L.S.: EU — ERN-RND registry (grant 947588); E-rare/BMBF — Treat-Ion (grant 01GM1907A); E-rare/BMBF — TreatHSP (grant 01GM1905A); Innovationsfond — ZSE-DUO (grant 01NVF17031); Innovationsfond — Translate NAMSE (grant 01NVF16024).

H.H.: receives support from the intramural fortüne program of the Medical Faculty of the University of Tübingen (grant 2554-0-0).

M.S.: consultancy honoraria from Orphazyme Pharmaceuticals unrelated to this project.

B.B.: Cofounder and shareholder of AIRAmed GmbH.

G.O.: grants from National Institutes of Health, National Ataxia Foundation, Biogen, Inc.; consultancies for uniQure biopharma B.V., IXICO Technologies Limited.

J.J.: none.

J.J.d.V.: none.

J.-S.K.: none.

D.T.-B.: received funding from the Deutsche Forschungsgemeinschaft (DFG), DHAG, and Bernd Fink Foundation.

H.J.: none.

J.I.: honoraria as speaker from Zambon and Exeltys.

R.J.: Paid employee of IXICO Plc.

S.R.: none.

J.D.: none.

M. Schmid: none.

R.W.: employee and shareholder of IXICO. RW holds IP rights and has received royalties in relation to the LEAP technology.

T.K.: research support from the Deutsche Forschungsgemeinschaft (DFG), the Bundesministerium für Bildung und Forschung (BMBF), the Bundesministerium für Gesundheit (BMG), the Robert Bosch Foundation, the European Union (EU), and the National Institutes of Health (NIH); has received consulting fees from Biohaven, Roche, UBC, Uniqure, and Vico Therapeutics; has received speaker honoraria from Novartis and Bayer.

3.4. Faber J*, Kügler D*, Bahrami E*, Heinz LS, Timmann D, Ernst TM, Deike-Hofmann K, Klockgether T, van de Warrenburg B, van Gaalen J, Reetz K, Romanzetti S, Oz G, Joers JM, Diedrichsen J; ESMI MRI Study Group; Reuter M. CerebNet: A fast and reliable deep-learning pipeline for detailed cerebellum sub-segmentation. Neuroimage. 2022; 264:119703.

Zielsetzung der Arbeit – Zielsetzung der Arbeit war es, ein Verfahren zur automatisierten Subsegmentierung des Kleinhirns auf T1-gewichteten MRTs zu etablieren, da die manuelle Segmentierung von anatomischen Strukturen zeitaufwendig ist und keine realistische Option für die Analyse von größeren Kohortendaten darstellt. Insbesondere sollte das resultierende Verfahren besser als die bisher verfügbaren automatisierten Verfahren die Verästelung der weißen Substanz abbilden.

Methoden und Ergebnisse – Zunächst wurde ein Manual zur standardisierten manuellen Segmentierung etabliert (Faber, Heinz et al. 2022) um die Reproduzierbarkeit der manuell erstellten Segmentierungen zu gewährleisten. Es wurden 27 disjunkte anatomische Segmente des Kleinhirns definiert: 20 hemisphärische Lobuli (Lobuli I-IV, Lobuli V, VI, Crus I, Crus II, Crus VIIB, VIIIA, VIIIB, I, X je rechts- und linkshemisphärisch) sowie fünf Vermis-Segmente (korrespondierend zu den hemisphärischen Lobuli Vermis-VI, -VII, -VIII, -IX, X) und je eine links- und eine rechtshemisphärische Segmentierung der weißen Substanz des Kleinhirns. Dem Manual folgend wurden insgesamt 30 T1-gewichtete MRT-Aufnahmen in einer 1mm isotropen Auflösung von Gesunden sowie SCA3 Mutationsträgern von zwei Personen manuell segmentiert. Anschließend erfolgte einen Konsensus-Rating unter Einschluss von neurologischer und neuroradiologischer Expertise. Die hier festgelegten Konsensus-Segmentierungen stellten schließlich den Goldstandard für Training, Validierung und Testung dar. Die resultierende automatisierte Segmentierungsanwendung basiert auf einem bereits etablierten UNet-basierten 2,5D Segmentierungsnetzwerk. Es erfolgte ein Vor-Training mit verschiedenen Augmentationen. Die finale Anwendung, CerebNet, zeigte eine bessere Performance in allen üblichen quantitativen Parametern zur Beurteilung der Exaktheit (Dice, Hausdorff-Abstand, Volumenähnlichkeit) im Vergleich zu den aktuellen state-of-the-art Methoden. Darüber hinaus zeigt es eine hohe Test-Retest-Zuverlässigkeit sowie eine hohe Empfindlichkeit in der Diskrimination für subtile Veränderungen des prä-

ataktischen Stadiums der SCA3. Auf einem Consumer-GPU benötigt die zerebelläre Subsegmentieurng nur wenige Sekunden.

Schlussfolgerungen – Die etablierte automatisierte Segmentierungsanwendung, CerebNet, ist mit gebräuchlichen Methoden zur Großhirnsegmentierung, wie etwa FreeSurfer und FastSurfer, kompatibel und erstellt eine automatisierte Subsegmentierung des Kleinhirns in insgesamt 27 disjunkte anatomische Strukturen unter Einschluss der Verästelung der weißen Substanz. In allen üblichen Kriterien zur Beurteilung der räumlichen Exaktheit war CerebNet etablierten Methoden überlegen. CerebNet bietet eine effiziente und validierte Möglichkeit für die Bewertung von Kleinhirnsubstruktur-Volumina in großen Kohortenstudien, die keine manuelle Segmentierung erlauben.

NeuroImage 264 (2022) 119703

Contents lists available at ScienceDirect

NeuroImage

journal homepage: www.elsevier.com/locate/neuroimage

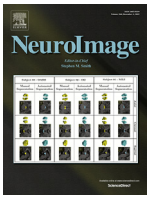

CerebNet: A fast and reliable deep-learning pipeline for detailed cerebellum sub-segmentation

Jennifer Faber[a,c,1], David Kügler[a,1], Emad Bahrami[a,b,1], Lea-Sophie Heinz[a], Dagmar Timmann[d], Thomas M. Ernst[d], Katerina Deike-Hofmann[e], Thomas Klockgether[a,c], Bart van de Warrenburg[f], Judith van Gaalen[f], Kathrin Reetz[g,h], Sandro Romanzetti[g], Gulin Oz[i], James M. Joers[i], Jorn Diedrichsen[j], ESMI MRI Study Group[2], Martin Reuter[a,k,l,*]

[a] *German Center for Neurodegenerative Diseases (DZNE), Bonn, Germany*
[b] *Computer Science Department, University Bonn, Bonn, Germany*
[c] *Department of Neurology, University Hospital Bonn, Germany*
[d] *Department of Neurology, Center for Translational Neuro, and Behavioral Sciences (C-TNBS), University Hospital Essen, University of Duisburg-Essen, Essen, Germany*
[e] *Department of Neuroradiology, University Hospital Bonn, Germany*
[f] *Department of Neurology, Donders Institute for Brain, Cognition, and Behaviour, Radboud university medical center, Nijmegen, The Netherlands*
[g] *Department of Neurology, RWTH Aachen University, Germany*
[h] *JARA-Brain Institute Molecular Neuroscience and Neuroimaging, Forschungszentrum Jülich, Germany*
[i] *Center for Magnetic Resonance Research, Department of Radiology, University of Minnesota, Minneapolis, MN, USA*
[j] *Departments of Computer Science and Statistical and Actuarial Sciences, Western University, London, ON, Canada*
[k] *A.A. Martinos Center for Biomedical Imaging, Massachusetts General Hospital, Boston, MA, USA*
[l] *Department of Radiology, Harvard Medical School, Boston, MA, USA*

ARTICLE INFO

2020 MSC:
00-01
99-00

Keywords:
CerebNet
Cerebellum
Computational neuroimaging
Deep learning

ABSTRACT

Quantifying the volume of the cerebellum and its lobes is of profound interest in various neurodegenerative and acquired diseases. Especially for the most common spinocerebellar ataxias (SCA), for which the first antisense oligonculeotide-base gene silencing trial has recently started, there is an urgent need for quantitative, sensitive imaging markers at pre-symptomatic stages for stratification and treatment assessment. This work introduces *CerebNet*, a fully automated, extensively validated, deep learning method for the lobular segmentation of the cerebellum, including the separation of gray and white matter. For training, validation, and testing, T1-weighted images from 30 participants were manually annotated into cerebellar lobules and vermal sub-segments, as well as cerebellar white matter. *CerebNet* combines *FastSurferCNN*, a UNet-based 2.5D segmentation network, with extensive data augmentation, e.g. realistic non-linear deformations to increase the anatomical variety, eliminating additional preprocessing steps, such as spatial normalization or bias field correction. *CerebNet* demonstrates a high accuracy (on average 0.87 Dice and 1.742mm Robust Hausdorff Distance across all structures) outperforming state-of-the-art approaches. Furthermore, it shows high test-retest reliability (average ICC > 0.97 on OASIS and Kirby) as well as high sensitivity to disease effects, including the pre-ataxic stage of spinocerebellar ataxia type 3 (SCA3). *CerebNet* is compatible with *FreeSurfer* and *FastSurfer* and can analyze a 3D volume within seconds on a consumer GPU in an end-to-end fashion, thus providing an efficient and validated solution for assessing cerebellum sub-structure volumes. We make *CerebNet* available as source-code (https://github.com/Deep-MI/FastSurfer).

* Corresponding author.
E-mail address: martin.reuter@dzne.de (M. Reuter).

[1] Contributed equally.

[2] *ESMI MR Study Group:* Paola Giunti (Ataxia Centre, Department of Clinical and Movement Neurosciences, UCL Queen Square Institute of Neurology & National Hospital for Neurology and Neurosurgery, University College London Hospitals NHS Foundation Trust, London, UK), Hector Garcia-Moreno (Ataxia Centre, Department of Clinical and Movement Neurosciences, UCL Queen Square Institute of Neurology & National Hospital for Neurology and Neurosurgery, University College London Hospitals NHS Foundation Trust, London, UK), Heike Jacobi (Department of Neurology, University Hospital of Heidelberg, Heidelberg, Germany), Johann Jende (Department of Neuroradiology, Heidelberg University Hospital, Heidelberg, Germany), Jeroen de Vries (Department of Neurology, Expertise Center Movement Disorders Groningen, University Medical Center Groningen, University of Groningen, The Netherlands), Michal Povazan (Johns Hopkins University School of Medicine, Baltimore, MD, U.S.), Peter B. Barker (Johns Hopkins University School of Medicine, Baltimore, MD, U.S.), Katherina Marie Steiner (Department of Neurology, Center for Translational Neuro, and Behavioral Sciences (C-TNBS), University Hospital Essen, University of Duisburg-Essen, Essen, Germany), Janna Krahe (Department of Neurology, RWTH Aachen University, Germany).

https://doi.org/10.1016/j.neuroimage.2022.119703.
Received 12 September 2022; Accepted 18 October 2022
Available online 27 October 2022.

1. Introduction

For decades, the cerebellum was attributed to have an exclusive role in motor control. Recently, growing evidence suggests a more general involvement of the cerebellum in the adaptive control also of cognitive and emotional processing. In fact, morphometric studies demonstrate significant cerebellar atrophy with age and in a number of non-motor brain diseases, e.g. schizophrenia, autism or Alzheimer's disease (Diedrichsen et al., 2015; D'Mello et al., 2015; Han et al., 2020a; Lin et al., 2020; Marek et al., 2018; Okugawa et al., 2003; Toniolo et al., 2018; Webb et al., 2009; Womer et al., 2016). In healthy humans, the representation of cerebral networks and cognitive domains has been investigated using functional connectivity (Buckner et al., 2011) as well as task functional MRI (King et al., 2019). These complementary studies have helped to increase knowledge about the role of the cerebellum in cognitive and emotional processes. This notwithstanding, the cerebellum is crucial for motor control, in particular metric and power of target movements. With regard to movement disorders, cerebellar atrophy is the characterizing feature in ataxias, which manifest as acquired, genetic, or sporadic degenerative diseases. With clinical features including progressive loss of balance, coordination deficits, and slurred speech, ataxia patients suffer substantial restrictions of mobility and communicative skills. In genetic ataxies, such as the worldwide most common autosomal dominantly inherited spinocerebellar ataxia type 3 (SCA3), the manifest or ataxic stage of the disease is preceded by a pre-ataxic stage, in which neurodegeneration is already quantifiable, e.g., as cerebellar atrophy, while manifest ataxia is not yet present (Faber et al., 2021; Kim et al., 2021; Rezende et al., 2018). Preventive interventions that aim to silence the disease gene in pre-ataxic mutation carriers offer a promising treatment option prior to clinical onset (McLoughlin et al., 2018). Now, that the first clinical gene silencing trial has recently started (ClinicalTrials.gov Identifier: NCT05160558), there is an urgent need for non-invasive biomarkers to assess disease manifestation and progression, and to quantify potential treatment effects as clinical scales lack sensitivity during the pre-ataxic stage. Accurate cerebellar volume estimation from structural MRI is a relevant neuroanatomical marker. However, fast automated determination of cerebellar volumes is required, as detailed, manual volumetry, especially of sub-regions, is too time-consuming. Clearly, automated segmentation will benefit various study designs, by reducing workload and by improving reliability.

In the present work, we introduce *CerebNet*, an automated method to sub-segment the cerebellum at the lobular level based on T1-weighted MRI. Our labels focus on a detailed boundary delineation between cerebellar gray matter (CGM) and cerebellar white matter (CWM) capturing the branches of CWM that reach into the cerebellar cortex based on T1-weighted MRI. Our deep learning method leverages the *FastSurfer* approach (Henschel et al., 2020) of multiple 2D networks and minimal pre-processing to obtain detailed boundary segmentations. Since *CerebNet* does not require any preprocessing steps and performs the localization and segmentation of 27 cerebellar regions in only 12 seconds per MRI, it is optimally suited to also efficiently process and screen in large data sets. With very labor-intensive manual reference segmentation, the methodological challenge is to achieve high accuracy and generalizability despite a small reference dataset. To this effect, we perform extensive pre-training on representative cross-study datasets and apply several data augmentation steps including realistic non-linear deformations to ensure wide applicability. Moreover, we validate our method with respect to test-retest reliability and in an association study of neuro-morphometric cerebellum markers across 109 SCA3 mutation carriers, including 42 pre-ataxic participants, as well as 41 healthy controls. Results reveal stronger group differences for *CerebNet* consistent with known patterns of neurodegenerative changes.

1.1. Protocols and anatomical reference

The Schmahmann atlas (Schmahmann et al., 1999) is the standard anatomical reference for cerebellar cortex sub-segmentation protocols (Bogovic et al., 2013b; Park et al., 2014) including the "Spatially Unbiased Infratentorial Template" (SUIT) (Diedrichsen, 2006). It introduces a unified terminology of the nomenclature. Slices of the cerebellum are directly compared with the corresponding slices of MR images, thus facilitating the identification of anatomical landmarks. Briefly summarized, the CGM is macroscopically subdivided into the midline vermis and four hemispheric lobes: the anterior, posterior-superior, posterior-inferior, and the flocculonodular lobe. The anterior and posterior lobes are further subdivided into lobules. The vermis is subdivided analogously to the hemispheres except for the anterior lobe. Like all previous protocols, ours follows the nomenclature introduced by Schmahmann (Schmahmann et al., 1999) and our segmentation is largely comparable to previous protocols (Bogovic et al., 2013b; Diedrichsen, 2006; Park et al., 2014). The protocols for segmenting the cerebellum on MR images differ in the level of detail at which single anterior lobules and vermal subsegments are distinguished or aggregated (Bogovic et al., 2013b; Diedrichsen, 2006; Park et al., 2014). Previous work has largely only differed in finding an aggregation compromise in the level of detail for segments I-V. We detail a comparison between the different segmentation protocols as well as to related automated segmentation procedures in the appendix of our protocol for manual segmentation(Heinz et al., 2022). It should be noted, that all previous protocols ignore the CWM strands projecting into the cerebellar cortex (Bogovic et al., 2013b; Diedrichsen, 2006; Park et al., 2014) simplifying the CGM/CWM boundary to a connection line across the base of CWM strands. In consequence, details at the CGM/CWM boundary of the cerebellum are not captured by any of the previous protocols. To allow deeper analysis of the GM/WM boundary in the cerebellum, we extend our protocol by a fine-grained segmentation of CWM strands projecting into the cerebellar cortex. To foster reproducibility and extensibility, we establish and publish our illustrated segmentation protocol online with this publication (Heinz et al., 2022).

1.2. Automated methods for cerebellar sub-segmentation

Several methods have been presented for segmenting cerebellar substructures including both semi-automated (Pierson et al., 2002) and fully automated (Bogovic et al., 2013c; Carass et al., 2018; Diedrichsen, 2006; Han et al., 2020b) approaches. While previous methods relied on atlas-based registration (Diedrichsen, 2006; Diedrichsen et al., 2009; Park et al., 2014; Plassard et al., 2016; Romero et al., 2017), artificial neural networks (Powell et al., 2008), support vector machines (Powell et al., 2008), level sets (Bogovic et al., 2013a), active appearance models (Price et al., 2014), and patch matching (Romero et al., 2017; Weier et al., 2014), recent work introduced deep learning (Han et al., 2020b; 2019).

The reference method "Spatially Unbiased Infra-tentorial Template" (SUIT) (Diedrichsen, 2006) pioneered fully automatic cerebellum sub-segmentation using non-linear registration to an atlas. Powell et al. (2008) compared atlas registration with fully connected neural network and support vector machine segmentation methods, and demonstrated superior performance of learning approaches. ACCLAIM (Bogovic et al., 2013a), which is based on the Multiple object Geometric Deformable Model framework (Bogovic et al., 2013c; Carass and Prince, 2016), adapts a random forest for boundary classification to produce topologically correct results. The Multiple Automatically Generated Templates brain segmentation algorithm (MAGeT) (Chakravarty et al., 2013; Park et al., 2014) creates a template library, then nonlinearly registers the target image to each template. The final segmentation is achieved by fusing multiple segmentations using majority voting. The Cerebellar Analysis Toolkit (CATK) (Price et al., 2014) adapts

Bayesian active appearance modeling (Patenaude et al., 2011) to generate statistical models for shape and texture and their inter-relationship as priors. RASCAL (Weier et al., 2014) utilizes a patch matching-based approach, which improves the multi-atlas segmentation fusion method of Coupe et al. (Coupé et al., 2011) via majority voting for label fusion and nonlinear registration. CERES (Romero et al., 2017), another patch matching-based segmentation tool, employs the Optimized PatchMatch Label fusion (OPAL) method (Giraud et al., 2016; Ta et al., 2014). CERES2 (Carass et al., 2018) improves upon CERES (Romero et al., 2017) by adding a patch-based boosted neural network method for error correction. CGCUTS (Yang et al., 2016) combines multi-atlas labeling and random forest classification in the context of a graph cut framework to produce the segmentation. Van der Lijn et al. (van der Lijn et al., 2009) present a method that combines an appearance model and atlas registration. Carass et al. (Carass et al., 2018) summarize and compare several cerebellum sub-segmentation methods, highlighting CERES2 (Carass et al., 2018; Romero et al., 2017) as the most performant 'traditional' (i.e. non deep-learning) approach. However, while image processing with CERES1 is supported online, CERES2 is unavailable to the scientific community.

The most recent cerebellum sub-segmentation tool, Anatomical Parcellation using a U-Net with Locally Constrained Optimization (ACAPULCO) (Han et al., 2020b), introduces a two-step deep learning method with two 3D convolutional neural networks (CNNs) to first localize and then sub-segment the cerebellum, outperforming the challenge winner CERES2 (Carass et al., 2018) in a head-to-head comparison. Preprocessing steps include bias field inhomogeneity correction and registration to MNI space. However, both the training and the evaluation procedure include some short-comings, e.g. by forcing nearest neighbor label interpolation both during training and evaluation, predominantly reducing detail in fine structures such as thin CWM strands. In fact, reported performance metrics were calculated entirely in MNI space, which required lossy nearest neighbor interpolation of manual reference labels to MNI space potentially mischaracterizing segmentation performance.

In contrast to ACAPULCO, our method does not require any preprocessing steps such as bias field correction or spatial (atlas) normalization/registration during inference. Moreover, to increase the anatomical variety in our training data, we employ various augmentation approaches, e.g. we generate realistic non-linear deformations via cross-subject registration of training images to various images from multiple datasets. To further improve the generalization of our model we pretrain the model on a compiled cross-study dataset. We examine the effect of data augmentations such as non-linear deformation and pre-training in several experiments. In our proposed method, the neural network architecture follows *FastSurferCNN*, a 2.5D approach in which three 2D networks for each axial, coronal, and sagittal view are trained and the final 3D prediction is created by view-aggregation (Henschel et al., 2020).

1.3. Contributions

This work presents five contributions:

- A detailed labeling protocol ensuring replicability and extensibility for the 25 cerebellar cortex labels and 2 cerebellar white matter segmentations including the fine branching, as well as a manual reference dataset of consensus cerebellar subsegmentation labels for training and testing.
- A training methodology with extensive data augmentation including realistic deformations to address the challenge of a small training dataset.
- Detailed method ablation to establish design choices in dedicated experiments on a subset of cases, not overlapping with the training or test sets.
- *CerebNet* consistently and significantly outperforms state-of-the-art cerebellum sub-segmentation methods with respect to accuracy and test-retest reliability.
- Sensitive *CerebNet* segmentations reproduce cerebellar atrophy effects in the pre-ataxic stage of spinocerebellar ataxia type 3 with a superior group separability.

2. Methods

We first describe the datasets for training, validation, and testing of *CerebNet*, then continue with the description of our method, and finally detail the evaluation.

2.1. Datasets

2.1.1. CerebNet dataset

We assemble a diverse cerebellum sub-segmentation dataset for training, validation and testing of models based on acquisitions from ongoing observational studies. This superset includes participants equally distributed between healthy controls as well as pre-ataxic and ataxic SCA3 mutation carriers, thereby covering a broad range of different degrees of cerebellar atrophy.

Participants 32 T1-weighted MRI of SCA3 mutation carriers and healthy controls were acquired at 4 sites: Bonn and Aachen, Germany, Nijmegen, The Netherlands and Minneapolis, MN, US. All participants provided written informed consent according to the guidelines set by the local institutional review boards. Two cases with visible motion artifacts were excluded, resulting in the final CerebNet dataset of 20 SCA3 mutation carriers, covering the whole disease course of SCA3 from early pre-ataxic to late ataxic disease stages, and 10 healthy controls of the same age range. In Table 1, we report demographics (age, sex) and ataxia severity, assessed with the Scale for Assessment and Rating of Ataxia (SARA) (Schmitz-Hübsch et al., 2006) for the three groups. For SCA3 mutation carriers, we also report the CAG repeat length. To divide SCA3 mutation carriers into pre-ataxic (SARA < 3, $N = 11$) and ataxic individuals (SARA ≥ 3, $N = 9$), we follow the established SARA cut-off value of 3, corresponding to the mean plus 2 standard deviations of the healthy control group distribution from the original SARA validation study (Schmitz-Hübsch et al., 2006).

MRI scans All T1-weighted MRI were acquired as MPRAGE on 3T SIEMENS scanners (Siemens Medical Systems, Erlangen, Germany). All scans share an isotropic resolution of 1mm, FOV 256×256 and 192 slices, acquired in sagittal direction with a 32-channel head coil. Bonn ($N = 16$, Skyra), Minnesota ($N = 7$, Prisma Fit), and Aachen ($N = 4$, Prisma) acquired at TR = 2500ms, TE = 4.37ms, TI = 1100ms, FA = 7°, while Nijmegen ($N = 4$, Trio) acquired at TR = 2300ms, TE = 3.03ms, TI = 1100ms, FA = 8°.

Segmentation Protocol Following the Schmahmann atlas (Schmahmann et al., 1999) as anatomical reference, we define 27 disjoint macroscopic subsegments of the cerebellum. In addition to 20 hemispheric lobules (10 for each hemisphere), we include 5 vermis labels and two CWM labels (left and right). The cerebellar segmentation is divided into 6 hierarchical steps, gradually moving from large-scale structures to the subdivision of cerebellar lobules. First, we delineate the CGM cortex with an exact outer boundary separating CGM from cerebrospinal fluid and other subtentorial structures, such as cranial nerves (*Step 1*). In this step, any inwardly projecting CWM branches are ignored. Subsequently, the four lobes (*Step 2*), and the vermis (*Step 3*) are segmented. We conduct the sub-segmentation of the hemispheric lobules (*Step 4*) as well as the subdivision of the vermis (*Step 5*). Finally, the fine delineation of the CWM including its branches into the CGM cortex band and a consistent boundary towards the brainstem is drawn (*Step 6*). The detailed protocol is publicly available for reproducibility (Heinz et al., 2022).

Manual Reference Standard The correct subdivision of the cerebellar cortex into lobules is critical, since the cerebellum shows a high morphological variability of its anatomical structure (Fig. 1). At the isotropic resolution of 1mm, it remains challenging to precisely determine whether a single small folia or branch belongs to one or an adja-

Table 1
Demographic and characterizing data of the *CerebNet* data set cohort consisting of pre-ataxic and ataxic SCA3 mutation carriers as well as healthy controls (HC). [1]Time to onset is given in years. The reported time from onset (defined as the first occurrence of gait disturbances) is given where available and for the remaining seven pre-ataxic mutation carriers, not yet experiencing gait disturbances, we estimated the time to onset following the model introduced by Tezenas et al. [42], which depends on both the number of CAG RL as well as the actual age; SD = standard deviation, CAG RL = CAG repeat length of the longer allele.

Group	N	**age** [years] mean ± SD [range]	sex m/f	SARA mean ± SD [range]	**Time to ataxia onset**[1] mean ± SD [range]	CAG RL mean ± SD
HC	10	43.9 ± 13.22 [22; 63]	4/6	0.3 ± 0.54 [0; 1.5]	n.a.	n.a.
pre-ataxic SCA3	11	31.6 ± 7.1 [20; 43]	4/7	1.4 ± 0.8 [0; 2.5]	-4.5 ± 6.4 [-13.8; 8.0]	72.4 ± 3.1
ataxic SCA3	9	44.6 ± 7.3 [32; 57]	6/3	12.6 ± 4.5 [7; 19]	8.4 ± 5.4 [1.0; 8.0]	70.89 ± 4.11

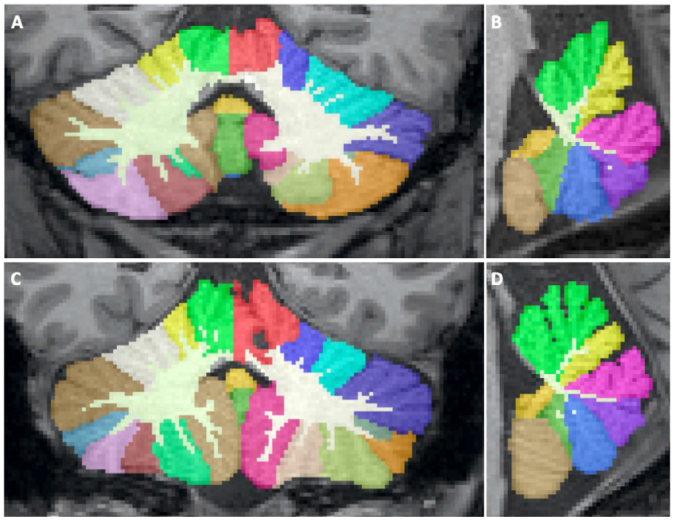

Fig. 1. Segmentation examples of a fully automated segmentation of *CerebNet* in a healthy control (A, B) as well as a symptomatic SCA3 patient (C, D) projected onto a coronal and sagittal slice.

cent lobule. To address this, all lobular boundaries within the cerebellar cortex (*Step 1-5*) are subsegmented by two experienced raters on all MRIs independently. To unify differences between the two raters, cortex segmentations are reviewed by an interdisciplinary team consisting of the experienced raters as well as a neurologist and a neuroradiologist. A consensus was reached for all cases. Furthermore, a team of four trained raters delineated the fine-grained CGM/CWM boundary (*Step 6*). The final consensus segmentation together with the CWM delineations represents the manual reference standard for training, validation, and testing of our method. We split the participants contained in the final reference dataset into 18/4/8 for training, validation, and testing. For individual splits, we preserve the distribution of controls, pre-ataxic and ataxic participants.

2.1.2. Cross-study pre-training dataset

For pre-training purposes, we compile a dataset of 160 T1-weighted images gathered from the Autism Brain Imaging Data Exchange II (ABIDE II) (Di Martino et al., 2017), the Alzheimers Disease Neuroimaging Initiative (ADNI) (Mueller et al., 2005), the UCLA Consortium for Neuropsychiatric Phenomics LA5c Study (LA5c) (Poldrack et al., 2016), the Open Access Series of Imaging Studies 1 and 2 (OASIS-1[3] (Marcus et al., 2007) and OASIS-2 (Marcus et al., 2010)), and the Minimal Interval Resonance Imaging in Alzheimers Disease (MIRIAD) (Malone et al., 2013). For these 160 cases, we automatically generate cerebellar sub-segmentation labels using SUIT v3.3 (Diedrichsen, 2006; Diedrichsen et al., 2009). SUIT is an atlas-based segmentation tool which provides segmentations of 28 sub-regions of the cerebellar cortex at the level of cerebellar lobules and a sub-segmentation of the vermis according to the Schmahmann atlas (Schmahmann et al., 1999). Since SUIT does not provide segmentations for CWM, we additionally process all 160 images with *FreeSurfer* (FS) (Fischl et al., 2002) and merge FS-generated CWM with the cerebellar sub-regions labels from SUIT. Gaps between cerebellar CWM and CGM are resolved by mapping them to the nearest CGM structure. The compiled external dataset is split into 140 training and 20 validation cases and is exclusively used for pre-training of our model.

2.1.3. Deformation dataset for augmentation

To increase variability of our training data, we generate realistic non-linear deformations for data augmentation. For this we generated an auxiliary dataset of 100 cases selected from ABIDE II (Di Martino et al., 2017), ADNI (Mueller et al., 2005), LA5c (Poldrack et al., 2016), OASIS-1[3] (Marcus et al., 2007) and OASIS-2 (Marcus et al., 2010), MIRIAD (Malone et al., 2013), and the Human Connectome Project (HCP) (Van Essen et al., 2012).

2.1.4. Test-retest dataset

We use the OASIS-1 (reliability subset) (Marcus et al., 2007) and Kirby (Landman et al., 2011) datasets for test-retest analysis. OASIS-1 contains 20 participants that were scanned no more than 90 days apart (all except 5 less than 30 days). The Kirby dataset consists of scan-rescan MPRAGE images of 21 healthy participants with one hour break between scanning sessions.

2.2. Cerebellar sub-segmentation method

This section introduces our cerebellar sub-segmentation pipeline, consisting of an initial localization step to extract the relevant cerebellum region, a subsequent multi-view ensemble for CNN-based segmentation, and a final view-aggregation step to merge the predictions. The pipeline accepts unprocessed 1.0mm T1-weighted images and outputs segmentation maps and tabulated volume reports. To achieve high accuracy, the relatively small size of the manual reference standard requires special consideration. We address it by pre-training with a representative cross-study dataset as well as applying data augmentation. Specifically, intensity and spatial data augmentation techniques such as realistic deformations increase the diversity presented to the network during training and, thus, its performance.

Localization To constrain the sub-segmentation network to the cerebellum and reduce memory and computational requirements, we crop a bounding box of $128 \times 128 \times 128$ isotropic 1mm voxels containing both cerebelli. The bounding box is placed symmetrically around the full cerebellar region obtained from a quick single-view (coronal) *FastSurfer* segmentation (Henschel et al., 2020). A visual inspection of this localization approach confirms the cerebellum is always correctly localized and fully contained within the bounding box in all cases.

Cerebellar Sub-segmentation Network The method for cerebellum sub-segmentation follows *FastSurfer* (Henschel et al., 2020). Briefly, in its

[3] Excluding cases from the OASIS-1 reliability section.

2.5D approach, *FastSurfer* utilizes an ensemble of three two-dimensional CNNs (*FastSurferCNN*) – each of these processing the MRI images sliced in a different direction (axial, coronal, and sagittal views). A final view-aggregation step combines the resulting label probability maps in probability space. *FastSurferCNN* is a U-Net-based fully CNN architecture with a dense encoder and decoder block per depth-level. In contrast to its predecessor (Guha Roy et al., 2019), the architecture extends the dense blocks and unpooling operations with a local competition approach (Estrada et al., 2018; 2020) and gathers information in the third dimension via spatial information aggregation (SPI). The SPI approach provides the network with a wider volumetric context by stacking additional three preceding and three succeeding neighboring slices for a total of 7 input channels. Both the view aggregation and the SPI approach together allow the method to process 3D information, while at the same time retaining the computational advantages of 2D networks, primarily lower memory requirements and sample efficiency, i.e. 1. a lower number of parameters compared to 3D networks and 2. 3D MRI are split into slices increasing the number of samples presented to the network.

Spatial Augmentations Spatial augmentations such as flipping, translation, rotation, and scaling were used during training to improve the robustness of our model. We encode these transformation as a 3×3 in-slice transformation matrix in homogeneous coordinates with coefficients uniformly sampled from predefined ranges. Random offsets along the in-slice-axes for translation are selected from -12 to 12mm to simulate cerebellum centroid variation. We sample the scaling factor from 0.95 to 1.2. The image is rotated in-slice with respect to its center with angles uniformly sampled from -20° to 20°. We also apply a random left-right flip, i.e., both the image and its labels are mirrored, but label IDs are swapped with respect to the mid-plane separating the two hemispheres keeping left-labels on the left.

Augmentation with non-linear Deformation To increase variability of our training data, we perform static augmentation with 500 non-linearly deformed training images. For this, we first non-linearly register each image of the Deformation (see Section 2.1.3) to 5 randomly selected images from the training split of the CerebNet dataset (see Section 2.1.1) using ANTs v2.3.1 (Avants et al., 2008). We ensure each manually labeled *CerebNet* case is at least paired once. For each of the resulting 500 anatomically realistic deformation fields, we then map both image and manual label from the training split of the CerebNet dataset using the obtained deformation field. In effect, this procedure drastically increases the anatomical variance presented to the network during training.

Intensity Augmentations Random MRI magnetic field inhomogeneities are synthesized and linearly superimposed to the images to increase the robustness of the model to bias field artifacts. We generate the augmented inhomogeneity field by linear-combination of randomly weighted cubic polynomial basis functions (Van Leemput et al., 1999). The coefficients of the basis functions are uniformly sampled from a -0.5 to 0.5 range.

2.3. Metrics for evaluation

To establish the quality and accuracy of *CerebNet* with respect to volumetric and geometric features, we evaluate the resulting segmentations with three common segmentation metrics: The *Dice Score*, calculated as the general label overlap, is well established as a good compromise between volumetric and geometric segmentation properties; the *Hausdorff Distance* serves as a metric for geometric and spatial similarity, and finally the *Volume Similarity* completely ignores overlap and spatial distance, but most directly evaluates the reliability for volumetric measures commonly used in statistical modeling.

Dice Score The Dice score (Dice) (Dice, 1945; Sørensen and Julius, 1948), is one of the most frequently used metrics in validating semantic segmentations. If P and G are the segmentation maps of the network prediction and ground-truth respectively, then Dice is defined as:

$$\text{Dice} = 2 \times \frac{|G \cap P|}{|G| + |P|}, \tag{1}$$

where $|.|$ represents cardinality. It measures overlap of 3D volumes on a scale between 0 and 1, where a value of 1 indicates exact agreement and 0 disjoint segmentations.

Hausdorff Distance To evaluate the quality of segmentation boundaries we calculate the distance between the manual and the automatic segmentation boundaries. In particular, this distance metric allows to test the overall accuracy of the boundary delineation emphasizing the correct contour. As this distance-metric decreases, segmentation boundaries more closely correspond to each other locally, i.e. more agreement of geometric details. Boundary distances can be quantified by the standard Hausdorff Distance (HD) or the Robust Hausdorff Distance (HD95). The standard HD measures the maximum distance and therefore is strongly affected by local outliers. HD95 – the 95% percentile of distances between surfaces (Huttenlocher et al., 1993) – is less sensitive to outliers and consequently more informative when analyzing the general trend. Formally, for boundaries B_G (of the ground-truth label map G) and B_P (of its predicted correspondent), we use their distances $D_{G \leftrightarrow P} = \{\min_{g \in B_G} \; d(p, g) \mid \forall p \in B_P\} \cap \{\min_{p \in B_P} \; d(p, g) \mid \forall g \in B_G\}$ to compute HD and HD95 as $d_{\text{HD}} = \max D_{G \leftrightarrow P}$ and $\text{P}(d < d_{\text{HD95}}) < 0.95$, $d \in D_{G \leftrightarrow P}$.

Volume Similarity Volume similarity (vol_{sim}) compares the absolute volume difference with the sum of volumes. Given V_G and V_P, the volumes of the ground-truth and predicted segmentations (G and P), vol_{sim} is calculated as

$$vol_{\text{sim}} = 1 - \frac{|V_G - V_P|}{V_G + V_P}. \tag{2}$$

Since this metric ignores overlap and geometric information, the optimal similarity (a value of 1) can be achieved for two segmentations of the same size, even if their spatial overlap is zero. However, its independence from spatial correspondence enables cross-acquisition comparison, e.g. for test-retest analysis, without requiring image alignment.

Intraclass Correlation Coefficient The Intraclass Correlation Coefficient (ICC) (Shrout and Fleiss, 1979) evaluates the reliability and agreement between measurements. Its values range from 0 to 1 with larger values representing higher reliability. We also compute the 95% confidence interval around the ICC. For test-retest scenarios, we calculate the ICC as a measure of agreement between two repeated scans of the same participant (relative agreement, single fixed rater). Since scans are acquired in close temporal proximity, we assume only little volumetric changes and thus a high ICC.

2.4. Implementation details

Here, we detail the training of *CerebNet* and our adaptations of state-of-the-art methods to establish compatibility with our labeling protocol.

CerebNet Training We train each network for axial, coronal, sagittal views independently for 70 epochs with a batch size of 128 using one NVIDIA Tesla V100 GPU with 32 GB RAM. We use the AdamW (Kingma and Ba, 2015; Loshchilov and Hutter, 2019) optimizer with a weight decay of 10^{-4} and an initial learning rate (LR) of 0.01. The *reduce on plateau* strategy for scheduling updates the LR based on the Dice score on the validation set. This strategy reduces the LR by a factor of 0.01, if there is no improvement in Dice score for 4 epochs.

ACAPULCO Re-Training In order to detach protocol and training data differences from method features, we retrain the deep learning method ACAPULCO (Han et al., 2020b) with our data following identical splits, hereafter referred to as ACAPULCO$^{\text{rt}}$. For this, we start with the published method code of ACAPULCO and configure the dataset loader to accept our dataset. Since we do not have access to the ACAPULCO training data, training our method on their data for comparison is not possible. We trained ACAPULCO with the publicly available source code and therein defined hyperparameters.

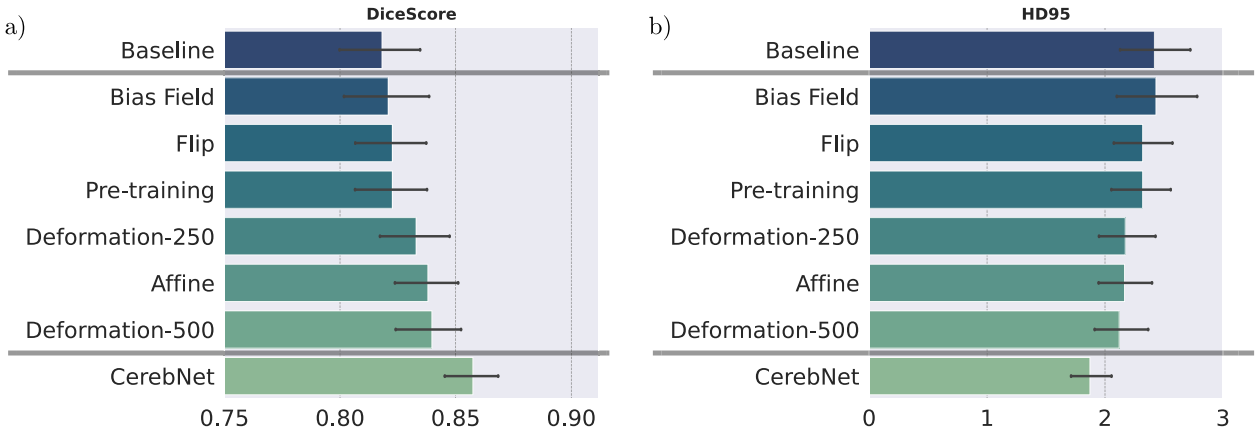

Fig. 2. Dice score (larger values are better) and Robust Hausdorff Distances (HD95, smaller values are better) on validation cases for comparison of baseline, individual method contributions (not cumulative) and *CerebNet*. *CerebNet* combines multiple data augmentations with pre-training on a representative cross-study dataset. Deformation-250/500 indicates the number of realistic deformation fields used for static augmentation. The baseline model is our network without augmentation or pre-training. Error bars indicate 95% confidence intervals.

SUIT + FS The leading traditional method (Carass et al., 2018), SUIT (Diedrichsen et al., 2009) does not rely on a deep learning approach and is only compatible with the CerebNet labels after combination with *FreeSurfer* (Fischl et al., 2002). In analogy to Section 2.1.2, we therefore merge SUIT cerebellum sub-segmentation labels with *FreeSurfer*'s CWM segmentation (SUIT + FS) to obtain the full set of labels.

3. Results

We report detailed results for multiple experiments to assess the performance of *CerebNet*. First, we ablatively establish the configuration and parameters of *CerebNet* on a validation hold-out set. Second, keeping method parameters fixed from here on, we compare the average performance of *CerebNet* with the state-of-the-art using four volumetric and geometric metrics: the Dice Score, two Hausdorff distances, and volume similarity. We investigate regional performance differences of these methods for all cerebellar sub-structures. Third, we contextualize the accuracy of *CerebNet* with differences between raters. Fourth, we compare the test-retest reliability of *CerebNet* with the state-of-the-art method ACAPULCO (Han et al., 2020b). Finally, we validate whether *CerebNet* reproduces known group differences between pre-ataxic and ataxic patients and healthy controls.

3.1. Ablation experiments

We perform several experiments to determine, how different changes to the data augmentation impact the performance of our method. In specific, we isolate the individual effects of different data augmentation methods and pre-training. We assess random flipping (Flip), bias field, affine deformation, and realistic non-linear deformation (Deformation-N, we test $N = 250$ and $N = 500$ deformation fields). While the baseline foregoes all data augmentation and pre-training, *CerebNet* combines all data augmentations with pre-training. All individual contributions improve results over the baseline (Fig. 2) in both Dice and Robust Hausdorff Distance (HD95) evaluations. Finally, the combination of all contributions clearly improves the results over any individual approach. We exclusively evaluate on validation cases for this analysis to avoid data-leakage.

3.2. Comparison with the state-of-the-art

In a summary evaluation, we compare the overall performance of *CerebNet*, ACAPULCO^{rt} (Han et al., 2020b) and SUIT + FS (Diedrichsen, 2006; Fischl et al., 2002) on the test subset of the CerebNet dataset (Section 2.1.1). On average across all segmented structures, *CerebNet* achieves a 0.870 per-structure Dice score and a 1.742mm Robust Hausdorff distance, which is the 95% percentile of surface-to-surface distances. In comparison with both state-of-the-art approaches, *CerebNet* outperforms either approach significantly in all four metrics ($p < .01$, see Fig. 3): the Dice score, Hausdorff distance (HD), Robust Hausdorff Distance (HD95) and volume similarity.

Results for individual structures are very consistent across all four metrics. Therefore, we focus further analysis and discussion on the Dice score and the Robust Hausdorff Distance. Specifically, we favor the robust implementation, since its robustness to outliers better reflects the accuracy across the surface, yet the high margin of 95% ensures larger structures (like CWM strands) are captured. Additionally, conclusions and reported significance values (derived by a Wilcoxon signed-ranked test) are completely independent of the choice of Hausdorff metric.

Dice Score CerebNet surpasses a 0.75 Dice score for all 27 individual structures and exceeds 0.95 Dice for the joint CWM. In fact, the least performing structures (specifically lobes VIIb and VIIIa/b) are "thin structures" sharing predominantly hard to define boundaries with other gray matter regions. *CerebNet* outperforms ACAPULCO^{rt} in 22 of 27 individual structures. In 14 out of 27 structures the improvement is significant (10 times $p < .01$ and 4 times $p < .05$, Fig. 4). For regions, with better performance of ACAPULCO^{rt}, the difference is usually small and never significant. *CerebNet* also significantly improves over ACAPULCO^{rt} segmentations for both merged gray matter and merged vermis regions ($p < .01$, Fig. 4). In comparison to the traditional SUIT + FS method, *CerebNet* always achieves better Dice scores, which are also statistically significant for all but three sub-structures (Fig. 4).

Robust Hausdorff Distance (HD95) On average, *CerebNet* achieves a HD95 distance of 1.742mm improving substantially over ACAPULCO^{rt} by 0.779mm. Across different vermis regions, the Crus I and lobe X regions and the merged gray matter region, *CerebNet* even exceeds a 1.25mm threshold. Larger distances remain in the lobes, where hard to reproduce lobe-to-lobe boundaries dominate the evaluation. Across all 27 structures, *CerebNet* outperforms ACAPULCO^{rt} in 26 of 27 structures (significantly for 14 structures, 5 times $p < .01$, 9 times $p < .05$, Fig. 4). In fact, the large performance differences for the merged CWM and CGM (both $\gtrapprox 2mm$) clearly indicate the differences between methods (Fig. 4). Compared with SUIT + FS, *CerebNet* demonstrates a superior performance consistently.

To quantify the robustness of *CerebNet*, we perform an outlier analysis for the Dice and Robust Hausdorff results. All data points are within 2.5 standard deviations of the per class mean.

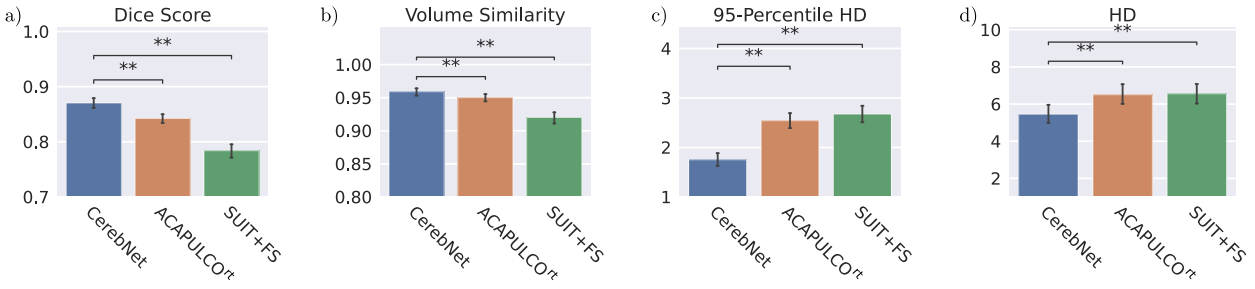

Fig. 3. Comparison of mean a) Dice score (larger values are better), b) Volume similarity (larger values are better), c) Robust Hausdorff Distance (HD95, smaller values are better), and d) Hausdorff Distance (HD, smaller values are better) over all structures and participants. *CerebNet* outperforms both ACAPULCO^{rt} (which is retrained on our dataset for direct comparison) and SUIT + FS. Error bars indicate 95% confidence intervals. Statistical significance for all results is confirmed by two-sided non-parametric Wilcoxon signed-rank tests (**: $p < .01$).

3.3. Inter-rater reproducibility

In our experience, delineation of cerebellar sub-structures, manual or automatic, is a challenging task due to the inherent uncertainty and lack of information to determine boundaries between cerebellar lobules even at 1mm isotropic resolution. To evaluate the *CerebNet* performance in the context of the reliability of manual segmentation, we analyze *CerebNet* segmentation errors together with the inter-rater variability. Figs. 4 and 5 share the same evaluation results for *CerebNet* in both cases comparing *CerebNet* predictions with the final "consensus segmentation" (after Step 6, see Section 2.1.1). However, for best annotation quality, labels from multiple raters are merged and harmonized in Step 6 of the protocol (see Section 2.1.1). To consistently and comparably represent the inter-rater reliability, we compare labels from one rater prior to this harmonization (after Step 5) to the "consensus". Since Step 5 data also does not include CWM labels, we exclude segmentation errors along the CGM/CWM boundary in the inter-rater evaluation (i.e. we mask out the CWM as defined in the "consensus") and only consider CGM regions for evaluation.

To evaluate the inter-rater variability, we utilize the Dice score and the Robust Hausdorff Distance (HD95). Fig. 5 illustrates per-region *CerebNet* and inter-rater Dice scores and HD95 on the *CerebNet* test set. Both volumetric and geometric segmentation scores are strongly correlated and – in most cases – at similar levels. Specifically, lower *CerebNet* performance values also map to lower inter-rater reliability in lobes V, VIIb and VIIIa/b. Results to lobe X as well as vermis VII/IX/X are outliers to this observation, where *CerebNet* provides good segmentations despite – in comparison – low inter-rater reliability.

3.4. Test-retest reliability

With the substantial time and labor requirements of manual segmentation, crucial external validation of methods is not easily possible. However, test-retest datasets with multiple scans of the same underlying anatomy and acquisition/machine properties offer the opportunity to test the reliability of methods. The OASIS-1 reliability dataset (Marcus et al., 2007) and Kirby dataset (Landman et al., 2011) are not only acquired at sites and in studies independent of the CerebNet dataset, but also feature 1.5T Siemens and 3T Philips scanners, respectively. To avoid influences of potentially error-prone image registration and interpolation, only per-structure volumes will be compared, as all geometric analysis would require alignment of baseline and follow-up scans.

Here, we compare the reliability of regional volumes with the intra-class correlation coefficient (ICC) and the volume differences derived from the two test-retest images. In Fig. 6, we plot the ICC values (and its 95% confidence interval) of *CerebNet* and ACAPULCO^{rt} for the two datasets. Statistical significance tests, however, are directly performed on volume differences using a Wilcoxon signed-rank test to compare the methods. The ICCs of *CerebNet* and ACAPULCO^{rt} range between 0.635 and 0.997 across both datasets with – in most cases – more consistent results (higher ICC) for *CerebNet*. In fact, the ICC is superior for *CerebNet* over ACAPULCO^{rt} in 24 of 27 sub-structures for the Kirby data and in 23 out of 27 sub-structures for the OASIS1 data set set as well as for the combined regions of the vermis and the left and right hemispheric CGM. This difference was significant in 17 (9) out of all 30 structures for the OASIS1 (Kirby) data set (only once in favor of ACAPULCO^{rt}, Fig. 6). In particular, *CerebNet* was more consistent as evidenced by much lower standard deviations and smaller 95% confidence intervals of the ICC for each sub-structure in comparison to ACAPULCO^{rt} (Fig. 6).

3.5. Volumetric changes in pre-ataxic and ataxic spinocerebellar ataxia type 3 (SCA3)

We analyzed the cerebellar volumes of 109 SCA3 mutation carriers and 41 healthy controls (HC), who are participants of ongoing observational studies and gave their written informed consent. MRI were acquired at 7 EU and 2 US sites. All T1-weighted images were acquired on 3T SIEMENS scanners (Siemens Medical Systems, Erlangen, Germany) with an isotropic resolution of 1mm. To establish generalizability of *CerebNet* to this dataset, we visually inspect a random subset of 5 cases per group (total $N = 15$) finding good segmentation quality with no outliers.

To investigate group differences between pre-ataxic and ataxic SCA3 as well as healthy controls, we used a linear mixed-effects model with the co-variables age and estimated total intracranial volume (eTIV) as well as group (pre-ataxic SCA3, ataxic SCA3 and HC) and sex as fixed and scanner as random factors, respectively. Ataxia severity was assessed with the Scale for Assessment and Rating of Ataxia (SARA) (Schmitz-Hübsch et al., 2006). We applied the common SARA cut-off value of 3 to divide the group of SCA3 mutation carriers into pre-ataxic (SARA < 3) and ataxic (SARA ≥ 3) individuals (Jacobi et al., 2020). The eTIV was assessed using *FreeSurfer* 6.0 (Buckner et al., 2004). Cerebellar volumes were compared between pre-ataxic SCA3 (N= 42, mean age 38.02 years, 62.91% female, mean SARA 1.25) and ataxic SCA3 (N= 67, mean age 49.94 years, 35.82% female, mean SARA 12.05) as well as healthy controls (N= 41, mean age 43.95, female 43.90%, mean SARA 0.27). In the post-hoc analyses of pairwise comparisons, we applied Bonferroni correction for multiple comparisons. P-values smaller than $p < .05$ after Bonferroni correction were considered significant.

For *CerebNet*-derived per-region volumes, pre-ataxic SCA3 mutation carriers already showed significant volume reduction in comparison to HC in the right lobules I-IV, left and right lobule X, vermis IX as well as the left and right CWM. We detected significant volume reduction of ataxic patients in comparison to pre-ataxic SCA3 mutation carriers in left and right lobule VI, Crus II, VIIb, VIIIa and left VIIIb, left and right X and the left and right CWM. These results reaffirm that cerebellar neurodegeneration already starts before the clinical onset of the

Fig. 4. Dice score (larger values are better) and Robust Hausdorff Distance (HD95) (smaller values are better) per sub-structure for *CerebNet*, ACAPULCO^{rt} and SUIT+FS. Illustrations show the cross-subject average of the metric (bar) and corresponding, bootstrapped 95% confidence intervals (error bars), data points (eight per bar, may overlap) as well as the significance level calculated by a Wilcoxon signed-rank test ($*$: $p < .05$ and $**$: $p < .01$). CGM: Cerebellar Gray Matter; CWM: Cerebellar White Matter.

disease and is ongoing throughout the disease course with a very early and continuous involvement of cerebellar white matter.

In Fig. 7, we evaluate the power of our neuro-morphometric measures to separate between different groups: HC and pre-ataxic SCA3 mutation carriers (top) as well as pre-ataxic SCA3 and ataxic SCA3 (bottom). While in a direct competition of methods, only *CerebNet* and the original ACAPULCO (Han et al., 2020b) are available publicly, we also include ACAPULCO^{rt} (which is retrained with our labels, see Section 2.4) to illustrate the impact of both our high-quality training data and its interaction with our segmentation pipeline. A clear difference between the methods is already apparent in the varying details of the highly significant CWM segmentations and its branches. Even ACAPULCO^{rt} does not achieve the degree of detail available in *CerebNet*, in spite of it using the same training data. While a direct comparison of p-values is usually not possible, here it is meaningful as the methods operate on exactly the same input images. This is because the p-values of the group effect are monotonically connected to the absolute value of the t-statistic (effect size divided by standard error). More significant effects, i.e. smaller p-values illustrated in Fig. 7 by more saturated colors, indicate better group separation. In the group comparison of pre-ataxic mutation carriers to HC, ACAPULCO showed unexpected, non-significant volume increases in two structures and ACAPULCO^{rt} in one structure (blue regions in Fig. 7). Comparing the p-values for group separation between pre-ataxic SCA3 mutation carriers and healthy controls, *Cereb-*

Fig. 5. Comparison of Inter-rater reliability and *CerebNet* by Dice score and Robust Hausdorff Distance (HD95) per sub-structure. Error bars indicate 95% confidence intervals. CGM is Cerebellar Gray Matter and CWM is Cerebellar White Matter (∗: $p < .05$ and ∗∗: $p < .01$).

Net showed smaller p-values in more structures than ACAPULCO (10 versus 4) as well as ACAPULCO^{rt} (9 versus 6). For the group separation between pre-ataxic and ataxic SCA3 mutation carriers, *CerebNet* showed smaller p-values in 15 structures compared to 6 for ACAPULCO and 13 compared to 11 for ACAPULCO^{rt}. Given that the true group differences for each sub-structure are unknown, these results cannot establish a final superiority, but they can assure that known and expected effects can be reliably detected and that this signal is recovered most strongly with *CerebNet*.

4. Discussion

Neuroanatomical volumetry is a promising imaging biomarker candidate to assess progressive neurodegeneration in clinical trials. The advantages are, first, that non-invasive T1-weighted MRI is widely available, second, that precise quantitative estimates can aid studies into disease progression even at early stages, and third, that these volume estimates permit assessing subtle changes to quantify atrophy rates in various disease stages and effects of potential interventions and disease modifying therapies. Especially quantitative estimates of cerebellar structures are highly relevant for studying ataxia, in particular for those ataxia disorders where clinical trials have already been initiated, such as SCA3. Therefore, with this work, we introduce a multi-stage protocol for reliable and repeatable cerebellum segmentation with carefully drawn and quality-assured boundaries, establish a manually segmented reference dataset, and develop and validate *CerebNet*, a fast and accurate method to automatically sub-segment the cerebellum into its lobules and the cerebellar WM from a T1-weighted MRI.

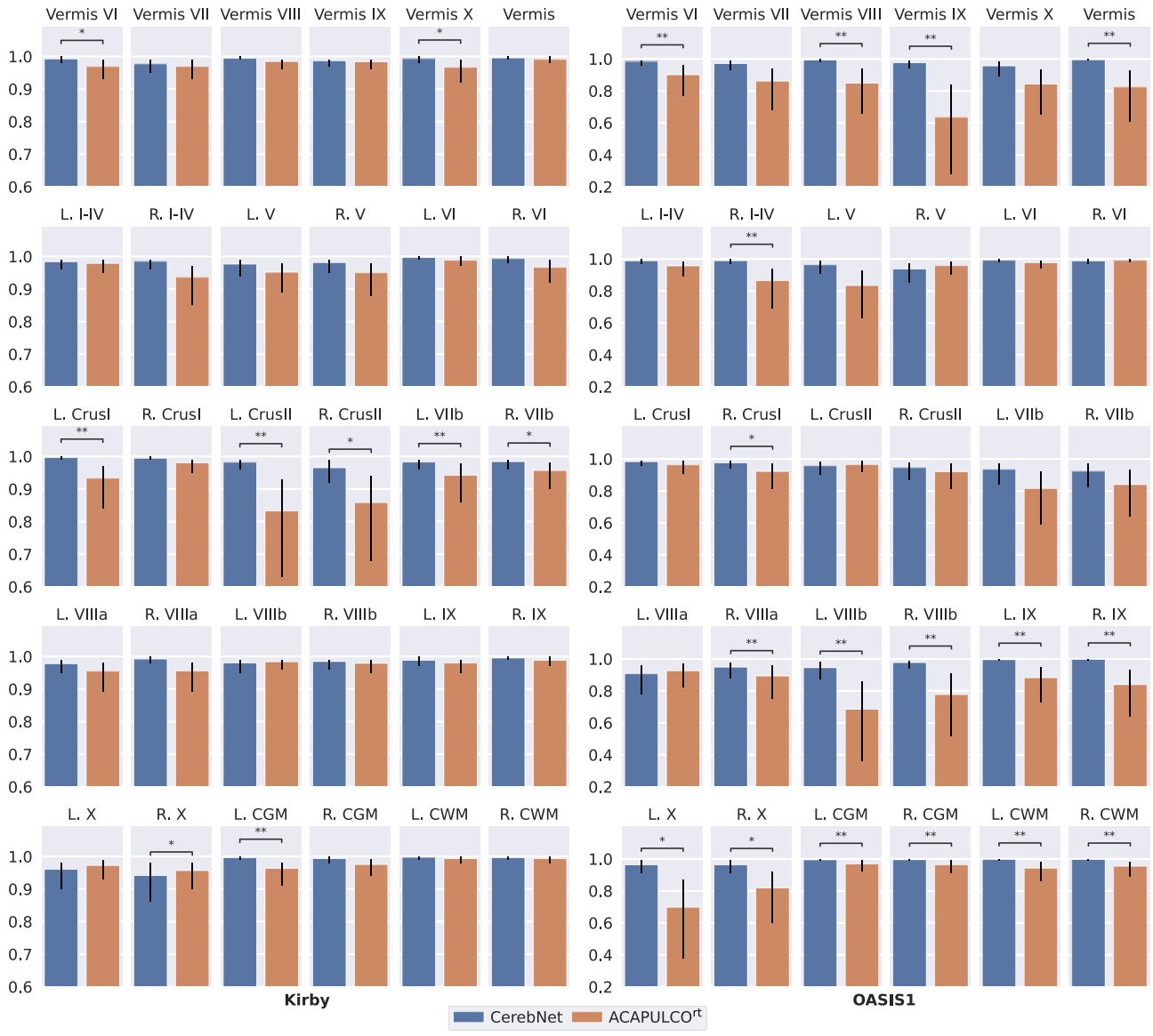

Fig. 6. Intraclass correlation coefficient (ICC) on volume of Kirby and OASIS1 datasets for test-retest analysis. Error bars indicate the 95% confidence interval. Statistical significance is calculated with a two-sided non-parametric Wilcoxon signed-rank test over the absolute volume difference, since ICC values cannot provide significance information. $*$ and $**$ annotations represent statistical significance for better volume consistency with $p < .05$ and $p < .01$, respectively.

Our method *CerebNet* employs a *FastSurferCNN* deep-learning model customized to our cerebellum training dataset. In contrast to state-of-the-art methods (Carass et al., 2018; Diedrichsen, 2006; Han et al., 2020b), *CerebNet* does not require any preprocessing, such as spatial normalization or bias field correction, thus preserving sufficient detail to segment even the fine branches of the white matter and simultaneously allowing rapid processing at only 12 seconds per MRI with one GPU (Nvidia Titan Xp). Fast MRI segmentation in general opens up multiple avenues of potential applications, ranging from direct feedback or field-of-view localization during image acquisition or fast clinical decision support by quantitative personalized measurements. In addition to speed, we demonstrate in an extensive validation that the *CerebNet* pipeline outperforms state-of-the-art approaches and provides detailed segmentation masks especially for white matter strands.

Our quantitative analysis illustrates *CerebNet*'s superior segmentation quality in both volumetric and geometric metrics. Furthermore, we demonstrate *CerebNet*'s superior test-retest reliability and show-case its utility to down-stream group analysis: While clinical scales lack sensitivity in pre-ataxic cases, simply due to the absence of symptoms, *CerebNet* reliably identifies patterns of cerebellar degeneration consistent with previous studies (Faber et al., 2020; Kim et al., 2021; Rezende et al., 2018). Consequently volumetric estimates of the cerebellum, especially subtle longitudinal changes, are promising imaging biomarker candidates to assess the effect of preventive genetic therapies during the pre-ataxic stage and might play a central role as stratification markers or even as secondary outcome parameters in clinical trials.

A qualitative inspection of the predicted segmentation maps illustrates the different character of the presented pipelines. *CerebNet*-derived segmentation maps feature the highest level of detail, especially visible at the intricate boundary between CWM and CGM (see Fig. 7). In fact, comparing predictions of *CerebNet*, ACAPULCO and ACAPULCO^{rt}[4], we find that the level of detail of ACAPULCO^{rt} lies between *CerebNet* and ACAPULCO (see Fig. 7), highlighting both the added value of our dataset with its manual segmentations (ACAPULCO^{rt} vs. ACAPULCO) and of our method (*CerebNet* vs. ACAPULCO^{rt}). In contrast to volu-

[4] Since the ACAPULCO training dataset is not available publicly, we cannot retrain *CerebNet* with this data.

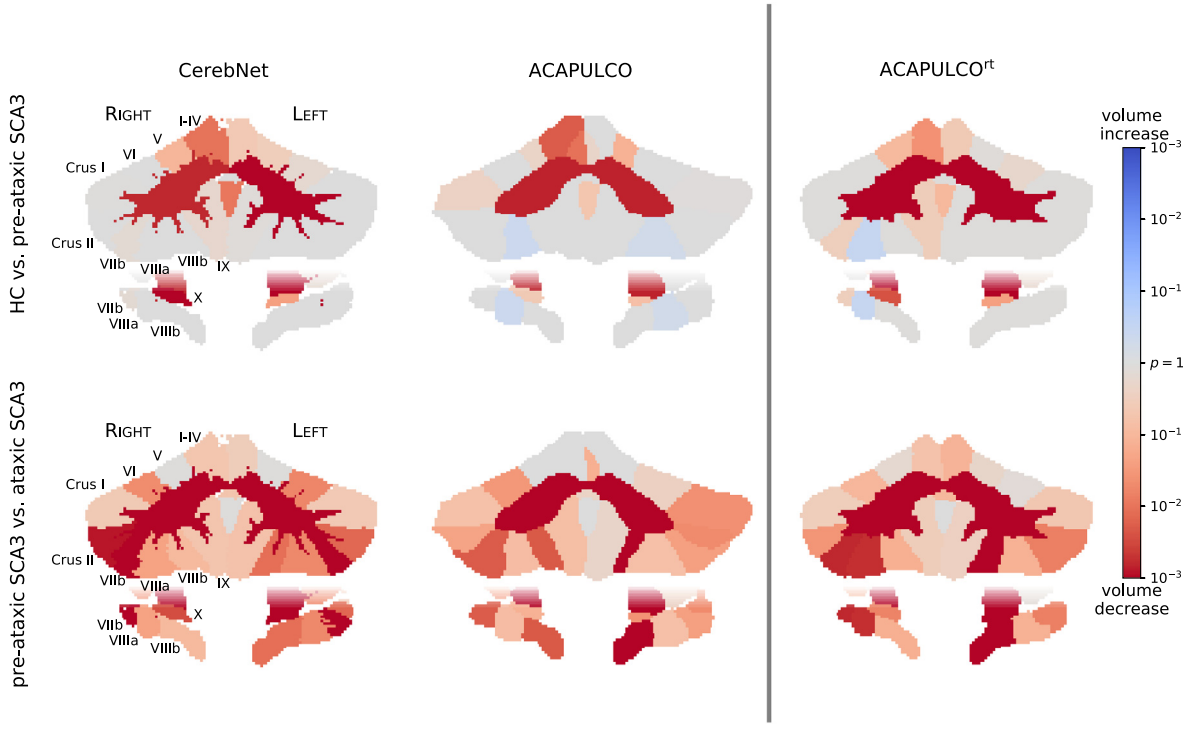

Fig. 7. Map of volume change in HC vs. pre-ataxic SCA3 (top) and pre-ataxic vs. ataxic SCA3 (bottom). Per-region p-values of the respective group comparisons are shown for 3 different methods: *CerebNet*, ACAPULCO (as distributed by Han et al., 2020b) and ACAPULCO^{rt} (ACAPULCO retrained on our dataset). Red colors indicate atrophy, blue colors indicate volume increase (color saturation corresponds to significance). (For interpretation of the references to colour in this figure legend, the reader is referred to the web version of this article.)

metric analyses, which are relatively robust to limited detail in segmentation maps, structural and geometric analyses, including thickness analysis, rely on accurate and detailed boundaries (Sörös et al., 2021). Because of the fine-grained furcations of CWM, the delineation of the CGM/CWM boundary is particularly challenging both for manual raters and automated methods. *CerebNet* especially improves these boundaries as proven by significantly improved Dice and Robust Hausdorff metrics over both ACAPULCO^{rt} and FreeSurfer (see L./R. CGM/CWM in Fig. 4).

In general, a critical limitation of learning-based approaches remains in the uncertain generalizability beyond images similar to those encountered during training. This limitation also applies to *CerebNet*. While our reference dataset features diversity in terms of severity of ataxia and cerebellar atrophy, the generalizability to other datasets is not guaranteed, since we only included T1w MRI of healthy controls and SCA3 mutation carriers acquired on SIEMENS scanners. Therefore, as for any method, dedicated experimental validation is required to confirm the validity under differing conditions, i.e. at least rigorous, manual quality checks of generated segmentations. Given the convincing test-retest performance (c.f. Fig. 6 Kirby dataset, which was acquired with Philips scanners), we are optimistic *CerebNet*'s extensive augmentation may already enable basic generalizability to other scan-settings. Furthermore, we visually inspected automatically generated segmentations of several clinically diagnosed sporadic and hereditary ataxias to verify whether *CerebNet* generalizes to other pathologies ($N = 14$: two randomly selected cases of MSA-C, RFC1, SCA1, SCA2 and SCA6, AOA2 as well as one case of SYNE1 and CTX each, including cases with severe atrophy, see also Fig. 9 in the Appendix). While not a formal validation for these pathologies, we found the segmentation quality among these cases comparable to our SCA3 cases without fails or unacceptable quality, further supporting the generalizability of *CerebNet*.

Obviously, volumetric analyses of other sporadic and hereditary neurodegenerative ataxias are canonical further research questions. Moreover, *CerebNet* may enable cerebellar analyses of aging, non-motor diseases (e.g. Alzheimer's disease or attention deficit hyperactivity disorder) and combined analyses of imaging and neuropsychological data. For these applications the focus may shift to parts of the cerebellum primarily involved in the adaptive control of non-motor processes. Since the functional representation of cognitive tasks is oriented across lobules along a parasagittal axis (King et al., 2019), the utility of segmentation along the anatomical boundaries of the hemispheric lobules is unclear for studies of the cerebellar involvement in cognitive and emotional processes.

In summary, *CerebNet* offers significant improvements and advantages for users in terms of runtime, accuracy, reliability and sensitivity to subtle cerebellar atrophy. Thus, we are confident, that *CerebNet* will enable and simplify the detailed morphometric analysis of the cerebellum.

Acknowledgments

We would like to thank Beate Brol, Tim Elter, Isabelle Finkel, and Sophia Wismeth for their contribution to the manual segmentation. This work was supported by the National Ataxia Foundations SCA Young Investigator Award as well as by DZNE institutional funds, by the Federal Ministry of Education and Research of Germany (031L0206, 01GQ1801), and by NIH (R01 LM012719, R01 AG064027, R56 MH121426, and P41 EB030006). JF is fellow of the Hertie Network of excellence in clinical Neuroscience. This publication is an outcome of ESMI, an EU Joint Programme - Neurodegenerative Disease Research (JPND) project (see www.jpnd.eu). The project is supported through the following funding organisations under the aegis of JPND: Germany, Federal Ministry of Education and Research (BMBF; funding codes 01ED1602A/B); Netherlands, The Netherlands Organisation for Health Research and Development; Portugal, Foundation for Science and Technology and Regional Fund for Science and Technology of the Azores; United Kingdom, Medical Research Council. This project has received funding from the European Unions Horizon 2020 research and innovation programme under grant agreement No 643417. For the

contribution of the Minnesota site, this work was in part supported by the National Ataxia Foundation and the National Institute of Neurological Disorders and Stroke (NINDS) grant R01NS080816. The Center for Magnetic Resonance Research is supported by the National Institute of Biomedical Imaging and Bioengineering (NIBIB) grant P41 EB027061, and the Institutional Center Cores for Advanced Neuroimaging award P30 NS076408 and S10OD017974 grant. Data used in the preparation of this article for pre-training and augmentation were obtained in part by the OASIS Cross-Sectional with principal investigators D. Marcus, R, Buckner, J, Csernansky J. Morris; P50 AG05681, P01 AG03991, P01 AG026276, R01 AG021910, P20 MH071616, U24 RR021382, and OASIS: Longitudinal: Principal Investigators: D. Marcus, R, Buckner, J. Csernansky, J. Morris; P50 AG05681, P01 AG03991, P01 AG026276, R01 AG021910, P20 MH071616, U24 RR021382. Further, data used in the preparation of this article were obtained from the MIRIAD database. The MIRIAD investigators did not participate in analysis or writing of this report. The MIRIAD dataset is made available through the support of the UK Alzheimer's Society (Grant RF116). The original data collection was funded through an unrestricted educational grant from GlaxoSmithKline (Grant 6GKC). Data used in preparation of this article were obtained from the Alzheimers Disease Neuroimaging Initiative (ADNI) database (adni.loni.usc.edu). As such, the investigators within the ADNI contributed to the design and implementation of ADNI and/or provided data but did not participate in analysis or writing of this report. A complete listing of ADNI investigators can be found at: http://adni.loni.usc.edu/wp-content/uploads/how_to_apply/ADNI_Acknowledgement_List.pdf. Data collection and sharing for this project was funded by the Alzheimer's Disease Neuroimaging Initiative (ADNI) (National Institutes of Health Grant U01 AG024904) and DOD ADNI (Department of Defense award number W81XWH-12-2-0012). ADNI is funded by the National Institute on Aging, the National Institute of Biomedical Imaging and Bioengineering, and through generous contributions from the following: AbbVie, Alzheimers Association; Alzheimers Drug Discovery Foundation; Araclon Biotech; BioClinica, Inc.; Biogen; Bristol-Myers Squibb Company; CereSpir, Inc.; Cogstate; Eisai Inc.; Elan Pharmaceuticals, Inc.; Eli Lilly and Company; EuroImmun; F. Hoffmann-La Roche Ltd and its affiliated company Genentech, Inc.; Fujirebio; GE Healthcare; IXICO Ltd.; Janssen Alzheimer Immunotherapy Research & Development, LLC.; Johnson & Johnson Pharmaceutical Research & Development LLC.; Lumosity; Lundbeck; Merck & Co., Inc.; Meso Scale Diagnostics, LLC.; NeuroRx Research; Neurotrack Technologies; Novartis Pharmaceuticals Corporation; Pfizer Inc.; Piramal Imaging; Servier; Takeda Pharmaceutical Company; and Transition Therapeutics. The Canadian Institutes of Health Research is providing funds to support ADNI clinical sites in Canada. Private sector contributions are facilitated by the Foundation for the National Institutes of Health (www.fnih.org). The grantee organization is the Northern California Institute for Research and Education, and the study is coordinated by the Alzheimers Therapeutic Research Institute at the University of Southern California. ADNI data are disseminated by the Laboratory for Neuro Imaging at the University of Southern California. Data were also provided in part by the Human Connectome Project, WU-Minn Consortium (Principal Investigators: David Van Essen and Kamil Ugurbil; 1U54MH091657) funded by the 16 NIH Institutes and Centers that support the NIH Blueprint for Neuroscience Research; and by the McDonnell Center for Systems Neuroscience at Washington University.

5. Appendix

5.1. Dice score and Hausdorff metric compared between CerebNet, ACAPULCO^{rt}, original ACAPULCO and SUIT + FS

To motivate our choice of pre-training with SUIT + FS and illustrate the impact of the dataset, we compare four methods on our test set: *CerebNet*, the ACAPULCO^{rt} (Han et al., 2020b) (both trained on our training set), as well as the original ACAPULCO (Han et al., 2020b) and SUIT + FS (Diedrichsen et al., 2009) (both trained on their individual datasets). We compare each prediction with our manually labeled reference segmentation to obtain average Dice and Robust Hausdorff metrics for each method in Fig. 8. Two observations are notable: 1. SUIT + FS outperforms the original ACAPULCO; 2. ACAPULCO^{rt} outperforms ACAPULCO (and SUIT + FS). Both results are expected and illustrate how much different labeling protocols (e.g. along the CGM/CWM border) can impact the performance and ranking of methods. These results confirm that inconsistent labeling protocols between training and test significantly impact the measured performance even to the level of contradicting previous rankings (Carass et al., 2018; Han et al., 2020b). Therefore, we 1. choose SUIT + FS for pre-training and 2. retrain ACAPULCO (yielding ACAPULCO^{rt}) so that our methodological comparison are fair and not impacted by the choice of protocols.

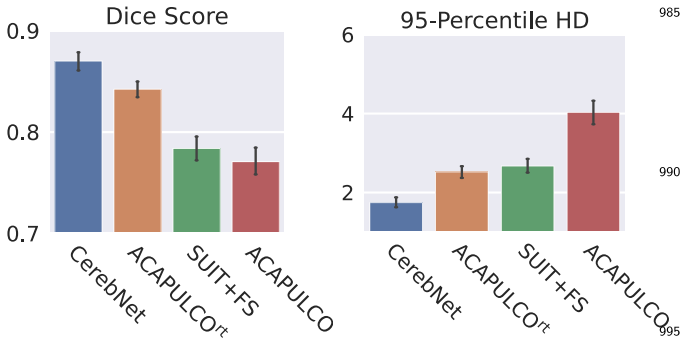

Fig. 8. Comparison of Dice and Robust Hausdorff Distance (HD95) metrics for CerebNet, the retrained ACAPULCO^{rt}, SUIT + FS as well as the original (published) ACAPULCO on our test set. Note, the direct comparison of *CerebNet* and the original ACAPULCO does not correct for the differences in the training datasets; ACAPULCO^{rt} corrects for this difference (see text).

This analysis also raises the question of how the performance of two pipelines may be compared fairly (a pipeline evaluation includes the impact of both the training dataset and the method). This is specifically difficult if protocols differ and higher quality reference standards are not available. While retraining on the same dataset yields a fair, direct comparison of methods (see for example section 3.2), pipeline comparisons, in situations where retraining is not feasible, require indirect evaluations based on segmentation-derived metrics instead of segmentation maps, e.g. whether and how well volume estimates can be used to differentiate between patient groups as done for SCA3 in Section 3.5.

5.2. Correlation of SARA sum scores with volumetric estimates

We perform a correlation analysis between the SARA sum score and regional volumes. Table 2 shows individual Kendell Tau coefficients for three methods: *CerebNet*, ACAPULCO (original) and ACAPULCO^{rt} (retrained). We also report whether the analysis achieved statistical significance. However, we would like to note that SCA3 is not a pure cerebllar disease like for example SCA6. The patterns of neurodegeneration in SCA3 include non-cerebellar structures, e.g. the basal ganglia or the peripheral nerve system. Progressive neurodegeneration of the cerebellum might be the main driver of ataxia severity in SCA3, but symptoms resulting from non-cerebellar manifestations, like e.g. spasticity or polyneuropathy have a direct impact on SARA items such as gait and stance. This should be taken into account in the interpretation of the correlation.

5.3. CerebNet segmentation in sporadic and hereditary ataxias

To illustrate the robustness of *CerebNet* to "out-of-distribution" samples, we show some qualitative examples of segmentations in Fig. 9.

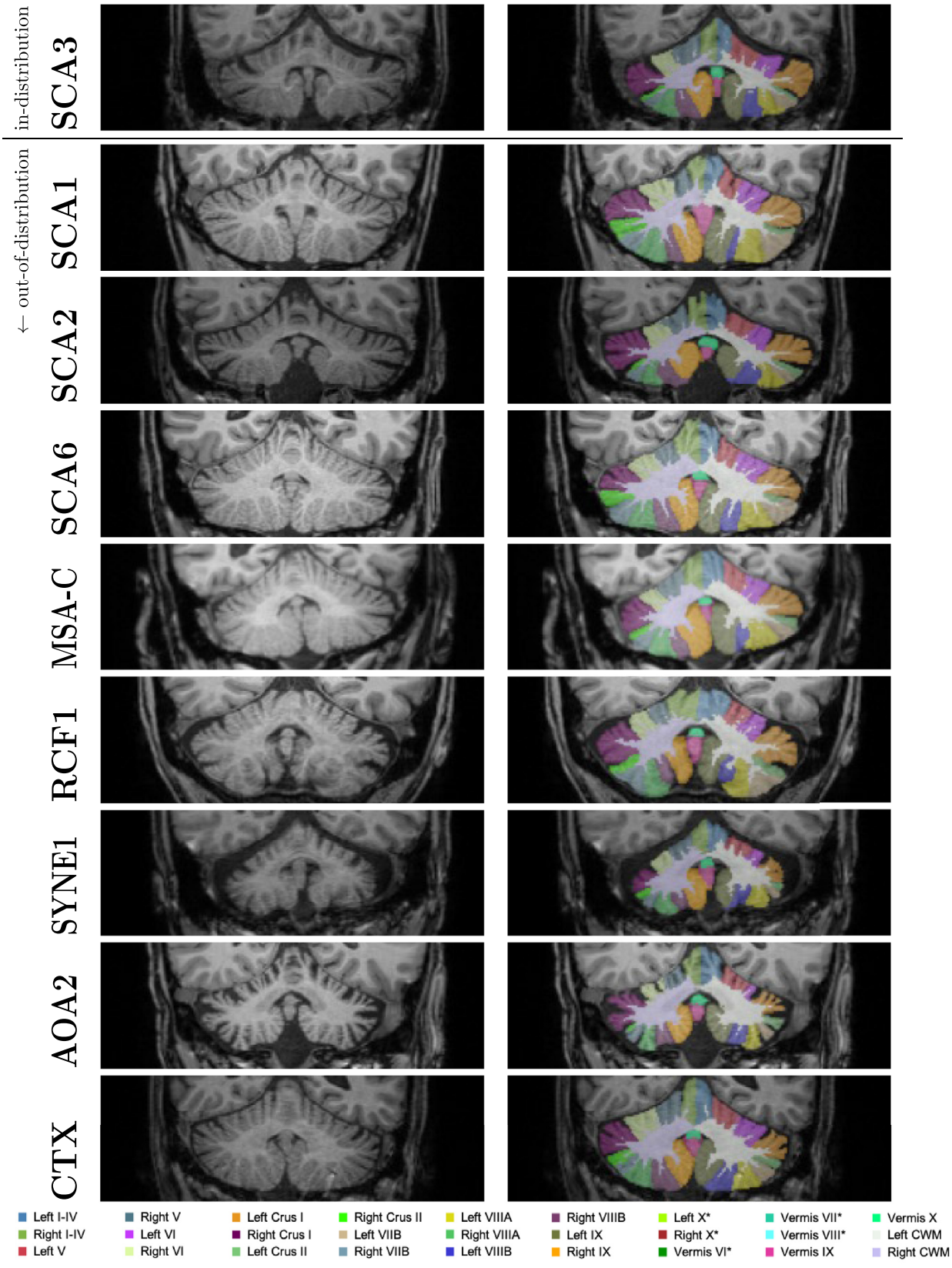

Fig. 9. Qualitative "out-of-distribution" evaluation of *CerebNet*: Segmentation maps for pathologies, which are not part of the training (SCA1, SCA2, SCA6, MSA-C, RFC1, SYNE1, AOA2 and CTX) together with an in-distribution example (SCA3). Images illustrated here are randomly picked from a larger repository of images and represent average performance. *: Label is not visible in the shown slice.

Table 2
Correlation of SARA sum score with each cerebellar volume for CerebNet, ACAPULCO and ACAPULCO^{rt}. Kendell Tau correlation coefficients are given, and statistical significance of the correlation is indicated by * ($p < .05$) and ** ($p < .01$). For each volume, the most negative, statistically significant correlation coefficient is printed in boldface.

	CerebNet	ACAPULO (original)	ACAPULCO^{rt} (retrained)
Left I-IV	-0.204**	-0.134*	**-0.211****
Right I-IV	**-0.235****	-0.167*	-0.208**
Left V	-0.0602	**-0.213****	-0.0593
Right V	-0.00294	**-0.194****	-0.0401
Left VI	**-0.306****	-0.227**	-0.284**
Vermis VI	-0.0954	-0.0197	-0.0874
Right VI	**-0.322****	-0.225**	-0.264**
L. Crus I	-0.252**	**-0.287****	-0.214**
R. Crus I	**-0.200****	-0.199**	-0.151*
L. Crus II	-0.219**	**-0.267****	-0.145*
R. Crus II	**-0.214****	-0.179**	-0.154*
Left VIIb	**-0.385****	-0.241**	-0.341**
Right VIIb	**-0.410****	-0.364**	-0.314**
Vermis VII	**-0.144***	-0.139*	-0.0765
Left VIIIa	**-0.299****	-0.113	-0.264**
Right VIIIa	-0.315**	-0.100	**-0.408****
Left VIIIb	-0.317**	-0.311**	**-0.374****
Right VIIIb	-0.254**	**-0.344****	-0.323**
Vermis VIII	**-0.182****	-0.0941	-0.170**
Left IX	**-0.258****	-0.159*	-0.232**
Vermis IX	-0.0650	-0.0327	-0.0760
Right IX	**-0.292****	-0.248**	-0.240**
Left X	**-0.265****	0.0101	-0.207**
Vermis X	-0.115	-0.0667	-0.0270
Right X	**-0.298****	-0.0598	-0.253**
CWM	**-0.583****	-0.440**	-0.549**

While these results indicate good performance across many pathologies, studies utilizing *CerebNet* to segment patients with these or other diseases should still ensure the performance also translates to their datasets by performing a formal validation, or, at least, rigorous quality assurance as laid out in the Discussion.

Data and Code Availability Statement

The MRI data is not publicly available because of data protection regulations. Access can be provided upon reasonable request to scientists in accordance with our Data Use and Access Policy. Requests to access the data should be directed to Jennifer Faber at Jennifer.Faber@dzne.de.

The source code of CerebNet will be made publicly available on Github (https://github.com/Deep-MI/FastSurfer) upon acceptance.

References

Avants, B.B., Epstein, C.L., Grossman, M., Gee, J.C., 2008. Symmetric diffeomorphic image registration with cross-correlation: evaluating automated labeling of elderly and neurodegenerative brain. Med. Image Anal. 12 (1), 26–41.

Bogovic, J.A., Bazin, P.L., Ying, S.H., Prince, J.L., 2013. Automated segmentation of the cerebellar lobules using boundary specific classification and evolution. In: Lecture Notes in Computer Science (including subseries Lecture Notes in Artificial Intelligence and Lecture Notes in Bioinformatics), Vol. 7917 LNCS, pp. 62–73.

Bogovic, J.A., Jedynak, B., Rigg, R., Du, A., Landman, B.A., Prince, J.L., Ying, S.H., 2013. Approaching expert results using a hierarchical cerebellum parcellation protocol for multiple inexpert human raters. NeuroImage 64, 616–629. doi:10.1016/j.neuroimage.2012.08.075.

Bogovic, J.A., Prince, J.L., Bazin, P.L., 2013. A multiple object geometric deformable model for image segmentation. Comput. Vision Image Understanding 117 (2), 145–157.

Buckner, R., Head, D., Parker, J., Fotenos, A., Marcus, D., Morris, J., Snyder, A., 2004. A unified approach for morphometric and functional data analysis in young, old, and demented adults using automated atlas-based head size normalization: reliability and validation against manual measurement of total intracranial volume. NeuroImage 23, 724–738. doi:10.1016/j.neuroimage.2004.06.018.

Buckner, R.L., Krienen, F.M., Castellanos, A., Diaz, J.C., Yeo, B.T., 2011. The organization of the human cerebellum estimated by intrinsic functional connectivity. J. Neurophysiol. 106 (5), 2322–2345. doi:10.1152/jn.00339.2011.

Carass, A., Cuzzocreo, J.L., Han, S., Hernandez-Castillo, C.R., Rasser, P.E., Ganz, M., Beliveau, V., Dolz, J., Ben Ayed, I., Desrosiers, C., Thyreau, B., Romero, J.E., Coupé, P., Manjón, J.V., Fonov, V.S., Collins, D.L., Ying, S.H., Onyike, C.U., Crocetti, D., Landman, B.A., Mostofsky, S.H., Thompson, P.M., Prince, J.L., 2018. Comparing fully automated state-of-the-art cerebellum parcellation from magnetic resonance images. NeuroImage 183, 150–172.

Carass, A., Prince, J.L., 2016. An overview of the multi-object geometric deformable model approach in biomedical imaging. In: Medical Image Recognition, Segmentation and Parsing, pp. 259–279.

Chakravarty, M.M., Steadman, P., van Eede, M.C., Calcott, R.D., Gu, V., Shaw, P., Raznahan, A., Collins, D.L., Lerch, J.P., 2013. Performing label-fusion-based segmentation using multiple automatically generated templates. Hum. Brain Mapp. 34 (10), 2635–2654.

Coupé, P., Manjón, J.V., Fonov, V., Pruessner, J., Robles, M., Collins, D.L., 2011. Patch-based segmentation using expert priors: application to hippocampus and ventricle segmentation. NeuroImage 54 (2), 940–954.

Di Martino, A., O'Connor, D., Chen, B., Alaerts, K., Anderson, J.S., Assaf, M., Balsters, J.H., Baxter, L., Beggiato, A., Bernaerts, S., Blanken, L.M.E., Bookheimer, S.Y., Braden, B.B., Byrge, L., Castellanos, F.X., Dapretto, M., Delorme, R., Fair, D.A., Fishman, I., Fitzgerald, J., Gallagher, L., Keehn, R.J.J., Kennedy, D.P., Lainhart, J.E., Luna, B., Mostofsky, S.H., Müller, R.A., Nebel, M.B., Nigg, J.T., O'Hearn, K., Solomon, M., Toro, R., Vaidya, C.J., Wenderoth, N., White, T., Craddock, R.C., Lord, C., Leventhal, B., Milham, M.P., 2017. Enhancing studies of the connectome in autism using the autism brain imaging data exchange II. Sci. Data 4 (1), 1–15.

Dice, L.R., 1945. Measures of the amount of ecologic association between species. Ecology 26 (3), 297–302. doi:10.2307/1932409.

Diedrichsen, Zotow, J., Ewa, 2015. Surface-based display of volume-averaged cerebellar imaging data. PLoS ONE 10, 1–18.

Diedrichsen, J., 2006. A spatially unbiased atlas template of the human cerebellum. NeuroImage 33 (1), 127138. doi:10.1016/j.neuroimage.2006.05.056.

Diedrichsen, J., Balsters, J.H., Flavell, J., Cussans, E., Ramnani, N., 2009. A probabilistic MR atlas of the human cerebellum. NeuroImage 46 (1), 39–46. doi:10.1016/j.neuroimage.2009.01.045.

D'Mello, A.M., Crocetti, D., Mostofsky, S.H., Stoodley, C.J., 2015. Cerebellar gray matter and lobular volumes correlate with core autism symptoms. NeuroImage 7, 631–639. doi:10.1016/j.nicl.2015.02.007.

Estrada, S., Conjeti, S., Ahmad, M., Navab, N., Reuter, M., 2018. Competition vs. concatenation in skip connections of fully convolutional networks. In: Shi, Y., Suk, H.-I., Liu, M. (Eds.), Machine Learning in Medical Imaging. Springer International Publishing, Cham, pp. 214–222.

Estrada, S., Lu, R., Conjeti, S., Orozco-Ruiz, X., Panos-Willuhn, J., Breteler, M.M.B., Reuter, M., 2020. Fatsegnet: a fully automated deep learning pipeline for adipose tissue segmentation on abdominal dixon MRI. Magn. Reson. Med. 83 (4), 1471–1483.

Faber, J., Giordano, I., Jiang, X., Kindler, C., Spottke, A., Acosta-Cabronero, J., Nestor, P.J., Machts, J., Düzel, E., Vielhaber, S., Speck, O., Dudesek, A., Kamm, C., Scheef, L., Klockgether, T., 2020. Prominent white matter involvement in multiple system atrophy of cerebellar type. Movement Disorders 35 (5), 816–824. doi:10.1002/mds.27987.

Faber, J., Schaprian, T., Berkan, K., Reetz, K., França Jr, M.C., de Rezende, T.J.R., Hong, J., Liao, W., van de Warrenburg, B., van Gaalen, J., Durr, A., Mochel, F., Giunti, P., Garcia-Moreno, H., Schoels, L., Hengel, H., Synofzik, M., Bender, B., Oz, G., Joers, J., de Vries, J.J., Kang, J.-S., Timmann-Braun, D., Jacobi, H., Infante, J., Joules, R., Romanzetti, S., Diedrichsen, J., Schmid, M., Wolz, R., Klockgether, T., 2021. Regional brain and spinal cord volume loss in spinocerebellar ataxia type 3. Movement Disorders doi:10.1002/mds.28610.

Fischl, B., Salat, D.H., Busa, E., Albert, M., Dieterich, M., Haselgrove, C., van der Kouwe, A., Killiany, R., Kennedy, D., Klaveness, S., Montillo, A., Makris, N., Rosen, B., Dale, A.M., 2002. Whole brain segmentation: automated labeling of neuroanatomical structures in the human brain. Neuron 33 (3), 341–355. doi:10.1016/S0896-6273(02)00569-X.

Giraud, R., Ta, V.T., Papadakis, N., Manjón, J.V., Collins, D.L., Coupé, P., 2016. An optimized patchmatch for multi-scale and multi-feature label fusion. NeuroImage 124, 770–782.

Guha Roy, A., Conjeti, S., Navab, N., Wachinger, C., 2019. QuickNAT: a fully convolutional network for quick and accurate segmentation of neuroanatomy. NeuroImage 186, 713–727.

Han, S., An, Y., Carass, A., Prince, J.L., Resnick, S.M., 2020. Longitudinal analysis of regional cerebellum volumes during normal aging. NeuroImage 220, 117062. doi:10.1016/j.neuroimage.2020.117062.

Han, S., Carass, A., He, Y., Prince, J.L., 2020. Automatic cerebellum anatomical parcellation using U-Net with locally constrained optimization. NeuroImage 218, 116819.

Han, S., He, Y., Carass, A., Ying, S.H., Prince, J.L., 2019. Cerebellum parcellation with convolutional neural networks. In: Proceedings of SPIE–the International Society for Optical Engineering, Vol. 10949, p. 19.

Heinz, L., Faber, J., Timmann, D., Ernst, T., Deike-Hofmann, K., Klockgether, T., 2022. Manual sub-segmentation of the cererbellum. medRxiv doi:10.1101/2022.05.09.22274814.

Henschel, L., Conjeti, S., Estrada, S., Diers, K., Fischl, B., Reuter, M., 2020. Fastsurfer - a fast and accurate deep learning based neuroimaging pipeline. NeuroImage 219, 117012.

Huttenlocher, D.P., Klanderman, G.A., Rucklidge, W.J., 1993. Comparing images using the hausdorff distance. IEEE Trans. Pattern Anal. Mach. Intell. 15 (9), 850–863.

Jacobi, H., du Montcel, S.T., Romanzetti, S., Harmuth, F., Mariotti, C., Nanetti, L., Rakow-

icz, M., Makowicz, G., Durr, A., Monin, M.L., Filla, A., Roca, A., Schols, L., Hengel, H., Infante, J., Kang, J.S., Timmann, D., Casali, C., Masciullo, M., Baliko, L., Melegh, B., Nachbauer, W., Burk-Gergs, K., Schulz, J.B., Riess, O., Reetz, K., Klockgether, T., 2020. Conversion of individuals at risk for spinocerebellar ataxia types 1, 2, 3, and 6 to manifest ataxia (RISCA): a longitudinal cohort study. Lancet Neurol. 19 (9), 738–747. doi:10.1016/S1474-4422(20)30235-0.

Kim, D.-H., Kim, R., Lee, J.-Y., Lee, K.-M., 2021. Clinical, imaging, and laboratory markers of premanifest spinocerebellar ataxia 1, 2, 3, and 6: a systematic review. J. Clin. Neurol. 17 (2), 187–199. doi:10.3988/jcn.2021.17.2.187.

King, M., Hernandez-Castillo, C.R., Poldrack, R.A., Ivry, R.B., Diedrichsen, J., 2019. Functional boundaries in the human cerebellum revealed by a multi-domain task battery. Nat. Neurosci. 22 (8), 1371–1378. doi:10.1038/s41593-019-0436-x.

Kingma, D.P., Ba, J., 2015. Adam: a method for stochastic optimization. In: Bengio, Y., LeCun, Y. (Eds.), International Conference on Learning Representations, ICLR.

Landman, B.A., Huang, A.J., Gifford, A., Vikram, D.S., Lim, I.A.L., Farrell, J.A.D., Bogovic, J.A., Hua, J., Chen, M., Jarso, S., Smith, S.A., Joel, S., Mori, S., Pekar, J.J., Barker, P.B., Prince, J.L., van Zijl, P.C.M., 2011. Multi-parametric neuroimaging reproducibility: a 3-t resource study. NeuroImage 54 (4).

van der Lijn, F., de Bruijne, M., Hoogendam, Y.Y., Klein, S., Hameeteman, R., Breteler, M.M.B., Niessen, W.J., 2009. Cerebellum segmentation in MRI using atlas registration and local multi-scale image descriptors. In: 2009 IEEE International Symposium on Biomedical Imaging: From Nano to Macro, pp. 221–224.

Lin, C.-Y., Chen, C.-H., Tom, S.E., Kuo, S.-H., for the Alzheimer's Disease Neuroimaging Initiative, 2020. Cerebellar volume is associated with cognitive decline in mild cognitive impairment: results from ADNI. Cerebellum 19 (2), 217–225. doi:10.1007/s12311-019-01099-1.

Loshchilov, I., Hutter, F., 2019. Decoupled weight decay regularization. In: International Conference on Learning Representations.

Malone, I.B., Cash, D., Ridgway, G.R., MacManus, D.G., Ourselin, S., Fox, N.C., Schott, J.M., et al., 2013. MIRIAD-Public Release of a multiple time point Alzheimer's MR imaging dataset. NeuroImage 70, 33–36. doi:10.1016/j.neuroimage.2012.12.044.

Marcus, D.S., Fotenos, A.F., Csernansky, J.G., Morris, J.C., Buckner, R.L., 2010. Open access series of imaging studies: longitudinal MRI data in nondemented and demented older adults. J. Cogn. Neurosci. 22 (12), 2677–2684.

Marcus, D.S., Wang, T.H., Parker, J., Csernansky, J.G., Morris, J.C., Buckner, R.L., 2007. Open access series of imaging studies (OASIS): cross-sectional MRI data in young, middle aged, nondemented, and demented older adults. J. Cogn. Neurosci. 19 (9), 1498–1507.

Marek, S., Siegel, J.S., Gordon, E.M., Raut, R.V., Gratton, C., Newbold, D.J., Ortega, M., Laumann, T.O., Adeyemo, B., Miller, D.B., Zheng, A., Lopez, K.C., Berg, J.J., Coalson, R.S., Nguyen, A.L., Dierker, D., Van, A.N., Hoyt, C.R., McDermott, K.B., Norris, S.A., Shimony, J.S., Snyder, A.Z., Nelson, S.M., Barch, D.M., Schlaggar, B.L., Raichle, M.E., Petersen, S.E., Greene, D.J., Dosenbach, N.U.F., 2018. Spatial and temporal organization of the individual human cerebellum. Neuron 100 (4), 977–993.e7. doi:10.1016/j.neuron.2018.10.010.

McLoughlin, H.S., Moore, L.R., Chopra, R., Komlo, R., McKenzie, M., Blumenstein, K.G., Zhao, H., Kordasiewicz, H.B., Shakkottai, V.G., Paulson, H.L., 2018. Oligonucleotide therapy mitigates disease in spinocerebellar ataxia type 3 mice. Ann. Neurol. 84 (1), 64–77. doi:10.1002/ana.25264.

Mueller, S. G., Weiner, M. W., Thal, L. J., Petersen, R. C., Jack, C. R., Jagust, W., Trojanowski, J. Q., Toga, A. W., Beckett, L., 2005. Ways toward an early diagnosis in Alzheimer's disease: The Alzheimer's Disease Neuroimaging Initiative (ADNI).

Okugawa, G., Sedvall, G.C., Agartz, I., 2003. Smaller cerebellar vermis but not hemisphere volumes in patients with chronic schizophrenia. Am. J. Psychiatry 160 (9), 1614–1617. doi:10.1176/appi.ajp.160.9.1614.

Park, M.T.M., Pipitone, J., Baer, L.H., Winterburn, J.L., Shah, Y., Chavez, S., Schira, M.M., Lobaugh, N.J., Lerch, J.P., Voineskos, A.N., Chakravarty, M.M., 2014. Derivation of high-resolution MRI atlases of the human cerebellum at 3T and segmentation using multiple automatically generated templates. NeuroImage 95, 217–231. doi:10.1016/j.neuroimage.2014.03.037.

Patenaude, B., Smith, S.M., Kennedy, D.N., Jenkinson, M., 2011. A Bayesian model of shape and appearance for subcortical brain segmentation. NeuroImage 56 (3), 907–922.

Pierson, R., Corson, P.W., Sears, L.L., Alicata, D., Magnotta, V., O'Leary, D., Andreasen, N.C., 2002. Manual and semiautomated measurement of cerebellar subregions on MR images. NeuroImage 17 (1).

Plassard, A.J., Yang, Z., Rane, S., Prince, J.L., Claassen, D.O., Landman, B.A., 2016. Improving cerebellar segmentation with statistical fusion. In: Medical Imaging 2016: Image Processing, Vol. 9784, p. 97842R.

Poldrack, R.A., Congdon, E., Triplett, W., Gorgolewski, K.J., Karlsgodt, K.H., Mumford, J.A., Sabb, F.W., Freimer, N.B., London, E.D., Cannon, T.D., Bilder, R.M., 2016. A phenome-wide examination of neural and cognitive function. Sci.. Data 3 (1), 1–12.

Powell, S., Magnotta, V.A., Johnson, H., Jammalamadaka, V.K., Pierson, R., Andreasen, N.C., 2008. Registration and machine learning-based automated segmentation of subcortical and cerebellar brain structures. NeuroImage 39 (1), 238–247. doi:10.1016/j.neuroimage.2007.05.063.

Price, M., Cardenas, V.A., Fein, G., 2014. Automated MRI cerebellar size measurements using active appearance modeling. NeuroImage 103, 511–521.

Rezende, T.J.R., de Paiva, J.L.R., Martinez, A.R.M., Lopes-Cendes, I., Pedroso, J.L., Barsottini, O.G.P., Cendes, F., França Jr., M.C., 2018. Structural signature of SCA3: from presymptomatic to late disease stages. Ann. Neurol. 84 (3), 401–408. doi:10.1002/ana.25297.

Romero, J.E., Coupé, P., Giraud, R., Ta, V.T., Fonov, V., Park, M.T.M., Chakravarty, M.M., Voineskos, A.N., Manjón, J.V., 2017. CERES: A new cerebellum lobule segmentation method. NeuroImage 147, 916–924.

Schmahmann, J.D., Doyon, J., McDonald, D., Holmes, C., Lavoie, K., Hurwitz, A.S., Kabani, N., Toga, A., Evans, A., Petrides, M., 1999. Three-dimensional MRI atlas of the human cerebellum in proportional stereotaxic space. NeuroImage 10 (3), 233–260.

Schmitz-Hübsch, T., du Montcel, S.T., Baliko, L., Berciano, J., Boesch, S., Depondt, C., Giunti, P., Globas, C., Infante, J., Kang, J.-S., Kremer, B., Mariotti, C., Melegh, B., Pandolfo, M., Rakowicz, M., Ribai, P., Rola, R., Schöls, L., Szymanski, S., van de Warrenburg, B.P., Dürr, A., Klockgether, T., 2006. Scale for the assessment and rating of ataxia. Neurology 66 (11), 1717–1720.

Shrout, P., Fleiss, J., 1979. Intraclass correlations: uses in assessing rater reliability. Psychol. Bull. 86 2, 420–428.

Sörös, P., Wölk, L., Bantel, C., Bräuer, A., Klawonn, F., Witt, K., 2021. Replicability, repeatability, and long-term reproducibility of cerebellar morphometry. Cerebellum.

Sørensen, Julius, T., 1948. A method of establishing groups of equal amplitude in plant sociology based on similarity of species and its application to analyses of the vegetation on danish commons 5, 1–34.

Ta, V.-T., Giraud, R., Collins, D.L., Coupé, P., 2014. Optimized patchmatch for near real time and accurate label fusion. In: Golland, P., Hata, N., Barillot, C., Hornegger, J., Howe, R. (Eds.), Medical Image Computing and Computer-Assisted Intervention – MICCAI 2014, pp. 105–112.

Toniolo, S., Serra, L., Olivito, G., Marra, C., Bozzali, M., Cercignani, M., 2018. Patterns of cerebellar gray matter atrophy across alzheimers disease progression. Front. Cell Neurosci. 12, 430. doi:10.3389/fncel.2018.00430.

Van Essen, D.C., Ugurbil, K., Auerbach, E., Barch, D., Behrens, T.E.J., Bucholz, R., Chang, A., Chen, L., Corbetta, M., Curtiss, S.W., Della Penna, S., Feinberg, D., Glasser, M.F., Harel, N., Heath, A.C., Larson-Prior, L., Marcus, D., Michalareas, G., Moeller, S., Oostenveld, R., Petersen, S.E., Prior, F., Schlaggar, B.L., Smith, S.M., Snyder, A.Z., Xu, J., Yacoub, E., 2012. The human connectome project: a data acquisition perspective. NeuroImage 62 (4), 2222–2231.

Van Leemput, K., Maes, F., Vandermeulen, D., Suetens, P., 1999. Automated model-based tissue classification of MR images of the brain. IEEE Trans. Med. Imaging 18 (10), 897–908.

Webb, S.J., Sparks, B.-F., Friedman, S.D., Shaw, D.W.W., Giedd, J., Dawson, G., Dager, S.R., 2009. Cerebellar vermal volumes and behavioral correlates in children with autism spectrum disorder. Psychiatry Res. 172 (1), 61–67. doi:10.1016/j.pscychresns.2008.06.001.

Weier, K., Fonov, V., Lavoie, K., Doyon, J., Louis Collins, D., 2014. Rapid automatic segmentation of the human cerebellum and its lobules (RASCAL)-Implementation and application of the patch-based label-fusion technique with a template library to segment the human cerebellum. Hum. Brain Mapp. 35 (10), 5026–5039.

Womer, F.Y., Tang, Y., Harms, M.P., Bai, C., Chang, M., Jiang, X., Wei, S., Wang, F., Barch, D.M., 2016. Sexual dimorphism of the cerebellar vermis in schizophrenia. Schizophr. Res. 176 (2), 164–170. doi:10.1016/j.schres.2016.06.028.

Yang, Z., Ye, C., Bogovic, J.A., Carass, A., Jedynak, B.M., Ying, S.H., Prince, J.L., 2016. Automated cerebellar lobule segmentation with application to cerebellar structural analysis in cerebellar disease. NeuroImage 127, 435–444.

3.5. Faber J, Berger M, Carlo W, Hübener-Schmid J, Schaprian T, Santana MM, Grobe-Einsler M, Onder D, Koyak B, Giunti P, Garcia-Moreno H, Gonzalez-Robles C, Lima M, Raposo M, Vieira Melo AR, de Almeida LP, Silva P, Pinto MM, van de Warrenburg BP, van Gaalen J, Jeroen de Vries J, Oz G, Joers JM, Synofzik M, Schöls L, Riess O, Infante J, Manrique L, Timmann D, Thieme A, Jacobi H, Reetz K, Dogan I, Onyike C, Povazan M, Schmahmann J, Ratai EM, Schmid M, Klockgether T. Stage-dependent biomarker changes in spinocerebellar ataxia type 3. medRxiv [Preprint]. 2023 Apr 25:2023.04.21.23287817, re-submitted after review

Zielsetzung der Arbeit – Zielsetzung der Arbeit war es, ein Stadienmodell für die SCA3 unter Einschluss von biochemischen und bildgebenden Biomarkern auszuarbeiten.

Methoden und Ergebnisse –Querschnittsdaten von 292 SCA3-Mutationsträger*innen, darunter 57 prä-ataktische Mutationsträger*innen, und 108 gesunden Kontrollpersonen wurden ausgewertet. Die Blutkonzentrationen des Krankheits-spezifischen Proteins, mutiertes ATXN3, und NfL wurden bestimmt. Es wurden die Volumina der Pons, der zerebellären weißen und grauen Substanz unter Verwendung eines automatisierten Verfahrens erhoben und in Relation zum Ganzhirnvolumen gesetzt. Die Biomarkerdaten von NfL sowie der bildgebenden Biomarkerdaten wurden in Relation zur gesunden Kontrollgruppe z-standardisiert.
Die Konzentrationen des mutierten ATXN3 waren durchgehend hoch, während NfL kontinuierlich anstieg und 11,9 Jahre vor Symptombeginn vom Normalwert abwich. Die Volumina von Pons und weißer Substanz des Kleinhirns nahmen kontinuierlich ab, allerdings wich die Atrophie erst deutlich später vom Normalbereich ab, mit 2,0 Jahren (Pons) und 0,3 Jahren (weiße Substanz des Kleinhirns) vor Symptombeginn. Basierend auf diesen Ergebnissen arbeiteten wir ein Stadienmodell für SCA3 aus: in der zeitlichen Abfolge das erste Stadium wurde als (i) „carrier stage“ übersetzt in etwa „Mutationsträgerstadium“ bezeichnet. Es umfasst SCA3 Mutationsträger*innen, die außer dem Vorhandensein der ATXN3-Mutation keine signifikanten Biomarkerveränderungen aufweisen. Es ist definiert durch SARA < 3 und einen NfL z-score < 2. (ii) Das zweite Stadium wurde mit „Biomarker-Stadium“ bezeichnet und umfasst prä-ataktische Mutationsträger*innen mit signifikanten Biomarker-Veränderungen. Es ist definiert durch SARA < 3 und einen NfL z- Score ≥ 2. (iii) Das

Ataxie-Stadium umfasst ataktische Mutationsträger*innen. Es ist definiert durch SARA ≥ 3 und wurde anhand der wesentlichen klinischen Meilensteine, dem Verlust des freien Gehens und der Rollstuhlpflichtigkeit weiter unterteilt.

Schlussfolgerungen – Die Analyse einer großen Kohorte gut charakterisierter SCA3 erlaubte es erstmals, ein Stadienmodell für SCA3 auszuarbeiten. Wichtigstes Ergebnis ist die Definition eines Biomarker-Stadiums vor Symptombeginn. Dieses ist durch Veränderungen in biochemischen und bildgebenden Biomarkern geprägt, die Kandidaten zur Erfassung von Progression als auch Prognose bevorstehender klinischer Verschlechterung darstellen. Die vorliegende Analyse bietet einen ersten Rahmen für weitere Studien, die auf die Ausarbeitung und Differenzierung eines Stadienmodells für SCA3 abzielen.

Stage-dependent biomarker changes in spinocerebellar ataxia type 3

Journal:	*Annals of Neurology*
Manuscript ID	ANA-23-0498.R2
Wiley - Manuscript type:	Brief Communication
Date Submitted by the Author:	n/a
Complete List of Authors:	Faber, Jennifer; University Hospital Bonn, Neurology; German Centre for Neurodegenerative Diseases, Clinical research Berger, Moritz; University of Bonn, Medical Faculty, Institute for Medical Biometry, Informatics and Epidemiology Wilke, Carlo; Hertie-Institute for Clinical Brain Research, Department of Neurodegenerative Diseases Hubener-Schmid, Jeannette; University of Tubingen, Institute of Medical Genetics and Applied Genomics Schaprian , Tamara; Center for Neurodegenerative Diseases (DZNE), CRP Santana, Magda; University of Coimbra Center for Neuroscience and Cell Biology Grobe-Einsler, Marcus; University Hospital Bonn, Neurology; German Centre for Neurodegenerative Diseases, Clinical research Onder, Demet; University Hospital Bonn, Neurology; German Centre for Neurodegenerative Diseases, Clinical research Koyak, Berkan; University Hospital Bonn, Neurology; German Centre for Neurodegenerative Diseases, Clinical research Giunti, Paola; University College London, Institute of Neurology Garcia-Moreno, Hector; University College London, Institute of Neurology, Gonzalez-Robles, Cristina; UCL Institute of Neurology, AtaxiaCentre Department of Clinical and Motor Neuroscience Lima, Manuela; Universidades dos Açores, Departamento de Biologia; Instituto de Investigação e Inovação em Saúde; Instituto de Biologia Molecular e Celular Raposo, Mafalda; Universidade dos Acores, Melo, Ana; Universidades dos Açores, Departamento de Biologia Pereira de Almeida, Luis; University of Coimbra, Center for Neurosciences; University of Coimbra, Faculty of Pharmacy Silva, Patrick; University of Coimbra, Center for Neurosciences Pinto, Maria; University of Coimbra, Center for Neurosciences van de warrenburg, Bart; Radboud university medical center, Neurology van Gaalen, Judith; Radboud university medical center, Neurology de Vries, Jeroen; University of Groningen, Department of Neurology Oz, Gulin; University of Minnesota, Radiology, CMRR Joers, James; University of Minnesota, Radiology, CMRR Synofzik, Matthis; Hertie Institute for Clinical Brain Research, Dept. of Neurodegnerative Diseases Schöls, Ludger; Universität Tübingen, Neurologische Klinik und Hertie-Institut für Klinische Hirnforschung Riess, Olaf; University of Tuebingen, Department of Medical Genetics Infante, Jon; University of Cantabria, Service of Neurology Manrique, Leire; University of Cantabria, Service of Neurology Timmann, Dagmar; Universitat Duisburg-Essen, Neurology

	Thieme, Andreas; University Hospital Essen, Department of Neurology Jacobi, Heike; University of Heidelberg, Department of Neurology Reetz, Kathrin; RWTH Aachen University, Department of Neurology Dogan, Imis; RWTH Aachen University, Department of Neurology Onyike, Chiadi; Johns Hopkins University Povazan, Michal; Johns Hopkins University School of Medicine Schmahmann, Jeremy; Massachusetts General Hospital, Neurology Ratai, Eva; A. A. Martinos Center for Biomedical Imaging, MGH Department of Radiology Schmid, Matthias; Medical Faculty, University of Bonn, Department of Medical Biometry, Informatics and Epidemiology Klockgether, Thomas; Universitatsklinikum Bonn, Department of Neurology; German Center for Neurodegenerative Diseases (DZNE); Universitatsklinikum Bonn, Department of Neurology
Domain:	Clinical and/or Desktop Research
Keywords:	Spinocerebellar ataxia, biomarker, disease modeling

Stage-dependent biomarker changes in spinocerebellar ataxia type 3

Jennifer Faber MD[1,2], Moritz Berger PhD[3], Carlo Wilke MD[,5], Jeannette Hubener-Schmid PhD[6], Tamara Schaprian MSc[1], Magda M Santana PhD[7,8], Marcus Grobe-Einsler MD[1,2], Demet Onder MD[1,2], Berkan Koyak MD[1,2], Paola Giunti MD[9,10], Hector Garcia-Moreno MD[9,10], Cristina Gonzalez-Robles MD[9,10], Manuela Lima PhD[11], Mafalda Raposo PhD[11,12], Ana Rosa Vieira Melo MSc[11], Luís Pereira de Almeida PhD[7,8], Patrick Silva MSc[7,8,13], Maria M Pinto MSc[7,8,13], Bart P. van de Warrenburg MD PhD[14], Judith van Gaalen MD[14,15], de Vries, Jeroen MD[16], Gulin Oz PhD[17], James M. Joers PhD[17], Matthis Synofzik MD[4,5], Ludger Schols MD[4,5], Olaf Riess MD[6], Jon Infante MD[18,19], Leire Manrique MD[18], Dagmar Timmann MD[20], Andreas Thieme MD[20], Heike Jacobi MD[21], Kathrin Reetz MD[22,23], Imis Dogan PhD[22,23], Chiadikaobi Onyike MD[24], Michal Povazan PhD[25], Jeremy Schmahmann MD[26], Eva-Maria Ratai PhD[27], Matthias Schmid PhD[1,3], Thomas Klockgether MD[1,2]

Author affiliations:

1 German Center for Neurodegenerative Diseases (DZNE), Bonn, Germany

2 Department of Neurology, University Hospital Bonn, Bonn, Germany

3 University of Bonn, Medical Faculty, Institute for Medical Biometry, Informatics and Epidemiology

4 Division Translational Genomics of Neurodegenerative Diseases, Hertie Institute for Clinical Brain Research & Center of Neurology, University of Tübingen, Germany

5 German Center for Neurodegenerative Diseases (DZNE), Tübingen, Germany.

6 Institute for Medical Genetics and Applied Genomics, University of Tuebingen, Tuebingen, Germany

7 Center for Neuroscience and Cell Biology (CNC), University of Coimbra, Coimbra, Portugal

8 Center for Innovative in Biomedicine and Biotechnology (CIBB), University of Coimbra, Coimbra, Portugal

9 Ataxia Centre, Department of Clinical and Movement Neurosciences, UCL Queen Square Institute of Neurology, University College London, London WC1N 3BG, UK

10 Department of Neurogenetics, National Hospital for Neurology and Neurosurgery, University College London Hospitals NHS Foundation Trust, London WC1N 3BG, UK

11 Faculdade de Ciências e Tecnologia, Universidade dos Açores, Ponta Delgada, Portugal

12 Instituto de Biologia Molecular e Celular (IBMC), Instituto de Investigação e Inovação em Saúde (i3S), Universidade do Porto, Porto, Portugal

13 Faculty of Pharmacy, University of Coimbra, Azinhaga de Santa Comba, 3000-548 Coimbra, Portugal

14 Department of Neurology, Donders Institute for Brain, Cognition, and Behaviour, Radboud university medical center

15 Department of Neurology, Rinjstate Hospital, Arnhem, The Netherlands

16 University Medical Center Groningen, Neurology

17 Center for Magnetic Resonance Research, Department of Radiology, University of Minnesota, Minneapolis, MN, USA

18 University Hospital Marqués de Valdecilla-IDIVAL, Santander, Spain

19 Centro de investigación biomédica en red de enfermedades neurodegenerativas (CIBERNED), Universidad de Cantabria, Santander, Spain

20 Department of Neurology and Center for Translational Neuro- and Behavioral Sciences (C-TNBS), University Hospital Essen, University of Duisburg-Essen

21 Department of Neurology, University Hospital of Heidelberg, Germany

22 Department of Neurology, RWTH Aachen University, Pauwelsstr. 30, 52074 Aachen, Germany

23 JARA-BRAIN Institute Molecular Neuroscience and Neuroimaging, Research Centre Juelich GmbH and RWTH Aachen University, 52074 Aachen, Germany

24 Department of Psychiatry and Behavioral Sciences, Johns Hopkins University School of Medicine, Baltimore, Maryland USA

25 Johns Hopkins University School of Medicine, Baltimore, MD 21205, USA

26 Ataxia Center, Laboratory for Neuroanatomy and Cerebellar Neurobiology, Massachusetts General Hospital and Harvard Medical School

27 Massachusetts General Hospital, Department of Radiology, A. A. Martinos Center for Biomedical Imaging and Harvard Medical School, Charlestown, Massachusetts, USA

Correspondence to: Jennifer Faber

Full address:

German Center for Neurodegenerative Diseases (DZNE), Bonn, Germany

Venusberg-Campus 1, 53127 Bonn

E-Mail: jennifer.faber@dzne.de

Running title: Biomarker changes in SCA3

Abstract

Spinocerebellar ataxia type 3/Machado–Joseph disease (SCA3) is the most common autosomal dominant ataxia. In view of the development of targeted therapies, knowledge of early biomarker changes is needed. We analyzed cross-sectional data of 292 SCA3 mutation carriers. Blood concentrations of mutant ATXN3 were high before and after ataxia onset, while neurofilament light deviated from normal 13.3 years before onset. Pons and cerebellar white matter volumes decreased and deviated from normal 2.2 years and 0.6 years before ataxia onset. We propose a staging model of SCA3 that includes a biomarker stage characterized by objective indicators of neurodegeneration before ataxia onset.

Introduction

Spinocerebellar ataxia type 3/Machado–Joseph disease (SCA3) is the most common autosomal dominantly inherited adult-onset ataxia disease worldwide with a progressive course leading to increasing disability and premature death. It is caused by unstable expansions of polyglutamine encoding CAG repeats, resulting in the formation of the abnormally elongated disease protein ATXN3.[1] Targeted therapies for SCA3 are being developed, and first safety trials of an antisense oligonucleotides (ASOs) have been initiated (https://clinicaltrials.gov, NCT05160558, NCT05822908). Future, preventive trials including SCA3 mutation carriers before ataxia onset are a realistic option. For the design of such trials, a thorough understanding of the dynamics of biomarkers that reflect the cascade of pathological events associated with SCA3 is a crucial prerequisite.

We analysed a large cross-sectional dataset of SCA3 mutation carriers ranging from the early phase before ataxia onset to the late advanced phase. Our aim was to delineate fluid and MRI biomarker changes in relation to ataxia manifestation that reflect key pathological changes of SCA3 and are known to be abnormal before ataxia onset, namely ATXN3, neurofilament light (NfL) as wells as MRI derived pons and cerebellar volumes.[2-10] By using a two-step regression analysis considering clinical as well as fluid and imaging biomarker, data we were for the first time able to propose a staging model of SCA3.

Materials and methods

Study participants

This prospective, longitudinal, observational cohort study is carried out at 14 sites in five European countries and the United States. Participants of the European Spinocerebellar Ataxia Type 3 / Machado-Joseph Disease Initiative (ESMI) cohort undergo annual standardized assessment including a clinical examination and biosampling. MRI is performed at 11 sites. SCA3 mutation carriers, their first-degree relatives and healthy controls (HC) are eligible for inclusion. The study protocol is available under the following link: https://idsn.dzne.de/esmi/study-protocols.

For this analysis, we used cross-sectional data of 292 SCA3 mutation carriers and 108 healthy controls of whom at least one fluid or MRI biomarker result was available at Jan 31, 2022. The

ESMI consortium previously published individual biomarker data separately, and the present analysis is largely based on the combination of these data.[3, 5, 8] The study was approved by the local ethics committees. Written informed consent according to the declaration of Helsinki was obtained from all participants.

Assessments

We used the Scale for the Assessment and Rating of Ataxia (SARA)[11] to assess the presence and severity of ataxia. Manifest ataxia was defined by a score of ≥ 3.

Using a single molecule counting immunoassay, we measured plasma concentrations of expanded ATXN3.[3] Serum concentrations of NfL were determined with an ultra-sensitive single-molecule array (Simoa) assay.[5] One single outlier with a value of NfL 4-fold higher than all other participants was excluded.

T1-weighted MRIs were acquired using a magnetization prepared rapid gradient-echo sequence (MPRAGE, TR = 2500 ms, TE = 4.37 ms, TI = 1100 ms, flip angle = 7 deg, FOV 256 mm x 256 mm, 192 slices with a voxel size of 1 mm isotropic) on Siemens 3T scanners (Siemens Medical Systems, Erlangen, Germany). Volumes of the pons, cerebellar white matter (CWM) and cerebellar grey matter (CGM)[7] were measured and normalized by each participants total intracranial volume.

In 243 study participants from whom DNA samples were available, repeat lengths of the expanded and normal alleles were centrally determined. For 43 participants, information about repeat lengths was taken from medical records; in six participants, no information was available.

Age of ataxia onset was defined as the reported first occurrence of gait disturbances. Forty-seven SCA3 mutation carriers did not yet experience gait disturbances (right-censored individuals). In a minority of patients (n = 14, 4.8%) with gait disturbance, information on the reported age of onset was missing (left-censored individuals). In these 61 SCA3 mutation carriers, the age of onset was estimated, as described below.

Statistical analysis

Statistical analysis was carried out using R version 4.1.1 (R Core Team 2022: R: A Language and Environment for Statistical Computing, R Foundation for Statistical Computing, Vienna, Austria).

To relate fluid and MRI biomarker data to the time from ataxia onset, we applied a conditional multiple imputation approach.[12] First, censored values of age of ataxia onset (or equivalently time from ataxia onset) were imputed fitting the parametric survival model by Tezenas du Montcel et al..[13] To account for interval censoring, covariate values were imputed with the conditional expectation for right-censored individuals (accounting for actual age) and with the unconditional expectation for left-censored individuals. Second, additive regression models were fitted for fluid and MRI biomarker values to the imputed covariate specifying a cubic P-spline with six B-spline basis functions and a second order difference penalty. This two-step procedure was repeatedly applied to 1000 bootstrap samples from the original sample. Final estimates of the spline coefficients and associated variance estimates were then calculated by applying Rubin's rule.

For regression, NfL concentrations and MRI volumes were z-transformed with respect to age as described before.[8] Since SARA scores and ATXN3 concentrations in healthy controls are close to 0, no z-transformation was performed and the raw values were used. The analysis of the z-scores of NfL and MRI biomarkers was additionally adjusted for sex and site in multivariable regression models, and the analysis of ATXN3 and SARA for sex, sites and age. To test for confounding effects of sex and site, and age, if applicable, a Bonferroni-Holm correction was applied.

Based on these regression models we defined the carrier, biomarker and ataxia stage. For a detailed description we refer to the results section. Fluid and imaging biomarker values as well as SARA sum scores were compared between the three stages using one-way ANOVA followed by pairwise comparisons using Tukey's test.

Results

Fifty-seven SCA3 mutation carriers before ataxia onset (35 female, mean age 35.5 years (standard deviation (SD) 9.0), mean time from ataxia onset -10.1 years (SD 8.6)), 235 ataxic SCA3 mutation carriers (109 female, mean age 51.3 years (SD 11.3), mean time from ataxia

onset 11.2 years (SD 7.8)) and 108 healthy controls (59 female, mean age 46.1 years (SD 14.0)) were included. MRI results, ATXN3 concentrations, and NfL levels were available in 161 (116 SCA3, 45 HC), 134 (122 SCA3, 12 HC), 327 participants (239 SCA3, 88 HC), respectively, with an overlap between all three markers in 38 participants (33 SCA3, 5 HC), between ATXN3 and MRI in 39 (34 SCA3, 5 HC), between NfL and MRI in 96 (70 SCA3, 26 HC), and between ATXN3 and NfL in 115 participants (103 SCA3, 12 HC).

Changes of SARA scores, fluid biomarker levels, and MRI volumes of SCA3 mutation carriers in relation to the time from ataxia onset are shown in Figure 1. Overlap of the NfL 95% CIs of SCA3 mutation carriers with the interval of mean ± 2 SD of controls ended 13.3 years before onset. The overlap of pons and CWM volumes with controls ended 2.2 years (pons) and 0.6 years (CWM) before ataxia onset. CGM volume only slightly decreased and stayed within the ± 2 SD range around the mean of controls during the entire disease course. Multivariable confounding analyses showed no evidence for an effect of sex and site for the MRI biomarker and NfL, and of sex, site and age for ATXN3 and SARA.

Based on the temporal sequence of biomarker changes, we defined the following disease stages: (i) The carrier stage includes mutation carriers before ataxia onset without significant biomarker abnormalities other than the presence of mutant ATXN3 (SARA < 3 and NfL z-score < 2). We chose NfL as a criterion, as the preceding analysis showed that levels of NfL were the first of the studied biomarkers to change. (ii) The biomarker stage includes mutation carriers before ataxia onset with significant biomarker changes in the absence of ataxia (SARA < 3 and NfL z-score ≥ 2). (iii) The ataxia stage includes ataxic mutation carriers, defined by SARA ≥ 3 (Figure 2). Changes of SARA and the analyzed biomarkers in each stage are shown in Figure 3.

Discussion

Using cross-sectional data from 292 SCA3 mutation carriers, we estimated the sequence and extent of fluid and imaging biomarker changes along the disease course. Based on the observed changes, we drafted a staging model of SCA3 that includes an initial asymptomatic carrier stage followed by the biomarker stage characterized by absence of ataxia, but changes of NfL as well as pons and cerebellar white matter volumes, finally leading into the ataxia stage, defined by manifest ataxia.[14]

This study has a number of limitations, the most important of which is its cross-sectional design. Even though ESMI is one of the largest SCA3 cohorts worldwide, the data volume, on particular of biomarkers was still limited resulting in only few individuals, in which all biomarkers were concurrently obtained. As MRI was only conducted at select sites, brain volume data were available of less than half of the participants resulting in increased variability. Enrolment of mutation carriers from regions with significant disease cluster, such as the Azores, and from non-cluster regions is a potential source of variability that might affect the modelling. However, an analysis of possible confounders did not show an effect of the study site. Additional sources of variability include potential inaccuracy of the estimated age of ataxia onset, and imperfect matching of the control population. Supplementation by longitudinal data and merging with data from other cohorts is therefore needed to corroborate our results.

Mutant ATXN3 was not used as a criterion for the definition of the biomarker stage, since concentrations were high detectable throughout the entire disease course characterizing it as a trait rather than a progression biomarker. The rise of NfL marks the first currently detectable damage to the nervous system in SCA3 and preceded ataxia onset by 11.9 years. This agrees with previous reports on NfL data of ESMI participants,[2, 5] as well as findings in other cohorts.[15, 16] Consequently, we used NfL as a criterion to define the biomarker stage in individuals prior to ataxia onset. While NfL is supposed to reflect the rate of degeneration,[5] volume loss rather represents the cumulated result of degeneration explaining why volume loss followed the rise of NfL.[15] Since pons and CWM volumes showed a continuous decrease and deviated from normal 2.0 and 0.3 years before ataxia onset, they may be considered for the stratification of mutation carriers close to the clinical onset. The prominent white matter loss is in line with autopsy and previous MRI findings that show relative sparing of cerebellar cortex in SCA3.[17,18, 19] Moreover, it is in line with observations of early oligodendrocyte pathology in mouse models of SCA3.[20]

The present data allowed for the first time to draft of a data-driven model of disease stages for SCA3 similar to that recently presented for Huntington's disease (HD).[21] Further studies including additional fluid and imaging biomarker data, such as MR spectroscopy and diffusion imaging,[6] may allow to further subdivide the biomarker stage. The present staging model of SCA3 is to be considered as a first draft that needs to be further refined and extended based

on more data and broad consensus. Nevertheless, it provides a robust framework for further studies aiming at elaboration and differentiation of a staging model of SCA3.

Acknowledgements

TK, MS, LS, JI, BvdW are members of the European Reference Network for Rare Neurological Diseases (ERN-RD, project number 739510). The ESMI consortium acknowledges Ruth Hossinger for the project management of the ESMI project and for all contributions made towards the success of this project.

This publication is an outcome of ESMI, an EU Joint Programme - Neurodegenerative Disease Research (JPND) project (see www.jpnd.eu). The project is supported through the following funding organisations under the aegis of JPND: Germany, Federal Ministry of Education and Research (BMBF; funding codes 01ED1602A/B); Netherlands, The Netherlands Organisation for Health Research and Development; Portugal, Fundação para a Ciência e Tecnologia (funding code JPCOFUND/0002/2015); United Kingdom, Medical Research Council (MR/N028767/1). This project has received funding from the European Union's Horizon 2020 research and innovation programme under grant agreement No 643417.

On the Azores ESMI Network is currently supported by the Regional Government (Fundo Regional para a Ciência e a Tecnologia-FRCT), under the PRO-SCIENTIA program.

At the US sites this work was in part supported by the National Ataxia Foundation and the National Institute of Neurological Disorders and Stroke (NINDS) grant R01NS080816. The Center for Magnetic Resonance Research is supported by the National Institute of Biomedical Imaging and Bioengineering (NIBIB) grant P41 EB027061, the Institutional Center Cores for Advanced Neuroimaging award P30 NS076408 and S10 OD017974 grant.

JF received funding as a fellow of the Hertie Network of Excellence in Clinical Neuroscience. MR is supported by FCT (CEECIND/03018/2018). BvdW receives funding from ZonMw, NWO, Gossweiler Foundation, Brugling Fonds, Radboudumc, Hersenstichting. DT received research grants from the Deutsche Forschungsgemeinschaft (DFG), European Union (EU), the Bernd Fink Foundation and the Once Upon a Time Foundation. CO receives funding from NINDS #U01

NS104326; National Ataxia Foundation; Robert and Nancy Hall Brain Research Fund. JS was supported in part by the National Ataxia Foundation and the MINDlink Foundation. JJ received grant support from NIH and Friedrich's Ataxia Research Alliance (FARA). AT received research grants from the University Medicine Essen Clinician Scientist Academy (UMEA)/Deutsche Forschungsgemeinschaft (DFG, grant number: FU356/12-1), the Mercator Research Foundation, the German Heredoataxia Society (DHAG) and "Freunde und Förderer der Neurologie der Universitätsmedizin Essen". At the Portuguese sites, MMS and LPA received funding from European Regional Development Fund (ERDF), through the Centro 2020 Regional Operational Program; through the COMPETE 2020 - Operational Programme for Competitiveness and Internationalisation, and Portuguese national funds via FCT – Fundação para a Ciência e a Tecnologia, under the projects: CENTRO-01-0145-FEDER-181240, 2022.06118.PTDC, UIDB/04539/2020, UIDP/04539/2020, LA/P/0058/2020, ViraVector (CENTRO-01-0145-FEDER-022095), ReSet - IDT-COP (CENTRO-01-0247-FEDER-070162), Fighting Sars-CoV-2 (CENTRO-01-01D2-FEDER-000002), BDforMJD (CENTRO-01-0145-FEDER-181240), ModelPolyQ2.0 (CENTRO-01-0145-FEDER-181258), MJDEDIT (CENTRO-01-0145-FEDER-181266); ARDAT under the IMI2 JU Grant agreement No 945473 supported by the European Union's H2020 programme and EFPIA; by the American Portuguese Biomedical Research Fund (APBRF) and the Richard Chin and Lily Lock Machado-Joseph Disease Research Fund. PS (SFRH/BD/148451/2019) and MMP (2022.11089.BD) are supported FCT.

PS was supported by Portuguese Foundation for Science and Technology (FCT) under the fellowship grant SFRH/BD/148451/2019. CW was supported by the Clinician Scientist Program of the Medical Faculty Tübingen (480-0-0).

Author contributions:

Conception and design of the study: JF, TK

Acquisition and analysis of data: JF, MB, TK, MS, CW, JHS, TS, MMS, MGE, DO, BK, PG, HCM, CGR, ML, MR, AM, LPA, PS, MP, BvdW, JG, JV, GO, MS, LS, OR, JI, LM, DT, AT, HJ, KR, ID, CO, MP, JS, EMR

Drafting a significant portion of the manuscript: JF, TK, MB, MS

Competing interests

GO consults for IXICO Technologies Limited, which provides neuroimaging services and digital biomarker analytics to biopharmaceutical firms conducting clinical trials for SCAs, and receives research support from Biogen, which develops therapeutics for SCAs. MS has received consultancy honoraria from Janssen, Ionis, Orphazyme, Servier, Reata, GenOrph, and AviadoBio, all unrelated to the present manuscript. LS received consultancy honoraria from Vico Therapeutics and Novartis unrelated to the present manuscript. LPA research group has private funding from PTC Therapeutics, Uniqure, Wave life Sciences, Servier, Blade Therapeutics and Hoffmann-La Roche AG outside the submitted work.

References

1. Paulson H. Machado-Joseph disease/spinocerebellar ataxia type 3. Handb Clin Neurol. 2012;103:437-49.
2. Garcia-Moreno H, Prudencio M, Thomas-Black G, et al. Tau and neurofilament light-chain as fluid biomarkers in spinocerebellar ataxia type 3. Eur J Neurol. 2022 Aug;29(8):2439-52.
3. Hubener-Schmid J, Kuhlbrodt K, Peladan J, et al. Polyglutamine-Expanded Ataxin-3: A Target Engagement Marker for Spinocerebellar Ataxia Type 3 in Peripheral Blood. Mov Disord. 2021 Aug 16.
4. Li QF, Dong Y, Yang L, et al. Neurofilament light chain is a promising serum biomarker in spinocerebellar ataxia type 3. Mol Neurodegener. 2019 Nov 4;14(1):39.
5. Wilke C, Haas E, Reetz K, et al. Neurofilaments in spinocerebellar ataxia type 3: blood biomarkers at the preataxic and ataxic stage in humans and mice. EMBO Mol Med. 2020 Jun 8:e11803.
6. Chandrasekaran J, Petit E, Park YW, et al. Clinically Meaningful Magnetic Resonance Endpoints Sensitive to Preataxic Spinocerebellar Ataxia Types 1 and 3. Ann Neurol. 2022 Dec 13.
7. Faber J, Kugler D, Bahrami E, et al. CerebNet: A fast and reliable deep-learning pipeline for detailed cerebellum sub-segmentation. Neuroimage. 2022 Oct 27;264:119703.
8. Faber J, Schaprian T, Berkan K, et al. Regional Brain and Spinal Cord Volume Loss in Spinocerebellar Ataxia Type 3. Mov Disord. 2021 Oct;36(10):2273-81.
9. Rezende TJR, de Paiva JLR, Martinez ARM, et al. Structural signature of SCA3: From presymptomatic to late disease stages. Ann Neurol. 2018 Sep;84(3):401-8.
10. Prudencio M, Garcia-Moreno H, Jansen-West KR, et al. Toward allele-specific targeting therapy and pharmacodynamic marker for spinocerebellar ataxia type 3. Sci Transl Med. 2020 Oct 21;12(566).
11. Schmitz-Hubsch T, du Montcel ST, Baliko L, et al. Scale for the assessment and rating of ataxia: development of a new clinical scale. Neurology. 2006 Jun 13;66(11):1717-20.
12. Atem FD, Sampene E, Greene TJ. Improved conditional imputation for linear regression with a randomly censored predictor. Stat Methods Med Res. 2019 Feb;28(2):432-44.
13. Tezenas du Montcel S, Durr A, Rakowicz M, et al. Prediction of the age at onset in spinocerebellar ataxia type 1, 2, 3 and 6. J Med Genet. 2014 Jul;51(7):479-86.
14. Klockgether T, Ludtke R, Kramer B, et al. The natural history of degenerative ataxia: a retrospective study in 466 patients. Brain. 1998 Apr;121 (Pt 4):589-600.

15. Coarelli G, Darios F, Petit E, et al. Plasma neurofilament light chain predicts cerebellar atrophy and clinical progression in spinocerebellar ataxia. Neurobiol Dis. 2021 Jun;153:105311.
16. Peng Y, Zhang Y, Chen Z, et al. Association of serum neurofilament light and disease severity in patients with spinocerebellar ataxia type 3. Neurology. 2020 Dec 1;95(22):e2977-e87.
17. Koeppen AH. The Neuropathology of Spinocerebellar Ataxia Type 3/Machado-Joseph Disease. Adv Exp Med Biol. 2018;1049:233-41.
18. Piccinin CC, Rezende TJR, de Paiva JLR, et al. A 5-Year Longitudinal Clinical and Magnetic Resonance Imaging Study in Spinocerebellar Ataxia Type 3. Mov Disord. 2020 Jun 9.
19. Chandrasekaran J, Petit E, Park YW, et al. Clinically meaningful MR endpoints sensitive to preataxic SCA1 and SCA3. Ann Neurol. 2022 Dec 13.
20. Schuster KH, Zalon AJ, Zhang H, et al. Impaired Oligodendrocyte Maturation Is an Early Feature in SCA3 Disease Pathogenesis. J Neurosci. 2022 Feb 23;42(8):1604-17.
21. Tabrizi SJ, Schobel S, Gantman EC, et al. A biological classification of Huntington's disease: the Integrated Staging System. Lancet Neurol. 2022 Jul;21(7):632-44.

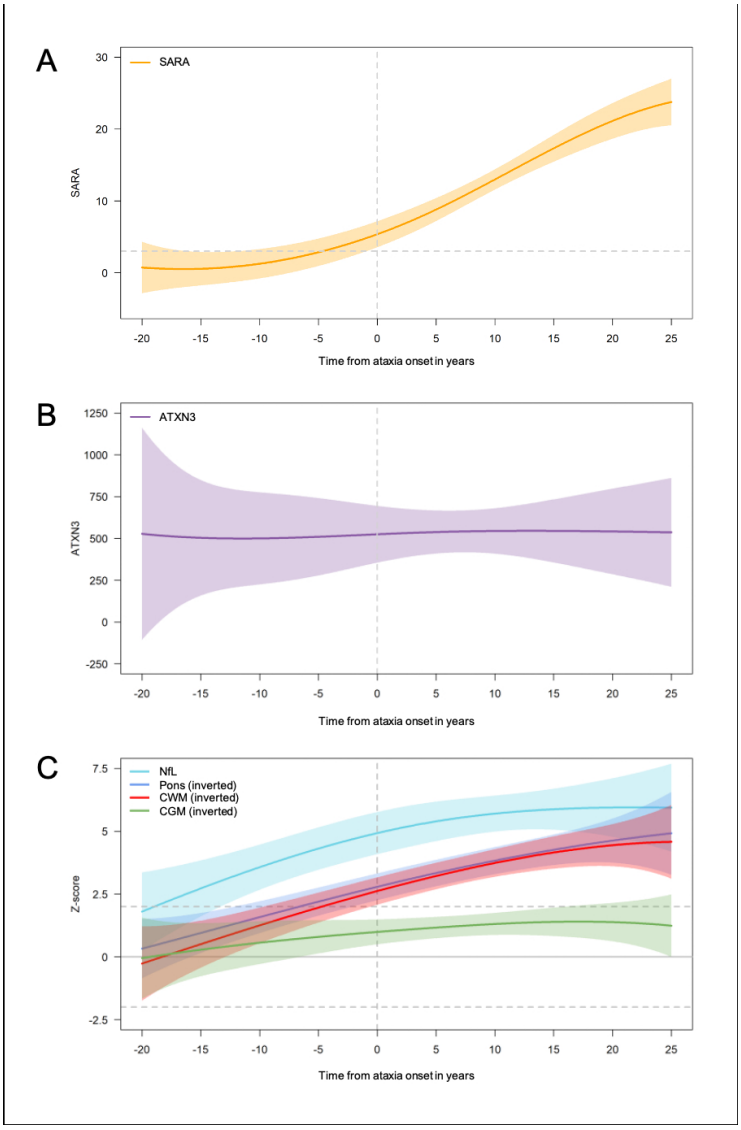

Scale for the Assessment and Rating of Ataxia (SARA) scores, fluid and MRI biomarker data in SCA3 mutation carriers in relation to time from ataxia onset. Data were analyzed with additive regression models on a time scale defined by ataxia onset. The time of ataxia onset is indicated with a vertical dashed line in all graphs. The estimated 95% CIs are shown by the shaded areas around the curves.
(A) SARA sum score. The SARA cut-off of 3 defining manifest ataxia is given as a dashed horizontal line.
(B) Plasma concentrations of elongated ATXN3. Data are given in ng/ml.
(C) Serum concentrations of neurofilament light (NfL), MRI volumes of the pons, cerebellar with matter (CWM) and grey matter (CGM). Data were z-transformed in relation to healthy controls of same age. Y-axis of volume values is inverted for better comparability of volume loss and NfL increase. Mean of healthy controls is given as a horizontal line, the 1 SD range by dashed, and the 2 SD range by dotted lines.

153x233mm (150 x 150 DPI)

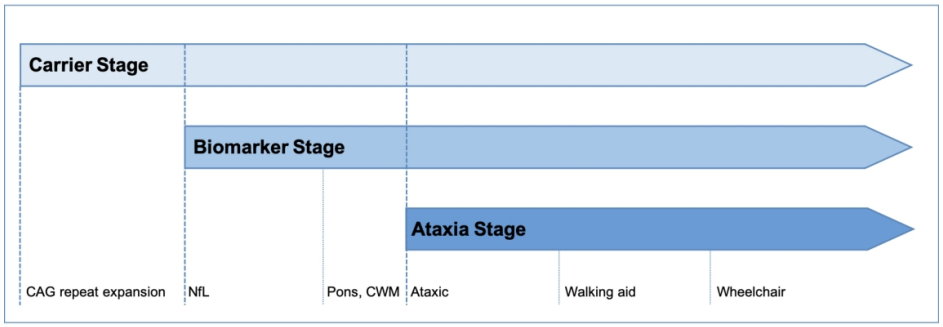

Staging model of SCA3. Proposed staging model of SCA3 based on the studied fluid and MRI biomarker data. The model includes an initial asymptomatic carrier stage followed by the biomarker stage defined by absence of ataxia, but a significant rise of NfL. The biomarker stage leads into the ataxia stage, which is defined by manifest ataxia. Following previous suggestions, the ataxia stage is further subdivided into three substages defined by milestones of gait deterioration.

2475x1749mm (72 x 72 DPI)

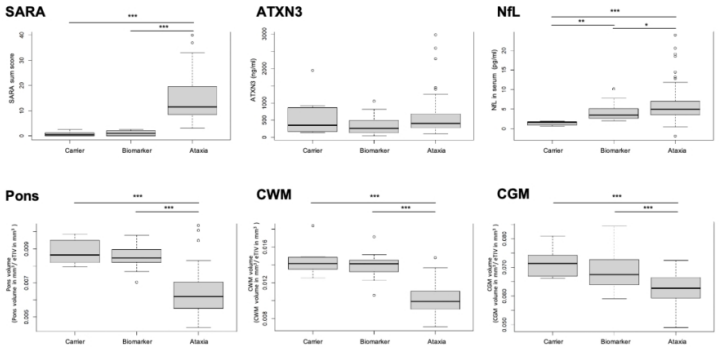

Scale for the Assessment and Rating of Ataxia (SARA) scores, fluid and MRI biomarker data in the carrier, biomarker and ataxia stage of SCA3. Data were analyzed with one-way ANOVA followed by pairwise comparisons using Tukey's test * p<0.01; **p<0.001. NfL - neurofilament light, CWM – cerebellar white matter, CGM – cerebellar grey matter, eTIV – estimated intracranial volume.

1749x2475mm (72 x 72 DPI)

Annals of Neurology - Decision on Manuscript # ANA-23-0498.R2

Annals of Neurology <onbehalfof@manuscriptcentral.com>

Di 17.10.2023 00:38

Posteingang

An: Faber, Dr. Jennifer <Jennifer.Faber@ukbonn.de>; Moritz.Berger@imbie.uni-bonn.de <Moritz.Berger@imbie.uni-bonn.de>; carlo.wilke@uni-tuebingen.de <carlo.wilke@uni-tuebingen.de>; jeannette.huebener@med.uni-tuebingen.de <jeannette.huebener@med.uni-tuebingen.de>; tamara.schaprian@dzne.de <tamara.schaprian@dzne.de>; mmsantana@uc.pt <mmsantana@uc.pt>; marcus.grobe-einsler@dzne.de <marcus.grobe-einsler@dzne.de>; demet.oender@dzne.de <demet.oender@dzne.de>; Berkan-Serdal-Can.Koyak@dzne.de <Berkan-Serdal-Can.Koyak@dzne.de>; p.giunti@ucl.ac.uk <p.giunti@ucl.ac.uk>; h.garcia-moreno@ucl.ac.uk <h.garcia-moreno@ucl.ac.uk>; cristina.robles@ucl.ac.uk <cristina.robles@ucl.ac.uk>; maria.mm.lima@uac.pt <maria.mm.lima@uac.pt>; mafalda.sb.raposo@uac.pt <mafalda.sb.raposo@uac.pt>; anarosavieiramelo@gmail.com <anarosavieiramelo@gmail.com>; luispa@cnc.uc.pt <luispa@cnc.uc.pt>; lpereiradealmeida@gmail.com <lpereiradealmeida@gmail.com>; pjsilva@cnc.uc.pt <pjsilva@cnc.uc.pt>; mariammpinto96@gmail.com <mariammpinto96@gmail.com>; bart.vandewarrenburg@radboudumc.nl <bart.vandewarrenburg@radboudumc.nl>; jvangaalen@live.nl <jvangaalen@live.nl>; j.j.de.vries01@umcg.nl <j.j.de.vries01@umcg.nl>; gulin@cmrr.umn.edu <gulin@cmrr.umn.edu>; jmjoers@umn.edu <jmjoers@umn.edu>; matthis.synofzik@uni-tuebingen.de <matthis.synofzik@uni-tuebingen.de>; Ludger.Schoels@uni-tuebingen.de <Ludger.Schoels@uni-tuebingen.de>; Olaf.Riess@med.uni-tuebingen.de <Olaf.Riess@med.uni-tuebingen.de>; jon.infante@scsalud.es <jon.infante@scsalud.es>; leire.manrique@scsalud.es <leire.manrique@scsalud.es>; dagmar.timmann-braun@uni-duisburg-essen.de <dagmar.timmann-braun@uni-duisburg-essen.de>; Andreas.Thieme@uk-essen.de <Andreas.Thieme@uk-essen.de>; heike.jacobi@med.uni-heidelberg.de <heike.jacobi@med.uni-heidelberg.de>; kreetz@ukaachen.de <kreetz@ukaachen.de>; idogan@ukaachen.de <idogan@ukaachen.de>; cuo@jhmi.edu <cuo@jhmi.edu>; mpovaza1@jhmi.edu <mpovaza1@jhmi.edu>; jschmahmann@mgh.harvard.edu <jschmahmann@mgh.harvard.edu>; ERATAI@mgh.harvard.edu <ERATAI@mgh.harvard.edu>; ext.Matthias.Schmid <Matthias.C.Schmid@uni-bonn.de>; Klockgether, Prof. Thomas <Thomas.Klockgether@ukbonn.de>;

Cc: klposton@stanford.edu <klposton@stanford.edu>; deborah_a_hall@rush.edu <deborah_a_hall@rush.edu>;

16-Oct-2023

Dear Dr Faber:

We are delighted to accept your manuscript entitled "Stage-dependent biomarker changes in spinocerebellar ataxia type 3" in its current form for publication in the Annals of Neurology.

Once we have vetted your submission files to be sure all of the technical requirements have been satisfied, your manuscript will be forwarded to our publisher, Wiley-Blackwell.

If you have any color figures, please be aware that the publisher will charge $650 for the first color figure, and $400 for each additional one. If your figures could be equally well represented in black and white, you can choose to have the color image appear online, and the black and white version on the printed page. To do this, take your color image into Photoshop (or a comparable program) and convert it to gray tone. Be sure to adjust the brightness and contrast so that the features you want to emphasize are clear. To use this method, though, you will have to make sure that neither the figure legend nor the text refers to color within the image, and that color contrast is not necessary for the image to be understandable.

You will receive a confirmation once the manuscript has been successfully transmitted to the publisher. Within six to seven weeks, your page proofs will arrive via e-mail from our Production Editor. If necessary, please configure your email security settings or spam filters to allow emails from anaprod@wiley.com to avoid any delays to publication. Please check your

proofs carefully for errors and return them promptly. The interval from acceptance to online publication is six to eight weeks, with print publication shortly thereafter.

This journal offers a number of license options for published papers; information about this is available here: https://authorservices.wiley.com/author-resources/Journal-Authors/licensing/index.html. The submitting author has confirmed that all co-authors have the necessary rights to grant in the submission, including in light of each co-author's funder policies. If any author's funder has a policy that restricts which kinds of license they can sign, for example if the funder is a member of Coalition S, please make sure the submitting author is aware.

Thank you for your fine contribution to the Annals.

Sincerely,
Dr Kathleen Poston
Associate Editor, Annals of Neurology

Dr Kenneth Tyler
Editor-in-Chief, Annals of Neurology

If you have any questions, please contact:

Daniel Roe, PhD,
Managing Editor
Annals of Neurology
AON@CUANSCHUTZ.EDU

Access the journal online: http://www.annalsofneurology.org
Submission and peer review: http://mc.manuscriptcentral.com/ana

NB: The editorial policy of the Annals of Neurology is to print corrections sparingly. We are reluctant to print corrections of errors that authors failed to pick up in the proofs, regardless of who introduced the error. Corrections of drug dosage mistakenly recommended will always be published.

4. Diskussion

MRT-Untersuchungen sind unerlässlich in der Diagnostik von Ataxieerkrankungen, primär zum Ausschluss erworbener Ursachen, aber auch zur Beurteilung typischer bildgebender Veränderungen. Bildgebende Biomarker bei degenerativen Ataxien sind Gegenstand der Forschung. Je nach Ataxieerkrankung steht hier das diagnostische Potential oder aber die Möglichkeiten zur Abbildung von Progression und Stratifikation oder Prognose im Vordergrund. Die hier dargestellten Arbeiten beleuchten diese verschiedenen Aspekte bildgebender Biomarker bei degenerativen Ataxien, zum einen das Potential bildgebender Veränderungen in der diagnostischen Abgrenzung der MSA-C von der deutlich langsamer progredienten SAOA und zum anderen, das Potential bildgebender Veränderungen als Progression- und Stratifikationsmarker im Krankheitsverlauf der weltweit häufigsten autosomal-dominant vererbten SCA3 unter Einschluss des prä-symptomatischen Stadiums. Im Kontext von bildgebenden Biomarkern ist es notwendig, Parameter zu wählen, die die Abbildung intra-individueller Trajektorien erlauben. Volumenwerte sind hierfür besonders geeignet. Allerdings stellt der hohe Arbeitsaufwand für manuelle Segmentierungen eine wesentliche Limitation dar, der die Nutzung automatisierter Verfahren notwendig macht. Die Neurodegeneration des Kleinhirns ist nachvollziehbarer Weise von zentralem Interesse bei Ataxieerkrankungen. Während die automatisierte Subsegmentierung des Großhirns bereits langjährig etabliert ist (FreeSurfer: http://surfer.nmr.mgh.harvard.edu/)(Fischl, Salat et al. 2002, Fischl, van der Kouwe et al. 2004), stehen nur wenige Verfahren zur automatisierten Subsegmentierung des Kleinhirns zur Verfügung.(Romero, Coupe et al. 2017, Carass, Cuzzocreo et al. 2018, Han, Carass et al. 2020) Diese haben deutliche Limitationen im Hinblick auf ihre Anwendbarkeit. Für die automatisierte zerebelläre Subsegmentierung mittels *CERES* ist es notwendig, die MRT-Daten auf einen externen Server zu übertragen.(Romero, Coupe et al. 2017) Dies ist teils durch die Einwilligungserklärungen der Probanden nicht ausreichend abgedeckt. *ACAPULCO* ist eine automatisierte Subsegmentierung, die auf einem neuronalen Netz basiert (Han, Carass et al. 2020). Grundlage hier sind allerdings manuelle Label, die die feine Verästelung der weißen Substanz im Kleinhirn nicht abbilden. Zusätzlich ist initial eine Ko-Registrierung in einen Standardraum notwendig, das bedeutet, die Segmentierung erfolgt nicht im nativen Bild. Im Rahmen der hier zusammengefassten Arbeiten entwickelten wir mit CerebNet ein

automatisiertes Verfahren zu Subsegmentierung des Kleinhirns, ebenfalls auf Basis neuronaler Netze. Die zugrunde liegenden manuellen Label, der sogenannte Goldstandard, wurden in einem aufwendigen Verfahren von zwei Ratern eingezeichnet und anschließend in Rahmen einer Konsensusfindung unter Einschluss neuroradiologischer Expertise festgelegt. Die Kohorte des Goldstandards umfasst SCA3 Mutationsträger*innen, insbesondere auch prä-symptomatische SCA3 Mutationsträger*innen. Zum einen, zeigte sich eine signifikante methodische Überlegenheit zu etablierten Verfahren (Faber et al., Abb. 3-6, pp. 7-10). Zum anderen, erhöhte das Training von *ACAPULCO*, mit den durch uns erstellten manuellen Goldstandard-Segmentierungen die Diskriminationsfähigkeit auf Gruppenebene zwischen prä-symptomatischen SCA3 und gesunden Kontrollen (Faber et al., Abb. 7, p. 11). Die Anwendung bei weiteren Ataxieerkrankungen wurde exemplarisch visuell geprüft und zeigte sehr zufriedenstellende Ergebnisse (Abb. 9, p13). Entsprechend verwendeten wir CerebNet auch für die Auswertungen von Kleinhirnvolumina in sporadischen und erblichen Ataxien.

Bei den sporadischen Ataxien stehen diagnostische bildgebende Biomarker im Vordergrund und erlangen zunehmend an Bedeutung, um die neuropathologisch definierte MSA-C von der SAOA abzugrenzen. Die Bedeutung bildgebend nachweisbarer Veränderungen wurde kürzlich auch in der Überarbeitung der Diagnosekriterien für MSA aufgewertet. Das Vorhandensein mindestens einer qualitativen bildgebenden Veränderung fand Eingang in die Kriterien für die Diagnose einer klinische nachgewiesenen MSA (Wenning, Stankovic et al. 2022). Die Überarbeitung der Diagnosekriterien für MSA war geleitet von dem Ziel der Verbesserung der Diagnosesicherheit, aber insbesondere auch der Verbesserung einer Diagnose früh im Krankheitsverlauf. Langfristiges Ziel ist es, damit auch einen frühen Beginn potentieller Therapien zu ermöglichen. Die im Rahmen dieser Arbeit vorgestellten quer- und längsschnittlichen Arbeiten zu MSA-C und SAOA zeigen das Potential bildgebender Marker in der Unterscheidung der beiden Patientengruppen (Faber, Giordano et al. 2020) sowie der prognostischen Relevanz bei klinisch noch nicht eindeutigem Phänotyp (Oender, Faber et al. 2023) auf. Bemerkenswert an der querschnittlichen Arbeit (Faber, Giordano et al. 2020) ist, dass, obwohl die beiden untersuchten Patientenkohorten von MSA-C und SAOA kein statistisch signifikant unterschiedliches Ausmaß an Atrophie der grauen und weißen Substanz zeigten, sich ein signifikanter Unterschied in der mikrostrukturellen Integrität der weißen Substanz

bei MSA-C sowohl im Kleinhirn und Hirnstamm als auch dem kortikospinalen Trakt fand. Diese Beobachtungen sind passend zu neuropathologischen Untersuchungen, die eine Betonung pathologischer Veränderungen in der weißen Substanz nachwiesen, entsprechend den charakteristischen alpha-Synuklein-Einschlüssen in Oligodendroglia (Wenning, Stefanova et al. 2008, Matsusue, Fujii et al. 2009). Die pathologischen Veränderungen des kortikospinalen Traktes ist darüber hinaus gut vereinbar mit klinischen Beobachtungen mit einer höheren Prävalenz von Pyramidenbahnzeichen bei MSA-C im Vergleich zu SAOA (da Rocha, Maia et al. 2007, Giordano, Harmuth et al. 2017). In der zweiten Arbeit zu sporadisch-degenerativen Ataxien lagen zusätzlich longitudinale Daten vor. Hier zeigte sich, dass Volumen von Pons und weißer Substanz des Kleinhirns sowie eine qualitative Erfassung bildgebender Parameter einen signifikanten Unterschied zwischen MSA-C und SAOA zeigten. Die qualitative Beurteilung umfasste eine gewichtete Beurteilung des „hot-cross-bun“-Zeichens, von Hyperintensitäten im mittleren Kleinhirnstiel sowie den Durchmesser der mittleren Kleinhirnstiels, zusammengefasst in einem Score. In der longitudinalen Kohorte bestand die Gelegenheit, Veränderungen mit hoher diagnostischer Relevanz zu untersuchen: Eine Subgruppe von Patient*innen erfüllte erst im Verlauf der Beobachtungszeit die klinischen Kriterien für MSA nach Gilman (Gilman, Wenning et al. 2008), so bezeichnete „klinische Konverter“. Hier konnten insgesamt vier Parameter als Risiko- bzw. protektive Faktoren für eine klinische Konversion identifiziert werden. Drei diese vier Parameter waren bildgebende Biomarker: Volumen von Pons und weißer Substanz des Kleinhirns waren protektive Faktoren, der qualitative Score und die klinischen Kriterien einer „möglichen MSA“(Gilman, Wenning et al. 2008) waren Risikofaktoren. Darüber hinaus, war der qualitative Score ein Prädiktor für eine raschere Krankheitsprogression. Wenngleich die zugrunde liegenden Fallzahlen sehr gering waren, unterstreichen auch diese Ergebnisse die Relevanz bildgebender Parameter bei MSA-C. Eine möglichst exakte Diagnosestellung bereits frühzeitig ist neben der Qualifikation für den Einschluss in klinische Studien insbesondere auch für eine Beratung der Patient*innen ein wesentlicher Faktor. In der klinischen Progression unterschieden sich nämlich MSA-C Patient*innen, die die MSA-Kriterien bereits bei Erstvorstellung erfüllten und solche Patient*innen, die erst im Laufe der Verlaufsbeobachtungen konvertierten nicht.

Im Gegensatz zu den sporadischen Ataxien ist bei hereditären Ataxien das einzig entscheidende Diagnosekriterium der Nachweis der krankheitsspezifischen Mutation.

Die Bedeutung bildgebender Biomarker liegt hier vielmehr in anderen Bereichen. Zum einen, sind zahlreiche Ataxien langsam fortschreitende Erkrankungen. Erste gentherapeutische Phase-I-Studien in den häufigsten autosomal-dominant vererbten Ataxien, SCA3 und SCA1, sind gestartet. Krankheitsspezifische Therapien erscheinen damit erstmals denkbar. Allerdings resultiert die vergleichsweise langsame klinische Progression (Ashizawa, Figueroa et al. 2013, Jacobi, du Montcel et al. 2015) in notwendigerweise relativ hohen Fallzahlen für klinische Prüfungen. Dies stellt eine Herausforderung dar, insbesondere im Bereich der seltenen Erkrankungen. Vorangehende Studien zeigten bereits, dass bildgebende Parameter klinischen Skalen überlegen sein können (Reetz, Costa et al. 2013, Adanyeguh, Perlbarg et al. 2018).

Verträglichkeit und Wirksamkeit der neuen gentherapeutischen Ansätze, die derzeit evaluiert werden, vorausgesetzt, stellt der Therapiebeginn schon vor Einsetzen der Ataxie den nächsten konsequenten Schritt dar. Um allerdings klinische Prüfungen in diesem Stadium zu ermöglichen, sind Biomarker unerlässlich, da klinische Skalen im prä-ataktischen Stadium nicht ausreichend sensitiv sind.

Bereits bei prä-ataktischen SCA3 zeigten sich Volumenminderungen in der Querschnittsfläche des Zervikalmarks, sowie der Medulla oblongata und Pons sowie dem Pallidum. Darüber hinaus, war der anteriore Lobus des Kleinhirns atrophiert. Unter Nutzung mathematischer Modelle, die den erwarteten Krankheitsbeginn schätzen (Tezenas du Montcel, Durr et al. 2014), war es möglich, eine einheitliche Zeitachse der Zeit bis bzw. seit Symptombeginn zu wählen. Die graphische Darstellung von Volumen versus Zeit mit lokaler Regression zeigte deutlich, dass die Atrophie von Zervikalmark, Hirnstamm und der weißen Substanz des Kleinhirns früher ausgeprägt vorhanden sind, als die etwa die Atrophie graue Substanz des Kleinhirns. Die Wiederholung in einer teils überlappenden Kohorte mit 42 prä-ataktischen SCA3 Mutationsträger*innen unter Nutzung der CerebNet-Subsegmentierung zeigte eine Volumenminderung im anterioren sowie posterior-inferioren Kleinhirn und anteilig dem Vermis, sowie erneut prägnant der weißen Substanz. Diese Ergebnisse passen zum zu Voruntersuchungen, die unter Verwendung von Voxel-basierter-Morphometrie (VBM) und vereinzelt Volumetrie eine Atrophie der grauen Substanz des Kleinhirns auf Gruppenebene für prä-ataktische SCA3 gezeigt haben (Reetz, Costa et al. 2013, Adanyeguh, Perlbarg et al. 2018, Hernandez-Castillo, King et al. 2018, Reetz, Rodriguez-Labrada et al. 2018, Rezende, de Paiva et al. 2018, Peng, Liang et al. 2019,

Piccinin, Rezende et al. 2020, Chandrasekaran, Petit et al. 2022). In den volumetrischen Auswertungen mit Unterschieden primär in der weißen Substanz sowie Lobulus X (Chandrasekaran, Petit et al. 2022). Darüber hinaus passt die Betonung von Veränderungen in der weißen Substanz insbesondere auch zur zunehmenden Evidenz einer starken Mitbeteiligung von Oligodendroglia in der Pathologie bei SCA3 (Ramani, Panwar et al. 2017, McLoughlin, Moore et al. 2018, Schuster, Zalon et al. 2022, Putka, Mato et al. 2023). Die graphische Darstellung der Veränderungen im zeitlichen Verlauf zeigt auch, dass mit zunehmendem Abstand vor Symptombeginn Abweichungen vom Gesunden deutlich geringer ausgeprägt sind mit Ausnahme des oberen Zervikalmarks, das durchgehend eine Minderung der Querschnittsfläche zeigte. Inwieweit dies möglicherweise eine Entwicklungsstörung reflektiert, bleibt zum aktuellen Zeitpunkt unklar. Deutlich wird durch die graphische Darstellung des zeitlichen Verlaufs allerdings, dass Ergebnisse bei Untersuchungen von präsymptomatischen Mutationsträger*innenn sicherlich von der Zusammensetzung des Kollektivs im Hinblick auf die Zeit bis zum Symptombeginn, analog zur Krankheitsdauer und Schweregrad, abhängen. Dies erklärt die zum Teil uneinheitlichen Ergebnisse entsprechender Gruppenvergleiche (Reetz, Costa et al. 2013, Adanyeguh, Perlbarg et al. 2018, Hernandez-Castillo, King et al. 2018, Reetz, Rodriguez-Labrada et al. 2018, Rezende, de Paiva et al. 2018, Peng, Liang et al. 2019, Piccinin, Rezende et al. 2020, Chandrasekaran, Petit et al. 2022). Passend zu neuropathologisch nachgewiesenen neuralen Einschlüssen in der Pons (Seidel, Siswanto et al. 2017, Koeppen 2018), zeigte das Pons-Volumen die kontinuierlichste und steilste Abnahme um den Beginn der Ataxie von allen weitergehend untersuchten Parameter (Abb. 1, p. 6). Darüber hinaus konnte ein Modell mit dem Schweregrad der Ataxie, der Anzahl der CAG-Wiederholungen im verlängerten Allel, sowie Alter und Geschlecht mit fast 50 % einen relevanten Anteil der Varianz des Pons-Volumen erklären, aber nur einen geringen Anteil der Varianz des Kleinhirnvolumens. Exemplarisch berechneten wir basierend auf einem linearen Zeitverlauf zudem Effektstärken, die aufgrund des querschnittlichen Studiendesigns allerdings nur eine eingeschränkte Aussagekraft haben. Dabei zeigte sich eine geringe Überlegenheit des Ponsvolumens gegenüber SARA.

Bereits frühere Untersuchungen zeigten eine Überlegenheit von bildgebenden Parametern gegenüber klinischen Skalen bei SCAs (Reetz, Costa et al. 2013, Adanyeguh, Perlbarg et al. 2018). Basierend auf diesen Vorarbeiten gingen wir einen

Schritt weiter mit dem Ziel, den Krankheitsverlauf der SCA3 in spezifische Stadien unter Einbeziehung von Biomarker-Daten zu unterteilen. Wir orientierten uns hier an dem kürzliche etablierten Modell für die Huntington-Krankheit (Tabrizi, Schobel et al. 2022). Einen wesentlichen Meilenstein und bisher meist einzigen Grenzpunkt stellt der Beginn der klinischen Symptomatik dar. Allerdings bedarf es auch hier einer einheitlichen Definition. Bisher wurde für die SCAs zwischen einer prä-symptomatischen oder prä-ataktischen Phase und einer symptomatischen oder ataktischen Phase unterschieden. Markiert je durch den Symptombeginn, der durch Beginn einer subjektiv vom/von der Patient*in wahrgenommenen Gangstörung definiert wurde, oder den „Ataxiebeginn“, der durch einen Schwellenwert in der Ataxieschwere gemessen mit der SARA Skala definiert ist. Dieser Schwellenwert ist abgeleitet vom Mittelwert plus zwei Standardabweichungen in der Validierungskohorte aus Gesunden.(Schmitz-Hubsch, du Montcel et al. 2006) Eine Ataxieschwere von gleich oder mehr als 3 Punkten im SARA wird als „ataktisch“ gewertet, darunter als „prä-ataktisch“. Beide Varianten haben Nachteile. Beide erfassen nicht alle möglichen ersten Symptome, wie zum Beispiel Doppelbilder. Die subjektive Einschätzung einer Gangstörung ist oftmals ungenau und hängt stark von der eigenen Körperwahrnehmung der Patient*innen ab. Inwieweit diese Definition eine Alltagsrelevanz besser widerspiegelt, bleibt fraglich. Letztlich wurde der SARA-Schwellenwert als Definition des Symptombeginns übernommen, da es sich hier um ein objektivierbares Kriterium handelt. Standardisierte Erhebung und die Verfügbarkeit von Trainings für Beurteilende stellen eine einheitliche Bewertung sicher (Grobe-Einsler, Amin et al. 2023). Das ataktische Krankheitsstadium wurde weiter unterteilt anhand wesentlicher Meilensteine mit hoher Relevanz für den Patienten: (i) Der Verlust des freien Gehens mit der Notwendigkeit zur Nutzung einer Gehhilfe und (ii) der Verlust der Gehfähigkeit mit der Notwendigkeit der Nutzung eines Rollstuhls (Klockgether, Ludtke et al. 1998). Für die Definition und Einteilung des prä-ataktischen Krankheitsstadiums wählten wir biochemische sowie bildgebende Biomarker-Kandidaten, die in vorangehenden Untersuchungen auf Gruppenebene einen signifikanten Unterschied zwischen prä-ataktischen Mutationsträger*innen und gesunden Kontrollen gezeigt haben: Das krankheitsspezifische Protein, mutiertes ATXN3, (Hubener-Schmid, Kuhlbrodt et al. 2021) Neurofilament light (NfL) als unspezifischer Marker für Neuronenverlust (Wilke, Haas et al. 2020, Garcia-Moreno, Prudencio et al. 2022) sowie das Volumen von Pons sowie grauer und weißer

Substanz des Kleinhirns (Faber, Schaprian et al. 2021, Chandrasekaran, Petit et al. 2022, Faber, Kugler et al. 2022). Alle verwendeten Biomarker wurden in Relation zu einer gesunden Kontrollgruppe z-standardisiert um die Vergleichbarkeit zwischen den verschiedenen Biomarker zu ermöglichen. Es zeigte sich eine Sequenz mit zunächst ansteigenden Werten von NfL beginnend etwa 12 Jahre vor dem geschätzten Krankheitsbeginn und Atrophie der Pons, etwa 2 Jahre, sowie der weißen Substanz des Kleinhirns, kurz vor dem Ataxiebeginn (Abb. 1, p. 16). Werte des krankheitsspezifischen Proteins, mutiertem ATXN3, zeigten keine relevante Änderung über die Zeit und waren durchgehend hoch. Auf der Grundlage dieser zeitlichen Abfolge der Biomarkerveränderungen definierten wir die folgenden Krankheitsstadien: (i) Das „Carrier-Stadium“, welches prä-ataxische Mutationsträger*innen ohne signifikante Biomarkerveränderungen außer dem Vorhandensein von mutiertem ATXN3, umfasst und ist definiert durch SARA < 3 und einen NfL z-score < 2. (ii) Das Biomarker-Stadium, welches prä-ataktische Mutationsträger*innen mit signifikanten Biomarker-Veränderungen, umfasst. Es ist definiert durch SARA < 3 und einen NfL z-Score ≥ 2. (iii) Das Ataxie-Stadium umfasst ataktische SCA3. Es ist definiert durch SARA ≥ 3 (Abbildung 2). Das Biomarker-Stadium ist weiterhin charakterisiert durch die im Verlauf auftretende Atrophie von Pons und weißer Substanz des Kleinhirns. Das Ataxie-Stadium ist weiterhin charakterisiert durch die o.g. klinischen Meilensteine des Verlusts des freien Gehens und schließlich Rollstuhlpflichtigkeit.

Es ist zu erwarten, dass das Biomarker-Stadium weiter unterteilt werden kann, insbesondere ist davon auszugehen, dass mikrostrukturelle Veränderungen der weißen Substanz, messbar mittels diffusionsgewichteter Bildgebung oder auch metabolische Auffälligkeiten, messbar mittels MR-Spektroskopie eine detailliertere Unterteilung erlauben (Rezende, de Paiva et al. 2018, Chandrasekaran, Petit et al. 2022). Letztlich ist es zudem möglich, dass andere bildgebende oder biochemische Biomarker zukünftig identifiziert werden, deren Abweichungen noch vor dem Anstieg von NfL beginnen. Basierend auf den aktuellen, querschnittlichen Daten scheint das Pons-Volumen ein geeigneter Biomarker zur Progressionsbeurteilung, insbesondere auch, da es über die klinische Manifestation hinweg eine kontinuierliche Abnahme zeigt. Weiterhin kommt es neben dem Volumen der weißen Substanz des Kleinhirns möglicherweise als Stratifikationsmarker prognostisch für den relativ nahen Symptombeginn in Frage.

Letztlich bedarf es longitudinaler Studien um diese Hypothesen zu prüfen. Neben der generellen Schwierigkeit, ausreichend große Kohorten bei seltenen Erkrankungen zu rekrutieren, ist die Notwendigkeit, Transitionen zu beobachten, also den Übergang von einem in das nächste Krankheitsstadium, eine enorme Herausforderung und wird stets einen limitierenden Faktor darstellen. In einer großen longitudinalen Beobachtungsstudie mit 252 erstgradigen Angehörigen von SCA1, SCA2, SCA3 und SCA6 Mutationsträger*innen wurden in einem ausgesprochen langen Beobachtungszeitraum von insgesamt 7 Jahren 61 Teilnehmer symptomatisch (entsprechend 24,2% aller Teilnehmer und 47,7% der Mutationsträger*innen) (Jacobi, du Montcel et al. 2020, Oender, Faber et al. 2023). In der longitudinalen Beobachtungsstudie bei sporadischen Ataxien waren es in einem noch längeren Beobachtungszeitraum von 12 Jahren 26 Patient*innenen, die initial als SAOA eingeschlossen wurden und erst im Verlauf die Diagnosekriterien einer wahrscheinlichen MSA-C nach Gilman erfüllten (entsprechend 10,5% der SAOA, und 6,4% aller eingeschlossenen Patient*innen) (Oender, Faber et al. 2023). Interessanterweise zeigte sich eine gewisse Überlappung in der Betonung von Veränderungen der weißen Substanz zwischen MSA-C und SCA3. Mit den typischen alpha-Synuklein-Einschlüssen ist MSA-C als Pathologie der Oligodendroglia etabliert, aber auch für die SCA3 häufen sich die Hinweise einer prominenten Affektion der Oligodendroglia (McLoughlin, Moore et al. 2018, Schuster, Zalon et al. 2022, Putka, Mato et al. 2023). Weitere longitudinale Daten, insbesondere unter Einschluss von SCA3 Mutationsträger*innen, die während des Beobachtungszeitraumes von einem in das nächste Krankheitsstadium übergehen ebenso wie konvertierende SAOA sind wichtig zur Prüfung der vermuteten Zusammenhänge. Aufgrund der Seltenheit der Erkrankungen, ist eine Zusammenführung und gemeinsame Analyse diverser, über die hier vorgestellten Konsortien hinausgehender Kohorten notwendig, um eine entsprechend große Zahl longitudinaler Daten zu erreichen.

5. Zusammenfassung

Bildgebende Biomarker bei degenerativen Ataxien haben in den sporadischen Ataxien des höheren Erwachsenenalters ein hohes diagnostische Potential und sind bei erblichen Ataxien, wichtige Parameter zur Beurteilung von Progression und

Stratifikation, insbesondere vor der klinischen Manifestation. Die hier vorgelegten Arbeiten beleuchten in der Zusammenschau diese verschiedenen Aspekte: Zum einen das Potential bildgebender Veränderungen in der diagnostischen Abgrenzung der MSA-C von der deutlich langsamer progredienten SAOA und zum anderen das Potential bildgebender Veränderungen als Progression- und Stratifikationsmarker im Krankheitsverlauf der SCA3, der weltweit häufigsten autosomal-dominant vererbten Ataxie . Im Kontext von bildgebenden Biomarkern empfiehlt es sich, solche zu wählen, die auch die Abbiledung intra-individuelle Trajektorien erlauben. Durch die Etablierung einer automatisierten Subsegmentierung des Kleinhirns wurde ein starkes Instrument zur Untersuchung des Potentials entsprechender - volumetrischer - Biomarker etabliert (Faber, Kugler et al. 2022).

In den beiden Arbeiten zu sporadischen Ataxien des höheren Erwachsenenalters, erfolgte zunächst eine quer-, dann längssschnittliche Analyse. Die querschnittliche Auswertung von bildgebenden Veränderungen erlaubte die Identifikation von Arealen, in denen sich die Patientengruppen der sporadischen Ataxien im höheren Erwachsenenalter, SAOA und die neuropathologisch definierte MSA-C unterscheiden. Bei in beiden Patientengruppen vergleichbar ausgeprägter Atrophie des Kleinhirns und Hirnstamms, zeigten sich Unterschiede in der Integrität der weißen Substanz des Kleinhirns, Hirnstamms und des kortikospinalen Traktes, betont in der Gruppe der MSA-C (Faber, Giordano et al. 2020). In der sich anschließende längsschnittliche Analyse wurden nun Trajektorien analysiert, unter anderem mit Verwendung der oben erwähnten automatisierten Segmentierungen des Kleinhirns. Es zeigte sich insbesondere, dass bildgebende Biomarker eine hohe Relevanz haben für die Vorhersage des Vorliegens einer MSA, als Risiko- bzw. protektive Faktoren. Hierzu zählen das Volumen von Pons und zerebellärer weißer Substanz sowie eine qualitative Beurteilung. Einzig die klinischen Kriterien für eine „mögliche“ MSA nach Gilman (Gilman, Wenning et al. 2008) erreichten hier ebenfalls Signifikanz als Risikofaktor (Oender, Faber et al. 2023).

Die beiden Arbeiten zur SCA3 unterstreichen die Bedeutung bildgebender Biomarker in der prä-ataktischen Krankheitsphase. Klinischen Skalen sind aufgrund der – noch – fehlenden Symptomatik nicht sensitiv. Entsprechend sind Biomarker die einzige Möglichkeit, um die Krankheitsausprägung und -progression zu beurteilen. Darüber hinaus können sie hilfreich sein in der Stratifikation von Patient*innen. Die Kombination mit biochemischen Biomarkern erlaubte ein erstes Stadienmodell für SCA3 unter

Einschluss eines Biomarker-positiven Stadiums vor Symptombeginn zu etablieren (Faber, Berger et al. 2023). Die dargelegten Ergebnisse bieten wichtige Anhaltspunkt für die Planung zukünftiger klinischer Prüfungen. Wir konnten zeigen, dass die Atrophie von Hirnstamm und Kleinhirn, insbesondere der Pons und weißen Substanz des Kleinhirns, bereits vor Beginn der klinischen Symptomatik messbar ist (Faber, Schaprian et al. 2021). In Relation zum geschätzten Beginn der Ataxie weicht das Volumen der Pons Die Volumina der weißen Substanz der Pons und des Kleinhirns wichen circa 2,0 Jahre bzw. 0,3 Jahre vor dem klinischen Beginn der Ataxie vom Normalwert ab (Faber, Berger et al. 2023). Sie stellen damit innerhalb des, dem klinisch manifesten Stadium vorangehenden, Biomarker-Stadiums potentielle Stratifikationsmarker dar für SCA3, deren Beginn der messbaren Ataxie bevorsteht.

6. Darstellung der Überlappung durch geteilte Autorenschaften

Die vorliegende Habilitationsschrift hat 4 publizierte Originalarbeiten zur Grundlage sowie einen preprint, der aktuell „resubmitted after review“ bei Annals of Neurology ist. Zwei der publizierten Originalarbeiten habe ich als alleiniger Erstautor verfasst. Eine Arbeit habe ich mit Frau Demet Önder mit geteilter Erstautorenschaft veröffentlicht. Frau Demet Önder ist eine wissenschaftlich engagierte Kollegin aus der Ataxiearbeitsgruppe. Die vorgestellte Arbeit beinhaltet sowohl die ausführliche Analyse klinischer Daten sowie biochemischer und genetischer Untersuchungen und die Auswertung der Bildgebung. Ich war federführend in der Bearbeitung und Auswertung der Bildgebungsdaten, Frau Demet Önder in der Auswertung der klinischen und biochemischen Daten. Die Festlegung des Konzeptes, sowie Gesamtschau und Analyse erfolgte gemeinschaftlich. Eine Arbeit habe ich mit Herrn Dr. David Kügler und Herrn Ehmad Bahrami mit geteilter Erstautorenschaft veröffentlicht. Das Konzept und die Initiierung sowie die manuellen Segmentierungen und finalen Prüfungen automatisiert erstellter Label erfolgten durch mich. Rein Training, Validierung und Test des neuronalen Netzes erfolgte durch die Kollegen der AG Prof. Martin Reuter.

7. Bibliographie

Adanyeguh, I. M., P. G. Henry, T. M. Nguyen, D. Rinaldi, C. Jauffret, R. Valabregue, U. E. Emir, D. K. Deelchand, A. Brice, L. E. Eberly, G. Oz, A. Durr and F. Mochel (2015). "In vivo neurometabolic profiling in patients with spinocerebellar ataxia types 1, 2, 3, and 7." Mov Disord **30**(5): 662-670.

Adanyeguh, I. M., V. Perlbarg, P. G. Henry, D. Rinaldi, E. Petit, R. Valabregue, A. Brice, A. Durr and F. Mochel (2018). "Autosomal dominant cerebellar ataxias: Imaging biomarkers with high effect sizes." Neuroimage Clin **19**: 858-867.

Arrasate, M., S. Mitra, E. S. Schweitzer, M. R. Segal and S. Finkbeiner (2004). "Inclusion body formation reduces levels of mutant huntingtin and the risk of neuronal death." Nature **431**(7010): 805-810.

Ashburner, J. (2007). "A fast diffeomorphic image registration algorithm." Neuroimage **38**(1): 95-113.

Ashburner, J. and K. J. Friston (2000). "Voxel-based morphometry--the methods." Neuroimage **11**(6 Pt 1): 805-821.

Ashizawa, T., K. P. Figueroa, S. L. Perlman, C. M. Gomez, G. R. Wilmot, J. D. Schmahmann, S. H. Ying, T. A. Zesiewicz, H. L. Paulson, V. G. Shakkottai, K. O. Bushara, S. H. Kuo, M. D. Geschwind, G. Xia, P. Mazzoni, J. P. Krischer, D. Cuthbertson, A. R. Holbert, J. H. Ferguson, S. M. Pulst and S. H. Subramony (2013). "Clinical characteristics of patients with spinocerebellar ataxias 1, 2, 3 and 6 in the US; a prospective observational study." Orphanet J Rare Dis **8**: 177.

Ashizawa, T., G. Oz and H. L. Paulson (2018). "Spinocerebellar ataxias: prospects and challenges for therapy development." Nat Rev Neurol **14**(10): 590-605.

Bettencourt, C., C. Santos, T. Kay, J. Vasconcelos and M. Lima (2008). "Analysis of segregation patterns in Machado-Joseph disease pedigrees." J Hum Genet **53**(10): 920-923.

Carass, A., J. L. Cuzzocreo, S. Han, C. R. Hernandez-Castillo, P. E. Rasser, M. Ganz, V. Beliveau, J. Dolz, I. Ben Ayed, C. Desrosiers, B. Thyreau, J. E. Romero, P. Coupe, J. V. Manjon, V. S. Fonov, D. L. Collins, S. H. Ying, C. U. Onyike, D. Crocetti, B. A. Landman, S. H. Mostofsky, P. M. Thompson and J. L. Prince (2018). "Comparing fully automated state-of-the-art cerebellum parcellation from magnetic resonance images." Neuroimage **183**: 150-172.

Carre, G., J. L. Dietemann, O. Gebus, S. Montaut, O. Lagha-Boukbiza, T. Wirth, S. Kremer, I. J. Namer, M. Anheim and C. Tranchant (2020). "Brain MRI of multiple system atrophy of cerebellar type: a prospective study with implications for diagnosis criteria." J Neurol **267**(5): 1269-1277.

Chandrasekaran, J., E. Petit, Y. W. Park, S. T. du Montcel, J. M. Joers, D. K. Deelchand, M. Povazan, G. Banan, R. Valabregue, P. Ehses, J. Faber, P. Coupe, C. U. Onyike, P. B. Barker, J. D. Schmahmann, E. M. Ratai, S. H. Subramony, T. H. Mareci, K. O. Bushara, H. Paulson, A. Durr, T. Klockgether, T. Ashizawa, C. Lenglet, G. Oz and R. Consortium (2022). "Clinically Meaningful Magnetic Resonance Endpoints Sensitive to Preataxic Spinocerebellar Ataxia Types 1 and 3." Ann Neurol.

Cortese, A., R. Simone, R. Sullivan, J. Vandrovcova, H. Tariq, W. Y. Yau, J. Humphrey, Z. Jaunmuktane, P. Sivakumar, J. Polke, M. Ilyas, E. Tribollet, P. J. Tomaselli, G. Devigili, I. Callegari, M. Versino, V. Salpietro, S. Efthymiou, D. Kaski, N. W. Wood, N. S. Andrade, E. Buglo, A. Rebelo, A. M. Rossor, A. Bronstein, P. Fratta, W. J. Marques, S. Zuchner, M. M. Reilly and H. Houlden (2019). "Biallelic expansion of an intronic repeat in RFC1 is a common cause of late-onset ataxia." Nat Genet **51**(4): 649-658.

Cortese, A., S. Tozza, W. Y. Yau, S. Rossi, S. J. Beecroft, Z. Jaunmuktane, Z. Dyer, G. Ravenscroft, P. J. Lamont, S. Mossman, A. Chancellor, T. Maisonobe, Y. Pereon, C. Cauquil, S. Colnaghi, G. Mallucci, R. Curro, P. J. Tomaselli, G. Thomas-Black, R. Sullivan, S. Efthymiou, A. M. Rossor, M. Laura, M. Pipis, A. Horga, J. Polke, D. Kaski, R. Horvath, P. F. Chinnery, W. Marques, C. Tassorelli, G. Devigili, L. Leonardis, N. W. Wood, A. Bronstein, P. Giunti, S. Zuchner, T. Stojkovic, N. Laing, R. H. Roxburgh, H. Houlden and M. M. Reilly (2020). "Cerebellar ataxia, neuropathy, vestibular areflexia syndrome due to RFC1 repeat expansion." Brain **143**(2): 480-490.

Cunha, P., E. Petit, M. Coutelier, G. Coarelli, C. Mariotti, J. Faber, J. Van Gaalen, J. Damasio, Z. Fleszar, M. Tosi, C. Rocca, G. De Michele, M. Minnerop, C. Ewenczyk, F. M. Santorelli, A. Heinzmann, T. Bird, M. Amprosi, E. Indelicato, A. Benussi, P. Charles, C. Stendel, S. Romano, M. Scarlato, I. Le Ber, M. T. Bassi, M. Serrano, T. Schmitz-Hubsch, S. Doss, G. A. J. Van Velzen, Q. Thomas, A. Trabacca, J. D. Ortigoza-Escobar, S. D'Arrigo, D. Timmann, C. Pantaleoni, A. Martinuzzi, E. Besse-Pinot, L. Marsili, E. Cioffi, F. Nicita, A. Giorgetti, I. Moroni, R. Romaniello, C. Casali, P. Ponger, G. Casari, S. T. De Bot, G. Ristori, L. Blumkin, B. Borroni, C. Goizet, C. Marelli, S. Boesch, M. Anheim, A. Filla, H. Houlden, E. Bertini, T. Klopstock, M. Synofzik, F. Riant, G. Zanni, S. Magri, D. Di Bella, L. Nanetti, J. Sequeiros, J. Oliveira, B. Van de Warrenburg, L. Schols, F. Taroni, A. Brice and A. Durr (2023). "Extreme phenotypic heterogeneity in non-expansion spinocerebellar ataxias." Am J Hum Genet.

da Rocha, A. J., A. C. Maia, Jr., C. J. da Silva, F. T. Braga, N. P. Ferreira, O. G. Barsottini and H. B. Ferraz (2007). "Pyramidal tract degeneration in multiple system atrophy: the relevance of magnetization transfer imaging." Mov Disord **22**(2): 238-244.

de Mattos, E. P., V. B. Leotti, B. W. Soong, M. Raposo, M. Lima, J. Vasconcelos, H. Fussiger, G. N. Souza, N. Kersting, G. V. Furtado, J. A. M. Saute, S. A. Camey, M. L. Saraiva-Pereira and L. B. Jardim (2019). "Age at onset prediction in spinocerebellar ataxia type 3 changes according to population of origin." Eur J Neurol **26**(1): 113-120.

Diedrichsen, J., J. H. Balsters, J. Flavell, E. Cussans and N. Ramnani (2009). "A probabilistic MR atlas of the human cerebellum." Neuroimage **46**(1): 39-46.

Diedrichsen, J. and E. Zotow (2015). "Surface-Based Display of Volume-Averaged Cerebellar Imaging Data." PLoS One **10**(7): e0133402.

Duennwald, M. L. (2011). "Polyglutamine misfolding in yeast: toxic and protective aggregation." Prion **5**(4): 285-290.

Durr, A. (2010). "Autosomal dominant cerebellar ataxias: polyglutamine expansions and beyond." Lancet Neurol **9**(9): 885-894.

Faber, J., M. Berger, W. Carlo, J. Hubener-Schmid, T. Schaprian, M. M. Santana, M. Grobe-Einsler, D. Onder, B. Koyak, P. Giunti, H. Garcia-Moreno, C. Gonzalez-Robles, M. Lima, M. Raposo, A. R. Vieira Melo, L. P. de Almeida, P. Silva, M. M. Pinto, B. P. van de Warrenburg, J. van Gaalen, J. Jeroen de Vries, G. Oz, J. M. Joers, M. Synofzik, L. Schols, O. Riess, J. Infante, L. Manrique, D. Timmann, A. Thieme, H. Jacobi, K. Reetz, I. Dogan, C. Onyike, M. Povazan, J. Schmahmann, E. M. Ratai, M. Schmid and T. Klockgether (2023). "Stage-dependent biomarker changes in spinocerebellar ataxia type 3." medRxiv.

Faber, J., I. Giordano, X. Jiang, C. Kindler, A. Spottke, J. Acosta-Cabronero, P. J. Nestor, J. Machts, E. Duzel, S. Vielhaber, O. Speck, A. Dudesek, C. Kamm, L. Scheef and T. Klockgether (2020). "Prominent White Matter Involvement in Multiple System Atrophy of Cerebellar Type." Mov Disord **35**(5): 816-824.

Faber, J., D. Kugler, E. Bahrami, L. S. Heinz, D. Timmann, T. M. Ernst, K. Deike-Hofmann, T. Klockgether, B. van de Warrenburg, J. van Gaalen, K. Reetz, S. Romanzetti, G. Oz, J. M. Joers, J. Diedrichsen, E. M. S. Group and M. Reuter (2022). "CerebNet: A fast and reliable deep-learning pipeline for detailed cerebellum sub-segmentation." Neuroimage **264**: 119703.

Faber, J., T. Schaprian, K. Berkan, K. Reetz, M. C. Franca, Jr., T. J. R. de Rezende, J. Hong, W. Liao, B. van de Warrenburg, J. van Gaalen, A. Durr, F. Mochel, P. Giunti, H. Garcia-Moreno, L. Schoels, H. Hengel, M. Synofzik, B. Bender, G. Oz, J. Joers, J. J. de Vries, J. S. Kang, D. Timmann-Braun, H. Jacobi, J. Infante, R. Joules, S. Romanzetti, J. Diedrichsen, M. Schmid, R. Wolz and T. Klockgether (2021). "Regional Brain and Spinal Cord Volume Loss in Spinocerebellar Ataxia Type 3." Mov Disord **36**(10): 2273-2281.

Fearnley, J. M., J. M. Stevens and P. Rudge (1995). "Superficial siderosis of the central nervous system." Brain **118 (Pt 4)**: 1051-1066.

Fischl, B., D. H. Salat, E. Busa, M. Albert, M. Dieterich, C. Haselgrove, A. van der Kouwe, R. Killiany, D. Kennedy, S. Klaveness, A. Montillo, N. Makris, B. Rosen and A. M. Dale (2002). "Whole brain segmentation: automated labeling of neuroanatomical structures in the human brain." Neuron **33**(3): 341-355.

Fischl, B., A. van der Kouwe, C. Destrieux, E. Halgren, F. Segonne, D. H. Salat, E. Busa, L. J. Seidman, J. Goldstein, D. Kennedy, V. Caviness, N. Makris, B. Rosen and A. M. Dale (2004). "Automatically parcellating the human cerebral cortex." Cereb Cortex **14**(1): 11-22.

Garcia-Moreno, H., M. Prudencio, G. Thomas-Black, N. Solanky, K. R. Jansen-West, R. Hanna Al-Shaikh, A. Heslegrave, H. Zetterberg, M. M. Santana, L. Pereira de Almeida, A. Vasconcelos-Ferreira, C. Januario, J. Infante, J. Faber, T. Klockgether, K. Reetz, M. Raposo, A. F. Ferreira, M. Lima, L. Schols, M. Synofzik, J. Hubener-Schmid, A. Puschmann, S. Gorcenco, Z. K. Wszolek, L. Petrucelli and P. Giunti (2022). "Tau and neurofilament light-chain as fluid biomarkers in spinocerebellar ataxia type 3." Eur J Neurol **29**(8): 2439-2452.

Gilman, S., G. K. Wenning, P. A. Low, D. J. Brooks, C. J. Mathias, J. Q. Trojanowski, N. W. Wood, C. Colosimo, A. Durr, C. J. Fowler, H. Kaufmann, T. Klockgether, A. Lees, W. Poewe, N. Quinn, T. Revesz, D. Robertson, P. Sandroni, K. Seppi and M. Vidailhet (2008). "Second consensus statement on the diagnosis of multiple system atrophy." Neurology **71**(9): 670-676.

Giordano, I., F. Harmuth, H. Jacobi, B. Paap, S. Vielhaber, J. Machts, L. Schols, M. Synofzik, M. Sturm, C. Tallaksen, I. M. Wedding, S. Boesch, A. Eigentler, B. van de Warrenburg, J. van Gaalen, C. Kamm, A. Dudesek, J. S. Kang, D. Timmann, G. Silvestri, M. Masciullo, T. Klopstock, C. Neuhofer, C. Ganos, A. Filla, P. Bauer, S. Tezenas du Montcel and T. Klockgether (2017). "Clinical and genetic characteristics of sporadic adult-onset degenerative ataxia." Neurology **89**(10): 1043-1049.

Globas, C., S. T. du Montcel, L. Baliko, S. Boesch, C. Depondt, S. DiDonato, A. Durr, A. Filla, T. Klockgether, C. Mariotti, B. Melegh, M. Rakowicz, P. Ribai, R. Rola, T. Schmitz-Hubsch, S. Szymanski, D. Timmann, B. P. Van de Warrenburg, P. Bauer and L. Schols (2008). "Early symptoms in spinocerebellar ataxia type 1, 2, 3, and 6." Mov Disord **23**(15): 2232-2238.

Grobe-Einsler, M., A. T. Amin, J. Faber, H. Volkel, M. Synofzik and T. Klockgether (2023). "Scale for the Assessment and Rating of Ataxia (SARA): Development of a Training Tool and Certification Program." Cerebellum.

Grobe-Einsler, M., A. Taheri Amin, J. Faber, T. Schaprian, H. Jacobi, T. Schmitz-Hubsch, A. Diallo, S. Tezenas du Montcel and T. Klockgether (2021). "Development of SARA(home) , a New Video-Based Tool for the Assessment of Ataxia at Home." Mov Disord.

Gruber, A., D. Hornburg, M. Antonin, N. Krahmer, J. Collado, M. Schaffer, G. Zubaite, C. Luchtenborg, T. Sachsenheimer, B. Brugger, M. Mann, W. Baumeister, F. U. Hartl, M. S. Hipp and R. Fernandez-Busnadiego (2018). "Molecular and structural architecture of polyQ aggregates in yeast." Proc Natl Acad Sci U S A **115**(15): E3446-E3453.

Gunawardena, S., L. S. Her, R. G. Brusch, R. A. Laymon, I. R. Niesman, B. Gordesky-Gold, L. Sintasath, N. M. Bonini and L. S. Goldstein (2003). "Disruption of axonal transport by loss of huntingtin or expression of pathogenic polyQ proteins in Drosophila." Neuron **40**(1): 25-40.

Han, S., A. Carass, Y. He and J. L. Prince (2020). "Automatic cerebellum anatomical parcellation using U-Net with locally constrained optimization." Neuroimage **218**: 116819.
Harding, I. H., P. Raniga, M. B. Delatycki, M. R. Stagnitti, L. A. Corben, E. Storey, N. Georgiou-Karistianis and G. F. Egan (2016). "Tissue atrophy and elevated iron concentration in the extrapyramidal motor system in Friedreich ataxia: the IMAGE-FRDA study." J Neurol Neurosurg Psychiatry **87**(11): 1261-1263.
Hernandez-Castillo, C. R., M. King, J. Diedrichsen and J. Fernandez-Ruiz (2018). "Unique degeneration signatures in the cerebellar cortex for spinocerebellar ataxias 2, 3, and 7." Neuroimage Clin **20**: 931-938.
Hubener-Schmid, J., K. Kuhlbrodt, J. Peladan, J. Faber, M. M. Santana, H. Hengel, H. Jacobi, K. Reetz, H. Garcia-Moreno, M. Raposo, J. van Gaalen, J. Infante, K. M. Steiner, J. de Vries, M. M. Verbeek, P. Giunti, L. Pereira de Almeida, M. Lima, B. van de Warrenburg, L. Schols, T. Klockgether, M. Synofzik, G. European Spinocerebellar Ataxia Type-3/Machado-Joseph Disease Initiative Study and O. Riess (2021). "Polyglutamine-Expanded Ataxin-3: A Target Engagement Marker for Spinocerebellar Ataxia Type 3 in Peripheral Blood." Mov Disord.
Jacobi, H., S. T. du Montcel, P. Bauer, P. Giunti, A. Cook, R. Labrum, M. H. Parkinson, A. Durr, A. Brice, P. Charles, C. Marelli, C. Mariotti, L. Nanetti, M. Panzeri, M. Rakowicz, A. Sulek, A. Sobanska, T. Schmitz-Hubsch, L. Schols, H. Hengel, L. Baliko, B. Melegh, A. Filla, A. Antenora, J. Infante, J. Berciano, B. P. van de Warrenburg, D. Timmann, S. Szymanski, S. Boesch, J. S. Kang, M. Pandolfo, J. B. Schulz, S. Molho, A. Diallo and T. Klockgether (2015). "Long-term disease progression in spinocerebellar ataxia types 1, 2, 3, and 6: a longitudinal cohort study." Lancet Neurol **14**(11): 1101-1108.
Jacobi, H., S. T. du Montcel, S. Romanzetti, F. Harmuth, C. Mariotti, L. Nanetti, M. Rakowicz, G. Makowicz, A. Durr, M. L. Monin, A. Filla, A. Roca, L. Schols, H. Hengel, J. Infante, J. S. Kang, D. Timmann, C. Casali, M. Masciullo, L. Baliko, B. Melegh, W. Nachbauer, K. Burk-Gergs, J. B. Schulz, O. Riess, K. Reetz and T. Klockgether (2020). "Conversion of individuals at risk for spinocerebellar ataxia types 1, 2, 3, and 6 to manifest ataxia (RISCA): a longitudinal cohort study." Lancet Neurol **19**(9): 738-747.
Jacobi, H., M. Rakowicz, R. Rola, R. Fancellu, C. Mariotti, P. Charles, A. Durr, M. Kuper, D. Timmann, C. Linnemann, L. Schols, O. Kaut, C. Schaub, A. Filla, L. Baliko, B. Melegh, J. S. Kang, P. Giunti, B. P. van de Warrenburg, R. Fimmers and T. Klockgether (2013). "Inventory of Non-Ataxia Signs (INAS): validation of a new clinical assessment instrument." Cerebellum **12**(3): 418-428.
Jennifer, F., H. Lea-Sophie, T. Dagmar, M. E. Thomas, D.-H. Katerina and K. Thomas (2022). "Manual sub-segmentation of the cererbellum." medRxiv: 2022.2005.2009.22274814.
Joers, J. M., D. K. Deelchand, T. Lyu, U. E. Emir, D. Hutter, C. M. Gomez, K. O. Bushara, L. E. Eberly and G. Oz (2018). "Neurochemical abnormalities in premanifest and early spinocerebellar ataxias." Ann Neurol **83**(4): 816-829.
Klockgether, T., T. Ashizawa, B. Brais, R. Chuang, A. Durr, B. Fogel, J. Greenfield, S. Hagen, L. B. Jardim, H. Jiang, O. Onodera, J. L. Pedroso, B. W. Soong, D. Szmulewicz, H. Graessner, M. Synofzik and I. Ataxia Global (2022). "Paving the Way Toward Meaningful Trials in Ataxias: An Ataxia Global Initiative Perspective." Mov Disord **37**(6): 1125-1130.
Klockgether, T., R. Ludtke, B. Kramer, M. Abele, K. Burk, L. Schols, O. Riess, F. Laccone, S. Boesch, I. Lopes-Cendes, A. Brice, R. Inzelberg, N. Zilber and J. Dichgans (1998). "The natural history of degenerative ataxia: a retrospective study in 466 patients." Brain **121 (Pt 4)**: 589-600.
Klockgether, T., C. Mariotti and H. L. Paulson (2019). "Spinocerebellar ataxia." Nat Rev Dis Primers **5**(1): 24.

Koeppen, A. H. (2018). "The Neuropathology of Spinocerebellar Ataxia Type 3/Machado-Joseph Disease." Adv Exp Med Biol **1049**: 233-241.
Lynch, D. R., J. M. Farmer, A. Y. Tsou, S. Perlman, S. H. Subramony, C. M. Gomez, T. Ashizawa, G. R. Wilmot, R. B. Wilson and L. J. Balcer (2006). "Measuring Friedreich ataxia: complementary features of examination and performance measures." Neurology **66**(11): 1711-1716.
Marek, M., S. Paus, N. Allert, B. Madler, T. Klockgether, H. Urbach and V. A. Coenen (2015). "Ataxia and tremor due to lesions involving cerebellar projection pathways: a DTI tractographic study in six patients." J Neurol **262**(1): 54-58.
Massey, L. A., C. Micallef, D. C. Paviour, S. S. O'Sullivan, H. Ling, D. R. Williams, C. Kallis, J. L. Holton, T. Revesz, D. J. Burn, T. Yousry, A. J. Lees, N. C. Fox and H. R. Jager (2012). "Conventional magnetic resonance imaging in confirmed progressive supranuclear palsy and multiple system atrophy." Mov Disord **27**(14): 1754-1762.
Matsusue, E., S. Fujii, Y. Kanasaki, T. Kaminou, E. Ohama and T. Ogawa (2009). "Cerebellar lesions in multiple system atrophy: postmortem MR imaging-pathologic correlations." AJNR Am J Neuroradiol **30**(9): 1725-1730.
McLoughlin, H. S., L. R. Moore, R. Chopra, R. Komlo, M. McKenzie, K. G. Blumenstein, H. Zhao, H. B. Kordasiewicz, V. G. Shakkottai and H. L. Paulson (2018). "Oligonucleotide therapy mitigates disease in spinocerebellar ataxia type 3 mice." Ann Neurol **84**(1): 64-77.
Oender, D., J. Faber, C. Wilke, T. Schaprian, A. Lakghomi, D. Mengel, L. Schols, A. Traschutz, Z. Fleszar, C. Dufke, S. Vielhaber, J. Machts, I. Giordano, M. Grobe-Einsler, T. Klopstock, C. Stendel, S. Boesch, W. Nachbauer, D. Timmann-Braun, A. G. Thieme, C. Kamm, A. Dudesek, C. Tallaksen, I. Wedding, A. Filla, M. Schmid, M. Synofzik and T. Klockgether (2023). "Evolution of Clinical Outcome Measures and Biomarkers in Sporadic Adult-Onset Degenerative Ataxia." Mov Disord.
Orozco Diaz, G., A. Nodarse Fleites, R. Cordoves Sagaz and G. Auburger (1990). "Autosomal dominant cerebellar ataxia: clinical analysis of 263 patients from a homogeneous population in Holguin, Cuba." Neurology **40**(9): 1369-1375.
Oz, G., I. H. Harding, J. Krahe and K. Reetz (2020). "MR imaging and spectroscopy in degenerative ataxias: toward multimodal, multisite, multistage monitoring of neurodegeneration." Curr Opin Neurol **33**(4): 451-461.
Paulson, H. (2012). "Machado-Joseph disease/spinocerebellar ataxia type 3." Handb Clin Neurol **103**: 437-449.
Paulson, H. L., V. G. Shakkottai, H. B. Clark and H. T. Orr (2017). "Polyglutamine spinocerebellar ataxias - from genes to potential treatments." Nat Rev Neurosci **18**(10): 613-626.
Pellecchia, M. T., I. Stankovic, A. Fanciulli, F. Krismer, W. G. Meissner, J. A. Palma, J. N. Panicker, K. Seppi, G. K. Wenning and G. Members of the Movement Disorder Society Multiple System Atrophy Study (2020). "Can Autonomic Testing and Imaging Contribute to the Early Diagnosis of Multiple System Atrophy? A Systematic Review and Recommendations by the Movement Disorder Society Multiple System Atrophy Study Group." Mov Disord Clin Pract **7**(7): 750-762.
Pellerin, D., M. C. Danzi, C. Wilke, M. Renaud, S. Fazal, M. J. Dicaire, C. K. Scriba, C. Ashton, C. Yanick, D. Beijer, A. Rebelo, C. Rocca, Z. Jaunmuktane, J. A. Sonnen, R. Lariviere, D. Genis, L. Molina Porcel, K. Choquet, R. Sakalla, S. Provost, R. Robertson, X. Allard-Chamard, M. Tetreault, S. J. Reiling, S. Nagy, V. Nishadham, M. Purushottam, S. Vengalil, M. Bardhan, A. Nalini, Z. Chen, J. Mathieu, R. Massie, C. H. Chalk, A. L. Lafontaine, F. Evoy, M. F. Rioux, J. Ragoussis, K. M. Boycott, M. P. Dube, A. Duquette, H. Houlden, G. Ravenscroft, N. G. Laing, P. J. Lamont, M. A. Saporta, R. Schule, L. Schols, R. La Piana, M. Synofzik, S. Zuchner and B. Brais (2023). "Deep Intronic FGF14 GAA Repeat Expansion in Late-Onset Cerebellar Ataxia." N Engl J Med **388**(2): 128-141.

Peng, H., X. Liang, Z. Long, Z. Chen, Y. Shi, K. Xia, L. Meng, B. Tang, R. Qiu and H. Jiang (2019). "Gene-Related Cerebellar Neurodegeneration in SCA3/MJD: A Case-Controlled Imaging-Genetic Study." Front Neurol **10**: 1025.
Peng, L., Z. Chen, Z. Long, M. Liu, L. Lei, C. Wang, H. Peng, Y. Shi, Y. Peng, Q. Deng, S. Wang, G. Zou, L. Wan, H. Yuan, L. He, Y. Xie, Z. Tang, N. Wan, Y. Gong, X. Hou, L. Shen, K. Xia, J. Li, C. Chen, R. Qiu, T. Klockgether, B. Tang and H. Jiang (2021). "New Model for Estimation of the Age at Onset in Spinocerebellar Ataxia Type 3." Neurology **96**(23): e2885-e2895.
Piccinin, C. C., T. J. R. Rezende, J. L. R. de Paiva, P. C. Moyses, A. R. M. Martinez, F. Cendes and M. C. Franca, Jr. (2020). "A 5-Year Longitudinal Clinical and Magnetic Resonance Imaging Study in Spinocerebellar Ataxia Type 3." Mov Disord.
Prudencio, M., H. Garcia-Moreno, K. R. Jansen-West, R. H. Al-Shaikh, T. F. Gendron, M. G. Heckman, M. R. Spiegel, Y. Carlomagno, L. M. Daughrity, Y. Song, J. A. Dunmore, N. Byron, B. Oskarsson, K. A. Nicholson, N. P. Staff, S. Gorcenco, A. Puschmann, J. Lemos, C. Januario, M. S. LeDoux, J. H. Friedman, J. Polke, R. Labrum, V. Shakkottai, H. S. McLoughlin, H. L. Paulson, T. Konno, O. Onodera, T. Ikeuchi, M. Tada, A. Kakita, J. D. Fryer, C. Karremo, I. Gomes, J. N. Caviness, M. R. Pittelkow, J. Aasly, R. F. Pfeiffer, V. Veerappan, E. R. Eggenberger, W. D. Freeman, J. F. Huang, R. J. Uitti, K. J. Wierenga, I. V. Marin Collazo, P. W. Tipton, J. A. van Gerpen, M. van Blitterswijk, G. Bu, Z. K. Wszolek, P. Giunti and L. Petrucelli (2020). "Toward allele-specific targeting therapy and pharmacodynamic marker for spinocerebellar ataxia type 3." Sci Transl Med **12**(566).
Putka, A. F., J. P. Mato and H. S. McLoughlin (2023). "Myelinating Glia: Potential Therapeutic Targets in Polyglutamine Spinocerebellar Ataxias." Cells **12**(4).
Ramani, B., B. Panwar, L. R. Moore, B. Wang, R. Huang, Y. Guan and H. L. Paulson (2017). "Comparison of spinocerebellar ataxia type 3 mouse models identifies early gain-of-function, cell-autonomous transcriptional changes in oligodendrocytes." Hum Mol Genet **26**(17): 3362-3374.
Reetz, K., A. S. Costa, S. Mirzazade, A. Lehmann, A. Juzek, M. Rakowicz, R. Boguslawska, L. Schols, C. Linnemann, C. Mariotti, M. Grisoli, A. Durr, B. P. van de Warrenburg, D. Timmann, M. Pandolfo, P. Bauer, H. Jacobi, T. K. Hauser, T. Klockgether, J. B. Schulz and I. axia Study Group (2013). "Genotype-specific patterns of atrophy progression are more sensitive than clinical decline in SCA1, SCA3 and SCA6." Brain **136**(Pt 3): 905-917.
Reetz, K., I. Dogan, R. D. Hilgers, P. Giunti, M. H. Parkinson, C. Mariotti, L. Nanetti, A. Durr, C. Ewenczyk, S. Boesch, W. Nachbauer, T. Klopstock, C. Stendel, F. J. Rodriguez de Rivera Garrido, C. Rummey, L. Schols, S. N. Hayer, T. Klockgether, I. Giordano, C. Didszun, M. Rai, M. Pandolfo, J. B. Schulz and E. s. group (2021). "Progression characteristics of the European Friedreich's Ataxia Consortium for Translational Studies (EFACTS): a 4-year cohort study." Lancet Neurol **20**(5): 362-372.
Reetz, K., R. Rodriguez-Labrada, I. Dogan, S. Mirzazade, S. Romanzetti, J. B. Schulz, E. M. Cruz-Rivas, J. A. Alvarez-Cuesta, R. Aguilera Rodriguez, Y. Gonzalez Zaldivar, G. Auburger and L. Velazquez-Perez (2018). "Brain atrophy measures in preclinical and manifest spinocerebellar ataxia type 2." Ann Clin Transl Neurol **5**(2): 128-137.
Rezende, T. J. R., J. L. R. de Paiva, A. R. M. Martinez, I. Lopes-Cendes, J. L. Pedroso, O. G. P. Barsottini, F. Cendes and M. C. Franca, Jr. (2018). "Structural signature of SCA3: From presymptomatic to late disease stages." Ann Neurol **84**(3): 401-408.
Romero, J. E., P. Coupe, R. Giraud, V. T. Ta, V. Fonov, M. T. M. Park, M. M. Chakravarty, A. N. Voineskos and J. V. Manjon (2017). "CERES: A new cerebellum lobule segmentation method." Neuroimage **147**: 916-924.

Ruano, L., C. Melo, M. C. Silva and P. Coutinho (2014). "The global epidemiology of hereditary ataxia and spastic paraplegia: a systematic review of prevalence studies." Neuroepidemiology **42**(3): 174-183.
Schmitz-Hubsch, T., S. T. du Montcel, L. Baliko, J. Berciano, S. Boesch, C. Depondt, P. Giunti, C. Globas, J. Infante, J. S. Kang, B. Kremer, C. Mariotti, B. Melegh, M. Pandolfo, M. Rakowicz, P. Ribai, R. Rola, L. Schols, S. Szymanski, B. P. van de Warrenburg, A. Durr, T. Klockgether and R. Fancellu (2006). "Scale for the assessment and rating of ataxia: development of a new clinical scale." Neurology **66**(11): 1717-1720.
Schuster, K. H., A. J. Zalon, H. Zhang, D. M. DiFranco, N. R. Stec, Z. Haque, K. G. Blumenstein, A. M. Pierce, Y. Guan, H. L. Paulson and H. S. McLoughlin (2022). "Impaired Oligodendrocyte Maturation Is an Early Feature in SCA3 Disease Pathogenesis." J Neurosci **42**(8): 1604-1617.
Seidel, K., W. F. den Dunnen, C. Schultz, H. Paulson, S. Frank, R. A. de Vos, E. R. Brunt, T. Deller, H. H. Kampinga and U. Rub (2010). "Axonal inclusions in spinocerebellar ataxia type 3." Acta Neuropathol **120**(4): 449-460.
Seidel, K., S. Siswanto, E. R. Brunt, W. den Dunnen, H. W. Korf and U. Rub (2012). "Brain pathology of spinocerebellar ataxias." Acta Neuropathol **124**(1): 1-21.
Seidel, K., S. Siswanto, M. Fredrich, M. Bouzrou, W. F. A. den Dunnen, I. Ozerden, H. W. Korf, B. Melegh, J. J. de Vries, E. R. Brunt, G. Auburger and U. Rub (2017). "On the distribution of intranuclear and cytoplasmic aggregates in the brainstem of patients with spinocerebellar ataxia type 2 and 3." Brain Pathol **27**(3): 345-355.
Stefanescu, M. R., M. Dohnalek, S. Maderwald, M. Thurling, M. Minnerop, A. Beck, M. Schlamann, J. Diedrichsen, M. E. Ladd and D. Timmann (2015). "Structural and functional MRI abnormalities of cerebellar cortex and nuclei in SCA3, SCA6 and Friedreich's ataxia." Brain **138**(Pt 5): 1182-1197.
Stoodley, C. J., J. P. MacMore, N. Makris, J. C. Sherman and J. D. Schmahmann (2016). "Location of lesion determines motor vs. cognitive consequences in patients with cerebellar stroke." Neuroimage Clin **12**: 765-775.
Tabrizi, S. J., S. Schobel, E. C. Gantman, A. Mansbach, B. Borowsky, P. Konstantinova, T. A. Mestre, J. Panagoulias, C. A. Ross, M. Zauderer, A. P. Mullin, K. Romero, S. Sivakumaran, E. C. Turner, J. D. Long, C. Sampaio and C. Huntington's Disease Regulatory Science (2022). "A biological classification of Huntington's disease: the Integrated Staging System." Lancet Neurol **21**(7): 632-644.
Tezenas du Montcel, S., A. Durr, M. Rakowicz, L. Nanetti, P. Charles, A. Sulek, C. Mariotti, R. Rola, L. Schols, P. Bauer, I. Dufaure-Gare, H. Jacobi, S. Forlani, T. Schmitz-Hubsch, A. Filla, D. Timmann, B. P. van de Warrenburg, C. Marelli, J. S. Kang, P. Giunti, A. Cook, L. Baliko, B. Melegh, S. Boesch, S. Szymanski, J. Berciano, J. Infante, K. Buerk, M. Masciullo, R. Di Fabio, C. Depondt, S. Ratka, G. Stevanin, T. Klockgether, A. Brice and J. L. Golmard (2014). "Prediction of the age at onset in spinocerebellar ataxia type 1, 2, 3 and 6." J Med Genet **51**(7): 479-486.
Traschutz, A., A. D. Adarmes-Gomez, M. Anheim, J. Baets, B. Brais, C. Gagnon, J. Gburek-Augustat, S. Doss, H. A. Hanagasi, C. Kamm, P. Klivenyi, T. Klockgether, T. Klopstock, M. Minnerop, A. Munchau, M. Renaud, F. M. Santorelli, L. Schols, A. Thieme, S. Vielhaber, B. P. van de Warrenburg, G. Zanni, R. D. Hilgers, P. consortium and M. Synofzik (2023). "Responsiveness of the SARA and natural history in 884 recessive and early onset ataxia patients." Ann Neurol.
Tsuji, S., O. Onodera, J. Goto, M. Nishizawa and D. Study Group on Ataxic (2008). "Sporadic ataxias in Japan--a population-based epidemiological study." Cerebellum **7**(2): 189-197.
Tu, P. H., J. E. Galvin, M. Baba, B. Giasson, T. Tomita, S. Leight, S. Nakajo, T. Iwatsubo, J. Q. Trojanowski and V. M. Lee (1998). "Glial cytoplasmic inclusions in white matter

oligodendrocytes of multiple system atrophy brains contain insoluble alpha-synuclein." Ann Neurol **44**(3): 415-422.
Wakabayashi, K., S. Hayashi, A. Kakita, M. Yamada, Y. Toyoshima, M. Yoshimoto and H. Takahashi (1998). "Accumulation of alpha-synuclein/NACP is a cytopathological feature common to Lewy body disease and multiple system atrophy." Acta Neuropathol **96**(5): 445-452.
Weidauer, S., E. Neuhaus and E. Hattingen (2023). "Cerebral Superficial Siderosis : Etiology, Neuroradiological Features and Clinical Findings." Clin Neuroradiol **33**(2): 293-306.
Wenning, G. K., I. Stankovic, L. Vignatelli, A. Fanciulli, G. Calandra-Buonaura, K. Seppi, J. A. Palma, W. G. Meissner, F. Krismer, D. Berg, P. Cortelli, R. Freeman, G. Halliday, G. Hoglinger, A. Lang, H. Ling, I. Litvan, P. Low, Y. Miki, J. Panicker, M. T. Pellecchia, N. Quinn, R. Sakakibara, M. Stamelou, E. Tolosa, S. Tsuji, T. Warner, W. Poewe and H. Kaufmann (2022). "The Movement Disorder Society Criteria for the Diagnosis of Multiple System Atrophy." Mov Disord **37**(6): 1131-1148.
Wenning, G. K., N. Stefanova, K. A. Jellinger, W. Poewe and M. G. Schlossmacher (2008). "Multiple system atrophy: a primary oligodendrogliopathy." Ann Neurol **64**(3): 239-246.
Wilke, C., E. Haas, K. Reetz, J. Faber, H. Garcia-Moreno, M. M. Santana, B. van de Warrenburg, H. Hengel, M. Lima, A. Filla, A. Durr, B. Melegh, M. Masciullo, J. Infante, P. Giunti, M. Neumann, J. de Vries, L. Pereira de Almeida, M. Rakowicz, H. Jacobi, R. Schule, S. A. Kaeser, J. Kuhle, T. Klockgether, L. Schols, S. C. A. n. s. group, C. Barro, J. Hubener-Schmid and M. Synofzik (2020). "Neurofilaments in spinocerebellar ataxia type 3: blood biomarkers at the preataxic and ataxic stage in humans and mice." EMBO Mol Med: e11803.
Wilke, C., D. Pellerin, D. Mengel, A. Traschutz, M. C. Danzi, M. J. Dicaire, M. Neumann, H. Lerche, B. Bender, H. Houlden, R. F. C. s. g. S. Zuchner, L. Schols, B. Brais and M. Synofzik (2023). "GAA-FGF14 ataxia (SCA27B): phenotypic profile, natural history progression and 4-aminopyridine treatment response." Brain.

8. Danksagung

Dank gilt meinem wissenschaftlichen Betreuer und Mentor im Bereich Neurologie und im Besonderen den Ataxien, Prof. Dr. Thomas Klockgether, der mir die vorliegenden klinisch-wissenschaftlichen Untersuchungen ermöglichte und meine berufliche und wissenschaftliche Entwicklung maßgeblich beeinflusste. Vielen Dank für die langjährige, konstruktive und zielorientierte Zusammenarbeit und Unterstützung.

Ich danke den Kolleg*innen und Mitarbeiter*innen, die meinen bisherigen beruflichen Weg mit mir beschritten haben, sowohl an der Klinik für Neurologie als auch dem Deutschen Zentrum für Neurodegenerative Erkrankungen. Hervorzuheben sind dabei die Kolleg*innen insbesondere meines ersten klinischen Einsatzgebietes, der Stroke Unit und Station 3, sowohl des pflegerischen Teams als auch Dr. Jens Reimann und Prof. Dr. Cornelia Kornblum und der Ataxieambulanz, im Besonderen Dr. Marcus Grobe-Einsler, Demet Önder und Dr. Berkan Koyak. Einen großen Dank möchte ich Dr. Felix Bode und Dr. Julian Zimmermann für freundschaftliche Unterstützung und das Ermöglichen der Forschungszeiten im Klinikalltag aussprechen. Am DZNE gilt mein besonderer Dank dem gesamten Team der Studienassistenz als auch Dr. Annika Spottke, Dr. Ina Vogt und Okka Kimmich sowie der gesamten Arbeitsgruppe für MR Physik unter der Leitung von Prof. Dr. Tony Stöcker.

Ein besonderer Dank geht an unsere Studienteilnehmer*innen, die durch ihre Teilnahme unsere wissenschaftliche Arbeit erst möglich machen.

Meinem Mann Jonathan und meinen beiden Töchtern, Hannah und Ulrike, gilt mein größter Dank für ihre bedingungslose Unterstützung zu jeder Zeit.

9. Wissenschaftlicher Lebenslauf

Aus Datenschutzgründen nicht angegeben.

10. Erklärung

Hiermit bestätige ich, dass ich die Richtlinien zur guten wissenschaftlichen Praxis der Universität Bonn, laut Habilitations-Ordnung, zur Kenntnis genommen habe und ich versichere, dass ich sie beim Verfassen der Habilitationsschrift beachtet habe. Insbesondere versichere ich, dass ich alle in der Habilitationsschrift benutzten Quellen und Hilfsmittel angegeben habe.

Bonn, den 20.05.2023

Dr. med. Jennifer Faber